Silicon Trackers for High Luminosity Colliders

Marco Bomben

Université Paris - Diderot

HABILITATION A DIRIGER DES RECHERCHES

Spécialité : " physique des particules "

présentée et soutenue publiquement par

Marco Bomben

le 26 mars 2018

Silicon Trackers for High Luminosity Colliders

Jury

Alessandra Tonazzo,	APC & Paris Diderot, Paris	Président du Jury
Dominik Dannheim,	CERN, Geneva	Rapporteur
François Le Diberder,	LAL & Paris Diderot, Paris	Rapporteur
Achille Stocchi,	LAL & Paris Sud, Paris	Rapporteur
Daniela Bortoletto,	University of Oxford, Oxford	Examinateur
Anna Macchiolo,	Max-Planck-Institut for Physics, Münich	Examinateur
Marc Winter,	IPHC, Strasbourg	Examinateur

A Simonetta

Acknowledgements

Contents

Foreword

I have started my career in experimental particle physics in November 2002, 2 days after having passed my last exam as undergraduate student. I joined the *BABAR* group of the "Università degli Studi di Trieste" to work on the semileptonic decay $\bar{B}^0 \to D^{*+}\ell^-\bar{\nu}_\ell$. That analysis was part of my "tesi di laurea" (master degree thesis); I studied the effects of hadronic form factor uncertainties on the decay branching ratio and the module of the Cabibbo Kobayashi Maskawa element V_{cb}. Everything was new and exciting for me; I remember with particular pleasure participating in collaboration meetings at SLAC, listening to interesting discussions about Monte Carlo, muon efficiencies (quite problematic...), soft pions, shape variables, trees and penguins... and then staying up late at night to understand the results of data fits with PAW and Minuit.

The work was done under the supervision of Prof. Livio Lanceri, who was Physics Analysis Coordinator of the *BABAR* collaboration at that time; I defended my "tesi di laurea" in November 2003, one week before the exam for the admission to the graduate program in physics. I got admitted and decided to keep working with the Trieste *BABAR* group.

During the first year of the PhD, 2004, I have worked on the completion of the analysis which was then published [1]; at that time it was the most precise determination of the most abundant neutral B meson decay - quite a nice start! Since the uncertainties due to the decay form factors were among the largest it was decided to determine at the same time the form factors and the branching ratio of the $\bar{B}^0 \to D^{*+}\ell^-\bar{\nu}_\ell$, together with $|V_{cb}|$ [2]. That work was carried together with the *BABAR* Trieste colleagues Dott. Fabio Cossutti and Dott. Giuseppe Della Ricca.

During the second year of my PhD I had the opportunity to spend 5 months at SLAC, as the on-call operation manager and data quality responsible of the *BABAR* silicon vertex tracker (SVT). I was very intimidated by the task since the SVT was *the BABAR* subdetector: its five shiny layers of double sided silicon microstrip sensors were making possible fundamental studies like CP violation in $B^0 \to J/\psi K_S^0$. It was a though period since the data taking was restarting after a stop of one year and there was a lot of pressure to take a lot of data. The PEP-II accelerator was breaking luminosity records one after the other but at the cost of problematic data taking conditions (high background, doses and dead time) for the SVT. Nonetheless I have enjoyed enormously that period; understanding the detector behaviour, working in close contact with colleagues of all around the world and discussing about possible improvements for the detector was the reason for keep working hard and doing my best despite the stressful situation. I remember in particular trying to understand the increase of the modules leakage current of one the external layers [3] made me interested about silicon detectors.

The topic of my PhD thesis was the measurement of CP violation in colour suppressed $b \to c$ decays. Working together with Dr. Chih-hsiang Cheng and Dr. Vitaly Eyges I had the opportunity to publish the first analysis of the $B^0 \to \overline{D}^{(*)0} h^0$ channel at the flavour

factories [4].

I successfully defended my PhD thesis in April 2007, again under the supervision of Prof. Livio Lanceri; from that moment on I have focused only on silicon tracking detector development for high luminosity colliders, which is indeed the subject of this manuscript, prepared to obtain the "Habilitation à Diriger des Recherches".

At that time I had decided to change research topic because I was interested in working on an experiment *from the beginning*, so to say. Part of the *BABAR* Trieste group was already involved in an R&D effort about a low mass silicon tracking system, the SLIM5 project. Together with Prof. Luciano Bosisio, Dott. Lorenzo Vitale, Dott. Irina Rashevskaya and Dott. Gabriele Giacomini I worked on characterising novel thin silicon strip detectors. Other than laboratory activity I have contributed to develop the reconstruction, analysis and simulation software for the SLIM5 demonstrator 2008 beam test [5], together with the colleagues from the Pisa group Dr. Nicola Neri and Dr. John Walsh. The experience within the SLIM5 project was great since I had the opportunity to follow almost all the project aspects concerning the strip detectors.

The SLIM5 project was also the opportunity to work with Dr. Giovanni Marchiori, whom I joined in September 2010 here at the "Laboratoire de Physique Nucléaire et de Hautes Energies" (LPNHE), to work on LHC radiation hard silicon pixel detectors for the High Luminosity phase of the ATLAS detector at the CERN Large Hadron Collider (LHC). Under the direction of my former *BABAR* colleague and *BABAR* SVT coordinator Dr. Giovanni Calderini I started investigating silicon detectors and test structures in the LPNHE clean room and working on TCAD (Technology Computer Aided Design) device simulations. We were working on the development of $n - on - p$ planar pixels within the ATLAS Upgrade Planar Pixel Sensor (PPS) R&D Project and in 2011 I was asked to become the beam test coordinator of the PPS collaboration. Over the years I had the opportunity to work with many master and PhD students from European, American and Japanese research Institutes, in CERN North Area experimental areas and at the DESY beam test facility. I was the coauthor of the publication summarising the PPS group beam test results. Together with Dr. Jens Weingarten of the II. Physikalischen Institut, Göttingen University, I have coordinated the work of two PhD students and published the results in 2012 [6].

Many more students defended their master and PhD theses which were based on data collected at beam tests coordinated by me.

At the LPNHE I have supervised 6 internships of undergraduate students since 2011; they worked with me on different topics, like measuring silicon detectors in the LPNHE clean room, performing TCAD simulation of edgeless pixel sensors[1] [7] for the High Luminosity LHC (HL-LHC), improving the clean room equipment and characterising pixel sensors prototypes. Other students from the LPNHE laboratory worked with me, either in clean room or at beam tests, for internships and PhD.

Among those students Audrey Ducourthial decided to continue working with me, and since October 2015 she is PhD student under my supervision in the LPNHE ATLAS group. Her main research topic is the development of silicon pixel sensors for the future ATLAS tracker, intended for the HL-LHC phase, and the analysis of the H Higgs boson decay to b quarks $H \rightarrow b\bar{b}$ channel.

She participated in many beam tests, measuring edgeless pixel prototypes developed in collaboration with the FBK foundry, and later reconstructing and analysing the data; the

---

[1]sensor characterised by a very slim un-instrumented area at the detector periphery

results have been recently published [8]. She also contributes to the modeling of radiation damage to pixel detectors: since 2017 an ATLAS Pixel sub-working group has been formed whose goal is to include in ATLAS Monte Carlo simulations the effects due to radiation damage to the ATLAS Inner Detector. Together with Dr. Benjamin Nachman of Lawrence Berkeley National Laboratory I coordinate this ATLAS working group which more than 10 master and PhD students, Audrey Ducourthial included, contribute to.

Radiation damage effects to pixel detectors could lead to a degradation of vertexing, tracking and jet flavour tagging performance. Together with Audrey Ducourthial I will work on assessing the impact of this degradation, in particular in the channel $H \rightarrow b\overline{b}$.

Audrey Ducourthial also started working on the optimisation of the jet flavour tagging algorithms for the HL-LHC ATLAS detector.

Memoir organisation

This memoir, prepared to obtain the "Habilitation à Diriger des Recherches", is the summary of my research activities after the PhD graduation. After an introduction to the context of my researches (Chapter 1) a discussion on silicon detectors will follow in Chapter 2. The motivations and main results of the SLIM5 project will be presented in Chapter 3, with a detailed discussion on strip detectors spatial resolution.

TCAD simulations are presented in Chapter 4, together with some case studies and applications. Chapter 5 summarises the LHC physics program, the ATLAS detector and in particular its pixel detector; it serves as an introduction to the next Chapter (6) where the modeling of radiation damage in detectors is presented, together with results for the current ATLAS data taking.

The new ATLAS Inner Tracker, intended for the Phase-II of the experiment, will be presented in Chapter 7; radiation hard and edgeless pixel sensors will be discussed in detail.

Finally research perspectives (Chapter 8) and a general summary of my past, present and planned activities will be given.

Whenever possible I have tried to include background material as an introduction to my research topics. Original contributions are to be found in Chapter 3 (Sections 3.5-3.7), Chapter 4 (Sections 4.1-4.4, 4.5.3, 4.6, 4.7), Chapter 6 and in Chapter 7 (Sections 7.4-7.6).

Chapter 1

Context and Motivations

To motivate the quest for silicon sensors for experiments at high luminosity collider it is necessary to present first the theoretical context for experimental particle physics. In this Chapter a short reminder of the Standard Model of particle physics will be presented, with a special focus on the Higgs mechanism for the quarks, which is responsible for the mixing of quarks and the violation of the CP symmetry in that sector.

1.1 Introduction

The Standard Model (SM) of particle physics [9–13] is the theory describing three of the four known fundamental forces in the universe (the electromagnetic, weak, and strong interactions), as well as classifying all known elementary particles in leptons, quarks, gauge and scalar bosons. In Figure 1.1 a schematic summary of the SM particles.
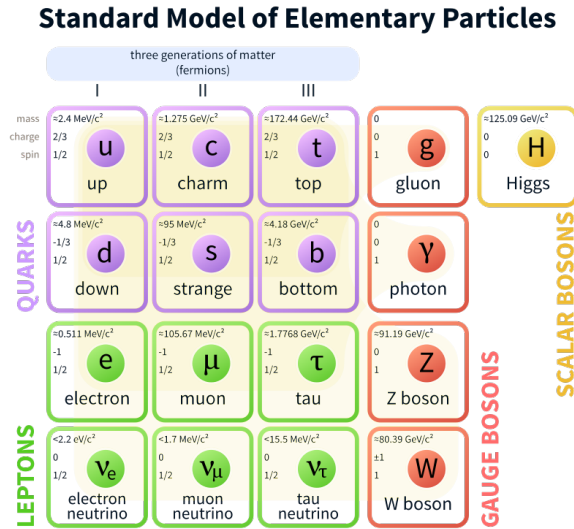
Figure 1.1: The Standard Model of elementary particles, with the three generations of matter, gauge bosons in the fourth column, and the Higgs boson in the fifth [14].

The last member that was added to the set of SM particles was the so called Higgs boson, proposed in the '60s of the last century (see for example [15, 16]), finally observed in 2012 by the ATLAS and CMS collaborations [17, 18]. All massive SM particles acquire their rest mass by the interaction with the Higgs field, with different mechanisms for quarks

and leptons (the "fermions") and for bosons. The details of the mechanism for the quarks will be presented in the next Section.

1.2 Mass terms in Standard Model Lagrangian and Quarks Mixing

As anticipated in the previous Section, in SM the elementary particles gain their mass through the so-called Higgs mechanism. Adding a scalar field with a vacuum expectation value v, the Lagrangian has appropriate mass terms. The simplest model uses a Higgs doublet scalar field:

$$\phi = \begin{pmatrix} \phi^+ \\ \phi^0 \end{pmatrix} \tag{1.1}$$

where $\phi^{0,+}$ are complex fields.

The Yukawa couplings of fermions to Higgs field in the SM Lagrangian are given by:

$$\mathscr{L}_Y = -\sum_{i,j} \left(g_d^{ij} \overline{Q}_L^i \phi d_R^j + g_u^{ij} \overline{Q}_L^i \overline{\phi} u_R^j + g_\ell^{ij} \overline{L}_L^i \phi \ell_R^j \right) + \text{h.c.} \tag{1.2}$$

where Q(L) represents the left handed quarks (leptons) doublets, the indices i,j run over the generations of fermions and $\overline{\phi}$ is the SU(2) doublet conjugate of ϕ. Couplings g_u, g_d and g_ℓ are in general represented by complex matrices.

Inserting the expectation value v in the Yukawa Lagrangian 1.2, we obtain:

$$\mathscr{L}_Y = -\sum_{k=u,d,\ell} \overline{k}_L \mathscr{M}_k k_R \tag{1.3}$$

where $\mathscr{M}_k^{ij} = v g_k^{ij}$ are mass matrices. In general these matrices are not diagonal and therefore introduce mixing between the different generations of quarks. Hence, the SM Lagrangian is not expressed in terms of mass eigenstates but instead in terms of the eigenstates of the weak interactions. We can, however, rewrite the fields using a unitary transformation:

$$\begin{aligned} u_l &= V_L^u u_L' &,& \quad u_R = V_R^u u_R' \\ d_l &= V_L^d d_L' &,& \quad d_R = V_R^d d_R' \end{aligned} \tag{1.4}$$

so $\mathscr{M}' = V_L^{\dagger k} \mathscr{M}_k V_R^k$ is the diagonal mass matrix.

Quark mass eigenstates are different from weak interaction eigenstates; we may want to write weak interactions in the mass eigenstate base.

Charged current weak interactions can be described in SM by the product of an operator J^μ (with $V - A$ structure) and the W boson:

$$\mathscr{L}_{int} = -\frac{g}{\sqrt{2}} (\mathscr{J}^\mu W_\mu^+ + \mathscr{J}^{\mu\dagger} W_\mu^-) \tag{1.5}$$

where g is the weak charge related to Fermi coupling constant by $G_F/\sqrt{2} = g^2/8M_W^2$, where M_W is the W boson mass.

Weak charged current for quarks are written then in this way:

$$\mathscr{J}^\mu = \sum_{i,j} V_{ij} J_{ij}^\mu = \sum_{i,j} \overline{u}_i' \gamma^\mu \frac{1}{2} (1 - \gamma_5) V_{ij}^{\text{CKM}} d_j' \tag{1.6}$$

where V_{ij}^{CKM} are the terms of Cabibbo, Kobayashi and Maskawa (CKM) matrix [19, 20], which is defined as $V_L^{\dagger u} V_L^d$ (see eq. 1.4), and is usually written in this form:

$$
V = \begin{pmatrix} V_{ud} & V_{us} & V_{ub} \\ V_{cd} & V_{cs} & V_{cb} \\ V_{td} & V_{ts} & V_{tb} \end{pmatrix} \tag{1.7}
$$

Quark mixing idea was first introduced by Cabibbo [19] in 1963 to explain weak transition among different quark generations. Christensen *et al.* [21] observed CP violation in neutral kaon system in 1964 Kobayashi and Maskawa [20] in 1973 proposed a third quark family and a complex phase in quark mixing matrix to accommodate CP violation in Standard Model (SM).

Quark mixing matrix parameters are unbounded from theory and need to be experimentally determined.

1.3 Tracking and Vertexing for Experimental Particle Physics

All the theoretical predictions about elementary particles presented in the previous sections (and many more) have been validated thanks to decades of experiments. In experimental particle physics we want to reconstruct the tracks and energy deposits of particles produced in collisions and measure their characteristics, like: energy, momentum, charge, and their lifetime, if it applies. If we now restrict to short-lived charged particles we can measure their decay vertex thanks to the reconstruction of the trajectories of their decay products; the distance between the production and the decay vertex is proportional to the lifetime of the particle (see also Figure 1.2).
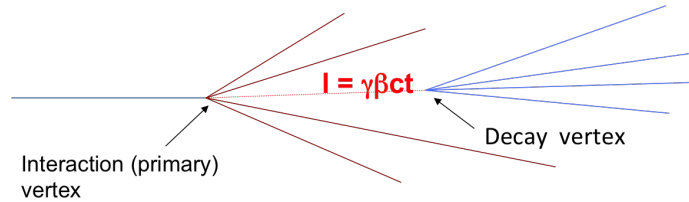
Figure 1.2: Schematic view of production and decay vertex of heavy flavour particles.

Lifetimes of τ leptons, charm and beauty hadrons range from 0.2 to 1.5 ps; these ranges of lifetimes means that these particles fly distances of single millimetres from the interaction vertex inside modern high energy physics experiments. To achieve the measurement goals we set above we then need particle detectors with sub-millimeter precision.

To *tag* the flavour of particles, like *b* and *c* quarks, the fact that hadrons containing bottom and charm quarks have sufficient lifetime that they travel some distance before decaying is exploited. A sketch illustrating the tagging of jets of particles that stemmed from a *b*-quark is shown in Figure 1.3. The flavour tagging algorithms, used for example by the ATLAS collaboration (see Chapter 5) look for tracks with significant impact parameters, secondary vertices and more sophisticated combinations of the two. The level of precision required will be discussed in the next Section.

Another example of the spatial precision required by particle physics comes from the so called "B Factories". At the Stanford Linear Accelerator Center (SLAC) asymmetric-energy electron-positron collider PEP-II [23] the $\Upsilon(4S)$ resonance was produced with a net boost in the laboratory frame. This configuration allowed to separate the subsequent
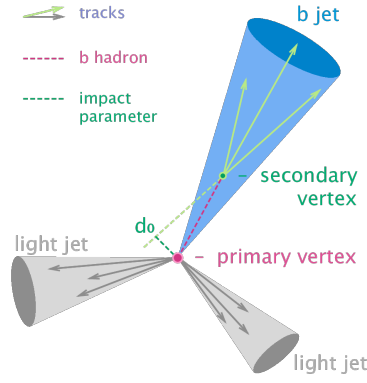
Figure 1.3: Diagram showing the common principle of identification of jets initiated by b-hadron decays (After [22])

decay vertices of the two B mesons produced by the $\Upsilon(4S)$ decay. In Figure 1.4 a schematic view of the working principle of the B Factories.
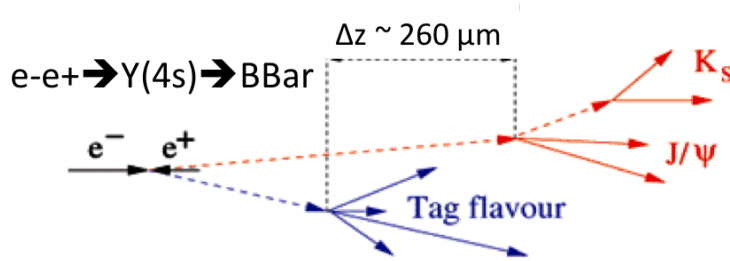
Figure 1.4: Schematic view of the B Factories working principle. The two B's decay vertices are separated by $\Delta z \sim \gamma\beta c\tau_b$

Thanks to the Lorentz boost $\beta\gamma$ of about 0.56 the decay vertices of the two B mesons could be separated by about 260 µm along the beam axis. Hence, to precisely measure these two vertices a detector with a spatial resolution of the order of $260/3 \sim 80$ µm was needed. The *BABAR* detector [24] recorded the events produced at the PEP-II collider; at the core of the *BABAR* detector there was the *BABAR* Silicon Vertex Tracker (SVT), the most relevant detector for the measurement of time dependent CP asymmetries in *BABAR*. The *BABAR* SVT was composed of five roughly cylindrical detection layers, made of double sided silicon strip modules. In order not to degrade by more than 10% the precision of CP violation measurements, the resolution was required to be better than 80 µm on fully reconstructed B decay vertices.

1.4   Space Point and Secondary Vertex Measurements

We now analyse the achievable precision on momentum resolution and on secondary vertex reconstruction; the goal is to understand their dependence on the geometry of the tracker, on its material budget and its measurement precision.

The base of tracking and vertexing is the measurement of space-points, *i.e.* the 3D position of the track traversing the sensing layer. This is the result of electrons and holes, produced by the track passing through the sensor bulk, collected by the sensing electrodes and digitised by the readout electronics. Diffusion and Lorentz angle deviation can deteriorate the space-point measurement precision; more details in Chapters 2 and 3.

Assuming a space point-resolution of σ_{point}, the (transverse) momentum resolution is well described by [25–27]:

$$\frac{\sigma_{p_T}}{p_T} = \left(\frac{p_T}{0.3|z|} \frac{\sigma_{point}}{L^2 B} \sqrt{\frac{720}{N+4}} \right) \oplus \left(\frac{\sigma_{p_T}}{p_T} \right)_{MS} \tag{1.8}$$

where p_T is the particle momentum (in GeV/c) transverse to the magnetic field B (in Tesla); L is the radial length, in meters (the space point-resolution of σ_{point} is measured in meters too). N is the number of equidistant measuring layers in the tracker and for this formulation it is assumed to be large. As it can be seen from Equation 1.8, other than a good space-point resolution, it is also important to have a large magnetic field and a long tracker lever arm; the latter in particular enters quadratically in the formula.

The charged particles ionise the medium through Coulomb interactions, which involve energy and *momentum* exchanges, hence the particle being tracked is subject to many (small) deflections. The collective term for all these deflections is *multiple scattering* (MS). The extrapolation from the detecting layer closest to the interaction point to the primary vertex has a slope that is smeared by θ_{MS} due to MS effects which is equal to [26]:

$$\theta_{MS} \approx \frac{0.0136\,\text{GeV/c}}{\beta p} \sqrt{\frac{x}{X_0}} \tag{1.9}$$

where p is the particle momentum, β its velocity in units of the speed of light, x is the material thickness and X_0 its radiation length. MS deteriorates the momentum resolution by [27][1]:

$$\left(\frac{\sigma_{p_T}}{p_T} \right)_{MS} = \frac{0.054}{\beta BL} \sqrt{\frac{x/\sin\theta}{X_0}} \tag{1.10}$$

with L and B as in Equation 1.8. Here $(x/\sin\theta)/X_0$ is the material thickness traversed by the particle, expressed in units of radiation length X_0, when the particle crosses the detector at an angle θ with respect to the detector surface.

As an example, the resolution of a 1 GeV/c p_T track in a L = 1 m, N = 10 layers tracker, immersed in a B =1 T solenoidal field, is about 1.0% if the space-point resolution σ_{point} is about 10 μm for tacks at normal incidence; the result is dominated by MS effects. For a 100 GeV/c p_T the resolution is about 2.0% and it is dominated by the error on the curvature measurement (first term of Equation 1.8).

The error on the secondary vertex reconstruction is linked to the precision on the transverse impact parameter d_0 [27]:

$$\sigma_{d0} \approx \frac{\sigma_{point}}{\sqrt{N}} \sqrt{1 + \frac{12(N-1)}{N+1}\left(\frac{r}{L}\right)^2} \oplus \theta_{MS} r_{pv} \sqrt{\frac{N(2N-1)}{6(N-1)^2}} \tag{1.11}$$

where the first term results from the extrapolation from the tracker to the primary vertex with r/L being the ratio of the extrapolation distance to the tracker length. It is clear it is better to have the first layer as close as possible to the interaction point (small r), and then have the outermost layer as far as possible (large L); increasing the number N of measurements help (central limit theorem); the resolution depends linearly on the space-point resolution. The second term is due to multiple scattering, where θ_{MS} is the multiple scattering angle (presented in Equation 1.9), and and r_{pv} the distance of the first layer to the primary interaction vertex. Minimising material and getting one layer as close as

---

[1]The formula reported in this manuscript is correct; the one in version v2 of [27] on arXiv is wrong. This was clarified in private discussion with the authors.

possible to the primary vertex helps; on the contrary, adding many layers here doen not help since each layer adds to the material budget, hence makes the MS effect more and more important.

For a 4-layer geometry like in ATLAS (see Figure 5.4) and a material thickness of typically around 3% X_0 this yields [27]:

$$\sigma_{d_0} \approx \frac{90\,\mu m\,GeV/c}{p} \oplus 7\mu m \tag{1.12}$$

1.5 Summary

The few examples above show the importance of sub-millimeter precision in determining elementary particles production and decay vertices, not only to measure particles' lifetimes but also to make fundamental measurements possible, like assessing the CP violation in the B meson sector. We will see in the next Chapter why silicon detectors are the standard choice for tracking and vertexing in High Energy physics experiments.

Chapter 2

Silicon Detectors for High Energy Physics

Pixel and strip detectors realised on high resistivity silicon substrates are nowadays the standard choice for high energy physics experiments. In this Chapter an introduction to silicon detectors will be given, focusing on those aspects that are relevant for the purpose of tracking and vertexing. Excellent books and reviews on the subject exists, like [27–34]. Here some extracts from those will be reported, just to introduce the subject. After reviewing the semiconductor basics (Section 2.1) and introducing the fundamental ideas about the $p-n$ junction (Section 2.2), a brief discussion on the Silicon dominance over the other semiconductors will be presented in Section 2.3. Silicon detectors and trackers will be presented in Section 2.4, before concluding the Chapter introducing the basic ideas about radiation damage in silicon (Section 2.5), and with a short summary (2.6).

2.1 Semiconductor Basics

In this Section only the concepts and equations that will be relevant for the discussion in the subsequent Chapters will be reviewed.

2.1.1 Crystals and Energy Bands

The physics of semiconductor devices is naturally dependent on the physics of semiconductor themselves [29]. In this brief introduction only crystalline semiconductors will be treated, with a particular focus on silicon. Most commonly used semiconductors are crystals with diamond (Si and Ge) or zinc blende (*e.g.* GaAs) lattice type. In Figure 2.1 a schematic view of the two arrangements is presented.
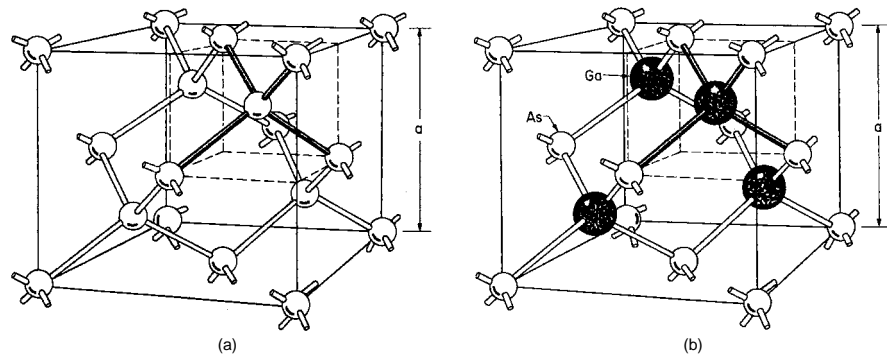
Figure 2.1: Diamond (a) and zinc blend (b) lattice. (After [28])

Due to the Pauli exclusion principle, electrons in crystals are organised in energy bands, each one containing many closely spaced levels; Figure 2.2 helps in picturing the situation for diamond lattice. At very large distances each atom has the same two energy levels; the energy levels are N-fold degenerate (N being the number of atoms), they indeed split into N closely spaced levels when the atoms are brought close together. For $N \rightarrow \infty$, one speaks of energy bands, rather than levels, and these bands broaden, merge and split again with even closer spacing [28].
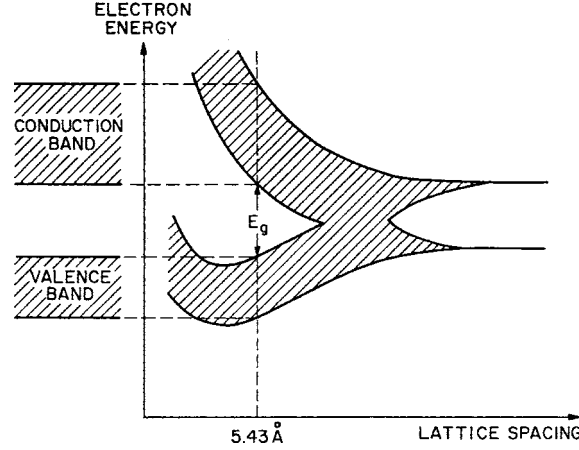
Figure 2.2: Energy levels of silicon atoms arranged in a diamond structure, as a function of lattice spacing. (After [28])

The spacing corresponding to silicon is indicated in Figure 2.2 and corresponds to the minimum total energy of the electrons and the lattice, not very far from the minimum energy of the electrons in the filled valence band. At low temperature one has a completely filled valence band and an empty conduction band; at room temperature the thermal energy is high enough to lift a few electrons to the conduction band, thus creating a weak conductivity due to free electrons and electrons vacancies, *i.e.* holes. In Figure 2.3 the energy band structures of several materials are reported, including semiconductors.
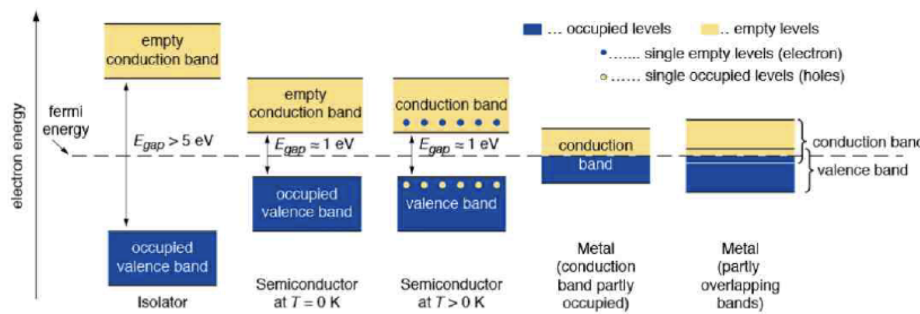
Figure 2.3: Energy band structure of several materials. For semiconductors the T = 0 K and T > 0 K situations are reported; for metals two possible band configurations are represented (After [31]).

The structure of an isolator, or insulator, is similar to that of a semiconductor, except that the band gap is much larger so that the occupation probability of states in the conduction band is zero. Conductors may either have overlapping valence and conduction bands or a partially filled conduction band. We can conclude that the main difference between conductors, semiconductors and insulators is the value of the band gap energy E_g.

12
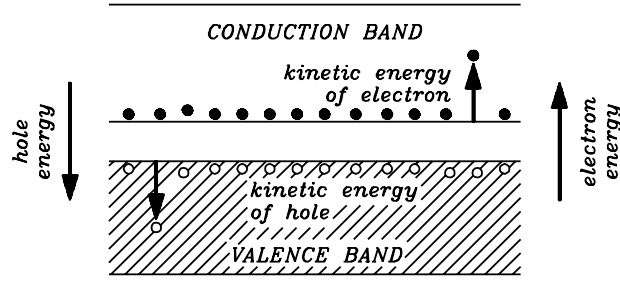
Figure 2.4: Potential and kinetic energy in the band representation (After [28]).

Focusing on the dynamics of carriers in crystalline materials, it can be proven that electrons in the conduction band and holes in the valence band are similar to free particles but with an effective mass (m_n^*, m_p^*) different from elementary electrons not imbedded in the lattice. This mass is furthermore dependent on other parameters such as the direction of movement with respect to the crystal axis. The kinetic energy of electrons is measured from the lower edge of the conduction band upwards, that of the holes downward from the upper edge of the valence band; Figure 2.4 presents the energy diagram for free electrons and holes in lattice.

This simplified picture presents important limitations; in particular it neglects the relative position in lattice reciprocal space of the minimum conduction band and the maximum of the valence band. If there is no difference among the two positions then the semiconductor is said to have "direct" bandgap; otherwise it is an indirect semiconductor. Figure 2.5 shows the difference between indirect semiconductors, like Silicon and Germanium, and direct ones, like Gallium Arsenide.
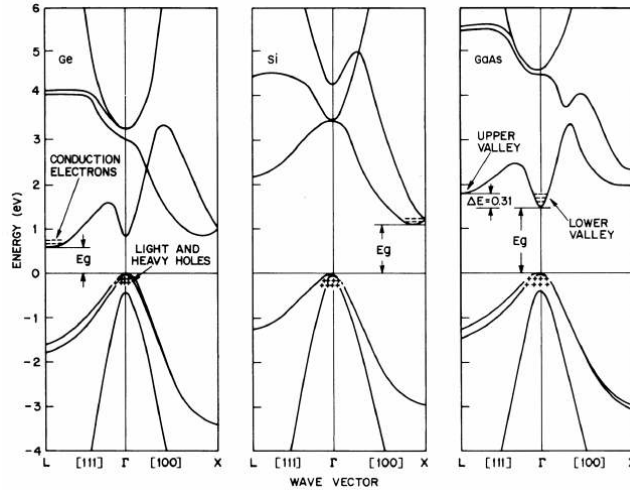
Figure 2.5: Germanium (left), Silicon (center) and Gallium Arsenide (right) band structures. (Bottom) valence bands; (top) conductive bands.

For indirect semiconductors, the process of creation or annihilation of an electron-hole pair requires not only a quantum of energy, like a photon, but also a net lattice momentum transfer, thanks to phonons. In Silicon at room temperature the bandgap energy value is of about $E_g \sim 1.12$ eV, while the mean ionisation energy ϵ is ~ 3.6 eV: the difference is due to the distance in the lattice reciprocal space of the edge of the conductive and the valence band.

2.1.2 Extrinsic Semiconductors and Doping

Intrinsic semiconductors contain a very limited number of impurities compared with the number of thermally generated electrons and holes. Electron states with energy E are occupied following the Fermi-Dirac statistics:

$$F(E) = \frac{1}{1 + \exp\left(\dfrac{E - E_F}{kT}\right)} \tag{2.1}$$

where E_F, the Fermi energy, is the energy at which the occupation probability of a (possible) state is one half, k is the Boltzmann constant and T is the absolute temperature. In Intrinsic semiconductors electrons and holes exist on account of thermal creation of electron-hole pairs, so we have:

$$p = n, \tag{2.2}$$

i.e. the concentration of electrons n equals that of holes p. We will assert the mass action law for semiconductors:

$$np = n_i^2 \tag{2.3}$$

where n_i is the *intrinsic carrier concentration*. The intrinsic carrier concentration depends only on the temperature T, the effective mass of the carriers m^* and the band gap energy E_g [28].

Intrinsic semiconductors are rarely used in semiconductor devices since it is extremely difficult to obtain sufficient purity in the material. Moreover, in most cases one intentionally alters the property of the material by adding small fractions of specific impurities. This procedure is called *doping*. Doping is the replacement of a small number of atoms in the lattice by atoms of neighbouring columns from the atomic table (with one valence electron more or less compared to the basic material). Depending on the type of added material, one obtains $n-$type semiconductors with an excess of electrons in the conduction band or $p-$types with additional holes in the valence band.

Doping Silicon with an element of the V group (P, As, Sb) leaves a valence electron of dopant atom loosely bound; those atoms are identified as *donor* dopants. The energy level of the donor is just below the edge of the conduction band; at room temperature most electrons are raised from the donor dopant to the conduction band. The doping with donors is illustrated in Figure 2.6. A semiconductor doped with donors is called a $n-$type semiconductor. There is an imbalance between electrons over holes in n-type semiconductors; electrons are the majority carriers, while holes the minority ones.

Doping Silicon with an element of the III group (B, Al, Ga, In) leaves one valence bond open; those atoms are identified as *acceptor* dopants. The energy level of the acceptor is just above the edge of the valence band; at room temperature most levels are occupied by electrons leaving holes in the valence band. The doping with acceptors is illustrated in Figure 2.7. A semiconductor doped with acceptors is called a $p-$type semiconductor. There is an imbalance between holes over electrons in p-type semiconductors; holes are the majority carriers, while electrons the minority ones.

In a doped semiconductor the relation $n = p$ does not hold, while the mass action law (Eqution 2.3) still does. Semiconductors where $n \neq p$ are called *extrinsic*. In a doped semiconductor electrons are merely redistributed among the various energy states, but not taken out of or put into the semiconductor itself, the crystal remains electrically neutral. The equation that states this charge-neutrality condition reads:
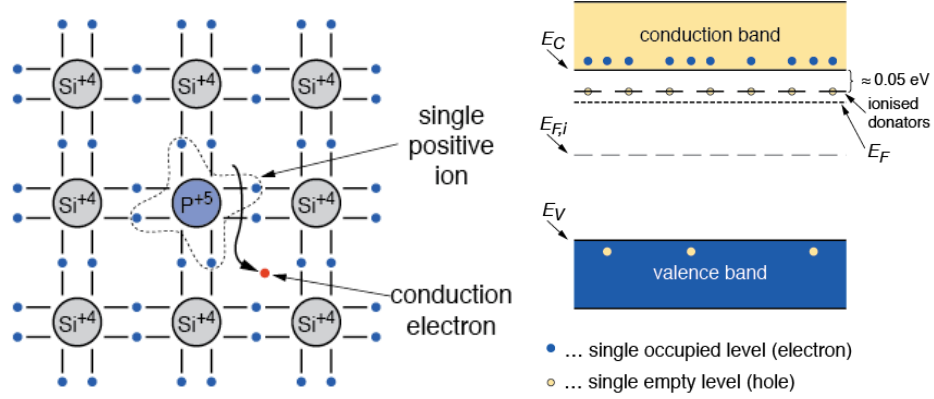
Figure 2.6: Doping Silicon with donor atoms. (Left) atom bonds with donor dopant; (right) energy bands diagram after donor doping. (After [31])
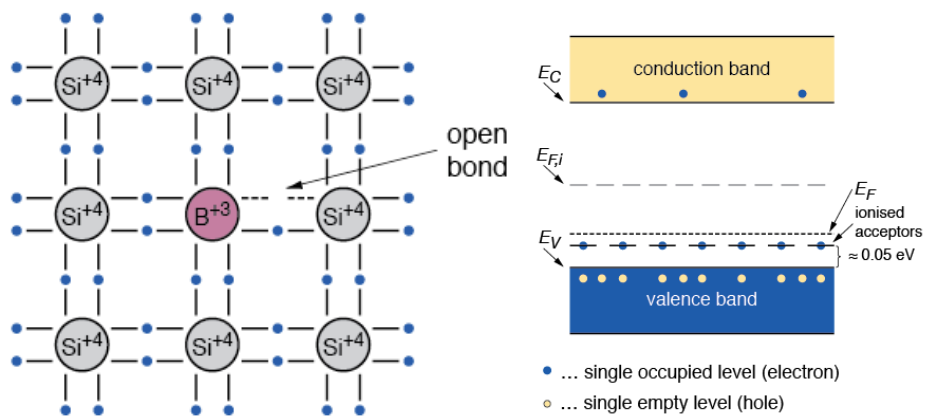
Figure 2.7: Doping Silicon with acceptor atoms. (Left) atom bonds with acceptor dopant; (right) energy bands diagram after acceptor doping.(After [31])

$$n + N_a^- = p + N_d^+, \tag{2.4}$$

where $N_{a(d)}^{-(+)}$ represent the charge density of ionised acceptors (donors) respectively. At room temperature dopants are normally ionised so it is safe to assume that $N_a^- \simeq N_a$ and $N_d^+ \simeq N_d$, hence $n - p = N_d - N_a$. From charge neutrality and mass action law it can be easily shown that for an n-type semiconductor the concentration of electrons n is equal to that of the donor dopants N_d to a very good level; with the same reasoning in a p-type semiconductor the concentration of holes p is equal to that of the acceptor dopants N_a.

The Fermi level for the intrinsic semiconductor E_i lies very close to the middle of the bandgap. When impurity atoms are introduced, the Fermi level must adjust itself to preserve charge neutrality. We assert that the in an n-type semiconductor where the donors concentration is N_d the Fermi level at temperature T is:

$$E_F = E_C - kT \ln\left(\frac{N_c}{N_d}\right) \tag{2.5}$$

where N_c is the effective density of states in the conduction band. Similarly, in a p-type semiconductor where the acceptors concentration is N_a the Fermi level at temperature T is:

$$E_F = E_V + kT \ln\left(\frac{N_v}{N_a}\right) \tag{2.6}$$

where N_v is the effective density of states in the valence band.

The Equations 2.5 and 2.6 can be expressed also as a function of the electrons and holes thermal equilibrium concentration n, p, and the intrinsic carrier concentration n_i, to evaluate the distance of the Fermi level E_F from the intrinsic value E_i in an extrinsic semiconductor:

$$E_F = E_i + kT \ln\left(\frac{n}{n_i}\right) \tag{2.7}$$

$$E_F = E_i - kT \ln\left(\frac{p}{n_i}\right) \tag{2.8}$$

2.1.3 Carrier Transport in Semiconductors and Continuity Equations

So far only semiconductors in equilibrium have been considered. We will now deal with semiconductors out of equilibrium through the application of an external voltage or because hit by light. These conditions will lead to an inhomogeneous distribution of charge carriers that we will describe through the *continuity equations*. But before getting to the continuity equations let's review very briefly the mechanisms of transport of the carriers, the drift and the diffusion.

If an electric field is present the charge carriers will be accelerated in between random collisions with the lattice (the typical time between collisions τ_c is of about 10^{-12} s), in a direction determined by the electric field and a net average drift velocity will be obtained, equal to:

$$\vec{v}_n = -\frac{q\tau_c}{m_n}\vec{E} = -\mu_n\vec{E} \tag{2.9}$$

$$\vec{v}_p = \frac{q\tau_c}{m_p}\vec{E} = \mu_p\vec{E} \tag{2.10}$$

where $\vec{v}_n$ and $\vec{v}_p$ are the drift velocities. The parameters μ_n, μ_p are the electrons and holes mobilities, respectively. For fields small enough the mobilities are constant, while at large fields the carrier velocities reach their saturation values $v_{s,n}$ and $v_{s,p}$. Other than on the electric field mobilities depend on temperature, and doping levels too.

If we now consider an inhomogeneous distribution of free charge carriers in a semiconductor crystal and neglect all effects that are due to electric fields it can be shown that there is a net flow of charges that smooths the charge distribution. This effect is called diffusion and it is mathematically described by the diffusion equation:

$$\vec{F}_n = -D_n \nabla n \tag{2.11}$$

$$\vec{F}_p = -D_p \nabla p \tag{2.12}$$

Here $\vec{F}_{n,p}$ are the fluxes, $D_{n,p}$ the diffusion constants and n, p the carrier concentrations, of electrons and holes respectively.

Combining the effects of drift and diffusion, one obtains the current densities:

$$\vec{J}_n = q\mu_n n \vec{E} + q D_n \nabla n \tag{2.13}$$

$$\vec{J}_p = q\mu_p p \vec{E} - q D_p \nabla p \tag{2.14}$$

q is the absolute value of the charge of the electron.

Mobility and diffusion are related to each other by the Einstein equation:

$$D_n = \frac{kT}{q}\mu_n \tag{2.15}$$

$$D_p = \frac{kT}{q}\mu_p \tag{2.16}$$

In a semiconductor, electrons and holes are constantly generated by thermal excitation of electrons form the valence band to the conduction band. We call G the generation rate per unit of volume and R the recombination rate per unit of volume. The generation process is counterbalanced, under thermal equilibrium, by a recombination process in which electrons and holes annihilate each other. When excess carriers are present the recombination process outweighs the generation one. There are two basic processes by which electrons and holes may recombine with each other. In the first process electrons from the conduction band make direct transition to vacant states in the valence band. In the second process electrons and holes recombine through intermediary states known as *recombination centers*. The recombination centers are usually impurities and lattice imperfections of some sort. We define the recombination lifetime τ_r the average time it takes for a minority carrier to recombine.

Now we can write the continuity equations which will describe the change in carrier concentration as the result of the drift, diffusion, generation and recombination phenomena:

$$\frac{\partial n}{\partial t} = \frac{1}{q}\nabla \cdot \vec{J}_n + G_n - R_n \tag{2.17}$$

$$\frac{\partial p}{\partial t} = \frac{-1}{q}\nabla \cdot \vec{J}_p + G_p - R_p \tag{2.18}$$

The electric field E is linked to the charge distribution ρ by the Poisson's equation:

$$\nabla \cdot \vec{E} = \frac{\rho}{\epsilon_{sc}\epsilon_0},\qquad(2.19)$$

where ϵ_{sc} is the relative permittivity of the semiconductor.

If in addition of an electric field a magnetic field is present too the path followed by electrons and holes is (on average) no longer parallel to the electric field. The movement of electrons and holes in the simultaneous presence of an electric and magnetic field is shown diagramatically in Figure 2.8 (in Silicon $H \sim B/\mu_0$, where μ_0 is the vacuum permeability). The angular deviation $\theta_{n,p}$ from the electric field direction is called "Lorentz
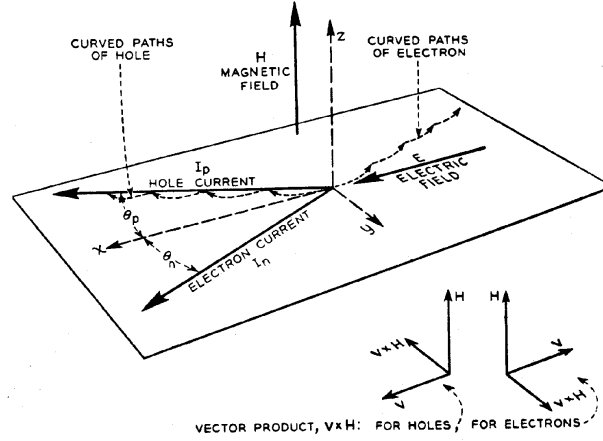
Figure 2.8: Electron and hole current in relation to electric and magnetic field. (After [32]).

angle"; its value is related to the magnitude of the magnetic field B and the Hall mobilities $\mu_{n,p}^{H}$[1]:

$$\tan\theta_{n,p} = \mu_{n,p}^{H}B\qquad(2.20)$$

2.2 The p-n Junction

At the interface of an n-type and p-type semiconductor the difference in the Fermi levels cause diffusion of surplus carries to the other material until thermal equilibrium is reached. At this point the Fermi level is equal. The remaining ions create a space charge and an electric field stopping further diffusion. The stable space charge region is free of charge carries and is called the depletion zone. In Figure 2.9 a p-n junction in thermal equilibrium, before and after its parts are brought in contact.

By applying an external voltage the depletion zone can be shrunk or enlarged. For particle detection purpose we are interested in maximising the depletion zone: within it there are virtually no free carriers and there is an electric field allowing the collection of the free carriers created by the ionising particles.

By looking at Figure 2.9 it is clear that to deplete more the junction volume a potential more positive on the n-side than on the p-side should be applied; we will refer to this polarisation as *reverse bias* voltage.

In the following we will restrict ourselves to abrupt junctions, *i.e.* when the doping of both p- and n-type sides of the junction are uniform. Moreover we will consider only the case of asymmetric junctions, where one of the two sides is heavily doped, much more

---

[1]they differ from the drift mobilities
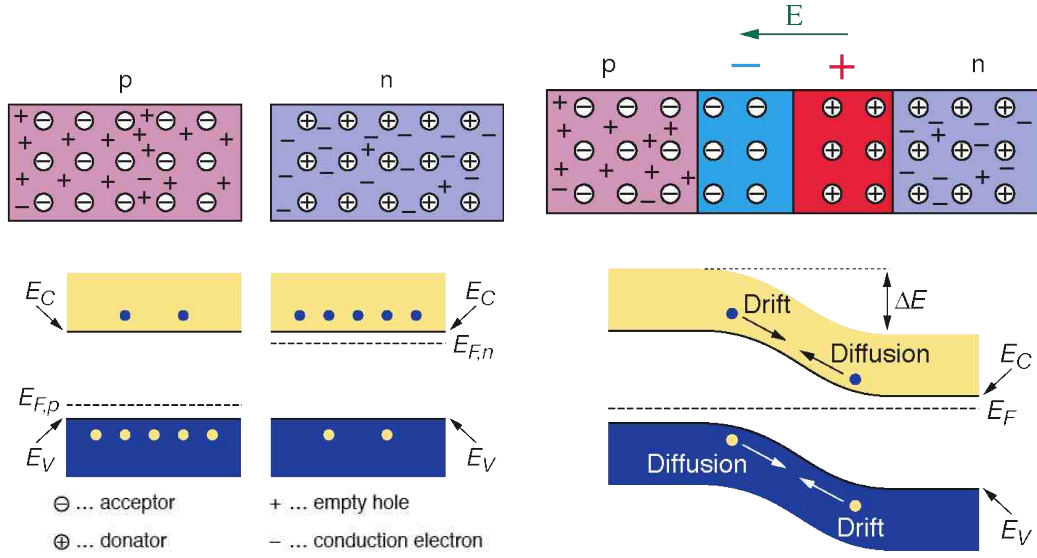
Figure 2.9: P-n junction formation. (Left) Two oppositely doped semiconductors are compared. (Rigth) The p-n junction is formed. (After [31]).

doped than the other one[2]. The heavily doped side is usually indicated with a +, hence we will talk of $p^+ - n$ and $n^+ - p$ junctions. In Figure 2.10 the charge distribution of an abrupt asymmetric $n^+ - p$ junction is depicted; the dopant concentration, the resulting bulk effective doping concentration and the bulk thickness are indicated too.
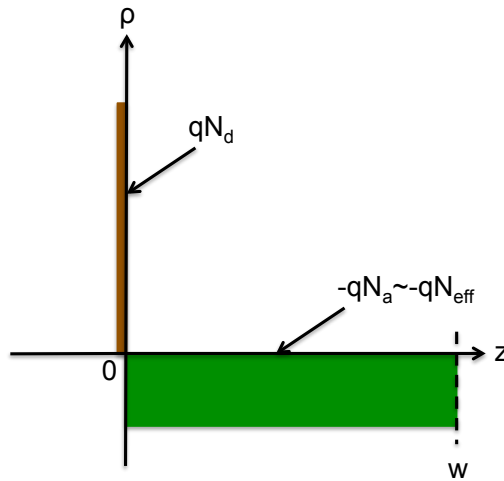
Figure 2.10: Charge distribution in an abrupt asymmetric $n^+ - p$ junction.

To estimate the voltage needed to completely deplete the junction bulk we introduce the concept of *effective doping concentration* N_{eff}:

$$N_{eff} = N_d - N_a \tag{2.21}$$

which will reduce to simply N_d for $p^+ - n$ junctions and $-N_a$ for $n^+ - p$ junctions. By integrating twice the Poisson's equation over the semiconductor thickness we get the voltage needed to achieve the complete depletion of the junction volume, the so-called *depletion*

---

[2]The way in which these junctions are fabricated is beyond the scope of this report

voltage V_{depl}, whose absolute value is equal to:

$$V_{depl} = \frac{q|N_{eff}|w^2}{2\epsilon_{sc}\epsilon_0} \tag{2.22}$$

where w is the total thickness of the lightly doped semiconductor volume. We stress the fact that the depletion voltage V_{depl} depends linearly on the effective doping concentration N_{eff} and quadratically on the semiconductor volume w.

Particle detectors exploiting the $p-n$ junction properties are labelles according to the type of the bulk: p-type detectors feature a p-type bulk, the opposite goes for $n-$type detectors.

If the applied voltage is less than the depletion one we can evaluate the depletion extension d_{depl} using again the Poisson's equation. It is instructive to express the result using the *resistivity* ϱ of the doped semiconductor:

$$\varrho^{-1} = q(N_a\mu_p + N_d\mu_n) \simeq qN_{eff}\mu \tag{2.23}$$

In Equation 2.23 first the most general expression is presented (under the assumption that the carriers concentrations are dominated by the dopants), then the approximated value for an abrupt and asymmetric junction is given; μ is the mobility of the majority carriers. We can then express the depletion extension d_{depl} as:

$$d_{depl} = \sqrt{2\epsilon_{sc}\epsilon_0\mu\varrho|V|} \tag{2.24}$$

Comparing Equations 2.22 and 2.24 a useful relation for under-depleted semiconductor bulks can be found:

$$d_{depl} = \sqrt{\frac{V}{V_{depl}}}\,w \tag{2.25}$$

where $V(< V_{depl})$ is the absolute value of the applied bias voltage.

In nowadays trackers for experiments at high energy colliders high resistivity materials are used ($\varrho \sim$ serveral kΩcm); hence, for thicknesses w of few hundreds of microns depletion voltages of (far) less than 100 V are achieved.

In $p-n$ junctions under reverse bias an electric field is present; if we refer to the case represented in Figure 2.10 the electric field distribution at depletion voltage along the bulk is like the one shown in Figure 2.11. The electric field depends linearly on the bulk depth z, with a maximum at the junction; the maximum value is proportional to the effective doping concentration.

Still referring to Figure 2.11, if a bias V greater than the depletion voltage V_{depl} is applied the electric field will have the following dependence on bulk depth z:

$$|\vec{E}(z)| = \frac{2V_{depl}}{w}\left(1 - \frac{z}{w}\right) + \frac{V - V_{depl}}{w} \tag{2.26}$$

The relation between the magnitude of the electric field and the position along the bulk is still linear but now the electric field is non-zero everywhere. The bulk is said to be over-depleted.

We have seen that the depleted region thickness d_{depl} grows proportionally to the square root of the applied (reverse) voltage V (Eq. 2.25). A partially depleted abrupt asymmetric junction can be modelled as a parallel plate capacitor where metallic plates are separated by d_{depl}. In the limit when $V < V_{depl}$ it's then easy to derive the junction capacitance C:
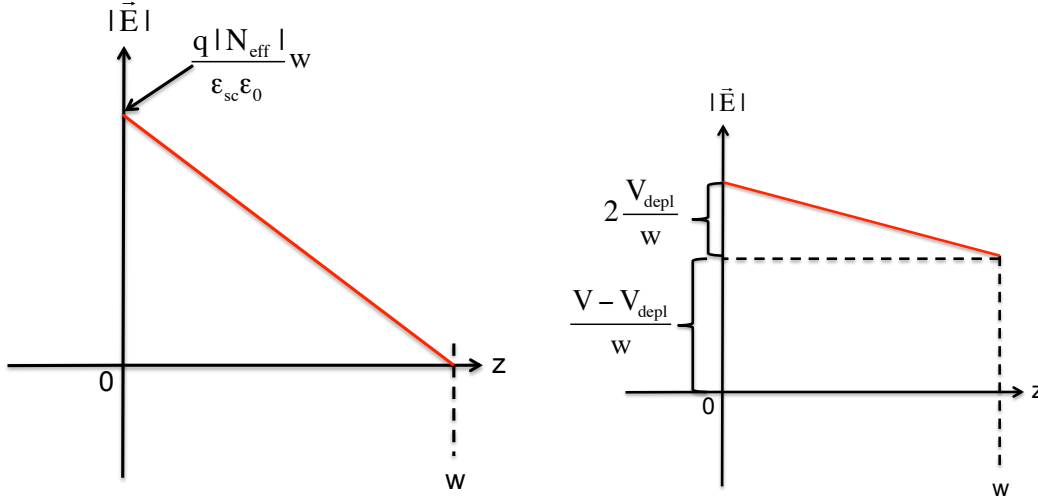
Figure 2.11: Electric field profiles in an abrupt asymmetric $n^+ - p$ junction. A doping profile like the one reported in Figure 2.10 is assumed. Electric field profile (left) at depletion voltage; (right) in over depletion.

$$C = \frac{A\epsilon_0\epsilon_{sc}}{w}\sqrt{\frac{V_{depl}}{V}} = A\sqrt{\frac{qN_{eff}\epsilon_0\epsilon_{sc}}{2}\frac{1}{V}} \tag{2.27}$$

where A is the surface of the $p - n$ junction. Equation 2.27 is used to extract the depletion voltage V_{depl} and the effective doping concentration N_{eff} in real $p - n$ junctions. An example of a C^{-2} vs V plot for an $n - on - p$ diode is shown in Figure 2.12.
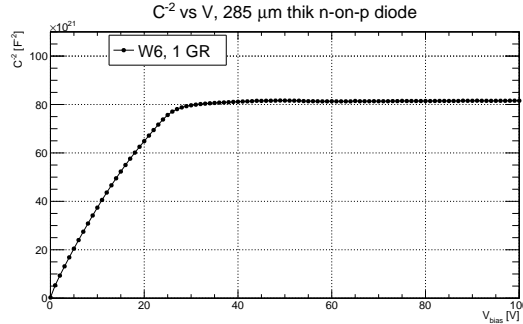
Figure 2.12: C^{-2} vs V of a 285 μm thick $n - on - p$ diode.

The bulk depletion corresponds to a linear increase of C^{-2}, up to a "kink", after which the capacitance C is basically constant. The voltage at which the "kink" happens is a good estimate of the depletion voltage V_{depl}.

The depleted region of a $p - n$ junction is out of equilibrium; in particular, since $pn < n_i^2$, in the depleted region the generation process is dominant over recombination. Thermally generated electron-hole paris are separated by the electric field and so they cannot recombine. A net flow of current appears, carriers will be collected at the ends of the semiconductor volume. If we assume a constant generation rate G the generated current for a depleted semiconductor of area A and thickness w is equal to:

$$I_{leak} = \frac{qwA}{2}G \tag{2.28}$$
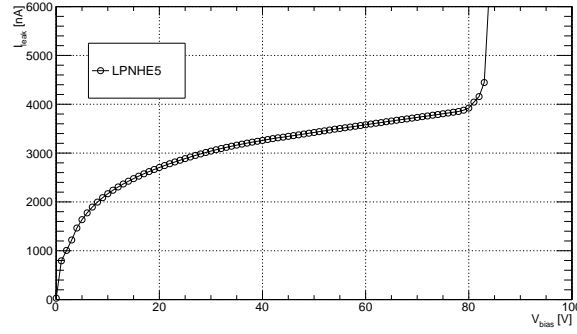
Figure 2.13: Leakage current as a function of reverse bias voltage for a pixel detector. See [7, 36].

The subscript *leak* in Equation 2.28 stands for *leakage*: the current resulting from thermally generated carriers in the depleted region is dubbed as *leakage current*.

Equation 2.28 can be rewritten introducing the concept of *generation lifetime* $\tau_g = n_i/G$:

$$I_{leak} = \frac{q n_i w A}{2\tau_g} \tag{2.29}$$

Nowadays Silicon material for ionising particle detectors can reach generation lifetimes τ_g up to 1 s, for a current density J of few pA/cm^2.

The leakage current of a depleted $p-n$ junction depends quite strongly on temperature: leakage current roughly doubles every seven degrees. The formula relating leakage current at different temperatures is the following:

$$\frac{I(T)}{I(T_0)} = \frac{T^2}{T_0^2} exp\left[-\frac{E_a}{2k}\left(\frac{1}{T} - \frac{1}{T_0}\right)\right] \tag{2.30}$$

where E_a is the equivalent of an activation energy (the experimental value of E_a for Silicon is ~1.21 eV [35]) and k the Boltzmann constant.

In Figure 2.13 the measured leakage current as a function of reverse bias voltage for a pixel detector. The pixels sensor was an $n-on-p$, 200 μm thick; the measurement was taken at room temperature. From Figure 2.13 it can be seen that a kind of plateau in the current is reached between 20 and 80 V; after that voltage the increase in current is huge. Indeed around 80 V an *avalanche breakdown* occurred. If an electron or hole is created in, or moved into, a high-field region inside a semiconductor, it may be accelerated strongly enough in between collisions to obtain sufficient energy for the creation of an electron-hole pair: an avalanche may thereafter develop [28]. Fields higher or of the order of 3×10^5 V/cm trigger a multiplication regime that gives rise to a breakdown. The voltage at which the phenomenon occurs is called *breakdown voltage*.

2.3 Why Use Silicon

Let's know focus only on Silicon. Silicon detectors replaced the gas based detectors in the tracking systems, since they offer a much better position information and an improved energy resolution. The reasons for this are to be found in the large density of silicon at room temperature, in the relatively low mean ionisation energy and in the possibility of use photolithography to realise charge collecting electrodes. These three characteristics allow to have large signals with a small active thickness and excellent spatial resolution.

Some of the Silicon properties that are relevant for high energy physics applications are summarised in Table 2.1.

Table 2.1: Summary of silicon properties relevant for high energy physics applications [28].

	Silicon	
Feature	Value	Comments
Density ρ	2.33 g/cm^3	compact and thin detectors
Energy bandgap E$_g$	1.12 eV	non-cryogenic operation
Mean ionisation energy ϵ	3.6 eV	large signals
Radiation length X$_0$	9.37 cm	thin detectors to minimize multiple scattering
Electron mobility μ_e	~1350 cm^{2}V/s	fast charge collection
Saturation velocity v_{sat}	~10^7 cm/s	fast charge collection

Other important characteristics that can explain the success of silicon are its large abundance, the possibility of changing its properties by doping, the existence of a natural oxide, and thanks to its stiffness it does not a container, in contrast to gases [34].

2.4 Silicon Detectors

We now focus on Silicon ionising particle detectors. They are all based on depleted $p - n$ junctions. We will first review the formation of signals and then the different detectors that were and are used in high energy physics, in particular those relevant to this report.

2.4.1 Signal Formation

A charged particle traversing the silicon sensor bulk produces electron holes pairs with a most probable value (MPV) of 80 pairs per µm (the energy loss probability distribution is described by the Landau distribution [37]). Because of the sensor's reverse polarization, the created charge carriers drift toward the sensor electrodes under the influence of the electric field present in the depleted region. This movement of the charge carriers in the electric field induces signals on the readout electrodes. To calculate the induced signal on the electrodes by the charge carriers drift the Shockley-Ramo theorem [38–40] can be used. The theorem states that the current i on an electrode induced by a moving point charge q is given by:

$$i(t) = q\vec{v} \cdot \vec{E}_w(\vec{r}) \tag{2.31}$$

where $\vec{v}$ is the instantaneous velocity of charge q. $\vec{E}_w$ is the electric field that would exist at the instantaneous position $\vec{r}$ of q under the following circumstances: the selected electrode at unit potential, all other electrodes at zero potential and all charges removed. $\vec{E}_w$ is called Ramo field or *weighting field*.

The sum of all the induced currents gives the total instantaneous current I(t):

$$I(t) = \sum i(t) = \sum q\vec{E}_w(\vec{r}) \cdot \vec{v}_{e,h}(t, \vec{r}) \tag{2.32}$$

where the carrier drift velocity is the product of the drift electric field $\vec{E}(\vec{r})$ with the carrier mobility $\mu_{e,h}$:

$$\vec{v}_{e,h}(t, \vec{r}) = \mu_{e,h}(\vec{E}, T)\vec{E}(\vec{r}) \tag{2.33}$$

A carrier that completes its path to the collecting electrode by moving from the position $\vec{r}_i$ where it was created to the final (electrode) position $\vec{r}_f$ induces the total charge Q given by the Ramo theorem, where $V_w(\vec{r})$ represents the *weighting* (or Ramo) potential evaluated at the position $\vec{r}$:

$$Q = -q \left(V_w(\vec{r}_f) - V_w(\vec{r}_i) \right) \tag{2.34}$$

The relation between the weighting potential and field is of course:

$$\vec{E}_w = -\nabla V_w \tag{2.35}$$

A carrier q that is produced at position $\vec{r}_i$ and trapped at position $\vec{r}_f$, before reaching the electrode, induces a smaller charge Q on the electrode by the same formula (carrier trapping will be presented in detail in Section 2.5.4). It has to be noticed that both trapped electrons and trapped holes reduce the final signal amplitude.

2.4.2 Pad detectors

We now consider $p - n$ junction *diodes*. A single p-n diode in reverse bias is the simplest silicon radiation detector; often it is called *pad* diode. Ionising particles interacting with the detector material produce electrons and holes in the depleted bulk volume; those carriers drift toward the collecting electrodes which are placed at the edge of the detector $p - n$ junction. To ensure a good ohmic contact heavily doped implants are present on both sides of the detector. In Figure 2.14 the schematic representation of a n-on-p pad diode silicon detector is shown. External voltage to ensure sensor bulk depletion is also indicated.
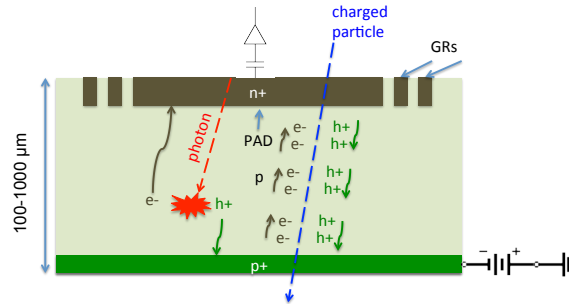
Figure 2.14: Silicon pad detector. Detector polarisation and carrier drift due to ionising particles is indicated too. The symbol on top of the n^+ implant is used to indicate the readout electronics.

The size of pad detectors varies between few mm^2 to few cm^2, including Guard Rings (GRs). GRs, placed all around the pad area, can help to improve the voltage-handling capability, since they act as a voltage divider, assuring a smooth transition of the voltage drop between one side and the other of the junction. Normally in pad diodes signals are read-out only from one side of the junction; it is customary to call that side as *frontside*, the other being the *backside*. For example, in Figure 2.14 the frontside is the n^+ one.

The pad side from which the depletion volume grows is called *junction* side; the other one is indicated as the *ohmic* side.

2.4.3 Microstrip detectors

The spatial resolution of pad detectors is roughly the size of the pad itself. It can be greatly improved by segmenting the electrodes, just one of them or both. Historically the first segmented silicon detector for high energy physics purpose was created by aluminum strips

deposited on a silicon wafer [41]. Nowadays so called *microstrip* detectors are realised by creating an array of heavily doped strips crossing the surface of the lightly doped silicon bulk. Each strips is read independently as shown in Figure 2.15.
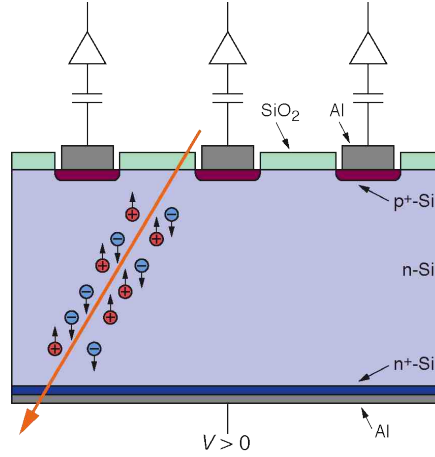
Figure 2.15: Silicon microstrip p-on-n detectors sketch. (After [31])

The typical spatial resolution of these detectors is of the order of (a fraction of) the strips pitch (50-80 μm nowadays). Adding one floating strip (*i.e.* not connected to a read-out channel) can greatly improve the spatial resolution without increasing the number of channels to be readout [42]. We will come back to the strip detectors and their spatial resolution in more detail in Section 3.6.

Microstrip detectors where the ohmic side is segmented too are called *double-sided microstrip detectors* (DSSDs); a scheme presenting the salient features of the DSSDs is shown in Figure 2.16
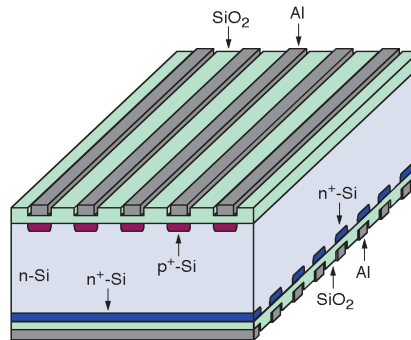
Figure 2.16: Schematic representation of a DSSD. (After [31])

DSSDs allow the reconstruction of two coordinates in one detector layer; this is very important to avoid deteriorating too much the spatial resolution due to the multiple scattering.

One important limitation of the DSSDs is the non unambiguous particle position measurement when more than one track is hitting the detector at the same time. As shown in the example in Figure 2.17, when two tracks hit the detector two valid but spurious combinations appear ("ghosts"), other than the two "true' valid positions due to the real tracks.

25
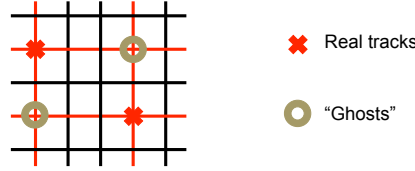
Figure 2.17: Schematic representation of the formation of ghost hits in DSSDs. The incidence positions of two particles are indicated as red crossed. Two additional valid combinations of the 1D information of both sides are indicated as brown open circles. Strips in red are those who recorded a signal. (After [31])

2.4.4 Pixel detectors

To measure unambiguously the position where the tracks cross the detector a detector capable of delivering both coordinates in one single measurement is needed: a *pixel* detector [43]. The concept of *hybrid pixels* detectors (HPDs) is presented in Figure 2.18. A
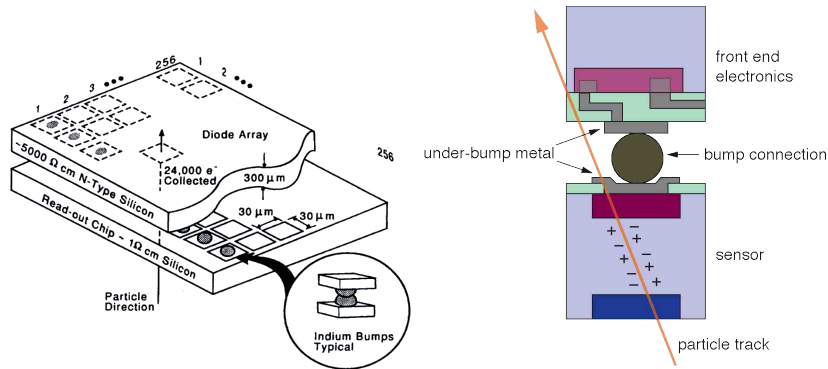
Figure 2.18: Schematic representations of an hybrid pixels detector. (Left) array of silicon $p - n$ diodes organised into a pixel detector. Each pixel cell is readout by a dedicated channel of the front-end electronics.(Right) detail of one pixel sensor cell connected via bump bonding to its front end electronics channel. (After [43, 44])

two dimensional array of $p - n$ diodes are organised in a matrix; each $p - n$ junction is readout by a dedicated readout integrated circuit (ROIC), providing the functionality of a hybrid pixel assembly; hence sensor and readout electronics are physically separated and linked by a *bump bonding*. The term *hybrid* refers to the fact that sensor and electronics are built onto separate substrates then joint together indeed by means of the bump bonding technique. The typical pitches of nowadays HPDs are of the order of 50 μm in the direction perpendicular to the magnetic field ("bending plane") and a couple of times larger in the beam direction.

HPDs, other than unambiguous position measurement, compared to DSSDs offer smaller leakage current (few pA) and smaller capacitance (few fF) per channel, given the much smaller size of the fundamental sensor cell; both aspects help in keeping the level of electronic noise small, hence to preserve high detector efficiency and spatial resolution. The main limitation of HPDs is the elevated number of channels to be readout (*e.g.*~27000 in ~ 4 cm^2 [45]). The high number of readout channels gives rise to complex solutions for sensor-electronics connection and large power consumption (0.1-1 W/cm^2 [45]).

A variation of the sensor of HPDs are the so-called 3D-silicon sensors. 3D-silicon sensors have been developed since the late 1990s [46] featuring columnar electrode implants driven into the Si substrate perpendicular to the sensor surface (Figure 2.19).

26
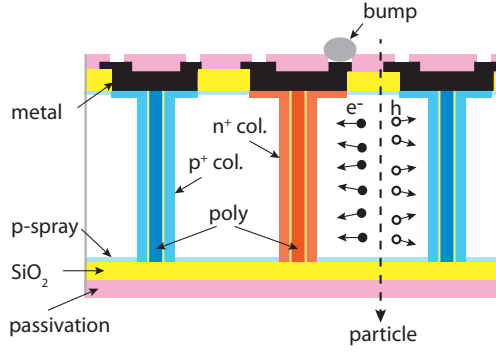
Figure 2.19: Single sided 3D-Si sensors with columns going completely through the sensor bulk. (After [27])

The electrode distance is made smaller (50 µm) than the typical sensor thickness (200-250 µm), thus rendering a shorter average drift distance for particles impinging on the sensor face than in the case of planar sensors. In addition high drift fields are obtained with still moderate bias voltages. Both these facts result in an increased radiation tolerance due to a reduced trapping probability (see 2.5.4).

2.4.5 Monolithic Pixel Detectors

The high number of interconnections and the total material budget are the main limitations imposed by the HPDs. One solution is to have on the same substrate the sensor and the frontend electronics: simple electronics circuits, like the first stage of the amplifier of each pixel, are integrated on the same silicon substrate. One example of sensor and frontend electronics integrations are the Monolithic Active Pixel Detectors (MAPS [47]), which are realised in commercial CMOS technology (for CMOS technology see for example [28]). The detector is realised on a thin layer of low-resistivity p-doped silicon, which is optimal for complex electronics design but does not allow having large depletion volumes and fast charge collection [33]. The conceptual drawing of an example of MAPS is presented in 2.20. The $p-n$ junction is realized between the n-well and the $p-$type epitaxy[3], but, be-
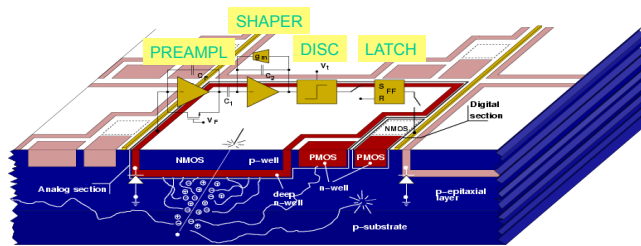
Figure 2.20: Conceptual drawing of an example of MAPS (After [48])

cause of the low resistivity, the depletion is partial even on the very thin ($\approx$10 µm) epitaxy layer and the collected charge is small ($\approx$1000e). The charge collection from the epitaxial layer to the n-well/p-epi diode happens through drift and diffusion of the carriers and takes about or more than 100 ns, *i.e.* 10 times longer than in the approaches based on high-resistivity silicon.

---

[3]epitaxy is semiconducting material made by epitaxial growth

Modern CMOS imaging sensors make use of 3D integration[4] of sensor and readout electronics, to combine high resistivity and fully depleted charge collection layers with high density CMOS circuitry, in order to achieve high speed and high collection efficiency (for low light operation). Such a combination of fully depleted high resistivity silicon with CMOS readout sounds like a requirement from particle physics, not from consumer electronics, but smartphone image sensors have independently evolved in this direction. Recently depleted monolithic active pixel sensors (DMAPS) started to be developed; they exploit medium to high (>100Ωcm) resistivity 8" silicon substrate wafers. A depletion layer develops due the high resistivity with only moderate bias voltages applied from the electronics side or a (specially processed) backside contact [27].

2.5   Radiation Damage

Silicon detectors are at the core of the modern High Energy Physics (HEP) experiments at colliders. High collision rates and high track densities translate into fluence of particles of several 10^{11} per square centimetre per hour for the detector layers closest to the interaction point [33]. This flux of particles is responsible for damage to the sensor and to the electronics.

Radiation-induced effects (radiation damage) are usually divided into bulk and surface defects. The former are caused by the displacement of crystal atoms while the latter include all effects in the covering dielectrics and the interface region. The most important surface effect is the increase of the oxide charge which saturates after some kilograys to values of about 10^{12} cm^{-2} [50]. At higher hadron fluence, bulk damage also becomes important. The main effects are: increase of leakage current, change of the operational voltage and reduction in signal amplitude. The following is a short description of the microscopic defects and the induced macroscopic effects.

2.5.1   Microscopic description

Inelastic collision between an incident particle and the silicon lattice can produce a displacement of an atom from its lattice site. This event creates an interstitial site and a vacancy, which collectively is called a *Frenkel defect*. An illustration of these defects, called also *point defects*, is give in Figure 2.21.
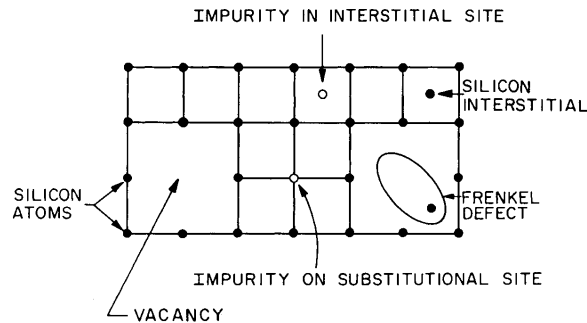
Figure 2.21: Types of point defects in a simple lattice. After [28].

Several point defects can group together to form a cluster; the probability depends on the incident particle type and its energy. An electron whose kinetic energy is above

---

[4]3D integration is a method of electrically connecting chips that consist of different kinds of devices by stacking them [49]

255 keV produce a Frenkel pair; above 8 MeV it produces a cluster. For neutrons the thresholds are of 185 eV and 35 keV, respectively [51]. In Figure 2.22 the results of a Monte Carlo simulation for the recoil of an atom with a primary energy E_R of 50 keV; this is the average energy imparted to a lattice atom from a 1 MeV neutron [51].
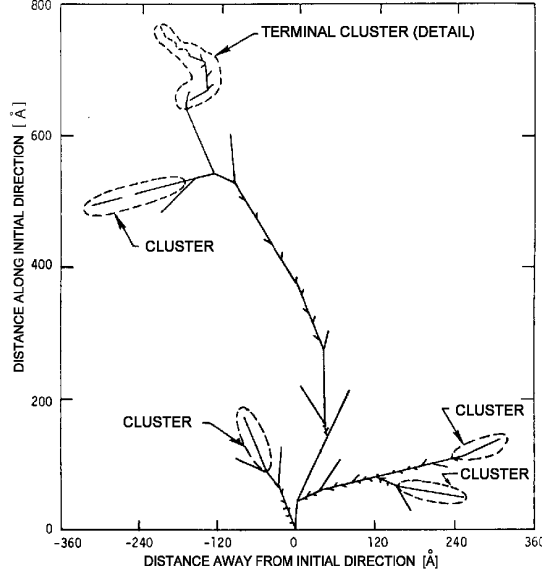
Figure 2.22: Monte Carlo simulation of a recoil-atom track with a primary energy E_R of 50 keV. After [52].

To be able to compare the damage caused by the different types of particles with different energies, radiation damage is scaled with the non-ionizing energy loss (NIEL). This quantity summarises all energy deposited in the crystal which has not been used for the fully reversible process of ionisation. Neutrons of 1 MeV are used as reference parti-cles [53]. The fluence Φ_{phys} of an arbitrary type of particle causes the same NIEL as the fluence Φ_{eq} of 1 MeV neutrons. The energy-dependent hardness factor κ of a certain type of particle which converts the "physical" fluence Φ_{phys} into the neutron equivalent fluence Φ_{eq} can be evaluated experimentally via the normalisation of the leakage current [33, 54]. In the following text all fluences are given in units of neutron equivalent fluence, $n_{\mathrm{eq}}/\mathrm{cm}^2$.

The primary defects caused by irradiation, silicon vacancies, and interstitials are not stable; *i.e.*, they are able to move through the crystal. This movement can lead to an *an-nealing* if defects meet during their migration through the crystal. But also secondary point defects with other defects already present in the crystal can be formed, which might be stable and display different electrical properties. Point defects in general cause energy levels in the band gap whose position can be measured by different spectroscopic meth-ods. They can be charged and, depending on the position of their energy levels, have an impact on the space charge in the depletion zone. As the mobility of the defects is strongly temperature-dependent it is clear that radiation-induced changes of sensor properties show a complex annealing behaviour due to the many possible secondary defects [33].

Among several defects detected with various techniques, there are some that prove to have a significant impact on the silicon diodes, being charged at ambient temperatures and thus, directly influencing the effective doping concentration N_{eff}. Their electrical parameters, energy level E_a and capture cross section σ are given in Figure 2.23 [55].

The radiation induced defects, primary or not, are responsible for macroscopic ef-fects, like: the increase of leakage current, since they can act as generation centers; the
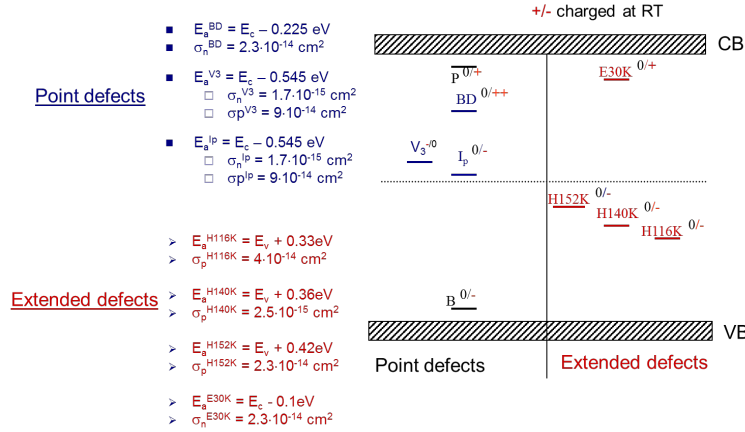
Figure 2.23: Radiation induced defects in silicon influencing the effective doping concentration N_{eff} and the leakage current. P and B are the doping impurities used to fabricate the silicon $p-n$ junctions. CB and VB stand for conduction and valence bands, respectively. (After [55])

change in operational voltage, as they can be charged; and, the most important effect after $\Phi=10^{15}$ n_{eq}/cm^2, the reduction of the signal amplitude, since they act as trapping centers. Let's now review some details of these macroscopic effects.

2.5.2 Leakage Current Increase

The energy levels in the band gap caused by the crystal defects act as generation-recombination centers. They lead to a decrease of the generation lifetime τ_g, hence to an increase of the leakage current I_{leak} generated in the volume. The rate of increase of leakage current ΔI per unit of fluence Φ and per unit of volume V is called α:

$$\alpha = \frac{\Delta I}{V\Phi} \tag{2.36}$$

The typical value of the normalised rate of increase of leakage current α right after irradiation is of several units of 10^{-17} A/cm. After irradiation the leakage current anneals with time as shown in Figure 2.24.
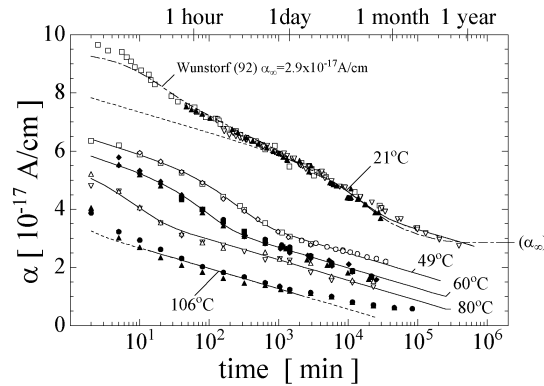
Figure 2.24: The normalised rate of increase of leakage current α as function of the cumulated annealing time. (After [51]).

The trends shown in Figure 2.24 can be parametrised for a time t at constant temperature T after an instantaneous irradiation with fluence Φ by [51]:

$$\alpha = \left(\alpha_I e^{-t/\tau} + \alpha_0 - \beta \log(t/t_0)\right) \tag{2.37}$$

where $\alpha_I = (1.23 \pm 0.06) \times 10^{-17}$ A/cm, τ follows an Arrhenius equation $\tau^{-1} = (1.2^{+5.3}_{-1.0}) \times 10^{13}$ s$^{-1} \times e^{(-1.11\pm0.05)\,\text{eV}/k_B T}$, $\alpha_0 = -(8.9\pm1.3) \times 10^{-17}$ A/cm $+ (4.6\pm0.4) \times 10^{-14}$ AK/cm $\times 1/\text{T}$, $\beta = (3.29 \pm 0.18) \times 10^{-18}$ A/cm , and $t_0 = 1$ min.

It has to be mentioned that other formulations of 2.37 are possible, suggesting the annealing to be a first-order process[5] with a temperature-independent α_0.

It has been measured that after 80 minutes at 60°C the α value is very close to 4×10^{-17} A/cm [51]; this value is often cited in literature as the reference value for the normalised rate of increase of leakage current α, but one has to bear in mind that it is the result of a particular annealing scenario.

It was shown [35] that the scaling of leakage current with temperature reported in Equation 2.30 is adequate even after irradiation to fluences largely exceeding Φ=10^{15} n$_{eq}$/cm^2.

2.5.3 Operational Voltage Shifts

There are several radiation-damage mechanisms that lead to a change in space charge and consequently to a change in the necessary operational voltage of detectors.

The original dopants such as Phosphorus or Boron may be captured into new defect complexes, thereby losing their original function as flat donors or acceptors. The new defect complexes may assume a charge state within the space-charge region different from the original dopants [28].

The evolution of acceptors and donors with fluence can be explained by the removal of acceptors or donors, via the formation of defect complexes containing acceptors/donors, and by the creation of acceptors and donors, via the formation defect complexes assuming positive/negative charge states in the space-charge region.

The dependence of the effective doping concentration N_{eff} (Eq. 2.21) on fluence is then expected to be the following:

$$N_{eff} = N_{d,0} e^{-c_d \Phi} - N_{a,0} e^{-c_a \Phi} + b_d \Phi - b_a \Phi \tag{2.38}$$

with $N_{d,0}$, $N_{a,0}$ donator and acceptor concentration before irradiation and c_d, c_a, b_d, b_a constants to be determined experimentally [28].

It has been observed that initial $n-$type material becomes $p-$type after moderate fluences ($\Phi \sim 2 - 5 \times 10^{12}$ n$_{eq}$/cm^2); this phenomenon is called *type inversion*. This is interpreted as donor removal and acceptor creation. The depletion voltage decreases rapidly with fluence at first and then it increases linearly, as it can be seen in Figure 2.25.

For initial high resistivity $p-$type material the acceptor removal and donor creation effects can be safely neglected and the change of the effective doping concentration N_{eff} has a simple linear dependence on the fluence Φ.

2.5.3.1 Annealing and Effective Doping Concentration

As already mentioned in the discussion on the leakage current, some defects can move freely through the crystal, they can anneal, *e.g.* a silicon interstitial could fill a vacancy in the lattice. The velocity of the annealing process depends on the average velocity of the movable defects, which in turn depends heavily on the temperature. Here we give a

---

[5]First-order process involves only one defect; second-order processes depend the interplay between two defects [28]
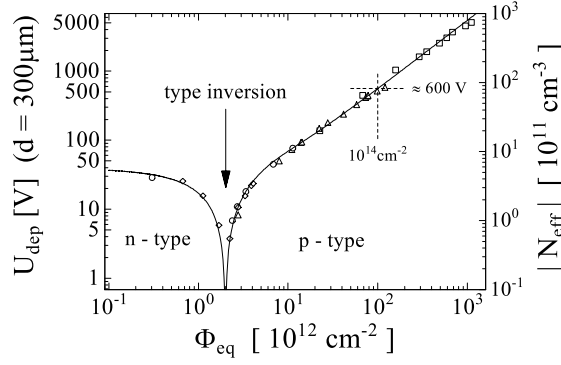
Figure 2.25: Change of the full depletion voltage of a 300 µm-thick silicon sensor and its absolute effective doping versus the normalized fluence, immediately after the irradiation (After [56].)

first description of the phenomena of annealing for the space charge distribution in the irradiated bulk; we will come back on this topic in more detail in Chapter 6.

With respect to the normalised rate of increase of leakage current α, where the annealing is always *beneficial* (α is never increasing), the effective doping concentration N_{eff} is subject to a *reverse* annealing too, which leads to an increase of N_{eff} An example of the interplay of beneficial and reverse annealing on N_{eff} is shown in Figure 2.26.
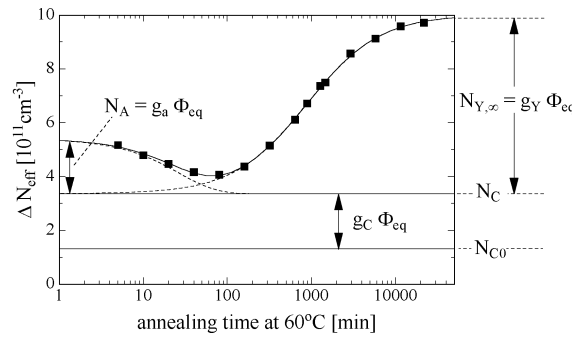
Figure 2.26: Annealing behaviour of the radiation induced change in effective doping concentration ΔN_{eff} at 60°C. The shown example is a $n-$type high resistivity sample, neutron-irradiated with a fluence of 1.4×10^{13}. (After [51])

For the effective doping or the bias voltage respectively the annealing process is subdivided into two periods. The beneficial annealing period which extends roughly for the first 80 minutes at 60°C; after the beneficial annealing period the effective doping concentration, hence the depletion voltage V_{depl}, is reduced to a minimum. Afterwards, the reverse annealing process sets in and leads to an increase of the V_{depl}, exceeding the initial V_{depl} directly after irradiation.

2.5.3.2 Heavily Irradiated Silicon Detectors

In the studies presented in the previous Sections the determination of the fluence and time dependence of the effective doping concentration N_{eff} simple unstructured diodes were used [51] and the full depletion voltage was deduced from CV measurements (Eq. 2.27). This method assumes a constant space charge which is not given for highly irradiated sensors where the field shows a double peak [57]. This can be qualitatively explained by defects being filled by carriers drifting under reverse bias voltage. In a $n-on-n$ detector electrons will flow toward the n^+ electrode while holes toward the p^+ one. So the chances

of having a negatively charged defect close to the n^+ electrode are higher than a positively charged one; the opposite goes for the defects close to the p^+ electrode. The mechanism was first proposed in [58]; it is illustrated in Figure 2.27.
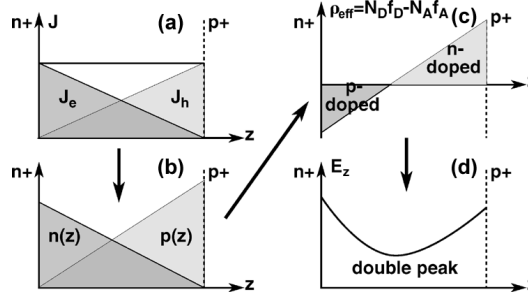
Figure 2.27: An illustrative sketch of the explanation of the double peak effect in electric field for a reverse biased irradiated device. (After [59])

In case of double peak in the electric field distribution the numbers derived for depletion voltage and effective doping concentration form the CV measurements are effective or average numbers.

An example of a $C^{-2}V$ measurement for an irradiated device is shown in Figure 2.28.
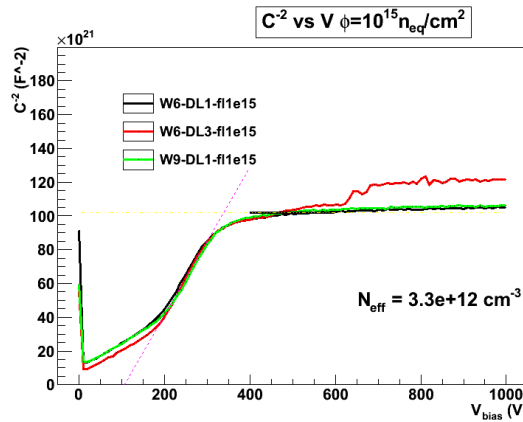
Figure 2.28: C^{-2} vs V of a 285 μm thick $n-on-p$ diode irradiated at CERN with 24 GeV/c protons, with an integrated fluence of $\Phi = 1 \times 10^{15}$ n_{eq}/cm^2, after having being annealed for 80 minutes at 60°C. Results from three diodes, coming from 2 different wafers, and with different number of GRs are reported.

The C^{-2} vs V curves reported in Figure 2.28, whose slope is proportional to the effective doping concentration N_{eff} in un-irradiated material, show a change in slope around 200 V; the curves reach a pleateau around 300 V. These two slopes are connected with the electric field setting on from both the front and the back side of the detector.

2.5.4 Trapping

Radiation-induced defects are responsible not only for generation-recombination centers increasing the leakage current and charged defects with dramatic influence on the full depletion voltage but also for trapping centers. Traps are mostly unoccupied in the

depletion region due to the lack of free charge carriers and can hold or trap part of the signal charge for a time longer than the charge collection time and so reduce the signal amplitude.

The typical trapping time τ_{tr} gets shorter and shorter with larger and larger fluence Φ; it has been found it is proportional to the inverse of fluence:

$$\tau_{tr}^{-1} = \beta \Phi \tag{2.39}$$

Measured values for β are about $4-6 \times 10^{-16}$ cm^2/ns for electrons and $6-8 \times 10^{-16}$ cm^2/ns for holes [60]. Larger β values for holes than for electrons mean that trapping is most severe for the former than the latter. It has also to be noticed that the hole mobility is about 1/3 of the electron one; so holes move slower and gets trapped more. Given these two conditions nowadays electrons collecting silicon detectors, like $n-on-n$ and $n-on-p$, are favoured over holes collecting ones, like $p-on-n$.

Given that in the saturation regime carriers take about 1 ns to traverse 100 μm in Silicon, the trapping effect starts to be the most impacting radiation damage effect after fluences in excess of $\Phi = 1 \times 10^{15}$ n$_{eq}$/cm^2. In Appendix A some estimations for the expected charge collection efficiency (CCE) in irradiated silicon pads are presented. For example, after $\Phi = 1 \times 10^{16}$ n$_{eq}$/cm^2 a 100 μm thick pad diode will be able to collect only about 27% of the signal amplitude prior to irradiation.

After irradiation segmented detectors, like DSSDs and HPDs, will allow to achieve CCE higher than the one for pads thanks to the steeper slope of the Ramo potential close to the collecting electrode; this will be treated in Chapter 6.

Trapping time τ_{tr} evolves with time and temperature as leakage current and depletion voltage do. In [61] it is shown that the trapping asymptotic probabilities of holes (electrons) will be around 30% larger (15% smaller) than initial probabilities at the same total fluence.

2.6 Summary

In this Chapter we reviewed the basics of semiconductor physics and the reasons for the success of silicon tracking sensors for HEP experiments. Advantages and limitations of the different silicon detectors were discussed. In the end radiation damage, one of the biggest challenges for actual and future silicon detectors at hadron colliders, was presented. This introduction will serve as a base for the next chapters.

Chapter 3

The SLIM5 Project

In this Chapter the SLIM5 R&D project will be presented. After a short summary of the project motivations, goals and timeline (Section 3.1), the Physics motivations of and the tracker requirements for SuperB and ILC will be briefly discussed in Section 3.2. The pixel (Section 3.3) and strip (Section 3.4) detector prototypes developed within the SLIM5 project will be then presented. In Section 3.5 the results in [5, 62, 63] will be discussed. A special Section (3.6) is devoted to the spatial resolution results of the striplets. Wrap up of the SLIM5 project will be finally outlined in Section 3.7.

3.1 The Project

The SLIM5 project [64] aimed at advancing the state-of-the-art in the development of thin tracking systems to be applied in High Energy Physics. The project was financed for three years (2006-2008) by INFN - National Scientific Committee 5 [65] and involved several Italian research institutes.

The SLIM5 collaboration worked on developing tracking systems for experiments at high luminosity flavour factories, like the proposed SuperB [66], and linear colliders. The goal was to deliver thin silicon tracking detectors with possibility of self-triggering thanks to the combination of data-driven data acquisition and pattern matching algorithm with very low latency. Double sides strip detectors (DSSDs) and monolithic active pixel sensor (MAPS) prototypes were produced in the framework of the project. Before describing them we now illustrate the required performance for such detectors.

3.2 Tracking and Vertexing Requirements for SuperB and ILC Experiments

Experiments at high luminosity colliders have to accomplish a high precision measurements exploiting at maximum the large dataset they are expected to integrate. This means that the experiments have to be very efficient and show excellent performance, even in presence of a very intense particle rate; this is particularly true for the tracking and vertexing detectors, which are the closest to the beams interaction point. It is also to be stressed that with sub-optimal tracking and vertexing performance there's no physics case for such experiments; hence the tracking and vertexing detectors are the crucial parts of experiments at high luminosity colliders.

We now review quickly some physics cases for SuperB and ILC and the related constraints on tracking detectors.
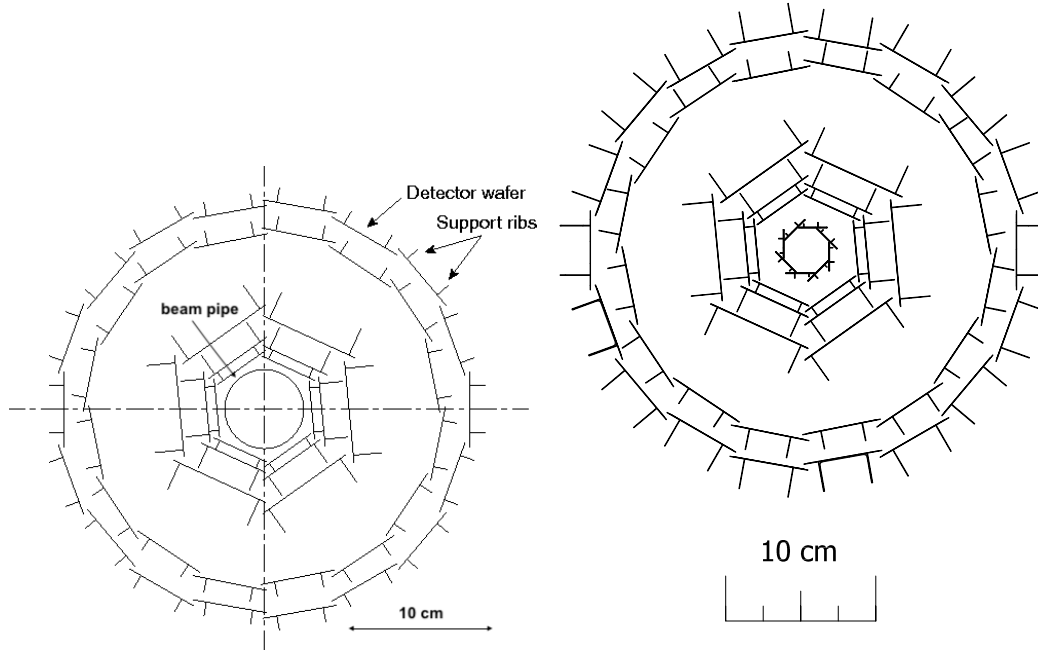
Figure 3.1: (left)Schematic view of *BABAR* SVT: tranverse section. (Adapted from [67]) The external radius is 144 mm. (right) Cross section of the SuperB SVT. (After [66])

3.2.1 SuperB

The SuperB project [66] was the proposal of a e^+e^- super flavour factory operating at the center-of-mass energy of the $\Upsilon(4S)$ resonance, capable of an instantaneous luminosity of $10^{36}\,\mathrm{cm}^{-2}\mathrm{s}^{-1}$, with the goal of integrating a 50–75 ab^{-1} dataset.

The SuperB physics program was to

a) determine the flavor structure of whatever New Physics (NP) discovered at the LHC, using the information on rare b, c, and τ decays, and on CP violation in b and c quark decays, or, if signatures of NP were not observed at the LHC, then

b) exploit the excellent sensitivity provided at the luminosity frontier by a SuperB factory, to observe NP at mass scales up to 10 TeV or more through observation of rare processes involving B and D mesons and studies of lepton flavour violation in τ decays.

The SuperB detector concept was based on the *BABAR* detector [24], with those modifications required to operate at a luminosity of $10^{36}\,\mathrm{cm}^{-2}\mathrm{s}^{-1}$ or more, and with a reduced center-of-mass boost. Higher luminosity and machine-related backgrounds, as well as the need to improve detector hermeticity and performance, required significant R&D to be able to implement this upgrade.

The planned vertexing and tracking detector, the SuperB Vertex Tracker (SVT), was intended to be an evolution of the *BABAR* SVT; see Figure 3.1 for a comparison. The main difference was the extra layer, Layer0, at a radius of 1.5 cm.

Precise vertex information, primarily extracted from accurate position measurements near the interaction point (IP) by the SVT is crucial to the measurement of time-dependent CP asymmetries in B^0 decays, which was the key element of the SuperB physics program. As in *BABAR*, the SuperB had to be able to provide efficient and accurate tracking for charged particles with transverse momenta lower than 100 MeV/c, which cannot reach the tracking Drift Chamber.
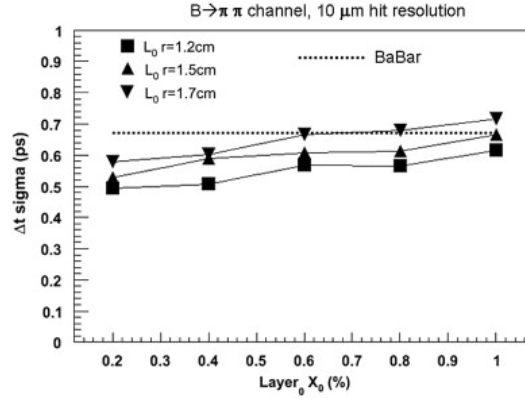
Figure 3.2: Resolution on the proper time difference of the two B mesons for the nominal SuperB boost, for different Layer0 radii, as a function of Layer0 thickness (in X_0 %). The BaBar resolution for the same decay channel, is shown with a dashed line. (After [68])

SuperB SVT had to be capable of maintaining adequate performance for time-dependent measurements in the presence of a lower boost of the center-of-mass (CM) frame ($\beta\gamma$ = 0.24 compared to $\beta\gamma$ = 0.55 of *BABAR*) and much higher background, mainly related to the increased instantaneous luminosity of about a factor of 100 larger than *BABAR*.

The planned beam pipe featured a reduced radius of about 1.0 cm which would have allowed the positioning of Layer0 at the desired average radius of about 1.5 cm. The additional (with respect to *BABAR* SVT) Layer0 measurement, along with the low radial material budget of the beam pipe (0.42% X_0) and of Layer0 (0.45% X_0 with the striplet option - see Section 3.4), was crucial for improving the decay vertex reconstruction of the B mesons and obtaining adequate proper-time resolution for time-dependent CP violation measurements.

Physics simulations for the B $\to \pi^+\pi^-$ decay channel showed that to retain or improve the vertexing performance of the *BABAR* SVT in the SuperB environment the following ingredients were necessary: the use of high granularity pixels (50 µm ×50 µm pitch), going indeed closer to the beam pipe and very low material budget [68]. Results are shown in Figure 3.2.

In summary, for the SuperB physics program a silicon tracker detector was needed with the capability to assure a space-point resolution of 10 µm, with a material budget below 1% of X_0, able to measure tracks with p_T lower then 100 MeV/c. The real detector would have had to withstand a particle rate of 100 MHz/cm^2, mainly due to machine background.

3.2.2 ILC

The International Linear Collider (ILC) is a proposed e^+e^- collider. Over the years the project evolved and now it features a machine capable of tuning its center of mass energy in the range of $\sqrt{s}$ = 250 − 550 GeV, with an option for 1 TeV [69]. In 2009, two detector projects (ILD & SiD) provided a Letter Of Intent (LOI) [70, 71].

The ILC physics goals cover a wide and ambitious program including top quark physics, electroweak precision measurements, direct and indirect searches beyond the Standard Model (BSM) like supersymmetry[1], dark matter searches, exotic searches, etc., and a com-

---

[1]Supersymmetry (SUSY) is a proposed type of spacetime symmetry where each SM particle is associated with another particle, known as its superpartner, the spin of which differs by a half-integer; for an introduction to SUSY see [72]
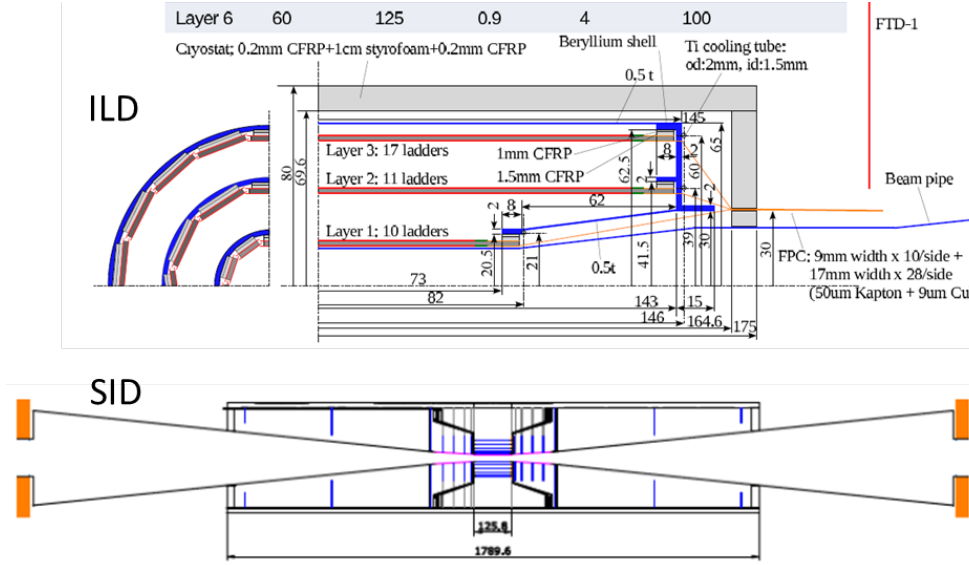
Figure 3.3: ILD and SiD schemes of the vertex detector (After [73])

plete and extensive Higgs physics program covering mass, couplings to fermions and bosons, quantum numbers and total width measurements. The expected level of precision for the majority of them will reach the percent level and will allow probing physics BSM [73].

To accomplish this ambitious physics program stringent requirements are imposed on tracking and vertexing performances (these requirements did not change much over a decade [73, 74]). The figure of merit of the future ILC vertex detector is the impact parameter (ip) resolution which is expected to be:

$$\sigma_{ip} = 5\,\mu\text{m} \oplus \frac{10}{p\beta(\sin\theta)^{3/2}}\,\mu\text{m} \tag{3.1}$$

when the momentum p is expressed in GeV/c (θ is the track angle with respect to the beam axis; see also Section 1.4).

This condition demands then for: a space-point resolution of about 3 µm (hence a pitch of less than 20 µm; a material budget per layer of about 0.1% of X_0; capabilities of performant tracking down to p_T of 100 MeV/c and even less.

The vertexing systems proposed by the two concept groups are both built around a central part based on pixel detectors; a comparison of ILD and SiD proposed solutions is presented in Figure 3.3. SiD features 5 pixel barrel layers and a total of 7 pixel disk layers per side; ILD plans for 3 double sided ladders plus , a system of pixels and strips disks in the forward region.

For both vertexing detectors pixels with integrated readout (at least partial) are promising solutions, like CMOS MAPS, DEPFET, etc. They will assure the needed small pitch and the low material budget (example: [75]).

In Summary, for the experiment at the future ILC a vertex detector with a space point resolution of 3 µm, a material budget per layer of about 0.1% of X_0 and the possibility of tracking down to p_T of 100 MeV/c and even less are needed.

3.3 The CMOS MAPS Apsel4D

As said in the introduction to this Chapter, within the SLIM5 project both pixel and strip detector prototypes were developed. We now review the salient features of the pixel detector prototype, the Apsel4D. More details can be found in [5, 63].

The Apsel4D (active pixel sensor electronics) chip was a 4096 element prototype CMOS MAPS detector in 130 nm triple well process with data-driven readout architecture, implementing twofold sparsification at the pixel level and at the chip. CMOS MAPS was the preferred solution because of the thickness of the substrate, hosting both the sensor and the read-out electronics, can be easily thinned down to 50 μm or less. The final chip featured a 4096 pixels matrix, 50×50 (μm)^2 pitch. The triple well option of CMOS commercial processes (see also Figure 2.20) for the collecting electrode was exploited, implementing a full signal processing chain at the pixel level with a sparsified readout architecture. In Figure 3.4 a picture of the Apsel4D chip is presented, together with a scheme of its architecture readout.
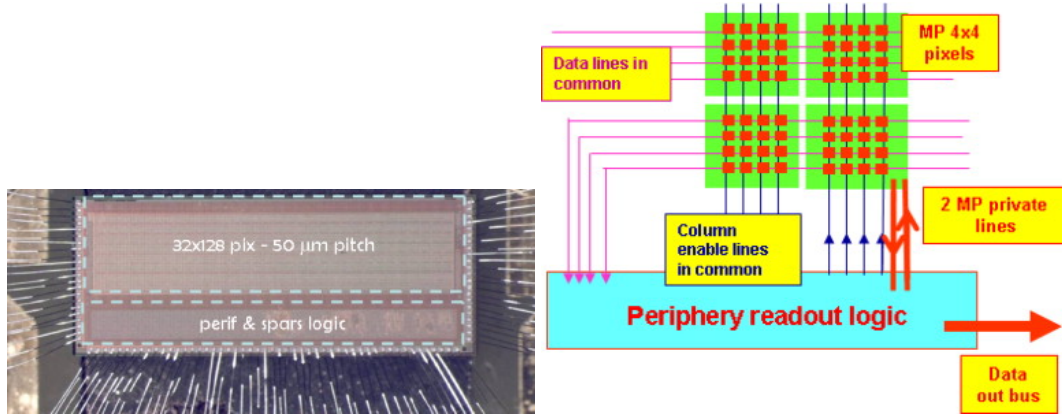
Figure 3.4: (left)The Apsel4D chip bonded to the chip carrier. (right)Schematic block diagram of the architecture for MAPS matrix readout.

The elementary pixel cell includes a collecting electrode, featuring a buried deep n-type layer, and the full readout chain for signal processing [76]. The processing chain consisted of a charge preamplifier with charge to voltage conversion independent of the detector capacitance, a shaping stage featuring a 200 or 400 ns peaking time and finally a discriminator used to compare the signal with a chip-wide threshold to provide digital information. The design of the front-end minimized the amount of PMOS transistors and related n-wells, which act like competitive parasitic electrodes. The fraction of deep n-well area (electrode) over the total n-well area was of about 90% (known also as the *fill factor*).

The readout architecture of the APSEL4D pixel, capable of performing on-chip data sparsification, was data-driven and permits the use of the tracker information to generate a Level 1 trigger. The sparsified readout was implemented thanks to the organisation of 4×4 pixels into a macro pixel (MP); each MP had only two private lines for point-to-point connection to the peripheral logic: one line was used to communicate that the MP has got hits, while the second private line was used to freeze the MP until it has been read out. Common horizontal lines are shared among pixels in the same row to bring data from the pixels to the periphery, where the association with the proper timestamp is performed before sending the formatted data word to the output bus. The architecture is presented in Figure 3.4.

The chip has been designed to run with a maximum matrix readout rate of 32 hit pixels/clock cycle and a local buffer of maximum 160 hits to minimize the matrix sweep time. The readout clock, designed to run up to 100 MHz, was operated at 20 MHz in the beam test. Noise performance were estimated in the laboratory to be of about 75 e (ENC) with 20% dispersion across the matrix; the threshold dispersion over the pixels was estimated be about 60 e.

3.4 The Striplets Detector

The DSSD detector prototype developed within the SLIM5 project was called "striplets". They were the baseline option for the Layer0 of the SuperB SVT. The striplets detector was designed and fabricated at FBK-IRST[2]. The striplets detector was indeed a double-sided strip detector, realised on high-resistivity $n-$type bulk. A picture of the striplets detector can be seen in Figure 3.5.
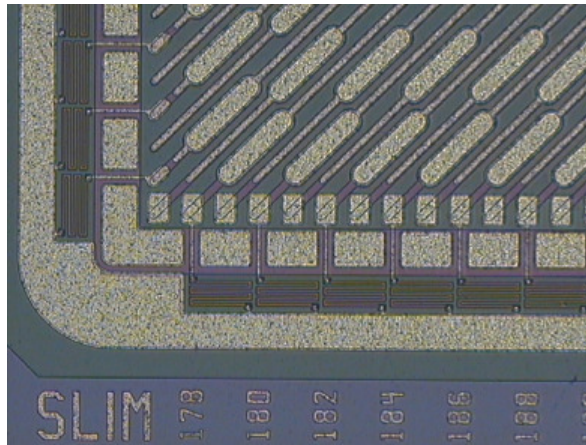
Figure 3.5: Detail of a corner of the SLIM5 striplet detectors.

The striplet geometry was optimized to limit the strip length (18 mm) and the material budget (double-sided, 200 μm thick). The strips were tilted by 45° with respect to the detector edge, as shown in Figure 3.5. The short strip length reduces the average occupancy per channel and allows coping with the increased strip-to-backside capacitance, given the thin bulk. The strips pitch was 50 μm on both sides; the detector active area was of 27×12.9 mm^2. The design allowed a long DSSD with short strips on both sides. The strips were AC coupled, with integrated capacitors and polisilicon biasing-resistors. In order to minimize the dead area along the edges, the resistors are placed outside the guard ring. The detector was fully depleted at 10 V bias.

The striplet sensor was read out by the data-driven FSSR2 chip [77], the second release of the Fermilab Silicon Strip Readout Chip, derived from the one originally designed for the silicon pixel detector of the BTeV experiment. The chip is completely data-driven and can be readout at up to 70 MHz. The chip features 128 analog channels, with address and time information for all hits; the output is purely digital; the chip measures 7.5 mm × 5 mm and the input pads have an effective pitch of 50 μm. A picture of the FSSR2 chip is shown in Figure 3.6

FSSR2 chip offers 8 programmable thresholds, with the first one acting as hit/no hit discriminator (*zero suppression* mode), so each hit has a 3-bits adc information. The de-

---

[2]now FBK-CMM: http://cmm.fbk.eu/
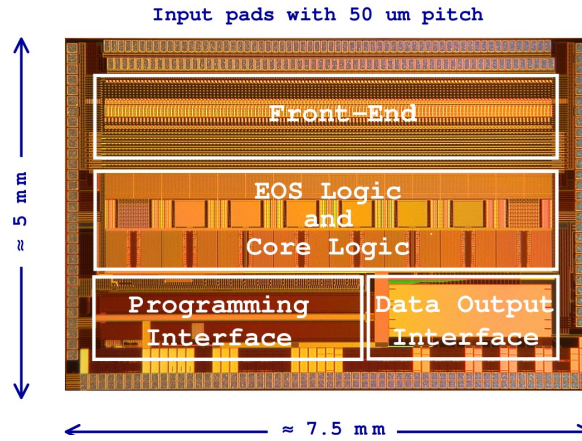
Figure 3.6: Annotated picture of the FSSR2 chip with input pads at the top. (Adapted from [77])

sign was optimised for positive signals; here for the first time it was used to read out negative signals too (ohmic side of the striplets). Due to the limited dynamic range for n-side just a hit/no hit information for negative signals was extracted.

In Figure 3.7 a striplet detector module is shown. One striplet sensor was read out by 3 FSSR2 chips per side, for a total of 384 wirebonded channels on each side.
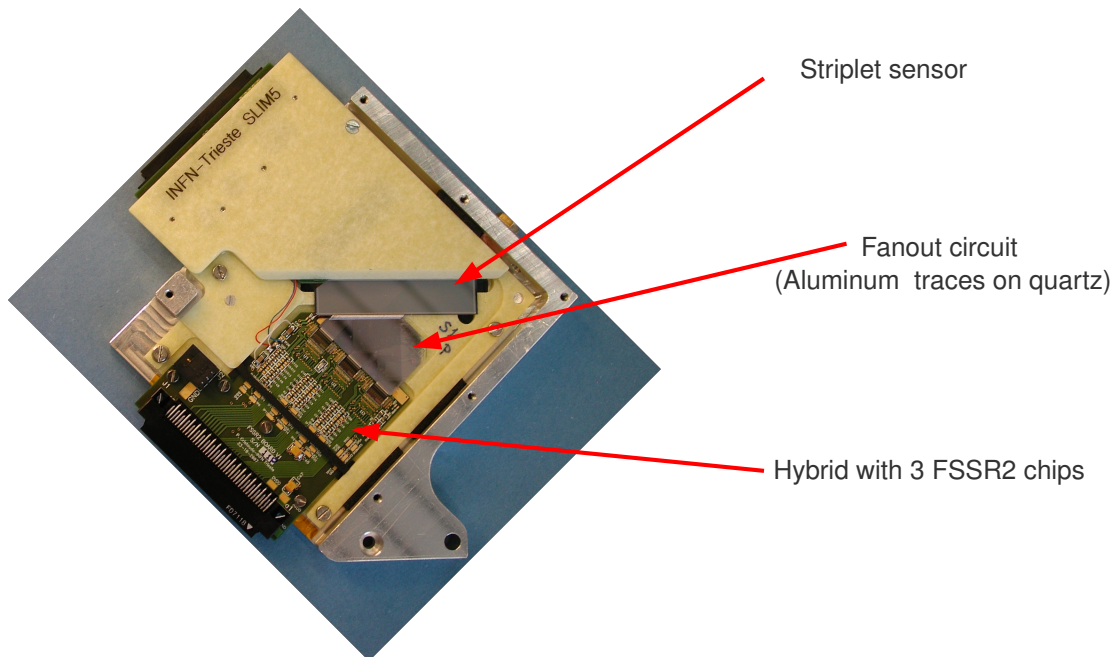
Figure 3.7: Annotated picture of an assembled striplet module. The sensor, the fanout circuit and the readout card, hosting 3 FSSR2 chips, are visible.

3.5 Performance of SLIM5 Detectors

To fully test the detector prototypes a demonstrator was built [5] and put on beam at the T9 facility of the CERN PS in September 2008.

3.5.1 The experimental set-up

At T9 facility of the CERN PS protons of 12 GeV/c, with spills of 400 ms and typically from 10^4 to 10^6 particles/spill, where impinging on the demonstrator, which was set-up as shown if Figure 3.8.
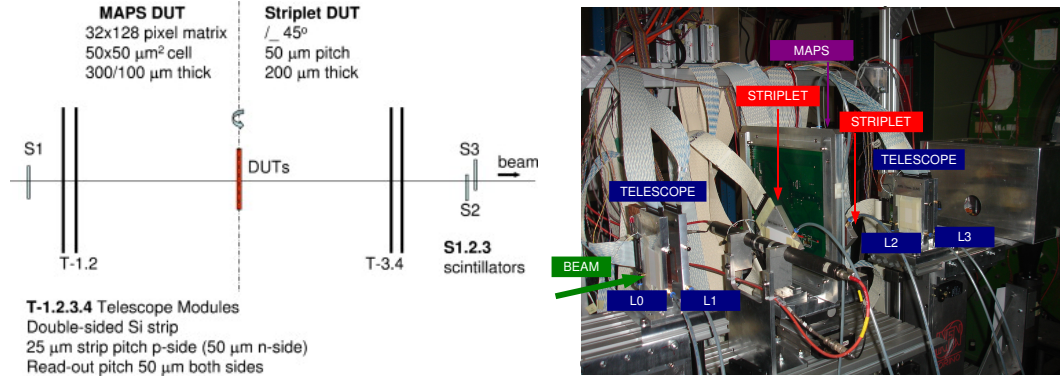
Figure 3.8: (left)The SLIM5 Beam Test Setup. (right)Picture of the SLIM5 demonstrator at the T9 facility of the CERN PS in September 2008. The telescope, 2 striplets modules and one Apseld4D are visible.

For the reference telescope four 2×2 cm^2 DSSDs were used; the strips where AC-coupled, with 25 (50) µm pitch on $p - (n-)$side. The readout pitch was the same (50 µm) for both sides, as the telescope modules too were readout by the FSSR2 chip. One pair was positioned upstream and the other downstream of the devices under test (DUTs). The scintillators (S1, S2 and S3) were used for trigger studies.

3.5.2 Apsel4D Results

Two Apsel4Ds were studied, one having with nominal thickness (300 µm) and the other thinned down to 100 µm only. The maximum efficiency was observed for the thinned chip; at the lowest threshold (400 e, about 40% of a MIP signal) it reached 92%, which roughly corresponds to the Apseld4D fill factor. Efficiency vs threshold results for Apsel4D are shown in Figure 3.9

The efficiency within the Apsel4D pixel cell was performed; given the tracking resolution of about 7 µm the Apsel4D pixel cell was divided in a 3×3 matrix. The results are reported in Figure 3.9

One observes a significant variation of sensibility within the pixel area, as expected. In particular, the central region is seen to be virtually 100% efficient, while the upper part of the pixel, especially the upper right-hand sub-cell, shows lower efficiency due to the presence of competitive n-wells.

The measured intrinsic hit resolution was about 14 µm for the X-coordinate and slightly better for the Y-coordinate: a modest improvement with respect to the single pixel hit resolution of 50 µ$/\sqrt{12}$=14.4 µm, mainly due to the absence of analog information and to the modest fraction of clusters of two or more pixels.

3.5.3 Striplets Results

The results from the beam test of a striplet module are outlined in this Section; in the following one a discussion on the impact of threshold on residuals will be presented.
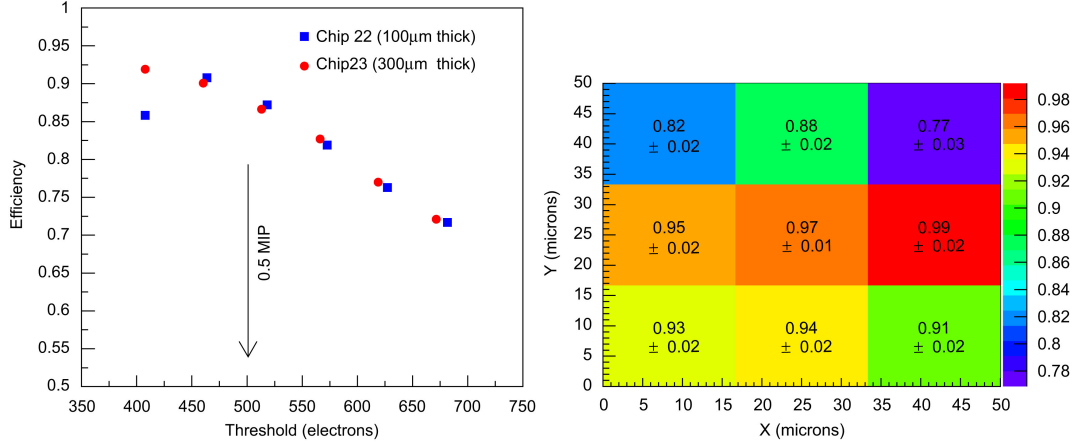
Figure 3.9: (left)Efficiency results for two MAPS detectors, taken from a single threshold scan. The statistical uncertainty on each point is smaller than the size of the plotting symbol. The point of low efficiency at the lowest threshold was probably due to temperature fluctuations during the measurements.(right) MAPS hit efficiencies measured as a function of position within the pixel. The picture, which is not to scale, represents a single pixel divided into nine sub-cells. The values are the efficiencies obtained in each sub-cell after taking into account track migration among cells. The uncertainties include the statistical uncertainty plus a systematic contribution coming from the track migration.

We have evaluated the input noise charge by measuring the fraction of hits over threshold as a function of the input charge at a given discriminator threshold. The results of the calibrations are summarised in Table 3.1.

Table 3.1: Calibration results for the striplet detectors.

Side	p	n
Noise (e)	630	1020
S/N	25	16
Gain (mV/fC)	96	67
Threshold (e)	4400	6300
Thr.Dis. (e)	880	780

Cluster of strips were created by grouping neighbouring strips that have fired. The charge pulse height distribution of clusters are shown in Figure 3.10.

The fitted MPV was found to be well compatible with the expected value for a MIP in 200 μm thick silicon detector. The region above 100 threshold DAC for the $n-$side was severely impacted by the limited dynamic range of the ADC, as it can be seen in Figure 3.10.

The hit-efficiency was of above 98% for both the $p-$ and the $n-$side. A detailed analysis of the hit-efficiency as a function of the position along the detector is shown in Figure 3.11.

As it can be seen efficiency was quite uniform over the entire sensor. Strips with efficiency below 1% where declared as dead and removed from the analysis. An electrical analysis after the beam test confirmed that the dead strips were indeed disconnected/malfunctioning channels.
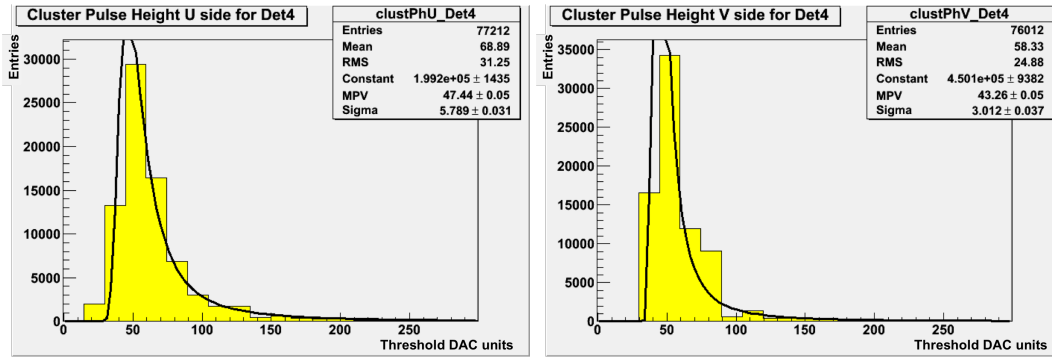
Figure 3.10: Cluster pulse height distribution for a striplet module. (left) $p-$ side; (right) $n-$side. Data is fitted with a Landau function.
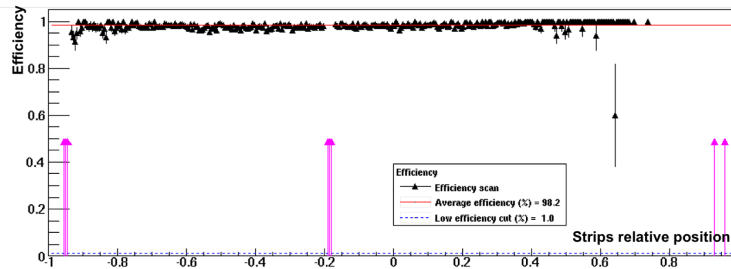
Figure 3.11: Efficiency of a striplet module as a function of the track impact position. Dead strips where removed from the analysis by selecting strips with efficiency greater than 1.0%; dead strips position is marked by magenta arrows.

The spatial resolution performance of the striplets will be discussed in detail in the next Section.

3.6 Discussion of the Striplets Spatial Resolution

In this Section the spatial resolution of the striplets will be discussed in detail. After a rather general introduction to the concepts of spatial resolution and how it can be inferred from the residuals distribution, the spatial resolution performance of the striplets will be presented. In particular the impact of the threshold will be examined.

3.6.1 Residuals and Spatial Resolution

The spatial resolution performance of position sensitive silicon detectors depends on various factors; some of them are related to the physics processes of charge creation and transport, others to the detector characteristics. Among the former there is the statistical fluctuation of the energy loss and the diffusion of the charge carriers produced by the MIP: the carriers created by a traversing MIP spreads due to diffusion according to $\sigma = \sqrt{2Dt}$ where D is the diffusion constant and t is the time the carriers travel to reach the collecting electrode; typical values of the diffusion spread σ are of few µm for detector thicknesses of 100-200 µm when the carriers velocities are saturated. Factors that influence the spatial resolution that are related to the detector characteristics are the analog or binary readout, the detector pitch and the signal-to-noise ratio.

Spatial resolution is usually estimated by taking the RMS of the residuals distribution. Residuals are defined as the difference between the position of the DUT hit associated to a track and the extrapolated position of the track itself on the DUT plane . The width of the residuals distribution depends on two main factors: the intrinsic resolution of the DUT σ_{DUT} (about the detector pitch divided by $\sqrt{12}$ - the so-called *binary resolution* [42]) and the pointing resolution of the tracking system σ_{trk}, which is the sum of the beam telescope resolution σ_{tele} [3] and the RMS deviation due to MS σ_{MS}. Hence the width of the residuals distribution σ_{res} is given by:

$$\sigma_{res} = \sigma_{\mathrm{DUT}} \oplus \sigma_{trk} \tag{3.2}$$

If the contribution of tracking resolution to the residuals is negligible with respect to the DUT one, then the DUT elementary cell, strip or pixel, can be resolved (examples can be found in 7.4); if not, then the residuals distribution is usually well described by a Gaussian distribution. In the latter case the DUT resolution σ_{DUT} can be obtained by deconvolution using Equation 3.2: $\sigma_{\mathrm{DUT}} \sim \sigma_{res} \ominus \sigma_{trk}$

Charge sharing between neighbouring strips (or pixels) allow the formation of clusters with 2 or more. Focusing on strips, when more than 1 strip fires it is important to assign to the multi-strips clusters the positions that give as a result the smallest possible residuals distribution, hence, the ultimate spatial resolution for the detector.

In [42] an excellent and complete discussion on the best algorithms to find the position of particle hits is given; the influence of detector parameters (thickness, pitch, floating strips, etc.) and of the track angle are investigated. The best algorithm for clusters of 2 strips is the so-called η position-finding algorithm (PFA), where:

$$\eta = \frac{S_R}{S_R + S_L} \tag{3.3}$$

---

[3]about the intrinsic resolution of each telescope plane divided by the square root of the number of telescope planes

where $S_{R(L)}$ is the signal amplitude of the right (left) strip in the cluster. Using the η PFA the cluster position x_η is defined as:

$$\frac{x_\eta}{P} = f(\eta) + \frac{x_L}{P} \tag{3.4}$$

where P is the detector pitch, x_L is the center position of the left strip in the cluster and $f(\eta)$ is a function that can be estimated directly on data:

$$f(\eta) = \frac{\int_0^\eta \frac{dN}{d\eta'} d\eta'}{\int_0^1 \frac{dN}{d\eta'} d\eta'} \tag{3.5}$$

under the assumption that the distribution of the number of tracks N is uniform over the detector.

The uncertainty on the position identified using the η PFA σ_η, hence the detector spatial resolution, is about the detector pitch P divided by the signal (S) over noise (N) ratio:

$$\frac{\sigma_\eta}{P} \sim \frac{N}{S} \tag{3.6}$$

The η algorithm is the optimal one for tracks at normal incidence or impinging at small angles. Despite it was used for the analysis of striplets data the width of residuals was much larger than expectations, about 16 μm with respect to ~14 μm that is the expected value for hits formed by just 1 strip. The reason for this poor resolution was investigated and the results are discussed in what follows.

3.6.2 Striplets Residuals and the Effect of Thresholds

In Figure 3.12 the residuals distribution for hits registered on the $p-$side of a striplet module is presented. The width of the fitted Gaussian is about 16 μm.
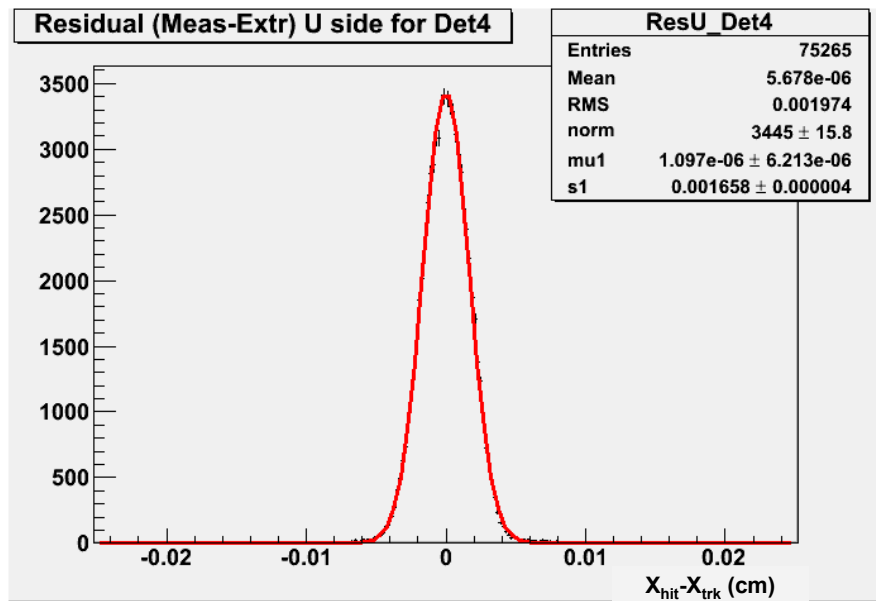
Figure 3.12: Residuals distribution for hits registered on the $p-$side of a striplets module. Points are data, the red line is the result of a Gaussian fit to the distribution.
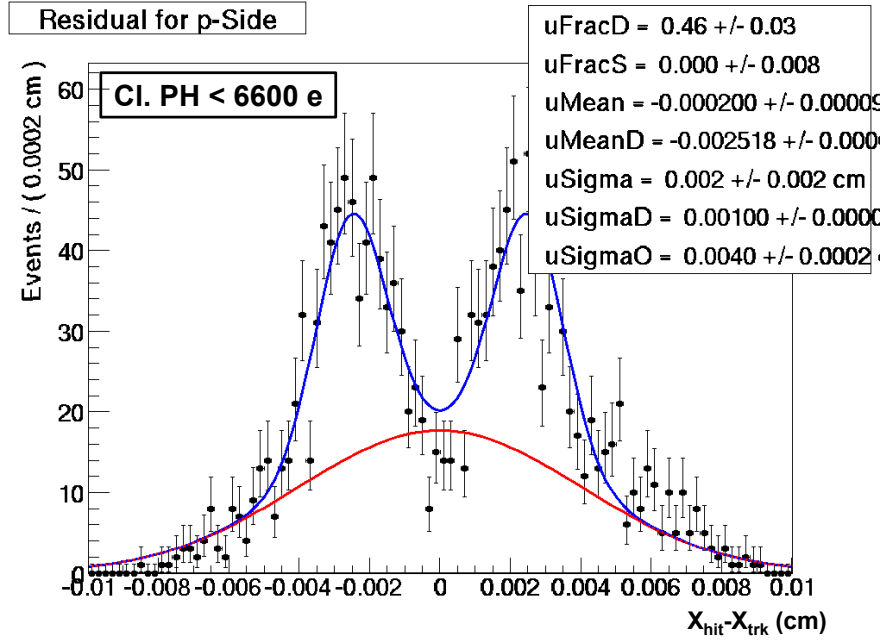
Figure 3.13: Residuals distribution for hits registered on the p−side of a striplets module when only clusters with ≤6600 e charge are considered. Data are represented as points with error bars. The fit function (blue solid line) is given in Equation 3.7; the red solid line is the outlier Gaussian contribution.

More than 82% of the analysed clusters contained just 1 strip when particles where impinging at normal incidence; 16% of the total had 2 strips. Hence the expected residuals width when all clusters are analysed together should have been slightly smaller than $50/\sqrt{12} \approx 14.4\,\mu$m.

The reason for the poor performance was found to be related to the high hit/no hit threshold set on the FSSR2 chip. In case of asymmetric charge sharing between two strips one of the two can have a signal that is below threshold, hence a true cluster of 2 strips is reconstructed as one with a single strip. In this case the cluster position is assigned to the center of the only strip whose signal is above threshold, so, on average, the error made in position assignment is about half of the pitch, *i.e.* 25 μm.

To confirm the hypothesis clusters with charge about or less than a third (6600 e) the one expected for a MIP where studied; the residuals distribution for these clusters is show in Figure 3.13.Two peaks around P/2 ≈ 25 μm are clearly visible: they correspond to the aforementioned true 2 strips clusters reconstructed as 1 strip only hit.

The residuals distribution was then fitted with a function containing three components: a core Gaussian, to model correctly reconstructed clusters; a double guassian, with mean fixed at ±25 μm, to model the mis-reconstructed 2 strips clusters; and finally an outlier Gaussian, with mean fixed at 0 μm, to take into account spurious hits [62]. The probability density function (PDF) as a function of the residual value x was:

$$f(x) = f_\mathrm{S}\mathrm{S}(x) + (1 - f_\mathrm{S})\Big[f_\mathrm{D}\mathrm{D}(x) + (1 - f_\mathrm{D})\mathrm{O}(x)\Big] \tag{3.7}$$

where S, D and O are the core, double and outlier Gaussian, respectively, and $f_\mathrm{S,D}$ are weights constrained between 0 and 1.

The distribution of residuals of all clusters are shown in Figure 3.14.

The fit results indicated that, once the dead strips are removed, the outlier component is negligible. On the contrary, about 7% of the data were described by the double Gaussian

a

b
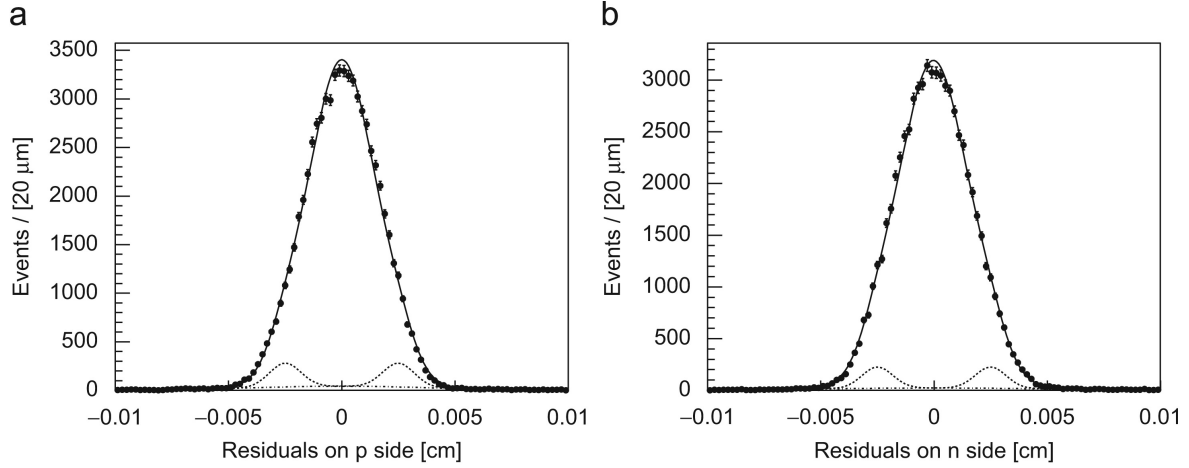
Figure 3.14: Residual fit for the striplets as a DUT for (a) p-side and (b) n-side. Data are points. The solid line is the fit function given in Equation 3.7; the dot-dashed line is the outlier Gaussian contribution, while the dashed line is all but the core Gaussian.

component.

The ultimate resolution was obtained using Equation 3.2, where σ_{res} is taken as the width of the core Gaussian of the fit function. We found a resolution of 13.6 µm for the $p-$side and 14.1 µm or the $n-$side, slightly better than the binary resolution for a 50 µm readout pitch and in agreement with the expected values for strip detectors with similar S/N.

3.6.2.1   Spatial Resolution as a Function of the Track Angle

The spatial resolution of striplets was studied as a function of of the incident track angle; the results are reported in Figure 3.15, where the average cluster size is shown too.

a

b
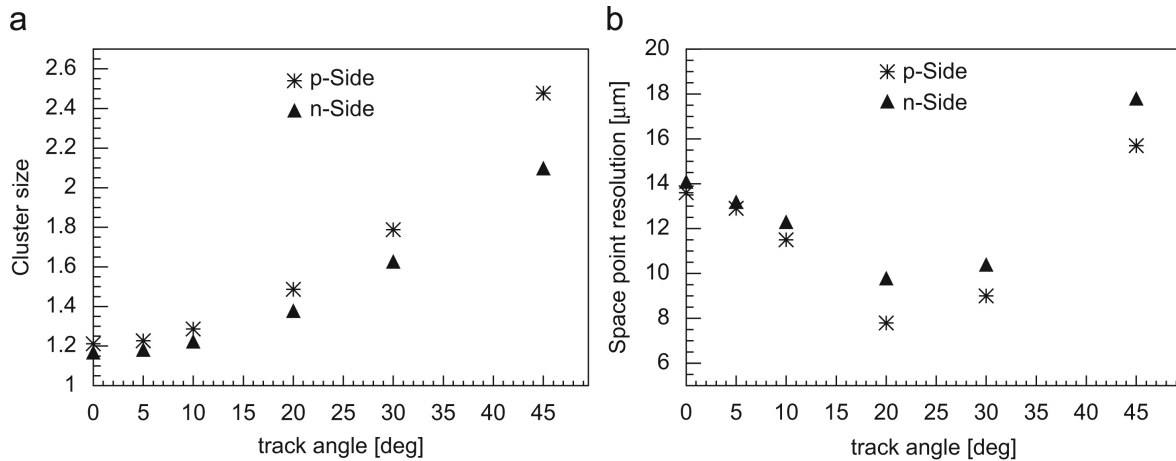
Figure 3.15: (a) Average cluster size for the striplets as a function of track angle. (b) Resolutions for the striplets as a function of track angle.

The average cluster size increases and therefore the resolutions improve considerably as a function of the incident angle up to 30°, after which the performance degrades. This is in good agreement with expectations [42]. At 45° the resolution is about 20% worse than that at normal incidence.

Cluster size was smaller for $n-$side than $p-$side for all angles investigated; as a consequence the resolution was worse for $n-$side than $p-$side. This is the result of higher

48

noise, higher threshold and limited ADC range for $n-$side (see Table 3.1).

The residuals distributions as a function of the incident track angle are presented in Figure 3.16.

As it can be seen the contribution of the double peak Gaussian is less and less important as the angle increases; this is due to the charge sharing being more and more symmetric. This analysis confirmed the validity of the hypothesis about the influence of the threshold on the residuals distribution.
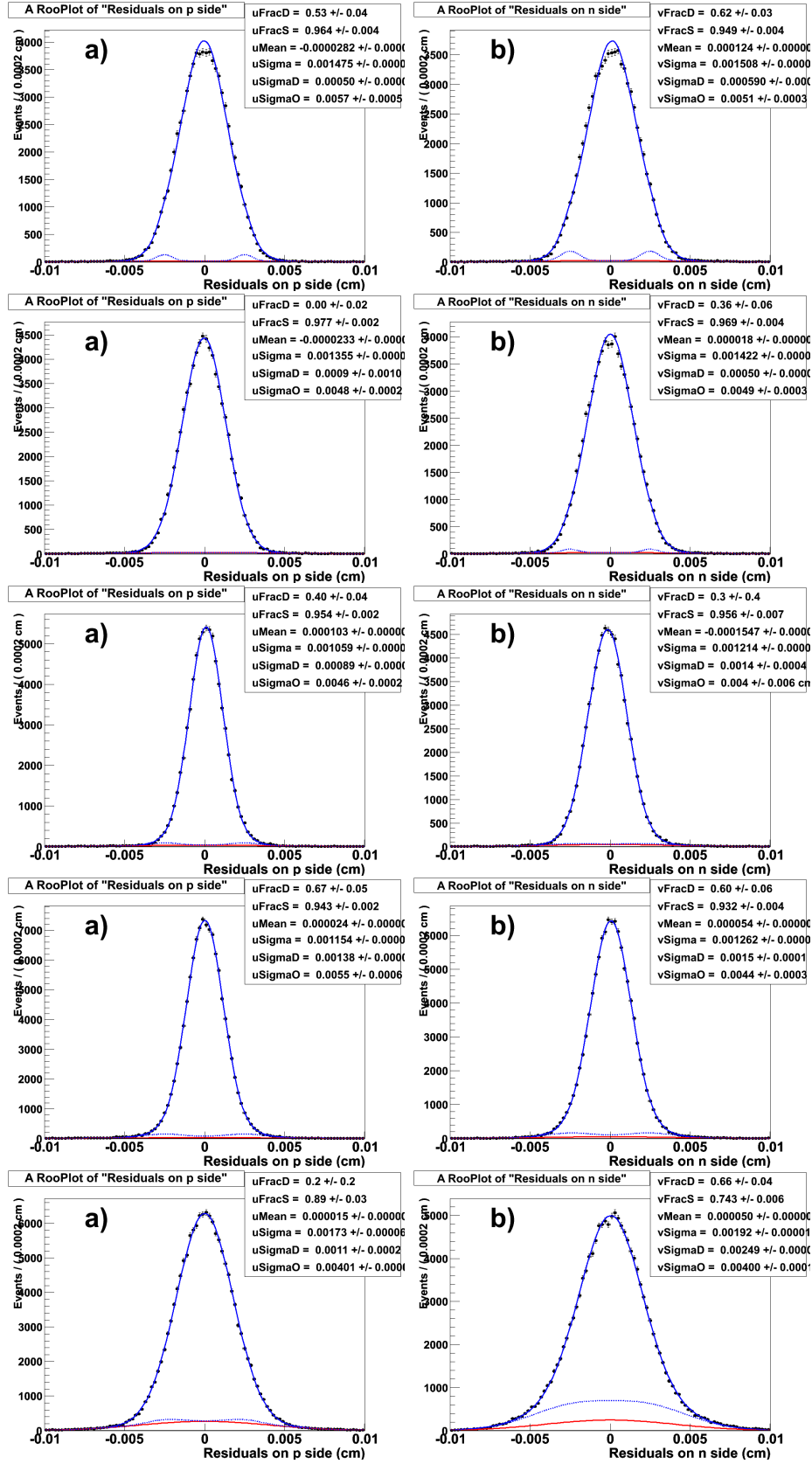
Figure 3.16: Residuals distribution of striplets detector at different incident track angle. From top to bottom raw the incident track angle was 5, 10, 20, 30 and 45°. (a) is for p−side, (b) for n−side. Points are data, the fit function is given in Equation 3.7.

3.7 Summary and Discussion

Thin silicon detectors with excellent spatial resolution are mandatory to fulfil the physics program of Super Flavour Factories and Linear Colliders. The solutions proposed by the SLIM5 collaboration, the CMOS MAPS Apsel4D and the DSSD striplets, proved to be an excellent starting point for the development of tracking and vertexing detectors for those experiments.

Indeed they were both "light" in terms of material budget, 0.1% and 0.2% of X_0 for the 100 μm thick Apsel4D and for the striplets (sensor only but no readout electronics present in the active area) respectively. The possibility for striplets to have the readout electronics outside the active area made them the preferred option for the layer0 of the proposed SuperB SVT. Hit-efficiency was high and matched the expectations for both Apsel4D and striplets. The Apsel4D chip hit efficiency was limited by the fill factor due to the competitive wells; for the striplets no major showstopper was found and the efficiency was close to 100%.

For what concerns the space-point resolution, both detectors matched the expected performance for 50 μm pitch detectors, but they suffered for the low number of clusters with more than 1 cell due to the high threshold.

Faster readout was in need for both solutions, even if FSSR2 chip was operated at up to 70 MHz.

Smaller pitches and better noise control were needed to match the specifications. In particular, as it was investigated throughly for striplets, the zero suppression mechanism impacts severely the spatial resolution if thresholds are relatively high and their effects are not corrected for.

Research continued for CMOS MAPS [78], improving the efficiency by increasing the fill factor, reducing the pitch to 40 μm and exploring vertical integration. Striplets would have benefited from a new readout chip.

Chapter 4

Technology Computer Aided Design Simulations

In this Chapter the basics of Technology Computer Aided Design, *TCAD*, simulations will be given. After introducing TCAD simulation tools (Section 4.1) and explaining their importance for the development of silicon detectors for HEP applications, some examples of TCAD based studies will be given, both for sensor design optimisation and device simulation (Sections 4.2 and 4.3). In Section 4.4 a discussion on the comparison of different TCAD tools is given, with a particular focus on the modelling of fundamental semiconductor physics. Section 4.5 will be devoted to the modelisation of radiation damage in TCAD simulation, a topic of very large interest in view of the new trackers for the actual ATLAS Pixel Detector (Chapter 6), but also for the the High Luminosity phase of the Large Hadron Collider (more details in Chapter 7). In Section 4.6 a detailed discussion on comparing Silvaco and Synopsys TCAD tools when used for radiation damage modelling will be given. A general summary (4.7) will close this Chapter.

4.1   Introduction

TCAD is a branch of electronic design automation that models semiconductor fabrication and semiconductor device operation. The modelling of the fabrication is termed Process TCAD, while the modelling of the device operation is termed Device TCAD. Included are the modelling of process steps (such as diffusion and ion implantation), and modelling of the behaviour of the electrical devices based on fundamental physics, such as the doping profiles of the devices.

The advantages TCAD based studies offer during the development of semiconductor sensors and electronics are multiple:

- they are predictive

- they provide insight

- they capture and visualise theoretical knowledge

TCAD based studies are predictive since they offer the possibility to explore alterative / innovative solutions providing quantitative predictions, allowing to test new hypothesis. They also offer insight: they allow the user to explore physical quantities otherwise impossible to access in reality, like point-by-point carriers distribution, electric field

lines, etc. In this sense they are also a powerful tool to learn semiconductor physics, provided a good base knowledge is present. Finally TCAD tools make it possible to literally visualise new ideas and the results they promise to offer.

In the following some examples of TCAD based sensor design and of predictions for HEP trackers will be given.

4.2 Sensor Design

The possibility to explore several designs for a silicon detector without having to realise them is an asset since it allows to reduce the number of submissions, allowing to save time and money. One example of such studies is given by the optimisation of the detector edge design. As already discussed in Section 2.4.2 it is important to control the voltage drop from one side of the junction to the other one. This is particularly true for nowadays silicon sensors where, to maximise the detector acceptance, the dead area at the detector edge has to be kept at a minimum (see also 7.5). One way to achieve small dead areas and and at the same time avoid large electric fields is to add several guard rings (GRs) that surround the sensitive area of the sensor. How many GRs include in the detector, how large their implants should be, which total area they should cover are some of the questions that TCAD simulations can address.

In order for the answers to be really reliable it is important to have access to information like the doping profiles of the various detector implants and dielectric thicknesses. This is often not possible, since the silicon foundries do not disclose these information. Some *a posteriori* analysis is possible, like Secondary Ion Mass Spectroscopy, *SIMS*. SIMS is a vacuum based technique which relies on the bombardment of a sample surface with a primary ion beam followed by mass spectrometry of the emitted ionised secondary ions. For SIMS see for example [79]. A result of the SIMS investigation [80] of a *p-spray* doping is shown in Figure 4.1.
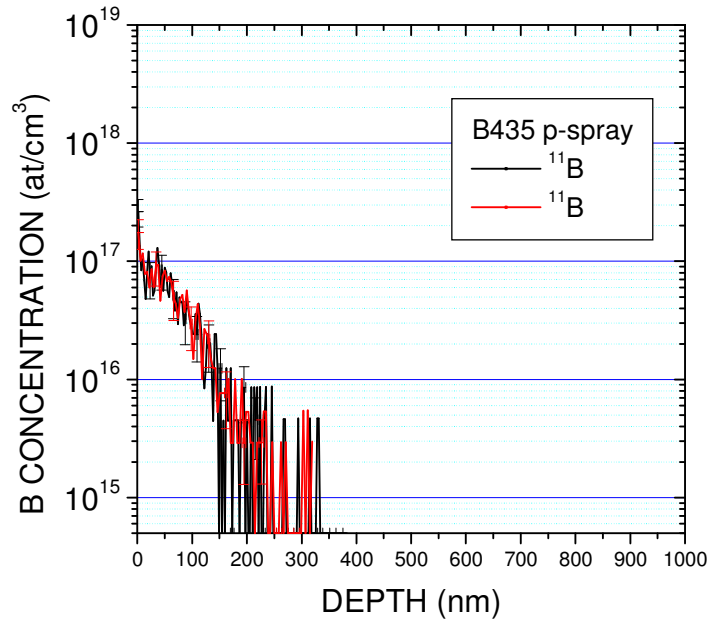
Figure 4.1: Boron depth profiles obtained in two points for each *p-spray* area on samples taken from an $n-on-p$ production.

P-spray is needed to counter the accumulation of electrons between n^+ implants in

an electron collecting detector, which otherwise would short the electrodes and degrade the detector performance. The positive oxide charge is responsible for the electron layer at the Si-SiO$_2$ interface [28].

Thanks to inputs like the ones from SIMS it is possible to make optimal choices for the detector edge design as it was done for the edgeless pixels sensors reported in [7]. An example of the agreement between real data and TCAD simulations is shown in Figure 4.2. In the Figure the IV curves of edgeless $n-on-p$ pixel test structures are compared. The
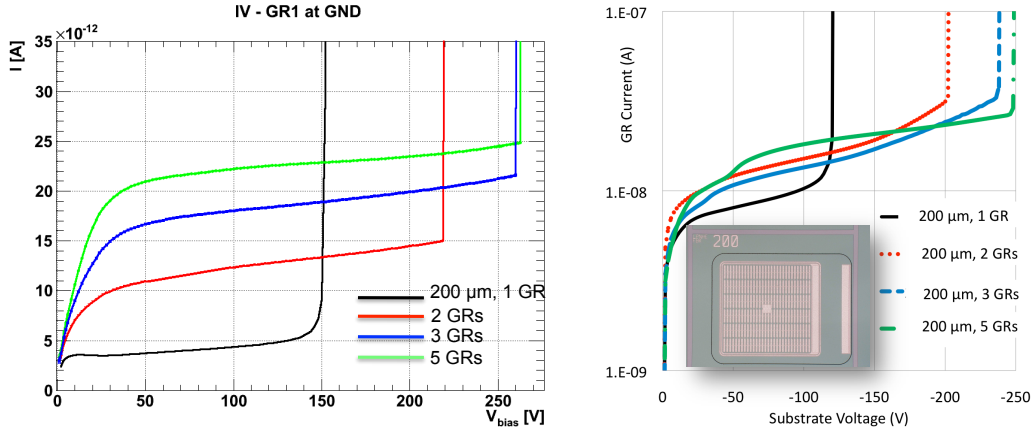
Figure 4.2: IV curves for edgeless $n-on-p$ pixel test structures. (left) TCAD simulations (right) Real data from [7]. Detectors with the same pixel-to-edge minimal distance and different number of GRs are compared. In the right figure a photo of the tested detector is shown in the inset. Vetical scales are different due to the simulated detector area which is smaller than the real one.

parameter of interest here is the breakdown (BD) voltage, which in the presence of p-spray depends critically on the dose of the implant and on the shape of the electrode on top of the n^+ implant.

As it can be seen for what concerns the BD voltage the level of agreement between real data and TCAD simulations is at 20% or better. This was an important achievement since the designs of the real sensors was driven by the TCAD simulations studies; they allowed to choose among different possible combinations of minimal pixel-to-edge distances and number of GRs. It has to be noticed that the vertical scales do not agree and this is expected since the area of the simulated detector is a small fraction of the real one.

A similar study, reported in Figure 4.3, showed that keeping the number of GRs fixed and simply increasing the minimal pixel-to-edge distance does not make the BD voltage larger.

This effect is due to the p-spray which is equipotential with the backside implant till it does not cross a n^+ implant, like a GR or the pixels. Hence, increasing the distance between the detector edge and the pixels but not adding more GRs does not allow a more smooth voltage drop, hence does not change the BD voltage. The fact the p-spray is equipotential was verified during the simulation studies, a test otherwise difficult to accomplish.

The one presented so far is a very simple but effective case in which TCAD simulations drive the sensors design. More sophisticated studies can be carried out, in which processes like etching, oxide growing, doping implantation and diffusion and many more can be simulated. These kind of studies are beyond the scope of this report; an example of such studies can be found in [81].
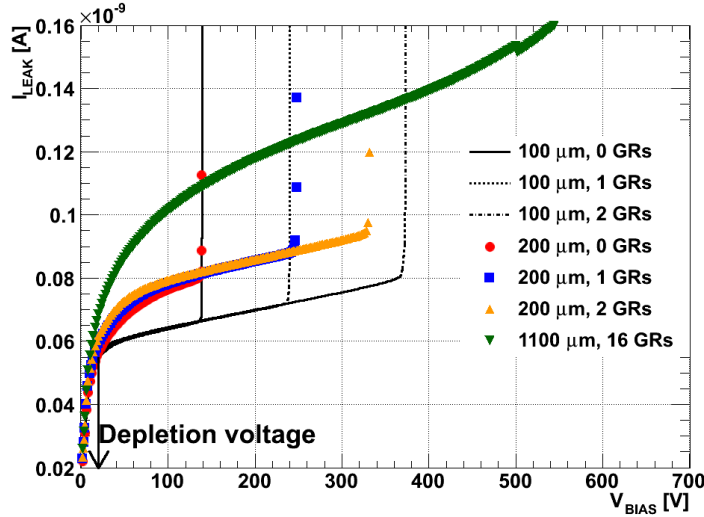
Figure 4.3: Simulated IV curves for edgeless $n-on-p$ pixel test structures. Detectors with different pixel-to-edge minimal distance and different number of GRs are compared.

4.3 Device Simulation

Device simulation allows to study the detector behaviour under numerous conditions like forward / reverse voltage, application of sinusoidal signals on electrodes, illumination with lasers or generally light, generation of charge in the bulk by charged particles, radiation induced traps in the bulk and at the surface, low temperature operation, etc., and of course combination of them. All these correspond to working condition for HEP detectors, hence predictions can be extracted for example for a heavily irradiated silicon detector in terms of charge collection efficiency, operating voltage and leakage current level.

Such studies again allow to make detector choices that save money and time and give access to quantities like carriers distribution otherwise impossible to measure. An example is given in Figures 4.4 and 4.5, where the result of 2D simulations of an $n-on-n$ detector are reported. Three collecting electrodes are simulated; the detector is 250 µm thick and the pitch is 250 µm. The over-depleted detector ($V_{bias} = 500$ V) is hit by a MIP; the MIP strikes at an angle of 20° with respect to the sensor surface. The detector was simulated after an irradiation fluence of $\Phi = 1 \times 10^{15}$ n_{eq}/cm^2, modeling the radiation damage using the Chiochia model [82] (more details in Section 4.5.2). By comparing the Figures 4.4 and 4.5 it can be seen that electrons drift faster than holes; a large fraction of holes have moved little from the original position while electrons have gained much more distance after 1 ns. This kind of simulation are needed to interpret data from beam tests when tracks are impinging at shallow angle. The charge profile in data can be compared over the signal amplitude from pixels in long clusters to the one predicted by TCAD simulations; this will allow to infer the electric field distribution inside the irradiated detector thanks to so-called *grazing angle* technique [83–85]; more on this in Section 4.5.

In case of edgeless sensors it is interesting to investigate the charge collection efficiency (CCE) in the un-instrumented area between the last collecting electrode and the detector edge. Other than the BD voltage, also CCE is an important factor on which optimise the detector design. In Figure 4.6 the result of a simulation study for an $n-on-p$ edgeless detector

The simulations indicate that it is possible to collect at least 50% of the signal ampli-
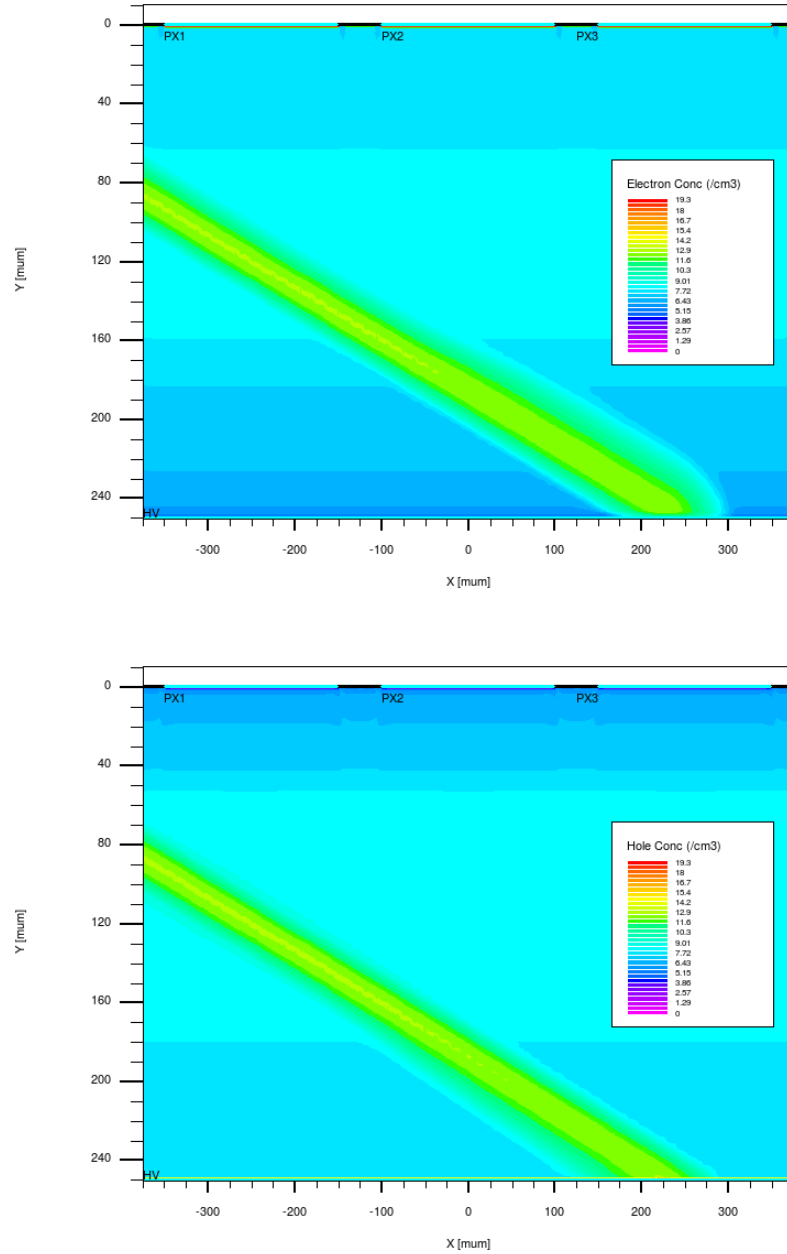
Figure 4.4: 2D simulations of an irradiated $n-on-n$ detector. Carriers concentration are reported when the detector is over depleted and a MIP just stroke. MIP was impinging at 20° with respect to the sensor surface. (Top) Electron concentration. (Bottom) Hole concentration.
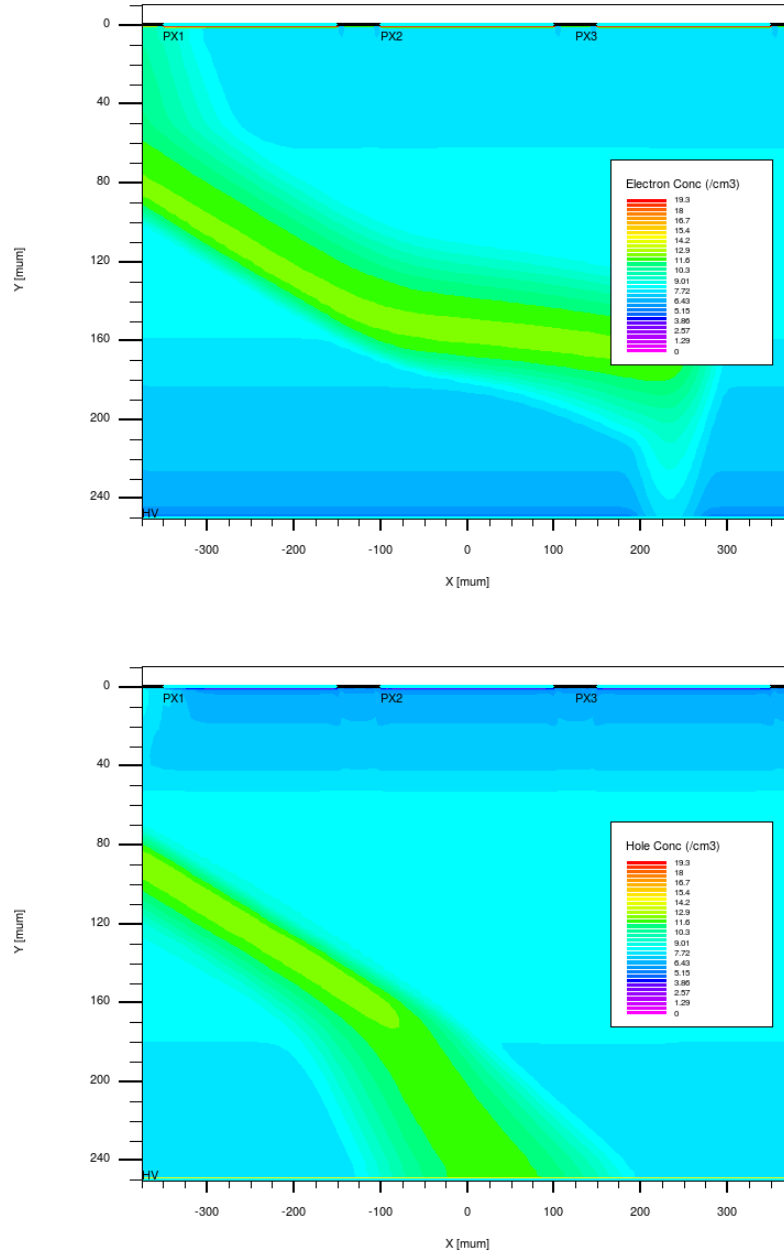
Figure 4.5: 2D simulations of an irradiated $n-on-n$ detector. Carriers concentration are reported when the detector is over depleted and 1 ns after a MIP stroke. MIP was impinging at 20° with respect to the sensor surface. (Top) Electron concentration. (Bottom) Hole concentration.
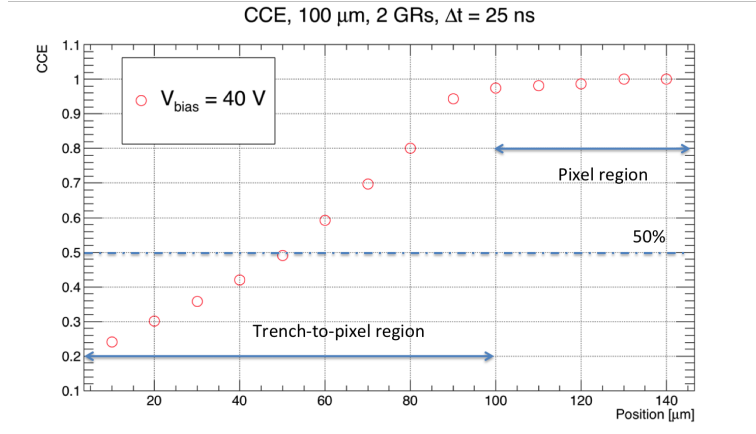
Figure 4.6: Simulated CCE as a function of the MIP impact point. It is the result of a 2D simulations of an $n-on-p$ edgeless detector. The bias voltage and the integration time are indicated.

tude for a MIP up to 50 µm away from the last collecting electrode. This is very promising for *active edge* detectors (see also 7.5).

4.4 Discussion on Fundamental Semiconductor Parameters and TCAD Simulations

The two most used commercial TCAD products in the HEP community for device simulations are Silvaco Atlas[1] and Synopsys Sentaurus[2]. In a test to see how much the two products differ in terms of physics models it turned out that at least in two fundamental semiconductor physics observables they were quite far apart. A 200 µm thick, 50 µm wide $n-on-p$ diode was simulated in 2D for these studies. More details can be found in [86].

The first observable under investigation was the thermal velocity of the carriers. Synopsys Sentaurus uses the following formulation as default for the carrier thermal velocities $v_{th,Syn}^{n,p}$:

$$v_{th,Syn}^{n,p} = v_0^{n,p} \sqrt{\frac{T}{300K}}, \tag{4.1}$$

and the default values for $v_0^{n,p}$ are 2.04(1.56)$\times 10^7$ cm/s.
Silvaco Atlas default for the carrier thermal velocities $v_{th,Sil}^{n,p}$ is:

$$v_{th,Sil}^{n,p} = \sqrt{\frac{3kT}{\text{M.VTHN(M.VTHP)}\, m_0}}, \tag{4.2}$$

where m_0 is the electron rest mass. For silicon the M.VTHN and M.VTHP parameters (the former for electrons, the latter for holes) are functions of the temperature T:

$$\text{M.VTHN} = 1.045 + 4.5 \times 10^{-4}\, \text{T} \tag{4.3}$$

$$\text{M.VTHP} = 0.523 + 1.4 \times 10^{-3}\, \text{T} - 1.48 \times 10^{-6}\, \text{T}^2 \tag{4.4}$$

The carrier thermal velocities v_{th} where evaluated between T = 250 K and T = 350 K for both Silvaco Atlas and Synopsys Sentaurus; the results are illustrated in Figure 4.7.
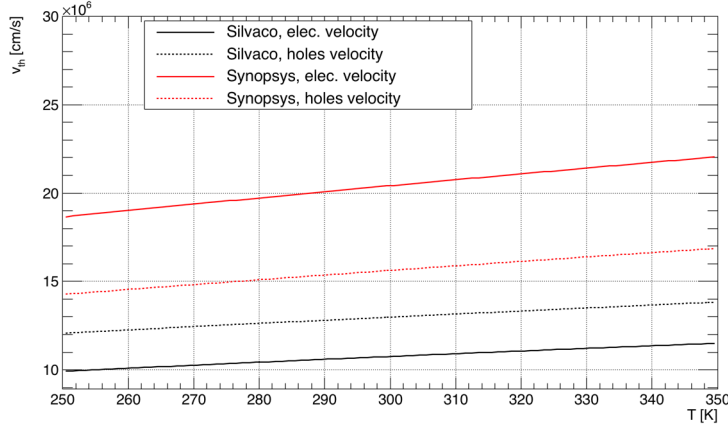
Figure 4.7: Carrier thermal velocities as a function of the temperature.

As it can be seen there is almost a factor of 2 of difference between the two tools for the electrons thermal velocities. The reason for this disagreement has to be found in the carriers mass value used in the thermal velocities calculation. While Synopsys uses the effective mass derived from the energy band curvature, Silvaco inserts the rest mass of the electron. Such a difference in the carriers thermal velocities should affect the carriers transport phenomena, the leakage current level and the effects due to radiation damage defects.

The second parameter that was investigated was the bandgap energy E_g. The default value in Silvaco for E_g at T =300 K is of 1.08 eV. This is surprisingly low compared to values in literature (see for example [28–30, 32]) which are comprised in the range 1.11-1.12 eV. The temperature dependence of E_g in both TCAD tools is the following [29]:

$$E_g(T) = E_g(0) - \frac{\alpha T^2}{T+\beta} = E_g(300) + \alpha\left[\frac{(300)^2}{300+\beta} - \frac{T^2}{T+\beta}\right] \equiv E_g(T_{ref}) + \alpha\left[\frac{(T_{ref})^2}{T_{ref}+\beta} - \frac{T^2}{T+\beta}\right] \quad (4.5)$$

where T_{ref} is some reference temperature. Both TCAD products agree on the α and β parameters values:

Table 4.1: Parameter values for the temperature dependence of the bandgap. See also Equation 4.5

parameter	value
α	4.73×10^{-4} eV/K
β	636 K

Silvaco tools are built on the value $E_g^{Sil}(300)$ =1.08 eV while Synopsys on $E_g^{Syn}(0)$ =1.1696 eV. Extrapolating $E_g^{Syn}(0)$ to T =300K from the one gets the expected $E_g^{Syn}(300)$ ~1.12 eV, in agreement with literature. Silvaco developers explained[3] the abnormal $E_g^{Sil}(300)$ value because of very low resistivity Silicon wafers used to estimate the bandgap energy when their TCAD tools was developed. They are aware of the issue and claim that the Silvaco TCAD tools are anyhow consistent with the $E_g^{Sil}(300)$ value chosen and predictions are reliable.

To test the latter statement the $E_g^{Sil}(300)$ value was changed in the Silvaco Atlas simulation package, and results compared. Again, a 200 μm thick, 50 μm wide $n-on-p$ diode

---

[3]private communication

was simulated using Silvaco 2D device simulator. Temperature was varied between -20°
and +20° in 5° steps. Several scenarios have been investigated:

default using default Silvaco parameters values

EG112 setting $E_g^{Sil}(300) = 1.12$ eV

Syn. Th. Vel. setting thermal velocities to the values used by Synopsys tool

EG112 & Syn. Th. Vel. combination of the two above

NO BGN turning off the model for bandgap narrowing based on the concentrations [87].

Several studies were performed using the Silvaco TCAD tools, including comparison
of simulated leakage current level with theoretical expectations, evaluation of the activation energy E_a (Equation 2.30) and scaling of leakage current with temperature. In what
follows the findings of these studies and a discussion of the results are presented.

Leakage Current Level In Figure 4.8 a comparison of the simulated leakage current in
the five scenarios for $t = 20°$C is presented. It is evident that the only parameter playing a
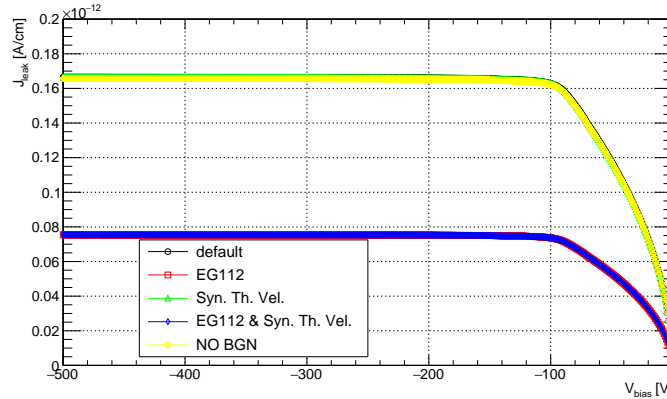
Figure 4.8: Simulated current density as a function of the bias voltage for different scenarios at
$t = 20°$C. See text for more details.

major role, as expected, is the bandgap energy $E_g^{Sil}(300)$.

To verify the validity of leakage current level from Silvaco tools the result at $V_{op} =
V_{depl} + 50$V bias were compared with the theoretical value evaluated using 2.29. Assuming the same value for generation and recombination lifetimes and taking the intrinsic
concentration value n_i from the simulation itself a current density of $J \sim 1.6 \times 10^{-13}$ A/cm
is expected, which is in excellent agreement with the value observed in simulations when
the default value of $E_g^{Sil}(300)$ is chose (*i.e.* 1.08 eV); on the contrary, as it can be seen
from Figure 4.8, when $E_g^{Sil}(300)$ is set to 1.12 eV the simulation results do not match the
theoretical expected values.

It has to be noted that the simulated current is purely bulk generated; this is also clear
from Figure 4.8: the current level is stable after the depletion voltage. This feature is not
realistic [88] but for the sake of understating bulk generated current properties in TCAD
simulations is very well suited since it allows to study the phenomenon without having
to deconvolve from the leakage current the surface effects, the trap assisted tunnelling
contribution, etc.

Temperature Dependence of Simulated Leakage Current and Activation Energy   The change of leakage current was studied for the different scenarios outlined before. For all temperature T times scenario S combination the leakage current $I_{leak}(V_{op}; T; S)$ at a operational voltage V_{op} was extracted. It was verified that the depletion voltage V_{depl} did not depend on scenarios nor temperatures.

The leakage current was then studied as a function of the reciprocal of the temperature and fitted with a function inspired by Equation 2.30:

$$I = I_{ref} \left(\frac{T}{T_{ref}} \right)^n exp \left[-\frac{E_a}{2k_B} \left(\frac{1}{T} - \frac{1}{T_{ref}} \right) \right] \qquad (4.6)$$

where n and E_a are free parameters, I_{ref} the simulated current at the reference temperature T_{ref} and k_B the Boltzmann constant. The results are reported in Figure 4.9. A 0.01 K error was assigned to the simulated temperature, the leakage current was evaluated at $V_{op} \pm 1.0$ V too and the largest shift used as an uncertainty estimate. In Figure 4.10 the parameter n of the fit function was fixed to 2.

The fit function 4.6 represent very well the data, whatever the scenario and the choice made for the parameter n (free to float or fixed to 2). This is an indication that the mechanism of temperature scaling is the same for all the configuration explored. The case, not presented here, of setting the parameter α of Equation 4.5 to zero was tested too but the results were deviating too largely from Equation 4.6 and considered unphysical.

In all scenarios the parameter n, when unconstrained, is compatible with the value of 2. So in the rest of the discussion we will consider only the case when $n = 2$ (Figure 4.10). A couple more scenarios where studied ($E_g^{Sil}(300) = 1.09$ eV and 1.11 eV) with the goal of studying the dependence of E_a on $E_g^{Sil}(300)$. The result are reported in Figure 4.11

From the Figure is manifest that the following relations hold:

$$E_a = E_g^{Sil}(300) + 0.05\,eV \qquad (4.7)$$

The activation energy range obtained from Equation 4.7 does not include the value found in literature of 1.21 eV [35] for bandgap energies between 1.08 and 1.12 eV.

Leakage Current Rescaling Based on Temperature   The relation 4.7 was used with Equation 2.30 to rescale leakage currents in the default scenario from different temperatures to the reference temperature, T = 293.15 K in this case. The rescaling was done separately for each voltage point. To verify the validity of the rescaling the scaled IV curves where divided by the IV curve at the reference temperature. For each temperature then the average and the RMS of these ratio was calculated. In Figure 4.12 the result of this study. It can be seen that after depletion (around -100 V) the ratio is very close to 1, much more than in underdepletion. If the average values are taken into account then it is possible to estimate to 1% the accuracy on average of the rescaling in the considered temperature range. The slope of the linear fit is compatible with 1 as the intercept with 0 within one standard deviation.

As a last test the ratio of IV curve of EG112 scenario to the default one was taken for $t = 20°$C; the curves were taken form 4.8. The result is reported in Figure 4.13.

The average value of the ratio is about 0.4522±0.0022 which is very close to the theoretical prediction based on Equation 2.30 used with relation 4.7.
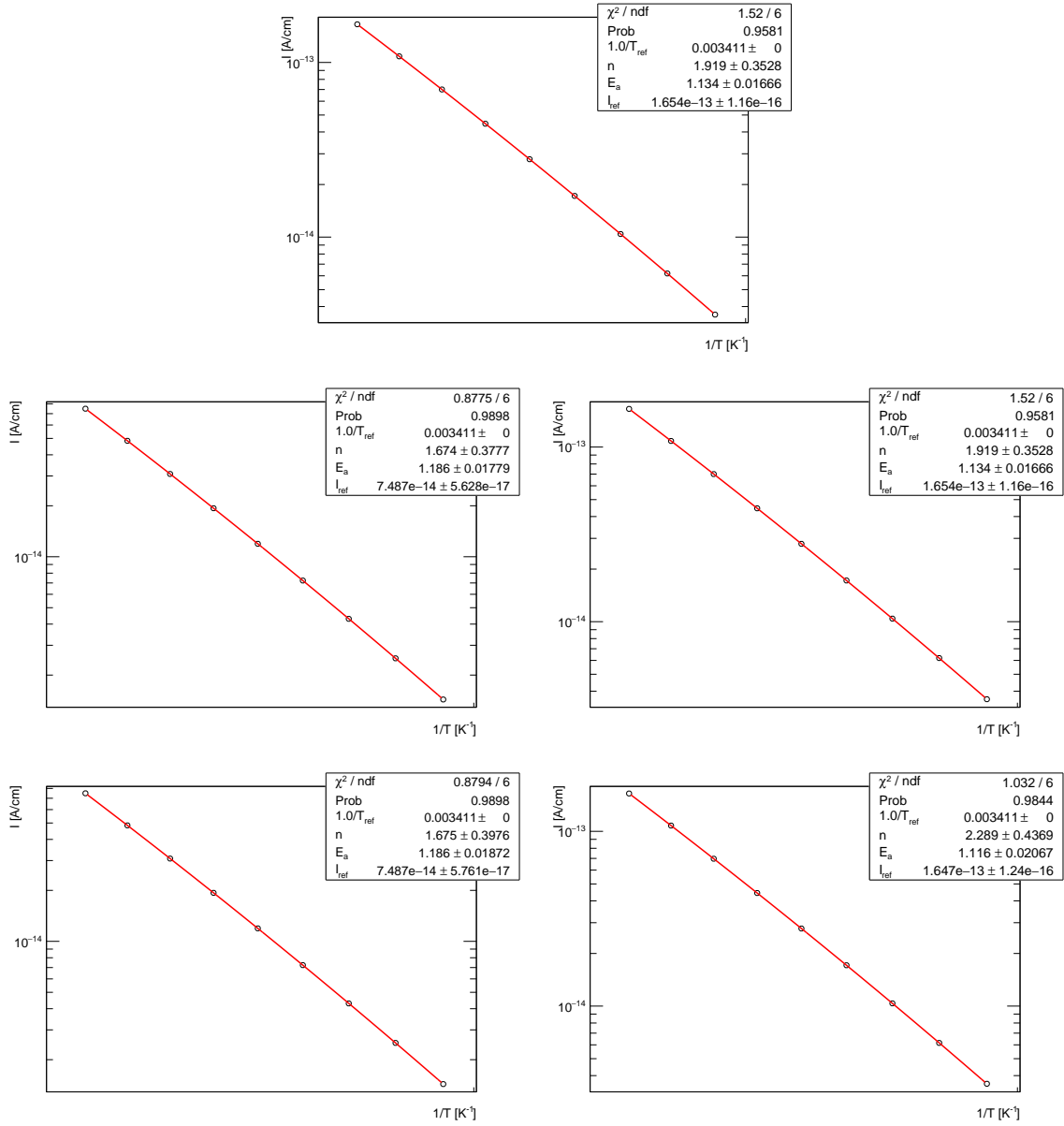
Figure 4.9: . Simulated leakage current at operational voltage V_{op} at different temperatures for different scenarios. (Top row) default scenario; (mid row) EG112 scenario on the left, Syn. Th. Vel. on the right; (bottom row) EG112 & Syn. Th. Vel. scenario on the left, NO BGN on the right. Data are points with error bars; data were fit with Equation 4.6 and the fit result is superimposed.
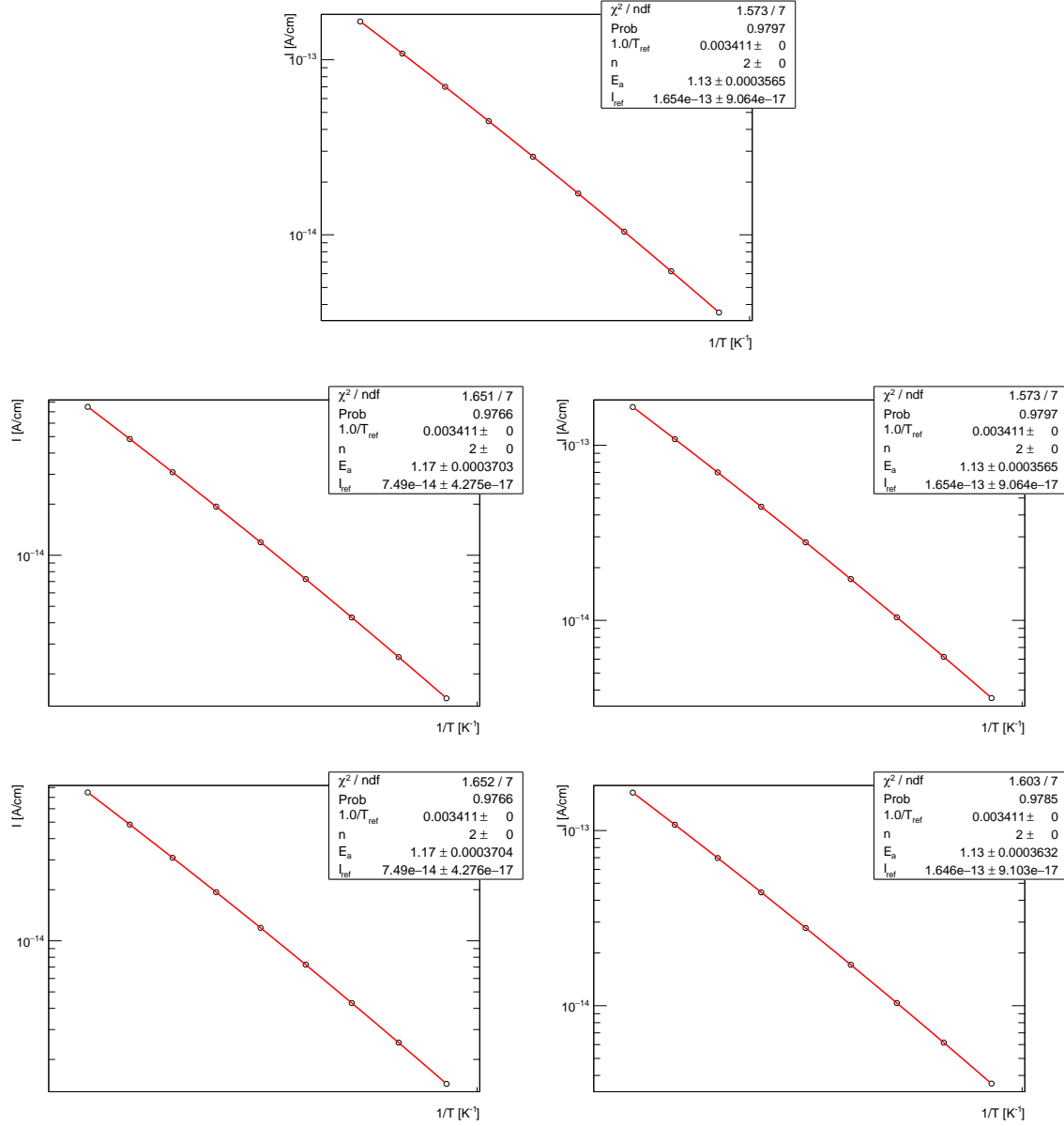
Figure 4.10: . Simulated leakage current at operational voltage V$_{op}$ at different temperatures for different scenarios. (Top row) default scenario; (mid row) EG112 scenario on the left, Syn. Th. Vel. on the right; (bottom row) EG112 & Syn. Th. Vel. scenario on the left, NO BGN on the right. Data are points with error bars; data were fit with Equation 4.6 and the fit result is superimposed. The parameter *n* was fixed to 2.
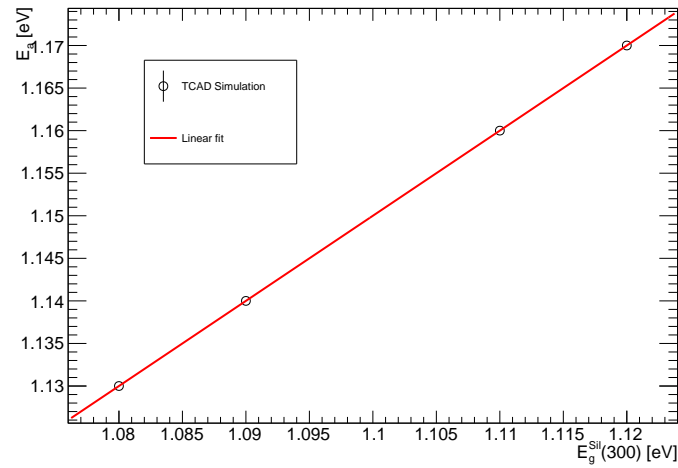
Figure 4.11: Activation energy as a function of the bandgap energy value at 300 K in Silvaco TCAD simulation. Data are points with error bars; a linear fit is superimposed.
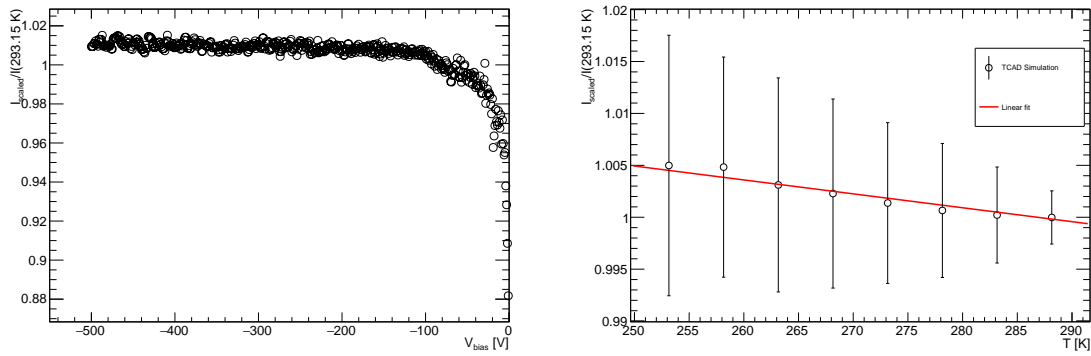
Figure 4.12: .(Left) ratio of IV curve at $t = -20°$ C to the one at $t = 20°$ C after the former has been rescaled to $t = 20°$. (Right) Average ratio of scaled currents to reference one as a function of the temperature. Both plots were created under the default scenario.
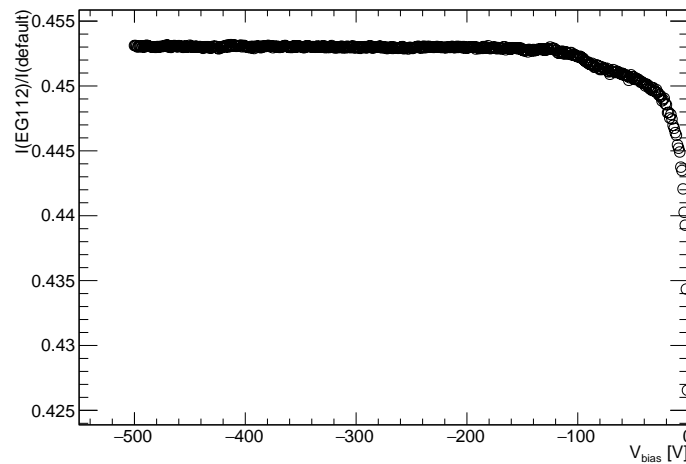
Figure 4.13: Ratio of IV curve under the EG112 scenario to the default one. The temperature was $t = 20°$ C for both scenarios.

Summary   It was shown that there are significant differences between the TCAD tools Synopsys Sentaurus and Silvaco Atlas on what concerns fundamental parameters like thermal velocities and bandgap energy. It is likely the two tools differ on other important aspects but two rather fundamental ones were already reported here. If for thermal velocities a simple rescaling of the carrier effective masses seem sufficient (more in the Section 4.6), the bandgap energy difference needs a more careful treatment.

It was shown that, despite the very low default value in Silvaco (1.08 eV at 300 K), the simulated leakage current level is in agreement with expectations based on intrinsic concentration and generation lifetime when the default value for bandgap energy is considered. TCAD simulated diode reverse leakage currents scale with temperature with the same formula which emerged from real data analysis; the fitted value of activation energy in simulated data is is very low, though: 1.17 eV maximum with respect to 1.21 eV. It was proved that it is possible to effectively rescale the simulated leakage currents from different temperatures to 20° C as it is done for real data, once the appropriate activation energy value for simulations is used.

In conclusion a working solution has been found for the Silvaco Atlas tool for what concerns the bandgap energy and the carriers thermal velocities, to make its predictions in agreement with data. Still it is a non perfect solution; it would preferable to have reliable results from simulations when the bandgap energy is set to its known value from literature and the derived activation energy close to the published data.

4.5   Modelling Radiation Damage in TCAD Simulations

In this Section the implementation, modelling and a study case of Radiation Damage in TCAD Simulations will be presented. This Section is an introduction to a subject that will be discussed again in Chapter 6.

4.5.1   Implementation of Radiation Damage in TCAD Simulations

As it was discussed in Section 2.5 energetic particles above a certain energy threshold create defects to the silicon lattice. It is possible to simulate defects using TCAD tools by adding trap centers, or simply *traps*, to the energy bandgap. Trap centers, whose associated energy lies in a forbidden gap, exchange charge with the conduction and valence bands through the emission and capture of electrons. The trap centers influence the density of space charge in semiconductor bulk and the recombination statistics. Device physics has established the existence of three different mechanisms, which add to the space charge term in Poissons's equation in addition to the ionized donor and acceptor impurities. These are interface fixed charge, interface trap states and bulk trap states. Here only bulk traps will be discussed. In particular this Section will describe the definition of bulk trap states and the implementation of these bulk trap states into Silvaco TCAD device simulations[4].

A donor-type trap can be either positive or neutral like a donor dopant. An acceptor-type trap can be either negative or neutral like an acceptor dopant. A donor-like trap is positively charged (ionized) when empty and neutral when filled (with an electron). An empty donor-type trap, which is positive, can capture an electron or emit a hole. A filled donor-type trap, which is neutral, can emit an electron or capture a hole. An acceptor-like trap is neutral when empty and negatively charged (ionized) when filled (with an

---

[4]https://www.silvaco.com/products/tcad/device_simulation/atlas/atlas.html
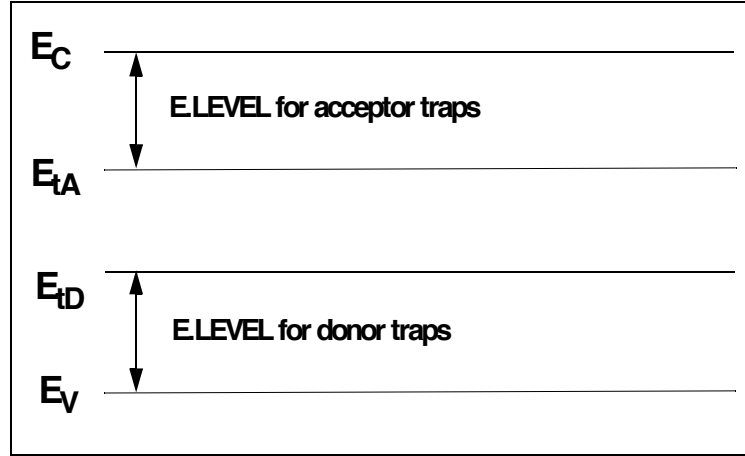
Figure 4.14: Definition of the trap energy level for acceptor and donor traps in reference to thec onduction and valence band edges. (After [89])

electron). A filled acceptor-like trap can emit an electron or capture a hole. An empty acceptor- like trap can capture an electron or emit a hole.

Figure 4.14 shows the terminology used within Silvaco TCAD to define the type of trap. The position of the trap is defined relative to the conduction or valence bands using E.LEVEL so for instance, an acceptor trap at 0.4eV would be 0.4eV below the conduction band [89].

The total charge caused by the presence of traps is added to the right side of the Poisson Equation; the generation-recombination equations will be modified including terms for taking into account that electrons are being emitted or captured by the donor and acceptor-like traps.

4.5.2   Radiation Damage Modelling in TCAD Simulations

We will now discuss which traps are to be added to TCAD Simulations to reproduce the experimental observations presented in 2.5. A list of defects relevant for silicon diode used in HEP was shown in Figure 2.23. Including all these defects is presently infeasible due to the overwhelming computational effort required and the large uncertainties associated with some levels.

Simplified approaches are therefore applied where only a subset of defects are simulated [58, 59, 82, 90–97]. Historically a simple model which accounts for the bulk damage just by means of one "equivalent" deep acceptor-like level was tried [90, 91] but it was failing at reproducing the double peak effect in the electric field distribution of heavily irradiated devices as shown in [57]. Two traps, one acceptor-like and one donor-like are more suited for this; several models where proposed, like [58, 59, 82, 96]. Further development involved the introduction of a second acceptor-like trap, very close to the midgap; this helped to better model the type inversion and the leakage current increase with fluence [93–95, 97]. At some point also 4 traps were considered but this was kind of unique trial [92].

An example of radiation damage model for TCAD simulations in given in Table 4.2; the traps characteristics are taken from [95].

For each trap it is specified if it is a donor- or an acceptor-like trap, its energy with respect to the relevant band edge (conduction / valence for an acceptor-/donor-like trap), the capture cross sections $\sigma_{e,h}$ for electrons and holes, respectively, and the introduction

Table 4.2: Relevant parameters for acceptors (A) and donor (D) deep levels in the bandgap, describing the radiation damage. (After [95])

Type	Energy (eV)	$\sigma_e(\text{cm}^2)$	$\sigma_h(\text{cm}^2)$	$\eta(\text{cm}^{-1})$
A	E_C -0.42	9.5×10^{-15}	9.5×10^{-14}	1.613
A	E_C -0.46	5.0×10^{-15}	5.0×10^{-14}	0.9
D	E_V +0.36	3.23×10^{-13}	3.23×10^{-14}	0.9

rate η which is the density of traps N_t per unit of fluence Φ.

In general the energy of the trap E_t is located some units of thermal energy kT away from the intrinsic energy level E_i, the introduction rate η is close to unity and the capture cross sections σ are included in the range $10^{-16} - 10^{13}$ cm^2.

4.5.3 Radiation Damage in TCAD Simulations Case studies

After the short review of radiation damage models for TCAD Simulations available in literature we now discuss briefly how to chose among them. The choice of the radiation damage model depends of course on the level of agreement with real data from irradiated detectors, but there is not a single model that can fit all possible real data. This is particularly evident when the electric field profile inside the irradiated device is investigated.

Combining beam test data with TCAD simulations in what is called the *grazing angle* technique [83–85] it makes possible to extract the electric field profile along the bulk depth of the irradiated detector. An example of such studies can be found in [59, 82]; the authors investigated $n - on - n$ pixel detectors irradiated at CERN with 24 GeV/c protons. The authors measured charge collection profiles as in Figure 4.15.

To model the local maxima around position 1000 µm a double peak distribution of the electric field is necessary; they show that a uniform space charge distribution cannot reproduce the measured charge profile. They propose a radiation damage model based on the work of [58], adapting the capture cross sections σ and the traps introduction rate η. Their predictions for the electric field distribution are shown in Figure 4.16.

Recent works [98] that exploited the same technique with $n - on - p$ 200 µm pixel modules irradiated to a fluence of $\Phi = 2.0 \times 10^{15}$ n$_{eq}$/cm^2 with 23 MeV protons at KIT[5] reported a charge collection profile more flat.

A comparison with TCAD simulations was performed and presented in [99]. Several models were tried and the best agreement was found when the Perugia 2006 model [94] was used. The agreement is qualitative but no other model gave better agreement. In particular models predicting a double peak distribution of the electric field were producing charge collection profiles more close to the ones presented in Figure 4.15 rather the one reported here.

The prediction for the electric field profile from the Perugia 2006 model is presented in Figure 4.18.

As it can be seen the simulated electric field is depending linearly on the bulk depth position, as it happens before irradiation.

---

[5]http://www.etp.kit.edu/english/irradiation_center.php
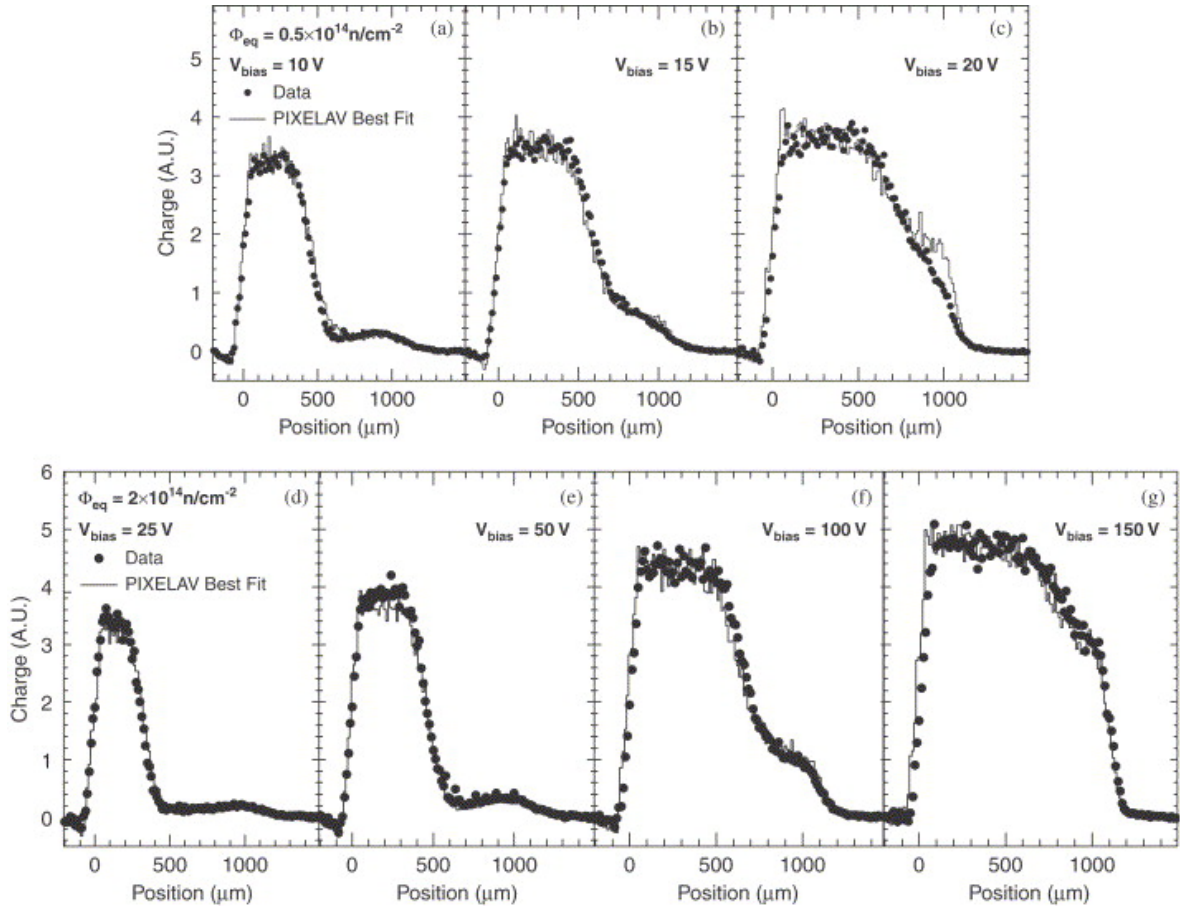
Figure 4.15: Measured (full dots) and simulated (histogram) charge collection profiles for a sensor irradiated to a fluence of $\Phi = 0.5 \times 10^{14}$ n_{eq}/cm^2 (a-c) and of $\Phi = 2.0 \times 10^{14}$ n_{eq}/cm^2 (d-g), and operated at several bias voltages. (After [82])
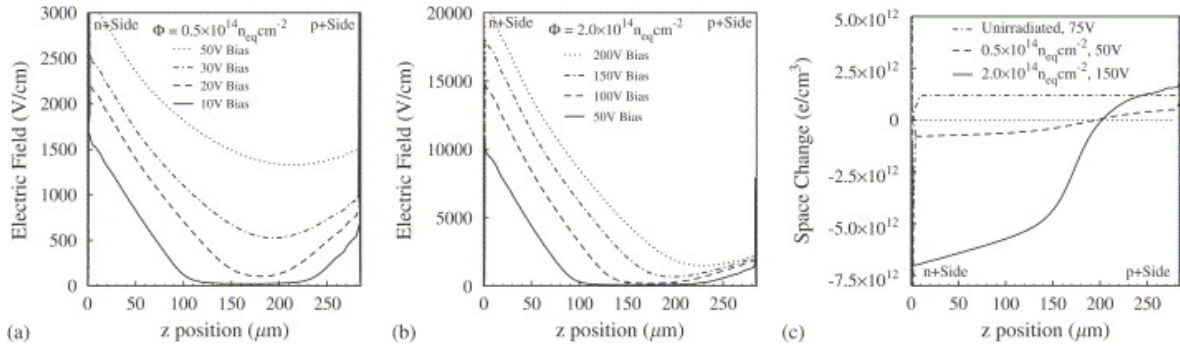
Figure 4.16: The z-component of the simulated electric field is shown as a function of z for a sensor irradiated to a fluence of $\Phi = 0.5 \times 10^{14}$ n_{eq}/cm^2 (a) and of $\Phi = 2.0 \times 10^{14}$ n_{eq}/cm^2 (b). (c) Space charge density as a function of the z coordinate for different fluences and bias voltages. (After [82])
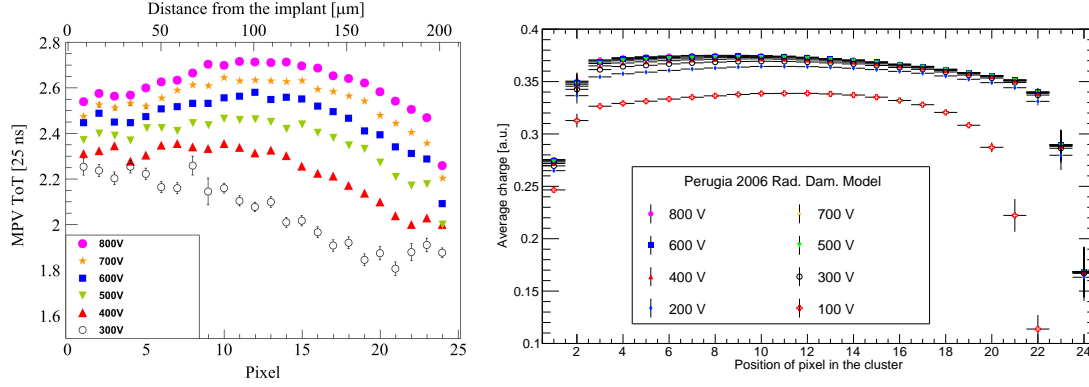
Figure 4.17: Comparison between (left) measured and (right) simulated charge collection profiles for $n-on-p$ 200 μm thick pixel modules irradiated to a fluence of $\Phi = 2.0 \times 10^{15}$ n_{eq}/cm^2. Tracks were impinging at 80° with respect to detector surface. (After [98, 99])
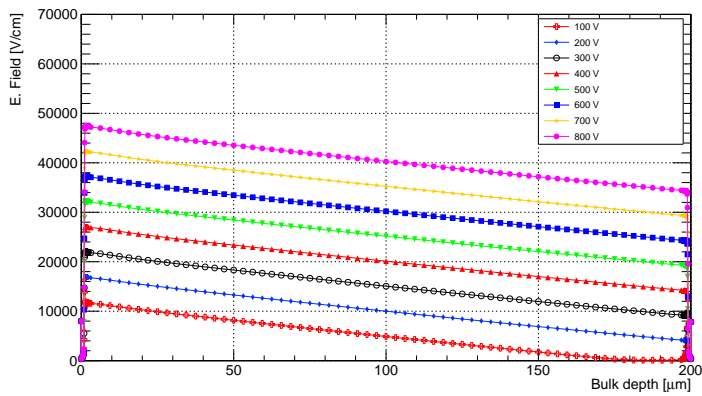
Figure 4.18: Simulated electric field profile for an $n-on-p$ 200 μm thick pixel modules irradiated to a fluence of $\Phi = 2.0 \times 10^{15}$ n_{eq}/cm^2. The radiation damage model used was Perugia 2006 [94].

4.6 Comparison of Radiation Damage Modelling in TCAD tools

As done for the un-irradiated detectors, a comparison between Silvaco Atlas and Synopsys Sentaurus was done for detectors simulated as if they were irradiated. The goal was to see if the results in terms of depletion voltage, leakage current and charge collection efficiency by the two tools for the same radiation damage model were compatible . The radiation damage model developed by the Perugia group with Synopsys Sentaurus and documented in [100] was used for the comparison; the model features 2 acceptors and 1 donor defects. The study was carried out in collaboration with one of the researchers of the Perugia group. The same 2D $n - on - p$ diode used for the studies reported in Section 4.4 was used. The result of the investigations are documented in [86] and some of them are reported and discussed here. First the investigated scenarios and then the results are presented; discussion will follow.

Similar to what was done for the carrier thermal velocities and the bandgap energy, several scenarios were investigated:

base setting $E_g^{Sil}(300) = 1.11$ eV

E_g = 1.08 eV using default Silvaco parameters values

Synopsys. Vel. setting thermal velocities to the values used by Synopsys tool

Synopsys. Vel.

& E_g **= 1.08 eV** combination of the two above

Moscatelli the results obtained by the Perugia group using Synopsys Sentaurus

The simulated fluences Φ were 0.5, 1, 3, 5, 7 and 10 in units of 10^{15} n_{eq} cm^{-2}. Numerical convergence problems in the simulations and the already explained difficulty in determining a clear depletion voltage limited the analysis at very large fluences. We now present the results for depletion voltage, leakage current and charge collection efficiency.

4.6.1 Depletion voltage

The investigations started with the depletion voltage, looking at the C^{-2} vs V curves. In Figure 4.19 the C^{-2} vs V curves for a fluence $\Phi = 0.5 \times 10^{15}$ n_{eq} cm^{-2} for the five different scenarios.

As it can be seen at this moderate fluence all the curves look similar but the depletion voltage is clearly changing from one scenario to the other. The analysis was carried on for all the investigated fluences Φ and the results are presented in Figure 4.19. The best agreement between the two tools is obtained when the *Synopsys. Vel. &* E_g *= 1.08 eV* scenario is considered. This is in agreement with what already presented in Section 4.4 for what concerns the band gap energy, but here the different carrier thermal velocity values play an important role. This is not surprising since the electron and hole lifetimes depend on the inverse of the carrier thermal velocities when the carriers recombination rate includes the effect of the radiation damage induce traps [51]. It is also important to notice that for lower bandgap energy values the depletion voltage gets larger; this is expected since for smaller band gap the traps get closer to the bands and because of this traps are more likely to be occupied, hence charged, so to influence the space charge
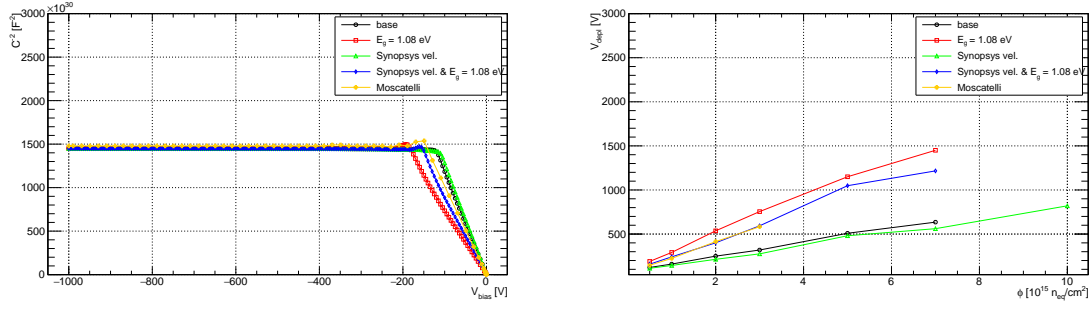
Figure 4.19: (left) C^{-2} vs V curves for a simulated fluence $\Phi = 0.5 \times 10^{15}$ n_{eq} cm^{-2} for the different scenarios. (right) Depletion voltages, determined from the C^{-2} vs V curves, as function of the simulated fluence Φ for the different scenarios.

in the sensor bulk; see also Appendix B. In all the investigated scenarios the depletion voltage increases almost linearly with the fluence; this is an expected feature, and it is important that both tools can reproduce it.

4.6.2 Leakage Current

Current vs Voltage curves where then compared for the different scenarios. The curves for a fluence $\Phi = 0.5 \times 10^{15}$ n_{eq} cm^{-2} for the five different scenarios are presented in 4.20.
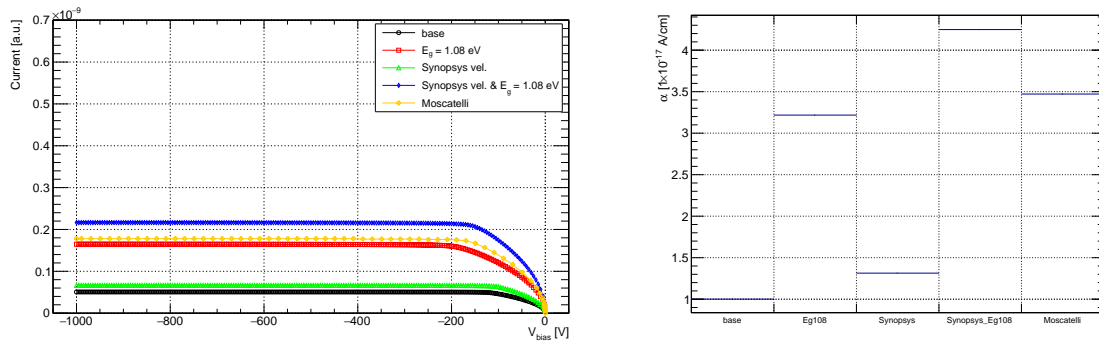
Figure 4.20: (left) I vs V curves for a simulated fluence $\Phi = 0.5 \times 10^{15}$ n_{eq} cm^{-2} for the different scenarios. (right) Normalised rate of increase of leakage current α for a simulated fluence $\Phi = 1 \times 10^{15}$ n_{eq} cm^{-2} for the different scenarios.

Also for the other fluences Φ the best agreement is realised in the E_g = *1.08 eV* scenario. The normalised rate of increase of leakage current α (Equation 2.36) was evaluated for all simulated fluences (but the largest one) in all scenarios; the result for $\Phi = 1 \times 10^{15}$ n_{eq} cm^{-2} is presented in Figure 4.20. As it can be seen, if it is true that the best agreement with the results published by the Perugia group is indeed obtained in the E_g = *1.08 eV* scenario, it is in the *Synopsys. Vel. &* E_g = *1.08 eV* scenario that the value of α gets closer to its typical value, about 4×10^{-17} A/cm [51]; Perugia model predicts $\alpha \sim 3 \times 10^{-17}$ A/cm. Lower bandgap energy and larger carrier thermal velocities mean of course larger current value and this is indeed what is shown in Figure 4.20.

From the analysis of the depletion voltage and the leakage current it is clear that the scenario that gives the best results is the *Synopsys. Vel. &* E_g = *1.08 eV* one. So for the charge collection efficiency (CCE) study only the *Synopsys. Vel. &* E_g = *1.08 eV* scenario was considered.

4.6.3 Charge Collection Efficiency

The Perugia group compared their predictions on CCE with the results on real data presented in [101]. The same simulation was run using Silvaco Atlas and the CCE as a function of the fluence Φ at a bias voltage V_{bias} = 900 V was studied. The results from the Perugia group and of this study were fitted with a function inspired by Equation A.11:

$$\frac{d}{w}\left[1 - e^{-\frac{w}{d}}\right] \qquad (4.8)$$

where $d = \dfrac{v^{(sat)}}{\beta \Phi}$ is the collecting distance and w the detector thickness. The parameter β was free in the fit while the saturation velocity $v^{(sat)}$ was constrained to the value used in the simulation tools. The results are presented in Figure 4.21 for the two simulations tools.
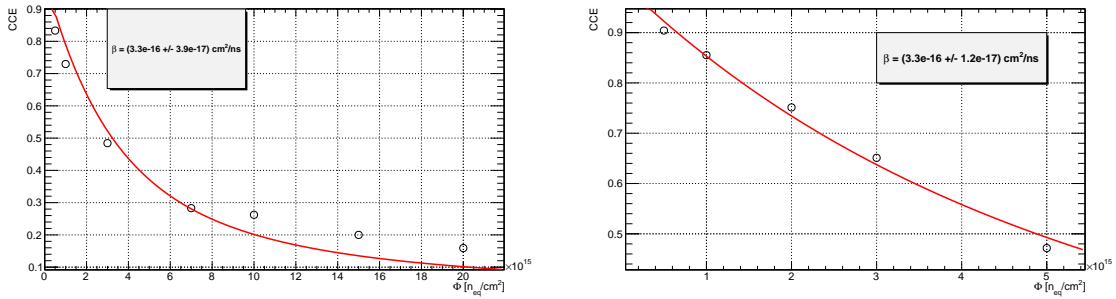
Figure 4.21: Simulated CCE as a function of the fluence Φ. (left) Perugia group result with Synopsys Sentaurus; (right) author study using SIlvaco Atlas. Points are data; the data are fitted with the function reported in the text.

As it can be seen the fit results for the trapping parameter β are completely compatible with each other:

$$\beta_{Syn} = (3.3 \pm 0.4) \times 10^{-16} \text{cm}^2/\text{ns}$$
$$\beta_{Sil} = (3.3 \pm 0.12) \times 10^{-16} \text{cm}^2/\text{ns}$$

$$(4.9)$$

4.6.4 Conclusions

As for the un-irradiated case, also for irradiated detectors it was shown that the default bandgap energy value in Silvaco Atlas is the one that gives the best results, both in terms of agreement with Synopsys Sentaurus and in reproducing real data. It is very important to validate radiation damage models developed on one tool using the other one, as it was shown above. Similar studies are planned for other radiation damage models.

4.7 Summary and Outlook

In this Chapter the basics of TCAD simulation of silicon detectors for HEP were presented. The motivations for such simulations were discussed and some examples outlined. It was shown that, despite some inconsistencies on measured fundamental parameters, TCAD

simulations can be used to get reliable predictions once some corrections are applied. The situation is far from optimal, in particular when it comes to the simulations of irradiated detectors. The best would be to find a common set of parameters for both simulation tools, verify that the predictions from the two programs are compatible when this set is used and then use consistently that set. This is part of an activity ongoing within the RD50 collaboration [102].

The issue of the proper choice of radiation damage models for TCAD simulations and the interest of using TCAD simulations together with beam test data from heavily irradiated detectors was discussed; its importance will be evident in Chapter 6.

Chapter 5

The ATLAS Experiment and its Pixel Detector

In this Chapter the ATLAS Pixel detector will be discussed. After a short introduction to the Large Hadron Collider (LHC) Physics program in Section 5.1, the ATLAS detector, one of the experiments at the LHC, will be presented (Section 5.2). Particular emphasis will be devoted to the the ATLAS Pixel Detector (Section 5.3). The radiation damage effects to the ATLAS Pixel Detector, and an effective tool to model them, will be the subject of the next Chapter.

5.1   The LHC Physics Program

Understanding the nature of electroweak symmetry breaking, and in particular specifically deciphering the Higgs mechanism, is the main goal of the ATLAS [103] and CMS [104] experiments at the LHC [105].

The LHC is a hadron accelerator and collider located about 100 m underground, in the former Large Electron Positron (LEP) collider tunnel, at the French-Swiss border in the vicinity of Geneva. As LEP, the LHC too was built by CERN, the European Organization for Nuclear Research. The LHC has a circumference of 27 km and uses superconducting magnets to bend proton beams with energy up to a design value of 7 TeV; hence the maximum achievable center-of-mass energy $\sqrt{s}$ for pp collisions is of 14 TeV. The design instantaneous luminosity of the LHC is L = 1.0×10^{34}/cm^2/s, which is equivalent to 10/nb/s. The pp total inelastic cross section σ_{tot} at $\sqrt{s}$ of 14 TeV is about 10^8 nb, so the event rate at the LHC is in the order of 10^9 Hz. The protons are packed in bunches of about 10^{11} particles; the bunch crossing frequency ν is of 40 MHz. The ratio of event rate to ν gives the average number of pp collisions per bunch crossing, the so-called *pile-up*; it is customarily indicated with µ and for the LHC design values is of about 25 interactions per bunch crossing.

At the LHC the most probable inelastic event is the production of QCD jets, whose cross-section is many orders of magnitude larger than the production of the most interesting physics channels; the latter are usually characterised by electroweak cross-sections. Figure 5.1 shows the production cross-sections for several representative processes at hadron colliders, as a function of the center-of-mass energy. It can be seen that the production cross section of a light Higgs boson (m = 150 GeV) is of the order of a few nb so the Higgs boson is produced about once every billion collisions of the LHC.

As already mentioned in Chapter 1 the ATLAS and CMS collaborations have both observed a particle (with mass ~ 125 GeV) compatible with the SM Higgs boson in 2012;

75
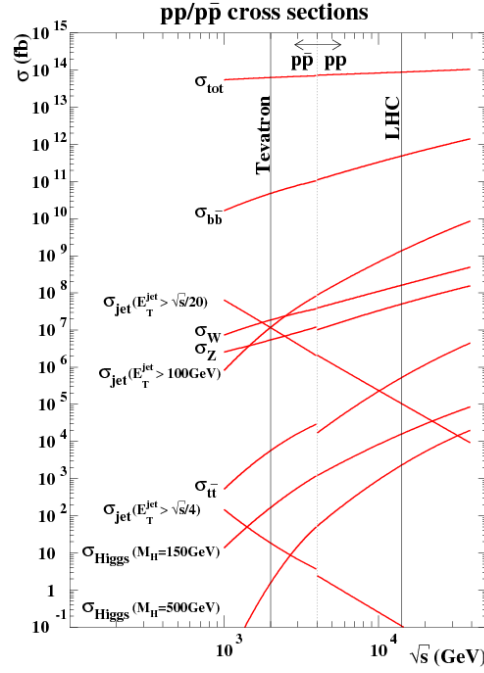
Figure 5.1: Production cross-sections for several representative processes at hadron colliders. (After [106])

since then the nature of that particle and its coupling to fundamental SM bosons and fermions keep being pursued. Recently ATLAS reported evidence of the H → bb decay [107] when it is produced in association with a W or Z boson; the CMS collaboration announced the first observation (by a single experiment) of Higgs boson decays to τ leptons [108]. The search for the Higgs boson decaying to second generation fermions is next on the agenda of the ATLAS and CMS collaborations (see for instance [109]).

Other than the study of the Higgs boson, a central goal of the physics program of the LHC is the exploration of particles and interactions at the TeV energy scale, which may hold answers to some of the most profound questions in particle physics, like what is dark matter made of and how the Higgs boson mass gets stabilised.

The total delivered luminosity so far from the LHC to the ATLAS experiment is shown in Figure 5.2 [110].

To exploit at best this dataset, to perform precision measurements and to face the high interaction rates, radiation doses, particle multiplicities and energies of the LHC pp collisions the ATLAS detector was built. In the next Section the salient features of this detector will be presented.
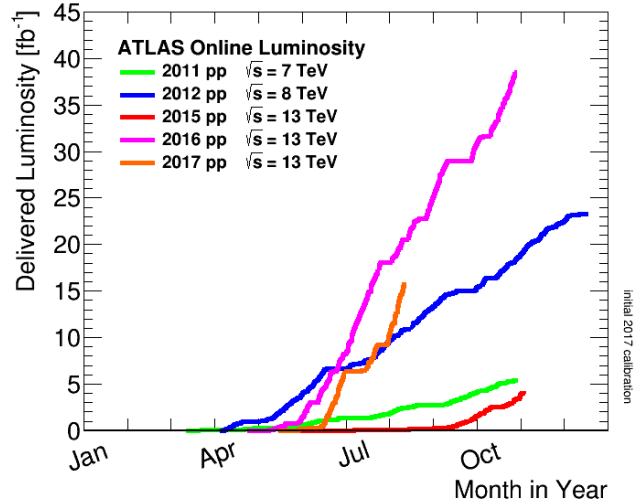
Figure 5.2: Cumulative luminosity versus day delivered to ATLAS during stable beams and for high energy pp collisions. (After [110])

5.2 The ATLAS Detector

ATLAS [103] is a general-purpose particle detector covering nearly the entire solid angle[1] around the collision point. It consists of an inner tracking detector surrounded by a thin superconducting solenoid, electromagnetic and hadronic calorimeters, and a muon spectrometer incorporating three large superconducting toroidal magnets. Figure 5.3 shows a schematic view of the ATLAS detector.
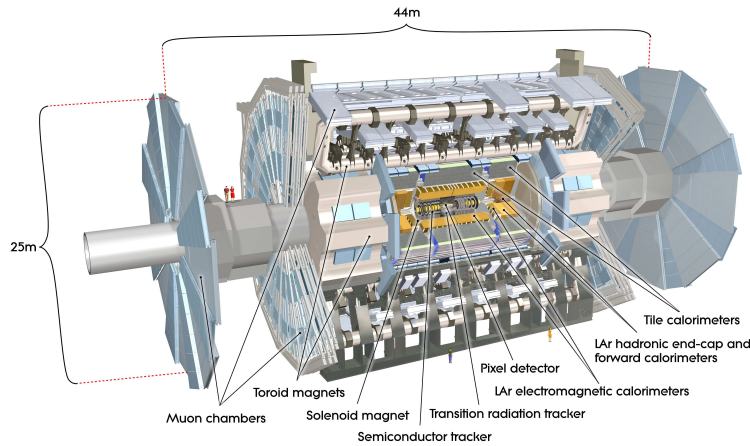
Figure 5.3: Cut-away view of the ATLAS detector. The dimensions of the detector are 25 m in height and 44 m in length. The overall weight of the detector is approximately 7000 tonnes. (After [103])

The inner tracking detector (ID or *inner detector*) [111], located within a 2 T axial magnetic field generated by the superconducting solenoid, is used to measure the trajectories

---

[1]ATLAS uses a right-handed coordinate system with its origin at the nominal interaction point (IP) in the centre of the detector and the z-axis coinciding with the axis of the beam pipe. The x-axis points from the IP towards the centre of the LHC ring, and the y-axis points upward. Cylindrical coordinates (r,ϕ) are used in the transverse plane, ϕ being the azimuthal angle around the z-axis. The pseudorapidity is defined in terms of the polar angle θ as $\eta = -\ln\tan(\theta/2)$. The distance in ($\eta$,$\phi$) coordinates, $\Delta R = \sqrt{(\Delta\phi)^2 + (\Delta\eta)^2}$, is also used to define cone sizes. Transverse momentum and energy are defined as $p_T = p\sin\theta$ and $E_T = E\sin\theta$, respectively.

and momenta of charged particles. The inner layers, consisting of high-granularity silicon pixel detectors, instrument a pseudorapidity range $|\eta| < 2.5$. A new innermost silicon pixel layer, the insertable B-layer [45] (IBL), was added to the detector between the first two LHC runs (Run 1 and Run 2 - see Figure 7.1). The IBL improves the ability to identify displaced vertices and thereby significantly improves the *b*-tagging performance [112]. More details on the pixel detector will be given in the next Section. Silicon strip detectors covering $|\eta| < 2.5$ are located beyond the pixel detectors. Outside the strip detectors and covering $|\eta| < 2.0$, there are straw-tube tracking detectors, which also provide measurements of transition radiation that are used in electron identification; the so-called Transition Radiation Tracker (TRT). Figure 5.4 shows the barrel section of the ID.
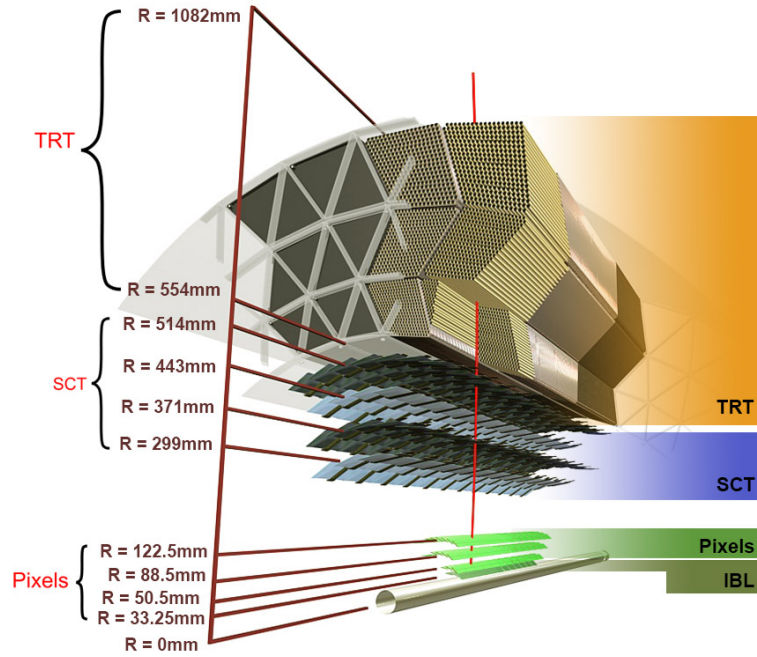
Figure 5.4: Schematic view of the barrel part of the ATLAS Inner Detector (ID), including the new Insertable B-Layer (IBL). (After [113])

The calorimeter system covers the pseudorapidity range $|\eta| < 4.9$. Within the region $|\eta| < 3.2$, electromagnetic calorimetry is provided by barrel ($|\eta| < 1.475$) and endcap ($1.375 < |\eta| < 3.2$) high-granularity lead/liquid-argon (LAr) electromagnetic calorimeters, with an additional thin LAr presampler covering $|\eta| < 1.8$ to correct for energy loss in material upstream of the calorimeters. Hadronic calorimetry is provided by a steel/scintillator-tile calorimeter, segmented into three barrel structures within $|\eta| < 1.7$, and two copper/LAr hadronic endcap calorimeters extend the coverage to $|\eta| = 3.2$. The solid angle coverage for $|\eta|$ between 3.2 and 4.9 is completed with copper/LAr and tungsten/LAr calorimeter modules optimised for electromagnetic and hadronic measurements, respectively.

The outermost part of the detector is the muon spectrometer, which measures the curved trajectories of muons in the field of three large air-core toroidal magnets. High-precision tracking is performed within the range $|\eta| < 2.7$ and there are chambers for fast triggering within the range $|\eta| < 2.4$.

The proton-proton interaction rate at the design luminosity of $L = 1.0 \times 10^{34}/\mathrm{cm}^2/\mathrm{s}$ is approximately 1 GHz, while the event data recording, based on technology and resource limitations, is limited to about 1 kHz. For this purpose ATLAS designed a two-level trigger system selects events to be recorded for offline analysis, to assure an overall rejection factor of 5×10^6 against minimum-bias processes while maintaining maximum efficiency for

the new physics. The Level-1 (L1) trigger system uses a subset of the total detector information to make a decision on whether or not to continue processing an event, reducing the data rate to approximately 100 kHz between. The subsequent level is a software-based high-level trigger that provides the reduction to a final data-taking rate of approximately 1 kHz [114]. A new Fast TracKer (FTK) system [115] will provide global ID track reconstruction at the L1 trigger rate using lookup tables stored in custom associative memory chips for the pattern recognition. This system is currently being installed and expected to be fully commissioned by the end of 2017.

5.3   The ATLAS Pixel Detector and the Insertable B Layer

This Section is devoted to the silicon pixel tracking system for the ATLAS experiment. The pixel detector was initially composed of three barrel layers plus a total of six disk layers, three at each end of the barrel region [116]. During the Long Shutdown 1 (LS1), between the LHC Run 1 and Run 2 (see Figure 7.1), a fourth barrel layer was inserted, at a smaller radius than the existing pixel detector; it is called the Insertable B-Layer (IBL) [45]. Figure 5.5 shows a schematic view of the ATLAS pixel detector in Run 2; the total detector length is 1442 mm.
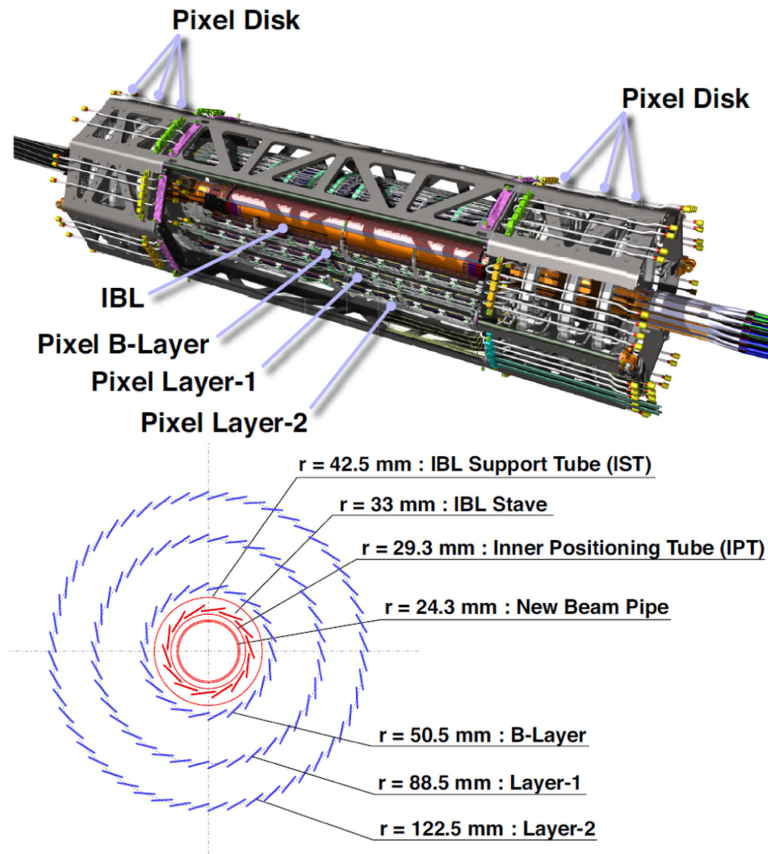
Figure 5.5: Schematic view of the ATLAS 4-Layer Pixel Detector for Run 2. On top the different pixel layers are indicated; at the bottom the radii of the four barrel layers are shown, together with the distance from the interaction point of the beam pipe and support structures. (After [117])

This Section will cover first the physics motivations and the salient features of the original pixel detector, and later discuss the IBL. The material presented here is taken from [45, 116].

5.3.1 Performance Requirements for the Pixel Detector and System Overview

The pixel detector system is the innermost element of the ATLAS ID. The pixel detector contains more than 80 million channels and provides pattern recognition capability in order to meet the track reconstruction requirements of ATLAS at the full luminosity of the LHC (L = 1.0×10^{34}/cm^2/s). It is the most important detector used in the identification and reconstruction of secondary vertices from the decay of, for example, particles containing a *b*-quark or for *b*-tagging of jets. In addition, it provides excellent spatial resolution for reconstructing primary vertices coming from the *pp* interaction region within ATLAS even in the presence of the multiple interactions at the LHC design luminosity.

In what follows the performance requirements for the pixel detector will be presented, then an overview of the system.

5.3.1.1 Pixel Detector Performance Requirements

The performance requirements that guided the design of the pixel detector are:

- coverage of the pseudorapidity range |η| < 2.5;

- impact parameter resolution in the transverse plane better than 15 µm;

- uncertainty in the longitudinal plane $\sigma(z)$ on the reconstruction of vertices of about 1 mm;

- three-dimensional-vertexing capabilities;

- very good b-jet tagging capabilities both in the high-level trigger and in the offline reconstruction;

- minimal material for all elements in the system, in order to reduce multiple scattering and secondary interactions;

- excellent efficiency for all pixel layers; and

- radiation hardness of the pixel detectors elements to operate after a total dose of 500 kGy and fluence $\Phi = 1 \times 10^{15}$ n$_{eq}$/cm^2

These performance requirements lead to the following major design choices:

- three pixel hits over the full rapidity range;

- minimal radius of the innermost layer (b-layer), set at 5 cm due to the practical limitations of clearances around the interaction region beam pipe vacuum system[2];

- the smallest pixel size achievable, which is set to 50 µm × 400 µm by electronics design limitations.

---

[2]this limit was then overcome with the installation of the IBL

5.3.1.2 Pixel Detector Overview

The pixel tracker is designed to provide at least three points on a charged track emanating from the collision region in ATLAS. The principal components of the pixel tracking system, before adding the IBL, were the following:

- the active region of the pixel detector, which is composed of three barrel layers and a total of six disk layers, three at each end of the barrel region;

- internal services (power, monitoring, optical input/output and cooling) and their associated mechanical support structures (also supporting the interaction region beam pipe) on both ends of the active detector region;

- a Pixel Support Tube into which the active part of the pixel detector and the services and related support structures are inserted and located; and

- external services that are connected to the internal services at the end of the Pixel Support Tube.

The active part of the pixel system consists of three barrel layers-Layer 0 (so-called b-layer), Layer 1 and Layer 2-and two identical endcap regions, each with three disk layers, as it cam be seen in Figure 5.5. The basic building block of the active part of the pixel detector is a module that is composed of silicon sensors, front-end electronics and flex-hybrids with control circuits. Modules are mounted on mechanical/cooling supports, called staves, in the barrel region. In the endcap modules are mounted on mechanical/cooling supports, called disk sectors; There are eight identical sectors in each disk. The concept of pixel module is illustrated in Figure 5.6.

A description of the pixel sensors and electronics characteristics follows.

5.3.1.3 Pixel Sensors

The total number of pixels in the system is approximately 67 million in the barrel and 13 million in the endcaps, covering a total active area of about 1.7 m^2. The sensors choice for ATLAS was of $n-on-n$ pixels on high resistivity, nominally 250 μm thick bulk. For each sensor tile, the 47232 pixel implants are arranged in 144 columns and 328 rows. For most of the pixel cells the pitch is of 400 μm × 50 μm; in 16 columns the pitch is of 600 μm × 50 μm. In each column eight pairs of pixel implants, located near the center lines, are ganged to a common read-out, resulting in 320 independent read-out rows or 46080 pixel read-out channels. This arrangement was chosen to allow for the connection of the sensor tile to 16 electronic front- end chips (see next Section). Oxygen impurities had been introduced in the bulk to increase tolerance of the silicon against bulk damage caused by charged hadrons [118, 119]. The sensors can be fully depleted before type inversion with bias voltages below 100 V. After type inversion the depletion zone grows primarily from the segmented n^+ implant when the region of highest electric field in the bulk now converts to p-type.

On the sensor front side, pixel structures are arranged and isolated by moderated p-spray impants, which have proven to be radiation tolerant with respect to surface damages induced by ionising charged particles for doses up to 500 kGy in silicon. The layout of the moderated p-spray impants is shown in Figure 5.7. This isolation technique avoids high field regions in the interface between the pixel isolation and the bulk and ensures radiation tolerance of the design. All 46080 read-out channels of a sensor tile are connected to a common bias grid structure, presented in Figure 5.7, by employing a punch-through
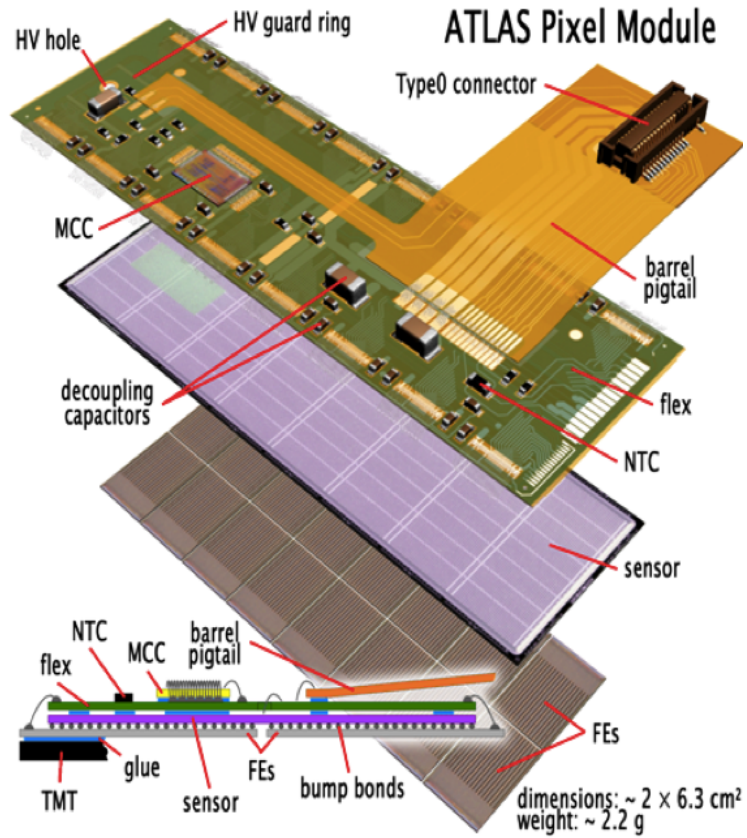
Figure 5.6: Assembly view and cross-section of an ATLAS Pixel Detector module. (After [116])
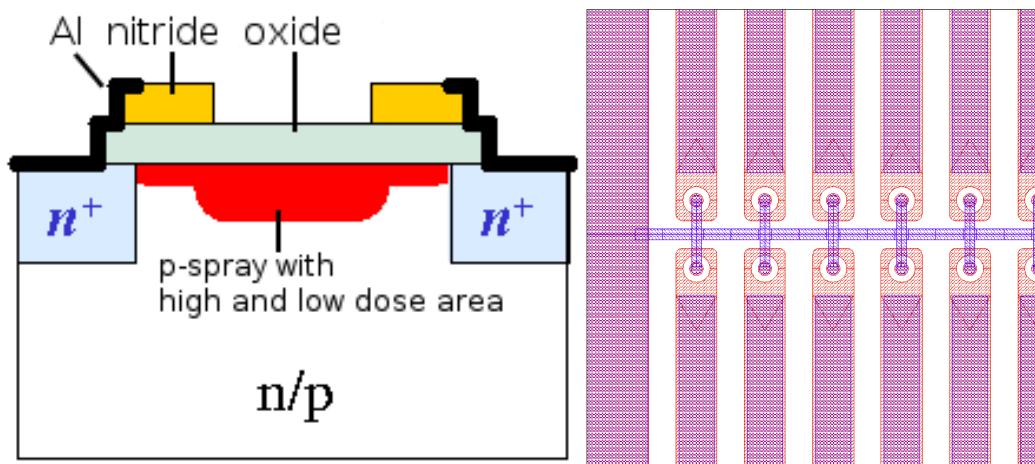
Figure 5.7: (left) Layout of the moderated p-spray isolation. (right) Layout detail of the bias grid (After [116])

connection technique to each channel. The method biases the entire sensor without requiring individual connections, but still ensures isolation between pixels. The bias grid has been used for quality assurance measurements before the read-out electronics are connected to the sensors.

On the sensor tile backside a series of guard rings (GRs) were defined by p^+ implants. The GRs assures a controlled potential drop from p^+ implant negative bias voltage to ground. A sketch of the pixel sensor edge, with the read out electronics on top is given in Figure 5.8.
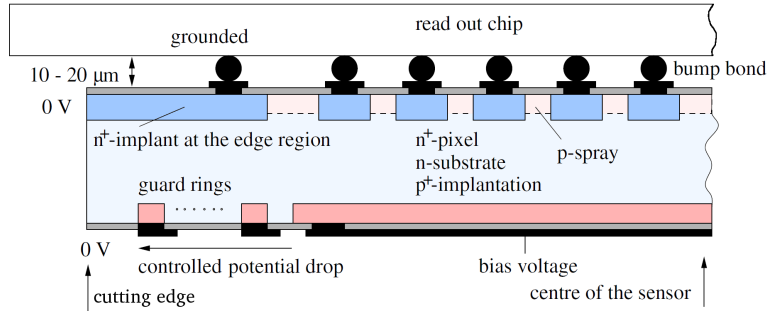
Figure 5.8: Cross section sketch of the ATLAS pixel module (After [120])

5.3.1.4 Pixel Electronics

A block diagram that illustrates the principal elements of the system architecture of pixel electronics is shown in 5.9.
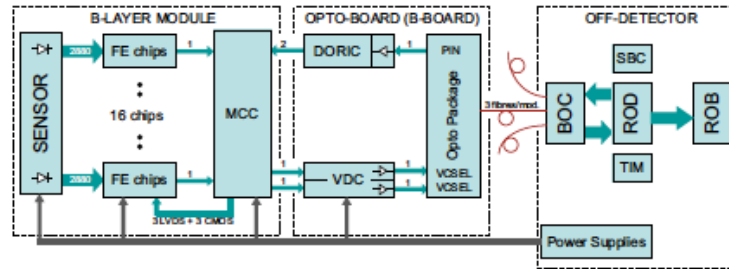
Figure 5.9: Block diagram of the pixel detector system architecture. (After [116])

There are 16 FEI3 [121] front-end chips (FE) in each pixel module and these are arranged in two rows of eight chips. The readout chip for the ATLAS pixel detector contains 2880 pixel cells of 400×50 μm^2 size arranged in an 18×160 matrix. Each pixel cell contains an analogue block where the sensor charge signal is amplified and compared to a programmable threshold using a comparator. The digital readout part transfers the hit pixel address, a hit leading edge (LE) timestamp, and a trailing edge (TE) timestamp to the buffers at the chip periphery. In these buffers a Time-over-Threshold (ToT) is calculated by subtracting the TE from the LE timestamp. Hits marked by trigger signals are selected for readout. Triggered hit data are then transmitted serially out of the chip in the same order as the trigger arrival. The duration of the ToT is measured by counting the cycles of the 40 MHz master chip clock. Due to the pulse shape of the preamplifier the ToT is a nearly linear function of the deposited charge. Evaluating this ToT information can therefore be used to infer the charge deposi ted by a passing particle. The ToT mechanism is presented in Figure 5.10.
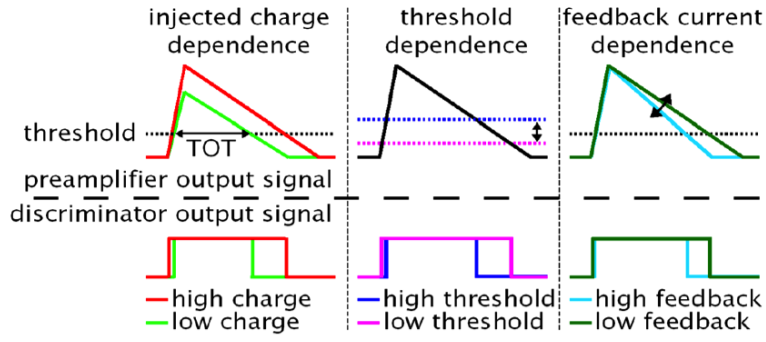
Figure 5.10: (left)Time-over-Threshold mechanism (ToT) and its dependence on the injected charge; (center) ToT dependence on threshold value; (right) ToT dependence on feedback current. (top) Shaper output; (bottom) discriminator output. (After [122])

The 16 FEs are read out by a Module Control Chip (MCC). Each module is then connected to the off- detector Read-out Drivers (RODs) through optical-fiber links (optolinks). One down link is used to transmit clock, trigger, commands and configuration data, while one or two up-links are used for event readout. The readout (R/O) architecture is "datapush". This means that each component in the chain (FE, MCC) always transmits at the maximum rate, and there is no busy mechanism to stop transmission when buffers are full.

5.3.1.5 Pixel Support and Services

As already mentioned in the system overview, the pixel system consists of three barrel layers and two identical endcap regions, each with three disk layers. Figure 5.11 shows the salient features of the pixel structure.
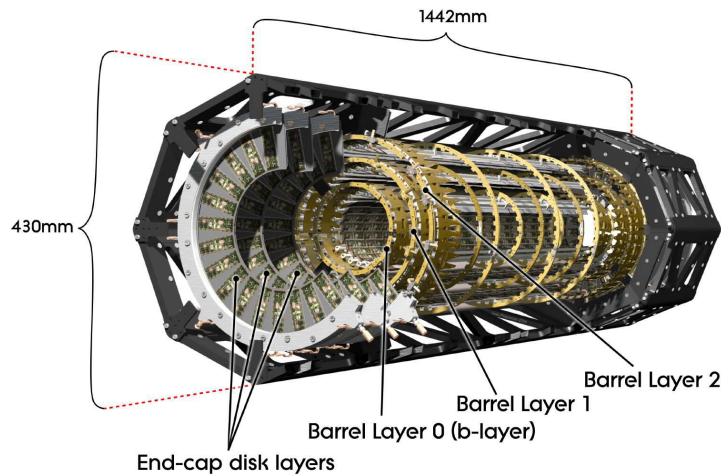
Figure 5.11: A schematic view of the active region of the pixel detector consisting of barrel and endcap layers. (After [116])

Modules are mounted on mechanical/cooling supports, called staves, in the barrel region. Thirteen modules are mounted on a stave and the stave layout is identical for all layers. The active length of each barrel stave is about 801 mm. The staves are mounted in half-shells manufactured from a carbon- fiber composite material. Two half-shells are

joined to form each barrel layer. The two endcap regions are identical. Each is composed of three disk layers, and each disk layer is identical. Modules are mounted on mechanical/cooling supports, called disk sectors. There are eight identical sectors in each disk.

The barrel shells and the endcap disks are supported by a spaceframe also manufactured from a carbon-fiber composite material (see Figure 5.11). Electrical, optical and cooling services are con- nected and routed within service panels (four on each end of the pixel detector) from patch panels (Patch Panel 0-PP0) at the ends of the supporting spaceframe to the end of the Pixel Support Tube. These services are supported by carbon fiber structures that also hold the beryllium vacuum pipe within the Pixel Support Tube. Electrical, optical and cooling connections are made at the end of the Pixel Support Tube.

5.3.2   Performance Requirements for the IBL and System Overview

The Insertable B-Layer (IBL) is a fourth layer added to the present Pixel detector between a new beam pipe and the pixel B-layer. The principal motivations for the IBL were:

- tracking robustness, to cope with predicted failures of the pixel layers, in particular the B-layer; a loss of data in the B-layer seriously deteriorates the impact parameter resolution, directly affecting the b-tagging. The IBL restores the full b-tagging efficiency even in case of a complete B-layer failure.

- Coping with luminosity effects, like increased event pile-up which leads to high occupancy that can induce readout inefficiencies. The presence of event pile-up requires redundancy in the measurement of tracks in order to control the fake rate arising from random combinations of clusters in events with high pile-up background. The addition of the IBL layer, with comparably low occupancy, helps to preserve tracking performance in face of luminosity effects.

- Tracking precision: The IBL located close to the interaction point improves the quality of impact parameter reconstruction for tracks, and thereby improves vertexing and b tagging performance. As a result, sensitivity for signals in physics channels involving b jets is improved, for instance for a low mass SM Higgs in the channel WH, H $\rightarrow b\bar{b}$.

Strong constraints and project specifications had a substantial impact on the technologies required for the IBL:

- the smaller radius of the IBL required development of a more radiation hard technology for sensors and electronics.

- The small radius between the new beam pipe needed to be able to insert the IBL and the existing pixel detector does not allow for tilting of modules in the longitudinal direction (along the beam). Sensors with either an active edge or a slim guard ring must therefore be developed to reduce geometrical inefficiencies. Full coverage in φ is possible by constructing modules with the same active width, but with only one row of front-end chips. The new front-end chip has five times the area of the chip in the existing pixel detector and covers an active area that is 90% of the sensor. (The active fraction of the present pixel modules is 75%.)

- Minimizing material is very important in the optimization of tracking and vertexing performance. The IBL radiation length will represent just 60% of the pixel B-layer.

85

Low radiation length was achieved by considering more aggressive technology solutions, in addition to new module design, technologies such as: local support structures (staves) made of low density carbon foams; CO_2 evaporative cooling, which is more efficient in term of mass flow and pipe size.

The IBL modules are supported by means of fourteen local supports, the Staves, arranged cylindrically around the beam pipe. Some overlap between modules is provided by tilting each stave about 14°. The nominal layer radius, that is the distance from the beam axis to the sensor's centre-of-mass, is R = 33.25 mm. The $r\phi$ view of the IBL layout is shown in Figure 5.12. The stave is L = 724 mm long. The IBL was successfully installed in May 2014.
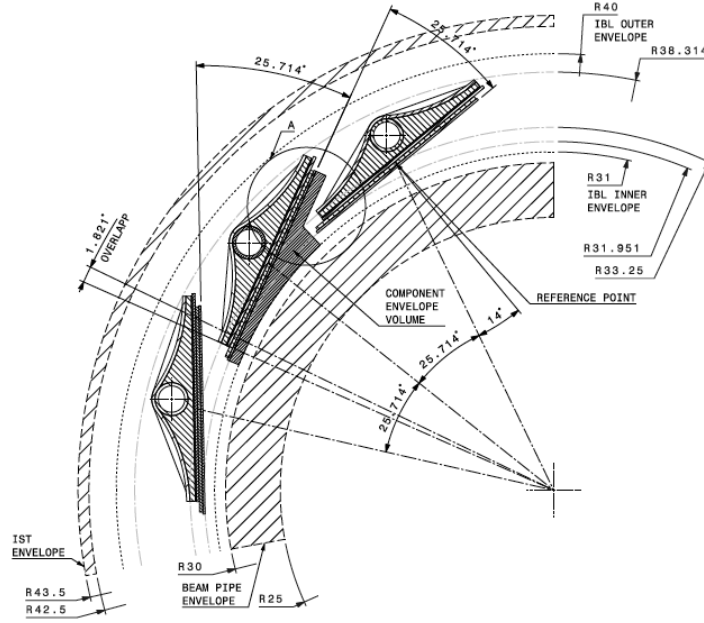
Figure 5.12: IBL layout: $r\phi$ view. (After [45])

5.3.2.1 IBL Pixel sensors

Two sensor technologies are used in the IBL: planar $n - on - n$ sensors of the same type that was used for the pixel detector, and 3D sensors, which are a technology that has not been used in a HEP experiment before. In 3D sensors the electrodes are columns in the silicon [46]. There can be varying numbers of electrodes per pixel which will have an influence on charge collection and noise; for IBL a design with two electrodes per pixel was chosen. A schematic view of the 3D sensors is shown in Figure 5.13.

Table 5.1: Comparison of parameters between planar and 3D IBL sensors.

	Planar	3D
Vendor	CiS	FBK/CNM
Wafer Thickness	200 μm	230 μm
Size in FE chips	2	1
Depletion voltage before irradiation	35-50 V	15 V
Depletion voltage at the end of the life	1000 V	180 V
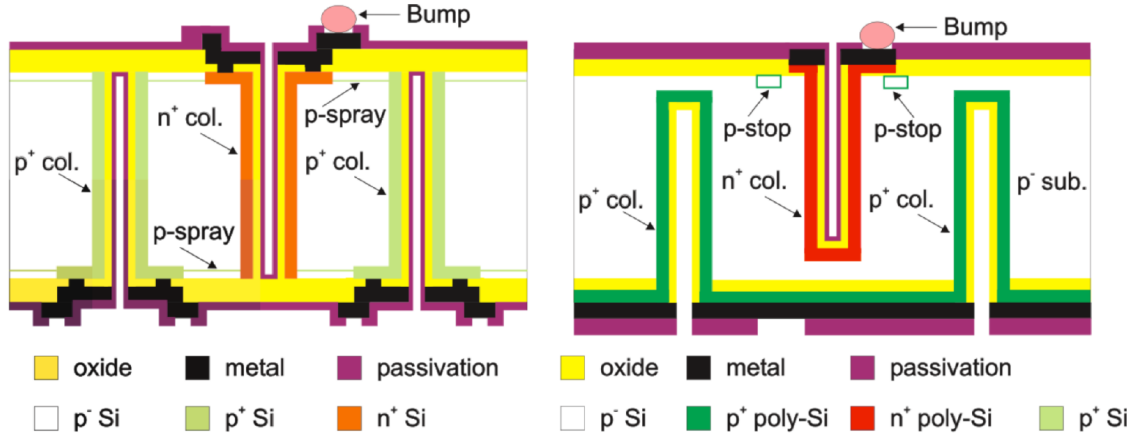
Figure 5.13:   Schematic cross-section of the 3D detector with passing-through columns from FBK (left) and with partial columns from CNM (right) fabricated on a $p-$type substrate (not to scale)(After [123])

The properties of the sensors are summarised in Table 5.1. Pixel pitch is 50 μm × 250 μm for both technologies. Both sensor types have a slim edge of 200 μ which is needed to avoid gaps in the coverage in z since shingling of the sensors in z is not possible for IBL. To reduce the area at the detector edge to 200 μ, with respect to 1.1 mm for pixel modules, two strategies were implemented: planar "moved" GRs inward, inside the area defined by n^+ pixel implants (see also Figure 5.14); 3D sensors has a forest of p^+ columns at bias voltage; in addition to that CNM sensor had a fence of n^+ columns shorted together to form a GR.
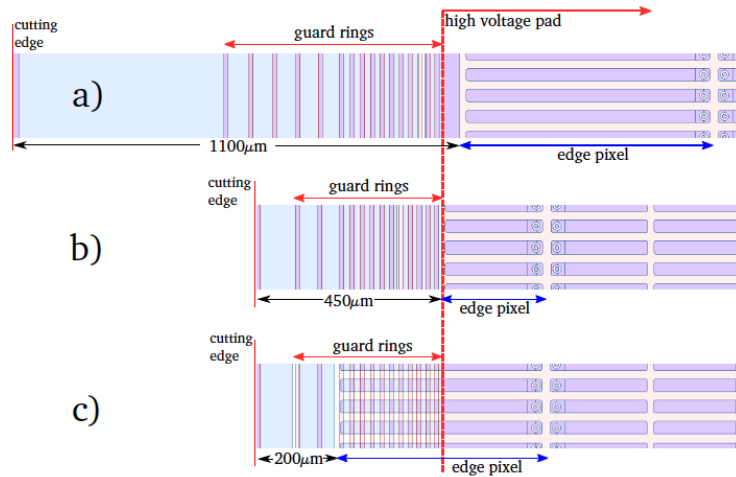
Figure 5.14: Top view of the sensor edge region of the ATLAS pixel (a), the conservative(b) and the slim edge (c) IBL design. The n^+ implantation is seen in blue the p^+ implantation in red. By reducing the number of guard rings, narrowing of the safety margin and by extending the edge pixels beyond the high voltage pad, the inactive edge could be reduced from 1100 μm for the ATLAS pixel design to 200 μ for the slim edge IBL design. (After [124])

Instead of choosing one technology over the other it was decided in the end to use a mix of sensors: 75% planar in the center of each stave, and 25% 3D on the outsides [125].

5.3.2.2 IBL Pixel Electronics

The frontend readout chip for IBL is the FE-I4 [126]. One FEI4 contains 26880 pixels which are arranged in 80 columns in z and 336 rows in ϕ. The size of one pixel is of course 250 µm × 50 µm. A crucial new feature of this chip with respect to the FEI3 readout chip is that the hits are stored in the pixel cells. A hit is only read out if a trigger request matches its timestamp, otherwise the hit is deleted. This reduces bandwidth use and power consumption inside the chip and allows for far higher occupancies.

The chip provides 4-bit ToT information for each hit compared to 8 of FEI3. To reduce data size the data of two neighboring pixels in ϕ are sent out in a single data word.

Figure 5.15 shows the FEI3 and FEI4 chip side-by-side.
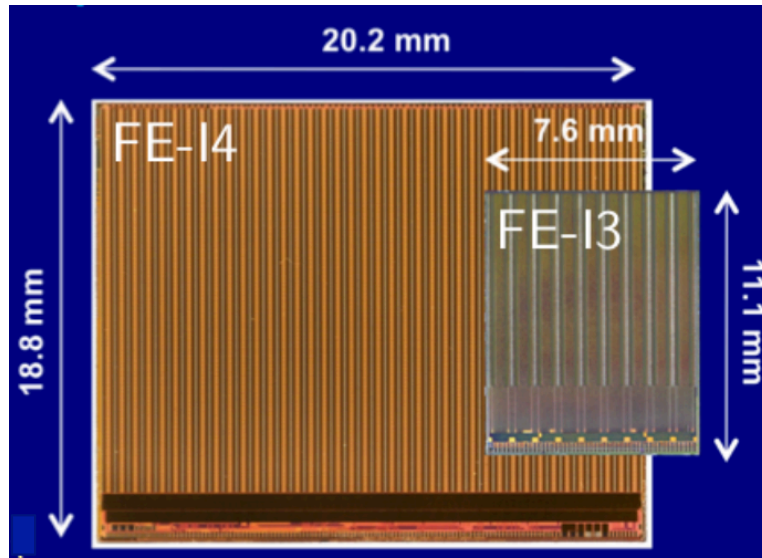
Figure 5.15: FEI3 and FEI4 chip side-by-side. Chips dimensions are indicated.

5.3.2.3 IBL Structure

The IBL is composed of 14 staves. Each stave contains 12 double-chip sensors in planar technology and 8 single-chip sensors in 3D technology. The total length of the active area of the save is 640 mm; including stave services it extends to 7 m.

The stave design is based on carbon foam material that provides a path for the heat generated in the sensors and in the front-end chips, to the cooling fluid boiling at low temperature in the cooling channel. The stiffness of the structure is provided by a quasi-isotropic carbon fiber laminate, the *Omega*, that is bonded to the foam. Figure 5.16 shows the cross section and a 3D view of the stave.

The cooling pipe is sandwiched between the carbon foam and the *Omega*. The pipe is hard bonded to the structure, the thermal contact being provided by a thermal compound based on epoxy-loaded resins. Inside the pipe CO_2 boiling assures the needed evacuation of the power dissipated by the IBL pixel modules. The target temperature for operating the IBL sensors is approximately -15°C, in order to minimise effects of reverse annealing on the sensors and to avoid thermal runaway. At the end of their lifetime planar sensors are expected to dissipate between 200 and 500 mW/cm^2, depending on the annealing history. The chip adds another 400 mW/cm^2, for a total of slightly less than 1 W/cm^2. After performing thermal simulations it was chosen to set a CO_2 evaporation temperature of $-40°$C and a mass flow per stave in the range of 1.5 to 2 g/s.

(a) Cross-section

(b) 3D view
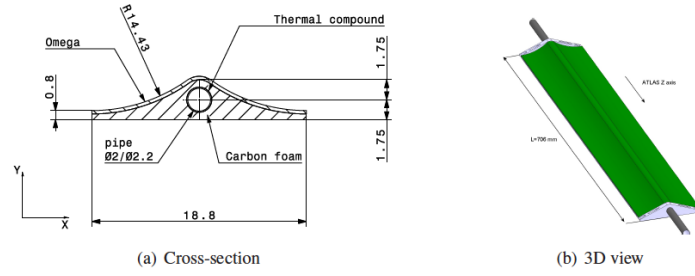
Figure 5.16: Cross section and 3D model of the IBL stave. Dimensions are in millimeters. (After [45])

5.4 Summary

In this Chapter the ATLAS Pixel detector has been presented, after a review of the physics program of the ATLAS experiment. In the next Chapter the radiation damage to the ATLAS pixel sensors will be described and a tool to model it will be discussed.

Chapter 6

Radiation Damage to the ATLAS Pixel Sensors

This Chapter presents a model for radiation damage to silicon sensors [127, 128] that is fast enough to be incorporated directly into the simulation of *digitization, i.e.* the conversion from energy depositions from charged particles to digital signals sent from module front ends to the detector readout system. This model is under development within the ATLAS Pixel group[1], and a publication is in preparation [127]. This Chapter is built on that document.

Figure 6.1 shows the flowchart of the ATLAS Monte Carlo simulation, from event generation to analysis; digitization step intervenes before reconstruction.
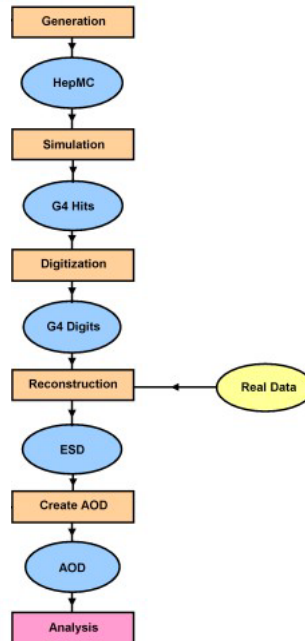
Figure 6.1: Flowchart of Monte Carlo simulation in ATLAS.

After introducing the motivations and the the fluences predictions for the actual ATLAS Pixel detector in Section 6.1, a model of charge deposition and measurement that includes

---

[1]This work is a collaborative effort, which Benjamin Nachman and I coordinate; the full list of involved researchers is the following: Mathieu Benoit, Julien Beyer, Marco Bomben, Rebecca Carney, Ian Dawson, Audrey Ducourthial, Gilberto Giugliarelli, Tommaso Lari, Anna Macchiolo, Lingxin Meng, Javier Llorente Merino, Paul Miyagawa, Benjamin Nachman, Lorenzo Rossini, Veronica Wallangen

radiation damage effects is documented in Section 6.2. Comparisons of the models with data are presented in Setion 6.3; conclusions and plans will be drawn in Section 6.4. In this report only planar sensors will be discussed; there is a parallel activity ongoing for 3D sensors.

6.1 Motivations and Expected Fluence for the ATLAS Pixel Detector

As discussed in the previous Chapter, silicon pixel detectors are at the core of the current ATLAS experiment. Given their close proximity to the interaction point, these detectors are subjected to an unprecedented amount of radiation over their lifetime: the innermost layers will receive fluences in excess of 10^{15} n_{eq}/cm^2. The modules comprising the detector are designed to be as radiation tolerant as possible, but their performance will still degrade over time. It is therefore critical to model the impact of radiation damage for an accurate simulation of charged particle interactions with the detector and the reconstruction of their trajectories.

Modelling radiation damage effects is especially relevant for the high luminosity upgrade of the LHC (HL-LHC - see also Chapter 7); the instantaneous and integrated luminosity will exceed current values by a factor of 100. The simulations for the present and future ATLAS detectors currently do not model the effect of radiation damage on the silicon sensors of the Pixel detector [129, 130].

As already discussed in Section 2.5, radiation damage in silicon occurs from both ionising and non-ionizing energy losses. Ionizing radiation leads to an accumulation of charge in the silicon dioxide (SiO_2) and charge trapping at the SiO_2-Si interface [50], affecting in particular the readout electronics. However, the focus here is bulk damage in the sensor due to non-ionising radiation [51]. We remind here that non-ionising radiation introduces defects into the sensor, which create energy levels in the band gap. When occupied, these states lead to three macroscopic detector effects: a change the effective doping concentration, reduced signal collection efficiency due to charge trapping, and an increase in sensor leakage current. The change in effective doping concentration has consequences for the depletion voltage and electric field profile. The ATLAS pixel planar sensors, being their bulk of $n-$type, are subjected to type inversion. The IBL underwent type inversion after about 3 fb^{-1} of data collected in 2015 and the second innermost layer (*b*-layer) inverted in the 2012 run after about 5-10 fb^{-1}. The effective doping concentration is further complicated by annealing in which new defects are formed or existing defects dissociate due to their thermal motion within the silicon lattice. As a result, radiation damage effects depend on both the irradiation and temperature history [51].

Complex radiation fields are simulated by propagating inelastic proton-proton interactions, generated by Pythia 8 [131, 132] through the ATLAS detector material using the particle transport code FLUKA [133, 134]. It is important to model as accurately as possible all the inner detector and calorimeter geometry details as high energy hadron cascades in the material lead to increased particle fluences in the inner detector, especially neutrons. A description of the ATLAS FLUKA simulation framework can be found in [135].

Predictions of the neutron-equivalent fluences per fb^{-1} in the ATLAS FLUKA inner detector geometry are available for different center-of-mass $\sqrt{s}$ values. In Figure 6.2 the prediction for $\sqrt{s} = 7$ TeV [136]; similar predictions exist for $\sqrt{s} = 8$ and 13 TeV.

The dominant contribution is from charged pions originating directly from the proton-proton collisions. The average values for the four pixel layers starting from the innermost
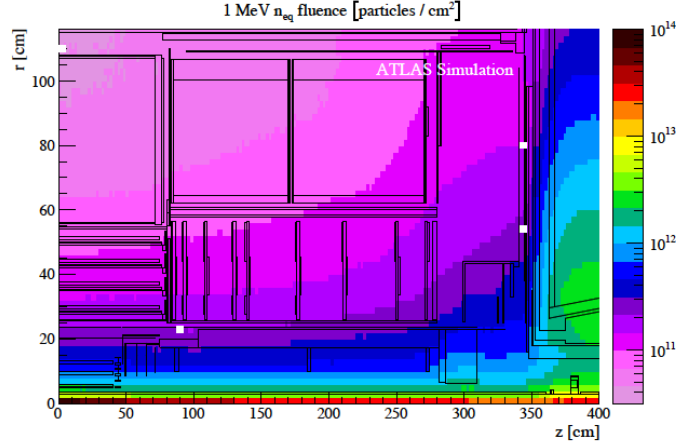
Figure 6.2: Quarter slice through the inner detector region of the geometry constructed in the FLUKA simulations. The colour contours represent the 1 MeV neutron-equivalent fluences, corresponding to an integrated luminosity of 1 fb^{-1} for $\sqrt{s} = 7$ TeV. The four white squares show the positions of the radiation monitors. (After [136])

one are 6.1×10^{12}, 2.9×10^{12}, 1.2×10^{12} and 7.8×10^{11} $n_{eq}/cm^2/(fb^{-1})$, respectively. Safety factors have not been applied to these numbers. The simulations predict some variation as a function of z. For example, in the IBL the maximum predicted value of 6.6×10^{12} $n_{eq}/cm^2/(fb^{-1})$ in the central location is about 10% higher than the end regions. The luminosity is determined by a set of dedicated bunch-by-bunch luminosity detectors [137] that are calibrated using the van-der-Meer beam-separation method [138].

By the end of the proton-proton collision runs in 2016, the IBL and b-layer had received integrated fluences approximately $\Phi = 2 \times 10^{14}$ n_{eq}/cm^2. Because the fluence decreases with distance, the outer two layers were exposed to less than half the fluence of the inner layers. The projected fluence on the IBL at the end of the LHC (300 fb^{-1}) is about $\Phi = 2 \times 10^{15}$ n_{eq}/cm^2.

The next Section describes the physics of the digitization model and the first collision data comparisons are shown in Section 6.3.

6.2 Digitization Modeling

6.2.1 Overview

Figure 6.3 presents a schematic overview of the physics models included in the digitization model.

Digitiser inputs are:

- the detector geometry and conditions, including the fluence (Section 6.2.2);

- the energy deposition from a charged particle, produced by Geant4 [139], possibly with corrections for straggling in thin silicon [140];

- the electric field, including radiation damage effects (Section 6.2.3); TCAD simulations are used to model the electric field.

Ionisation energy is converted into electron-hole pairs (~ 3.6 eV/pair) which experience random motion from diffusion. Chunks of fundamental charge carriers drift toward
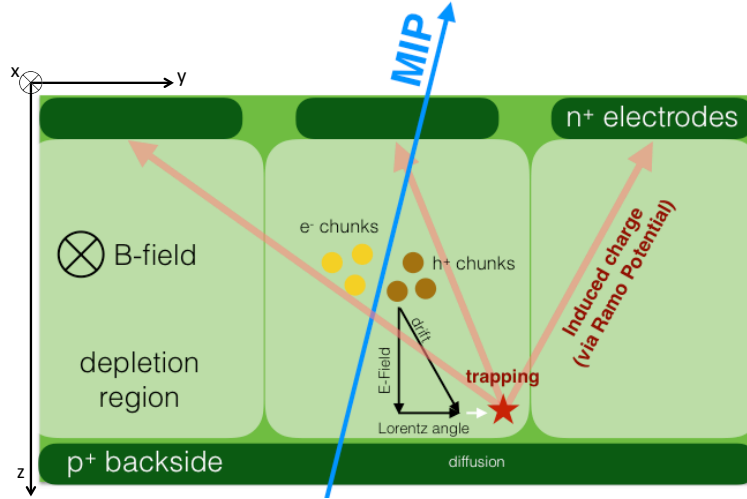
Figure 6.3: A schematic diagram illustrating the components of the digitizer model described in this note. The blue line represents a minimum ionizing particle traversing the pixel sensor. Chunks of electrons and holes, each representing $\mathcal{O}(10)$ fundamental charges, are transported to the electrodes. Holes drift toward the backplane under the influence of the electric field and also experience transverse motion due to the magnetic field (deflecting at the Lorentz angle). Thermal diffusion also changes the position of the charges. Before being collected, electrons or holes may be trapped by defects in the silicon. Even though the charge chunk may be trapped, it still induces a charge on the primary and neighbor electrodes via the Ramo potential. Pixel local coordinate system is indicated; it will be used through out the Chapter. (After [127])

the pixel electrodes (electrons) or backplane (holes) under the influence of the electric field, with a field- and temperature-dependent mobility. The number of fundamental charges per chunk is tuned to save time and a correction is applied to account for an over-estimation of fluctuations. In addition to drifting toward the electrodes under the influence of the electric field, there is a transverse component to the drift due to the 2 T magnetic field in the ATLAS inner detector. A field- and temperature-dependent Lorentz angle is combined with the mobility to compute the time for a charge carrier to be collected (Section 6.2.4 and 6.2.5). This time is compared to a fluence-dependent trapping time (Section 6.2.6), the characteristic time a charge carrier will travel for before it is trapped. If the drift time is longer than the trapping time, the chunk is declared trapped. The location of the chunk at the trapped position is calculated based on the starting position and trapping time (Section 6.2.4). Since moving charges induce a current in the collecting electrode, signal is induced on electrodes from trapped charges as well. This induced charge also applies to neighboring pixels, which contributes to charge sharing. The induced charge from trapped chunks is calculated from the initial and trapped positions using the weighting potential (Section 6.2.7). The sum of the collected and induced charge is then converted into a ToT that is used by cluster and track reconstruction tools.

6.2.2 Luminosity to Fluence

The most important input to the radiation damage digitizer is the estimated particle fluence. Section 6.1 introduced the baseline FLUKA simulation that is used to determine the conversion factor between integrated luminosity and fluence. This prediction yields a conversion of about 59.6×10^{11} $n_{\text{eq}}/\text{cm}^2/\text{fb}^{-1}$ for the IBL and 29.2×10^{11} $n_{\text{eq}}/\text{cm}^2/\text{fb}^{-1}$ for the b-layer. In order to establish systematic uncertainties on these predictions, the

fluence is converted into a prediction for the leakage current. The leakage current can be precisely measured and therefore provides a powerful constraint on the FLUKA simulation. For a time t at constant temperature T after an instantaneous irradiation with fluence Φ, the predicted leakage current is given by Equation 2.37 already presented in Section 2.5.

The full leakage current is then estimated by discretizing time into four hour periods, averaging luminosity and temperature information, and then sum over time in Equation 2.37. This leads to a complication in the α_0 parameter that has no explicit time dependence, but does depend on temperature. One proposal [51] is to absorb the temperature dependence in Equation 2.37 into the logarithm term as an effective scaling of the time axis:

$$I_{\text{leak}} = V \cdot \Phi \cdot \left(\alpha_I e^{-t/\tau} + \alpha_0^* - \beta \log(\Theta(\text{T})\, t/t_0) \right), \tag{6.1}$$

where $\alpha_0^* = 7.07 \cdot 10^{-17}$ A/cm is the value of α_0 from Equation 2.37 evaluated at a reference temperature $T_{\text{ref}} = 21°$C and the time scaling function $\Theta(\text{T})$ is defined by

$$\Theta(\text{T}) = \exp\left[-\frac{E_I^*}{k} \left(\frac{1}{\text{T}} - \frac{1}{\text{T}_{\text{ref}}} \right) \right], \tag{6.2}$$

where $E_I^* = (1.3 \pm 0.14)$ eV. For a fixed time period with constant temperature, Equation 2.37 and Equation 6.1 are mathematically identical. However, the latter allows for a natural extension to non-constant temperature:

$$I_{\text{leak}} = V \cdot \sum_{i=1}^{n} \cdot \phi_i \cdot t_i \cdot \left[\alpha_I \exp\left(-\sum_{j=i}^{n} \frac{t_j}{\tau(\text{T}_j)} \right) + \alpha_0^* - \beta \log\left(\sum_{j=i}^{n} \frac{\Theta(\text{T}_j) \cdot t_j}{t_0} \right) \right], \tag{6.3}$$

where ϕ_i is the fluence rate, t_i is the time in period i, and T_i is the temperature in period i. The first sum is over all time periods and the two sums inside the exponential and logarithm functions are over the time between the irradiation in time period i and the present time.

Using the measured module temperature as a function of time, Equation 6.3 is used to predict the leakage current. Module properties were updated every ten minutes. A constant luminosity-to-fluence conversion factor is fit to the data per module group; module groups differ by their distance along the beam direction from the geometric center of the detector.

6.2.3   Electric Field Modeling

The radiation-induced states in the silicon band gap affect the electric field in the pixel cells by altering the electric field distribution in the bulk[2]. Since many variables used in signal formation calculations depend on the electric field (drifting time, Lorentz angle deviation, etc.), including radiation damage effects requires a careful parameterisation of the electric field in the pixels.

---

[2]There are also changes at the surface, but the focus here is on the deformations on the electric field within the sensor.

Section 6.2.3.1 introduces the default model used for subsequent studies, as well as provides references to alternative models in the literature. Annealing evaluation is discussed in Section 6.2.3.2. The fluence-dependent depletion voltage calculation is presented in Section 6.2.3.3 and the resulting field profiles are shown in Section 6.2.3.4. Section 6.2.3.5 provides a brief comparison between the default model and alternative models.

6.2.3.1 Simulation Details

As already mentioned in Section 2.5, investigation of the electric field profile in the bulk of irradiated silicon sensors have shown that the electric field is no longer linear with the bulk depth after irradiation. In these materials, the irradiation causes two junctions, one at the pixel side and one at the opposite side, as first explained by Eremin, Verbitskaya, and Li (EVL) [58]. These two junctions give rise to an electric field with two maxima at the two edges of the sensor and a minima somewhere in the middle of the bulk. Electric field profiles are discussed in more detail in Section 6.2.3.4

This important and striking feature of irradiated planar sensors is simulated using the *Chiochia model* [82], already introduced in Section 4.5.2, implemented in the Silvaco TCAD package (see Chapter 4). The simulation is performed over volume that corresponds to a quarter of an ATLAS IBL pixel sensor cell, to take advantage of symmetry. Figure 6.4 highlights the geometry used in the simulation. The electric field is computed at $T = -10°C$ using an effective doping concentration of $1.6 \times 10^{12}/cm^3$ (corresponding to about 50 V depletion for unirradiated sensors) with a resolution of $1 \ \mu m^3$. The Chiochia model is a double-trap model with one acceptor and one donor trap with activation energies set to $E_c - 0.52$ eV and $E_v + 0.48$ eV [58], respectively. Reference [82] gives suggested values of the concentrations and capture cross-sections. The capture cross section for the acceptor and donor levels for holes, σ_h^A, σ_h^D are fixed at 1.65 ($\times 10^{-15}$ cm^2) and the same quantities for electrons (σ_e^A, σ_e^D) are fixed at 6.60×10^{-15} cm^2. The acceptor and donor concentrations vary with fluence are interpolated from the values presented in [82]. In particular, the acceptor concentrations are set to $0.35, 0.68,$ and $1.36 \times 10^{15}/cm^3$ for $1, 2,$ and $5 \times 10^{14} \ n_{eq}/cm^2$ and the corresponding donor concentrations for the same fluences are $0.5, 1.0,$ and $3.39 \times 10^{15}/cm^3$.
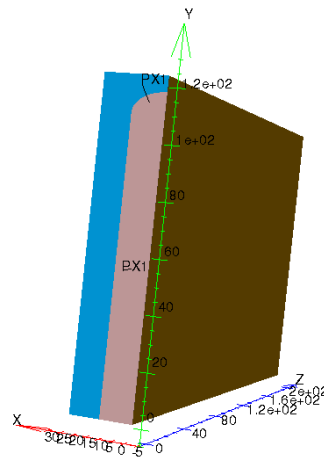

Figure 6.4: A schematic setup of the geometry for the planar TCAD simulation.

While the Chiochia model is used as default, there are additional radiation damage models (EVL [58], Petasecca [141], New Delhi [96], etc.), some of which are investigated

in Section 6.2.3.5. The TCAD simulations for planar are valid for silicon that has been instantaneously irradiated to a given fluence. In reality, the irradiation and thermal history play an important role in the effective doping concentration, which influences the calculated electric field profile. These effects are accounted for with a model of annealing, as described in the next Section.

6.2.3.2 Annealing

The irradiation and thermal history are accounted for in the prediction of the effective doping concentration with the Hamburg model (see [51] and references therein); changes to the effective doping concentration are of course impacting the electric field profiles too. In this model, the effective doping concentration has the following form:

$$N_{\text{eff}}(t) = (N_{\text{eff}}(0) - N_D^{\text{removable}}(0)) + N_D^{\text{removable}}(t) - N_A^{\text{stable}}(t) - N_A^{\text{beneficial}}(t) - N_A^{\text{reverse}}(t), \tag{6.4}$$

where $N_D^{\text{removable}}(0)$ is the initial concentration of removable donors. The fraction of removable donors at low doping concentrations like here is 100% for charged particle irradiation, which dominates the inner pixel layers in the ATLAS detector. The time-dependence of the terms on the right-hand side of Equation 6.4 are described by the following differential equations:

$$\frac{d}{dt}N_D^{\text{removable}}(t) = -c\phi(t)N_D^{\text{removable}}(t) \qquad \text{removal of donors for } n\text{-type during irradiation} \tag{6.5}$$

$$\frac{d}{dt}N_A^{\text{stable}}(t) = g_c\phi(t) \qquad \text{introduction of stable defects during irradiation} \tag{6.6}$$

$$\frac{d}{dt}N_A^{\text{beneficial}}(t) = g_A\phi(t) - k_A(\text{T})N_A^{\text{beneficial}}(t) \quad \text{beneficial annealing} \tag{6.7}$$

$$\frac{d}{dt}N_N^{\text{reverse}}(t) = g_Y\phi(t) - k_Y(\text{T})N_A^{\text{reverse}}(t) \quad \text{reverse annealing - neutrals} \tag{6.8}$$

$$\frac{d}{dt}N_A^{\text{reverse}}(t) = -k_Y(\text{T})N_N^{\text{reverse}}(t) \qquad \text{reverse annealing - acceptors} \tag{6.9}$$

where $\phi(t)$ is the irradiation rate in $n_{\text{eq}}/\text{cm}^2/\text{s}$. Equation 6.5 represents the effective removal of the initial dopants by mobile defects. The removal constant is $c = 6.4118 \times 10^{-14}/\text{cm}^2$. The second equation, Equation 6.6 represents the constant addition of stable (non-annealable) defects which electrically act as acceptors. Two additional defects are introduced in Equation 6.7 and 6.8. These short-lived defects are introduced during irradiation with rates g_a and g_Y and then decay with sufficiently high temperatures. The temperature-dependence of the decay rates are modeled with an Arrhenius equation, $k_i(\text{T}) = k_{i,0}e^{-\text{E}_i/k\text{T}}$, where $k_{A,0} = 2.4 \times 10^{13}/\text{s}$, $k_{Y,0} = 7.4 \times 10^{14}/\text{s}$, $\text{E}_A = 1.09$ eV and $\text{E}_Y = 1.325$ eV. For the beneficial annealing (Equation 6.7), the acceptor-like defects introduced during irradiation decay to neutral states with a time constant that is $\mathcal{O}$(days) at 20°C. In contrast, for reverse annealing, neutral-like defects are introduced during irradiation (Equation 6.8). The neutral defects can decay into acceptor-like states (Equation 6.9), decreasing (increasing) the effective doping concentration before (after) space-charge sign inversion. The timescale for reverse annealing is $\mathcal{O}$(weeks) at 20°C. The solutions of the differential equations 6.5-6.9 at constant temperature are:

$$N_D^{removable}(t) \qquad = N_{c,0} \cdot \left(1 - e^{-c\phi_{eq}t}\right) \qquad\qquad (6.10)$$

$$N_A^{stable}(t) \qquad = g_c \phi_{eq} t \qquad\qquad (6.11)$$

$$N_A^{beneficial}(t) \qquad = \frac{g_A \phi_{eq}}{k_A} \left(1 - e^{-k_A t}\right) + N_0 \cdot e^{-k_A t} \qquad\qquad (6.12)$$

$$N_A^{reverse}(t) \qquad = \frac{g_Y \phi_{eq}}{k_Y} \left(k_Y t + e^{-k_Y t} - 1\right) + N_0^{nd} \left(1 - e^{-k_Y t}\right). \qquad\qquad (6.13)$$

While the introduction rates g_c, g_A, and g_Y have been measured elsewhere (e.g. [118]), the reported values vary significantly amongst different materials and irradiation types and so are fit with *depletion voltage data* from the ATLAS pixel detector described in the next section (Section 6.2.3.3). Using the fitted introduction rates, the luminosity, and temperature profiles, the above model described in Equations 6.10- 6.13 is used to predict the effective doping concentration as a function of time. Figure 6.5 shows the predicted effective doping concentration for the IBL.
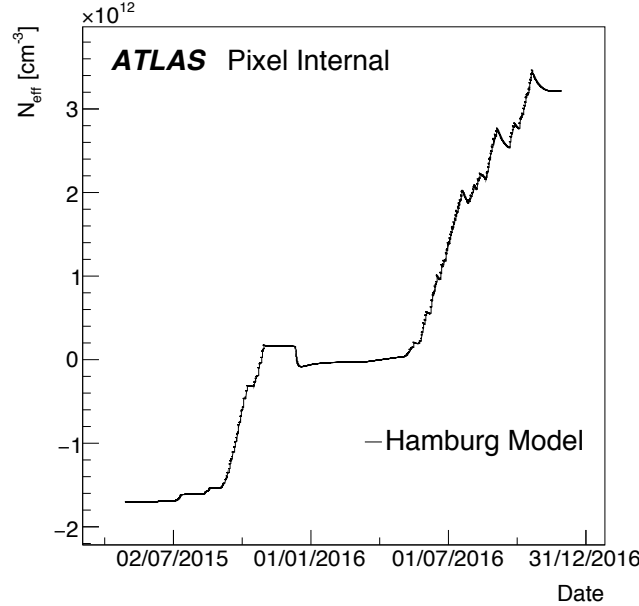
Figure 6.5: The predicted effective doping concentration as a function of time for the IBL using the Hamburg model described in Equations 6.10- 6.13. Donors lead to a negative effective doping concentration while acceptors contribute a positive concentration. (After [127])

The sensor is initially doped with about $10^{12}/cm^3$ of phosphorous, which is a donor (making the bulk *n*-type). Space charge sign inversion ($N_{eff} = 0$) is predicted to have occurred near the end of the 2015 data-taking run.

The predictions from the Hamburg model are incorporated into the TCAD calculations described in Section 6.2.3.1 by scaling the effective doping concentration as shown in Figure 6.5.

6.2.3.3 Depletion Voltage

Here the fit to the depletion voltage of the ATLAS pixel modules is described; the goal is to extract the introduction rates g_c, g_A, and g_Y mentioned in the previous Section.

The *depletion region* is the volume over which the lifetime of generated carriers is long enough to be collected. In order to maintain a high charge collection efficiency, it is critical that the depletion region extends to the whole sensor bulk. The size of this region depends on the bias voltage and the doping concentration, which changes with fluence. For unirradiated ATLAS planar sensors the depletion region grows from the backside up until type inversion, after which the region grows from the pixel implant. For highly irradiated sensors, the notion of *fully depleted* is not well-defined since there can be regions inside the sensor bulk that have very low field, even if the top and bottom of the (planar) sensor have a strong electric field. This is described in more detail in Section 6.2.3.4.

Despite the caveats about depletion at high fluence, at moderate fluences the notion of the depletion region is important for calibrating the Hamburg model that was introduced in Section 6.2.3.2. The full depletion voltage $U_{\text{full depl.}}$ in the Hamburg model is defined as usual as:

$$U_{\text{full depl.}} = |N_{\text{eff}}| \cdot \frac{q w^2}{2 \epsilon \epsilon_0},\tag{6.14}$$

where w is the sensor depth. Figure 6.6 shows the simulated depletion voltage as a function of time for the IBL (left) and b-layer (right). For calibration of the model, measurements with the ATLAS Pixel Detector were obtained by performing bias voltage scans of the mean ToT of hit-clusters on reconstructed particle trajectories. The depletion voltage is extracted by fitting two linear functions to the rising and the plateau region of the measured data. The intersection of the two lines is defined to be the depletion voltage (blue bars in Figure 6.6). Another method which was also used to obtain the full depletion voltage is a scan of the cross-talk between adjacent pixels (green and red bars in Figure 6.6, the different colors indicate different information sources). Since the pixels are isolated only after full depletion this is a powerful measurement tool. Unfortunately, this method is only applicable before space-charge sign inversion since otherwise the pixels are isolated already at low bias voltages much before full depletion.
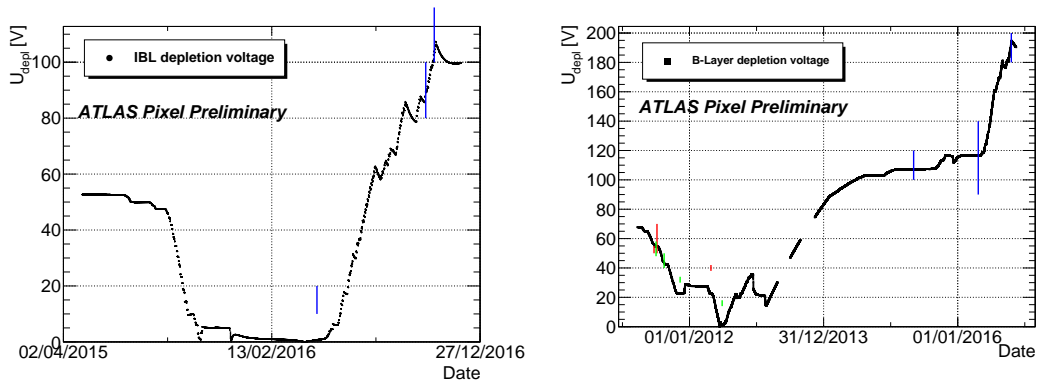
Figure 6.6: Simulated depletion voltage of IBL (left) and b-layer (right) according to the Hamburg model as a function of time from the date of their installation until end of 2016. The shown simulation uses the adapted introduction rates. Blue bars indicate measurements of the depletion voltage using the bias voltage scan method while red and green bars display earlier measurements using cross-talk scans. (After [142])

Due to the huge parameter space given by the introduction rates, the time necessary for the simulation, and a focus on physically rather than mathematically correct parameter combinations, the adjustment of the introduction rates was performed by hand. The

derived introduction rates are summarized in Table 6.1. The value of g_A was chosen close to the literature values since the measurements were done at insensitive points in time with respect to beneficial annealing. The value of g_Y was estimated from the reverse annealing during the long shutdown 1 (LS1) which was an extended period when the detector was maintained at room temperature. Since the IBL was installed after LS1 and has not undergone significant reverse annealing, the g_Y value of the b-layer is used also for the IBL.

Table 6.1: Introduction rates of the Hamburg model as obtained by fitting the simulated depletion voltage to the available measurements.

Parameter	IBL [$\times 10^{-2}$cm^{-1}]	B-Layer [$\times 10^{-2}$cm^{-1}]
g_A	1.35	1.35
g_Y	6.0	6.0
g_C	1.1	0.45

Table 6.2 lists the bias voltages that are used throughout the rest of the note unless otherwise specified.

Table 6.2: The calculated depletion voltages as a function of fluence for ATLAS planar sensors. For the planar sensors, the depletion voltage is computed using the Hamburg model after determining the introduction rates from Equation 6.4 by fitting the data. A fluence of 1×10^{14} (2×10^{14}) was reached around 09.07.2016 (08.09.2016). Values in parentheses are directly from the TCAD simulation based on a CV analysis (prior to the N$_{eff}$ correction).

Φ (n_{eq}/cm^2)	Depletion Voltage (Planar) (V)
0	53 (50)
1×10^{14}	51 (20)
2×10^{14}	83 (40)
5×10^{14}	(125)

In radiation damage models like [58, 82] annealing effects are not included. We have devised an effective modelling of annealing of annealing effects for TCAD radiation damage models; it will be presented in Section 6.2.3.6.

6.2.3.4 Electric Field Profiles

For planar sensors, the field is largely independent of x and y, perpendicular to the sensor depth. Figure 6.7 shows the z-dependence of the electric field, averaged over x and y, for an ATLAS planar sensor for various fluences and a fixed bias voltage of 80 V. Before irradiation the field is approximately linear, reaching a maximum of about $2V/w \sim 8 \times 10^{-4}$ MV/mm, where V is the bias voltage and w is the depletion depth. After type inversion, the field maximum is on the opposite side of the sensor. With increasing fluence, there is a minimum in the electric field in the center of the sensor. For a fluence of $\Phi = 5 \times 10^{14}$ n_{eq}/cm^2 for 80 V (under-depleted - see Section 6.2.3.3), this minimum is broad and occupies nearly a third of the sensor.

Similar predictions have been prepared for higher bias voltages and larger fluences.

6.2.3.5 Model Comparisons and Systematic Uncertainties

Detailed model comparisons are in preparation, but already the data presented in Section 6.3 can be used to constrain various simulations as well as tune parameters and de-
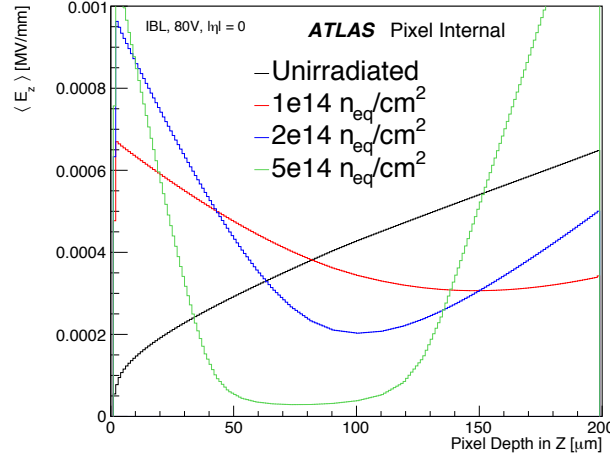
Figure 6.7: The electric field magnitude in the z direction, averaged over x and y for a the ATLAS IBL sensor biased at 80 V and at various fluences. (After [127])

rive systematic uncertainties for predictions for higher luminosity data. In addition to the Chiochia model for the planar sensors, the Petasecca model was also briefly investigated. While the model itself is supported by beam test data [141], it is found to disagree qualitatively on the fluence for type-inversion with the Chiochia model and does not display a two-peaked electric field profile after irradiation. Therefore, this alternative model was not studied in further detail.

Next, Chiochia model parameters are varied. The summary of the parameters variations is presented in Table 6.3.

Table 6.3: Variations of Chiochia model [143] parameters.

State/variation	η	E_t	σ_e	σ_h
acceptor	±10%	~ ±0.4%	±10%	±10%
donor	±10%	~ ±0.4%	±10%	±10%

Figures 6.8 and 6.9 show the electric field for variations in respectively the acceptor and donor trap parameters for a fluence of 10^{14} n_{eq}/cm^2 and a bias voltage of 80 V. The normalization of all the curves is fixed by the bias voltage and therefore all the curves cross at a point.

It can be seen that the electric field profile is almost insensitive to the capture cross-sections, moderately sensitive to the fluence dependence of the trap concentrations (η), and highly sensitive to the energy level of the traps. Similar variations are observed when the trap concentrations are varied by ±10% and the energy levels are varied by ± 10% of the thermal energy V_{th} ($V_{th} = kT$), which corresponds roughly to 0.4% of the energy level. The latter number is chosen as a benchmark because the occupancy probability scales exponentially with the energy as $\sim e^{E/kT}$ [144]; see also Appendix B. Interestingly, when the acceptor energy is moved closer to the conductive band by 0.4%, the electric field looks symmetric around the mid-plane; moving the acceptor even closer to the conduction band would probably result in depletion starting from the backside. As expected, varying one parameter value for the acceptor trap has on the electric field an effect that is opposite to the one that is obtained when the same parameter is changed for the donor trap. All the observed changes in the electric field are consistent with expectations (see for example [144]).
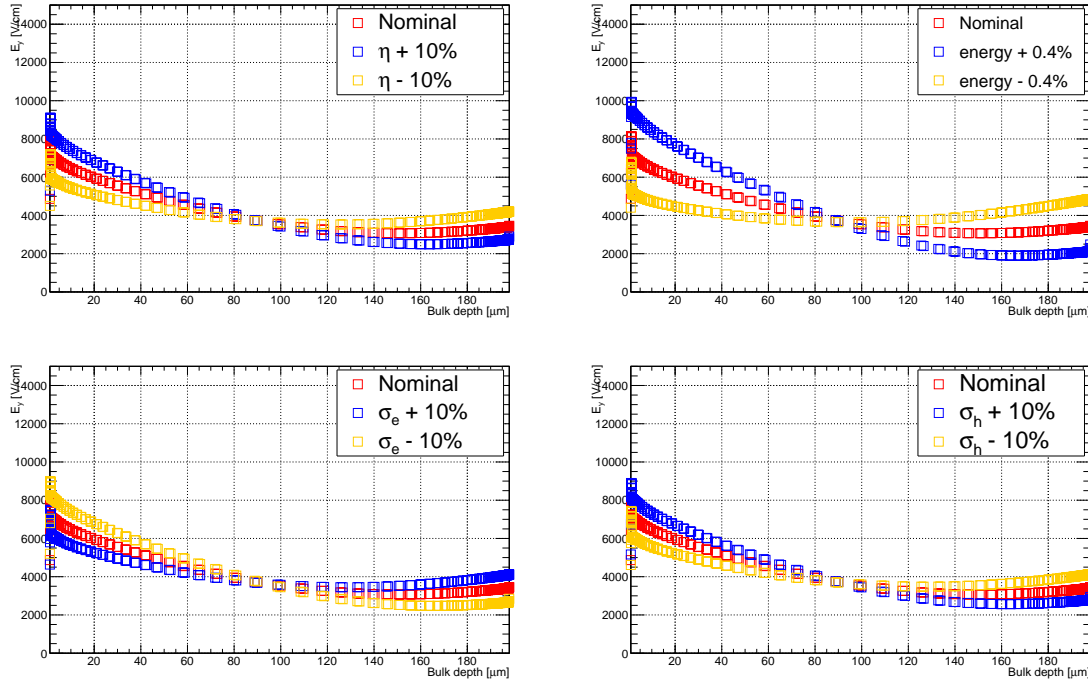
Figure 6.8: The z dependence of the electric field in an ATLAS planar sensor, averaged over x and y, for a simulated fluence of $\Phi = 1 \times 10^{14}$ n_{eq}/cm^2, after varying parameters of the acceptor trap in the Chiochia model. (Top) The left plot shows a $\pm 10\%$ variation in the fluence dependence of the acceptor trap concentrations while the right plot shows a variation in the acceptor trap energy level by 0.4%. (Bottom) The left plot shows a $\pm 10\%$ variation in the electron capture cross section, the right one a $\pm 10\%$ variation in the hole capture cross section. The bias voltage was set to 80 V in all cases.
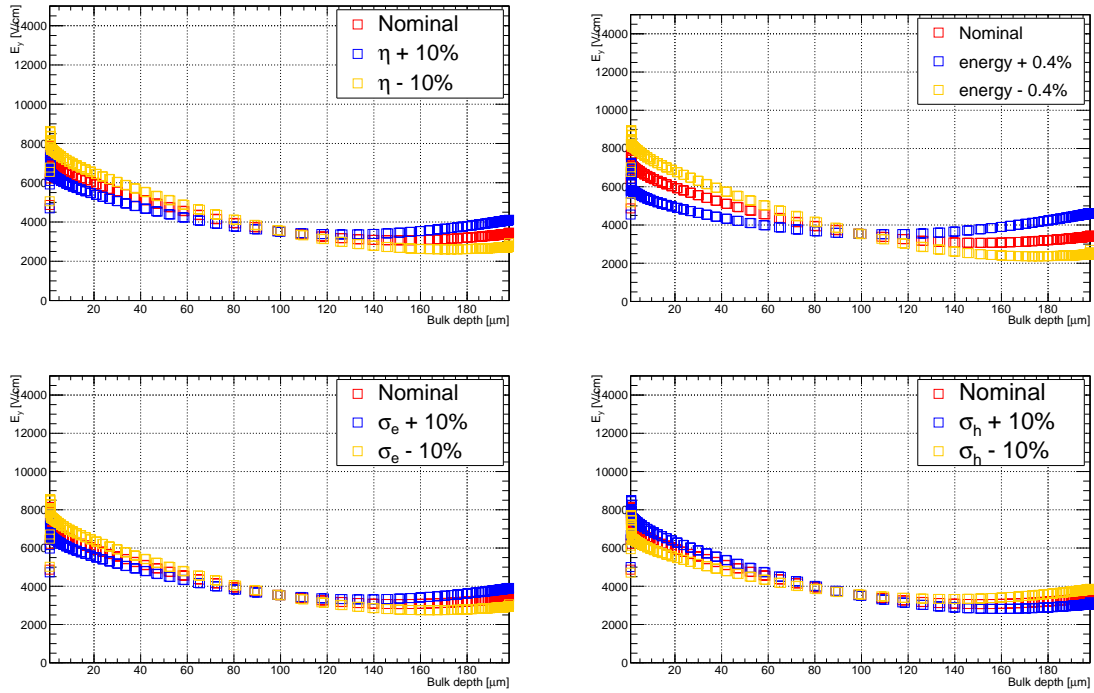
Figure 6.9: The z dependence of the electric field in an ATLAS planar sensor, averaged over x and y, for a simulated fluence of $\Phi = 1 \times 10^{14}$ n_{eq}/cm^2, after varying parameters of the donor trap in the Chiochia model. (Top) The left plot shows a $\pm 10\%$ variation in the fluence dependence of the acceptor trap concentrations while the right plot shows a variation in the acceptor trap energy level by 0.4%. (Bottom) The left plot shows a $\pm 10\%$ variation in the electron capture cross section, the right one a $\pm 10\%$ variation in the hole capture cross section. The bias voltage was set to 80 V in all cases.

6.2.3.6 Effective modelling of annealing effects into TCAD simulations

There is no known recipe to include the annealing effects presented in Section 6.2.3.2 into TCAD based predictions. One challenge for incorporating annealing effects is that both the Hamburg and TCAD models are based on multiple effective deep traps [58,82] and the effective states are not exactly in one-to-one correspondence. Furthermore, the Hamburg model does not make a prediction for the depth dependence of the effective doping concentration (Equation 6.14 assumes it is constant) while the TCAD model predicts a non-trivial dependence, resulting in the complicated electric field profile discussed in Section 6.2.3.4. The non-constant charge density from TCAD is demonstrated in Figure 6.10 for an ATLAS IBL planar sensor after radiation damage. For $\Phi = 1 \times 10^{14}$ n_{eq}/cm^2 the space charge density is negative and shows an almost linear dependence on the bulk depth, while for higher fluences the functional form is more complicated, exhibiting sizable regions where the charge density is positive, in agreement with the model first proposed in [58].

Figure 6.10: The z dependence of the normalised charge density ρ/e in a simulated ATLAS IBL planar sensor, averaged over x and y, for simulated fluences of $\Phi = 1$, 2 and 5×10^{14} n_{eq}/cm^2. The bias voltage was set to 150 V in all cases.

One way to emulate annealing effects from the Hamburg model in the TCAD simulation is to match the effective doping concentration from the former to the average charge density of the latter:

$$\langle \rho/e \rangle_{TCAD} = (N_{eff})_{Hamburg}. \tag{6.15}$$

Table 6.4 collects predictions from the Hamburg model (see Section 6.2.3.2) for the effective concentration of donors and acceptors as well as their difference N_{eff} for two points in time.

Table 6.4: Predictions from the Hamburg model for the effective donor (N_D) and acceptor (N_A) concentrations as well as their difference (N_{eff}) for two points in time during Run 2. Section 6.2.3.2 for details.

date	Φ [n_{eq}/cm^2]	N_{eff} [cm^{-3}]	N_D [cm^{-3}]	N_A [cm^{-3}]
9/7/2016	1×10^{14}	1.62×10^{12}	0.08×10^{12}	1.7×10^{12}
8/9/2016	2×10^{14}	2.72×10^{12}	0.08×10^{12}	2.8×10^{12}

Figure 6.11 shows the charge density predicted by TCAD simulations in four different scenarios with a bias voltage of 150 V and the two fluences reported in Table 6.4.
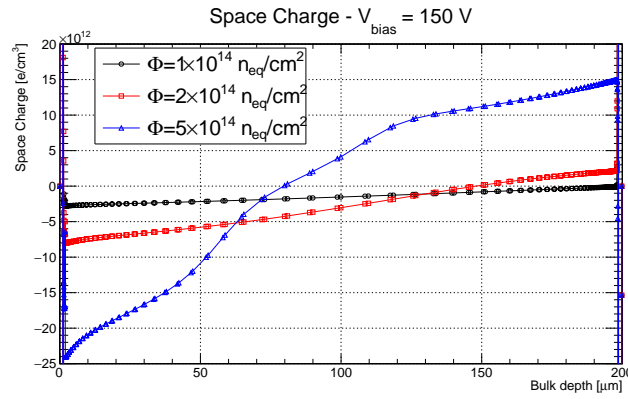
Figure 6.11: The z dependence of the normalised charge density ρ/e in a simulated ATLAS IBL planar sensor, averaged over x and y, for simulated fluences of (left) $\Phi = 1$ and (right) 2×10^{14} n_{eq}/cm^2. The bias voltage was set to 150 V in all cases. Four scenarios were simulated; see text for more details.

The *Reference* scenario is the default setup described in Section 6.2.3.1 with no modifications to emulate annealing. Another extreme, labeled *Annealed*, considers the acceptor and donor traps in the Hamburg model TCAD as in one-to-one correspondence. Therefore, instead of matching the effective doping concentration as in Equation 6.15, the acceptor and donor densities in TCAD are directly set to the values in Table 6.4. Moreover, since shallow defects are not affected by deep traps in TCAD, the way to account for the fact that in Hamburg model the shallow donors are supposed to be completely annealed out is to reduce significantly the initial concentration of shallow donors. So, additionally, the doping level in the starting material is set to 8×10^{10} cm^{-3}; as a reminder the initial donor concentration was of about 1.6×10^{12} cm^{-3}. The Annealed scenario is qualitatively different than the un-annealed line and would predict an electric field that is linear (more below), which is in contrast to various measurements elsewhere [82] and also shown later in this paper (Section 6.3.2). Therefore, a compromise is made in which only the average effective doping concentration is matched between the models, following Equation 6.15. There is some freedom in how to do the matching because donors and acceptors can be independently varied. For high fluences ($\gtrsim 10^{13}$ n_{eq}/cm^2), deep and shallow donor states are more likely than acceptors to be completely removed [51]. Therefore, we vary only the acceptor concentrations when solving Equation 6.15. The values that match the Hamburg model are +3% for $\Phi = 1 \times 10^{14}$ n_{eq}/cm^2 and −1.6% for $\Phi = 2 \times 10^{14}$ n_{eq}/cm^2. For reference, the space charge distributions for +10% and −5% for the two fluences are also shown, respectively. The average charge density in the various scenarios is summarised in Tables 6.5 and 6.6 for the two fluences shown in Figure 6.11.

Table 6.5: Results for average and RMS of effective doping concentration over the sensor bulk from TCAD simulation for different scenarios. Fluence Φ was 1×10^{14} n_{eq}/cm^2; bias voltage V_{bias} was 150 V. Refer to the text for more details.

$\Phi = 1 \times 10^{14}$ n_{eq}/cm^2		
Scenario	$\langle N_{eff} \rangle$ [cm^{-3}]	RMS [cm^{-3}]
Reference	-1.5×10^{12}	0.4×10^{12}
Annealed	-1.45×10^{12}	0.04×10^{12}
N_A+10%	-2.2×10^{12}	0.6×10^{12}
N_A+3%	-1.7×10^{12}	0.5×10^{12}

The electric field profiles corresponding to the four scenarios shown in Figure 6.11 are presented in Figure 6.12. For the Annealed scenario (shown only for reference), the profile

Table 6.6: Results for average and RMS of effective doping concentration over the sensor bulk from TCAD simulation for different scenarios. Fluence Φ was 2×10^{14} n_{eq}/cm^2; bias voltage V_{bias} was 150 V. Refer to the text for more details.

$\Phi = 2 \times 10^{14}$ n_{eq}/cm^2		
Scenario	$\langle N_{eff} \rangle$ [cm^{-3}]	RMS [cm^{-3}]
Reference	-2.9×10^{12}	2.1×10^{12}
Annealed	-2.34×10^{12}	0.01×10^{12}
N_A-5%	-2.3×10^{12}	2.8×10^{12}
N_A-1.6%	-2.7×10^{12}	2.1×10^{12}

is nearly linear while this is not the case for the other scenarios, especially at the higher fluence $\Phi = 2 \times 10^{14}$ n_{eq}/cm^2.
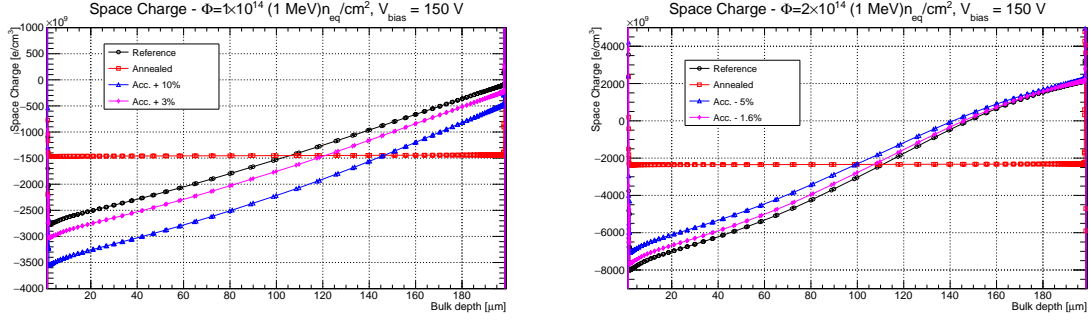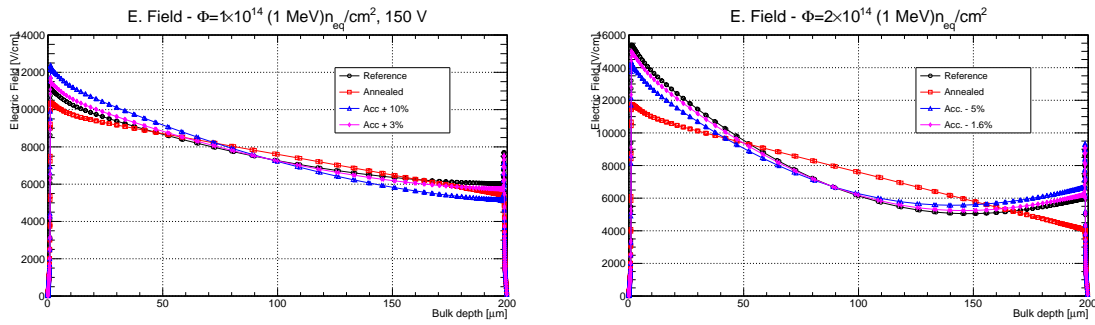

Figure 6.12: The z dependence of the electric field in a simulated ATLAS IBL planar sensor, averaged over x and y, for simulated fluences of (left) $\Phi = 1$ and (right) 2×10^{14} n_{eq}/cm^2. The bias voltage was set to 150 V in all cases. Four scenarios were simulated; see text for more details.

In summary, increasing the acceptor traps density by 3% at fluence $\Phi = 1\times10^{14}$ n_{eq}/cm^2, and reducing it by 1.6% at fluence $\Phi = 2\times10^{14}$ n_{eq}/cm^2 the effect of annealing predicted by Hamburg model can be emulated with the TCAD simulations. These variations are currently within the model variations described in Section 6.2.3.5 that are used to set systematic uncertainties on the radiation damage model parameters. Therefore, no additional corrections or uncertainties are applied to the simulation to account for annealing for the current radiation levels.

6.2.4 Time-to-Electrode, Location-at-Trap

Numerically propagating charges through the silicon sensor can be computationally expensive, but fortunately can be computed once per geometry and set of conditions (temperature, bias, and fluence). Electrons and holes drift with a velocity given by the mobility: μ_C, where $C \in \{e, h\}$. The mobility is parameterized as a function of electric field and temperature [145]:

$$\mu_C(E) \approx \frac{v_{s,C}}{E_{c,C}}\left(1 + \left(\frac{E}{E_{crit,C}}\right)^{\beta_C}\right)^{-1/\beta_C}, \tag{6.16}$$

where the values for the saturation velocity v_s, critical E-field E_{crit} and temperature exponent β can be found in Table 6.7.

Table 6.7: Physical constants describing the mobility of charge carriers in silicon. The first three rows are reformatted from Ref. [145] and the Hall scale factor is from Ref. [146].

quantity	electrons	holes
v_s (μm/ns)	$116 \times (T/273\text{ K})^{-0.87}$	$88 \times (T/273\text{ K})^{-0.52}$
E_{crit} (kV/cm)	$6.0 \times (T/273\text{ K})^{1.55}$	$15 \times (T/273\text{ K})^{1.68}$
β	$1.0 \times (T/273\text{ K})^{0.66}$	$1.1 \times (T/273\text{ K})^{0.17}$
r	$1.13 + 8 \times 10^{-4} \times (T/K - 273)$	$0.72 - 5 \times 10^{-4} \times (T/K - 273)$

Importantly, the saturation velocity for electrons is much higher than for holes. The magnetic field modifies the mobility by the Hall scattering factor r by $\mu \mapsto r\mu$, with the temperature-dependent r given in Table 6.7. Fundamental charge carriers drift with a velocity given by $v(E) \sim r\mu(E)E$ and the charge collection time is estimated via

$$t_{\text{collection}}(\vec{x}_{\text{initial}}) \sim \int_{\vec{x}_{\text{initial}}}^{\vec{x}_{\text{final}}} \frac{ds}{r\mu(E)E}, \tag{6.17}$$

where s is determined by the equations of motion $\vec{v} = r\mu(E)\vec{E}$ and $\vec{x}_{\text{final}}$ depends on the type of the charge carrier. For planar sensors, the field is nearly independent of x and y, so the time to the electrode is parameterized in z and the integral in Equation 6.17 is one-dimensional. Representative time-to-electrode values are shown in Figure 6.13 for planar sensors.
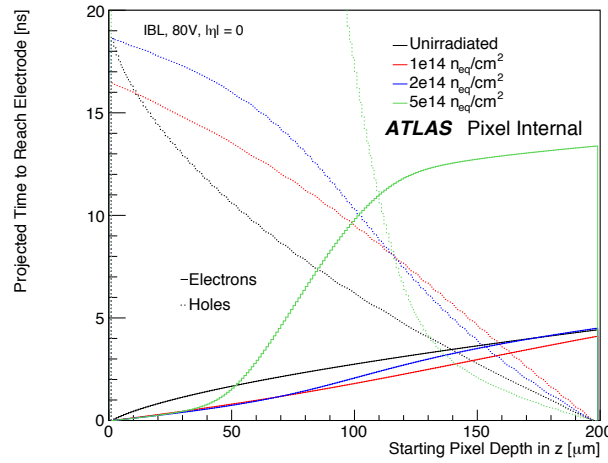
Figure 6.13: The time for an electron or hole to drift all the way to the collecting electrode (electrons) or back plane (holes) in an ATLAS IBL planar sensor biased at 80 V as a function of the depth (z) using the averaged electric fields shown in Figure 6.7. (After [127])

Since the mobility of holes is much less than for electrons, it takes holes much longer on average to fully drift. The collection time varies with fluence, bias voltage, and distance to the electrode, but is on average $\mathcal{O}(1)$-$\mathcal{O}(10)$ ns for $\Phi \lesssim 10^{15}$ $n_{\text{eq}}/\text{cm}^2$.

For charges that are trapped (see Section 6.2.6), one must know the location of the trapped charge. The position-at-trap can be calculated in a similar fashion as the time-to-electrode from Equation 6.17. In particular,

$$\vec{x}_{\text{trap}}(t_{\text{to trap}}) \sim \int_0^{t_{\text{to trap}}} r\mu(E)\vec{E}dt. \tag{6.18}$$

Representative position-at-trap maps are shown in Figure 6.14 for planar sensors.
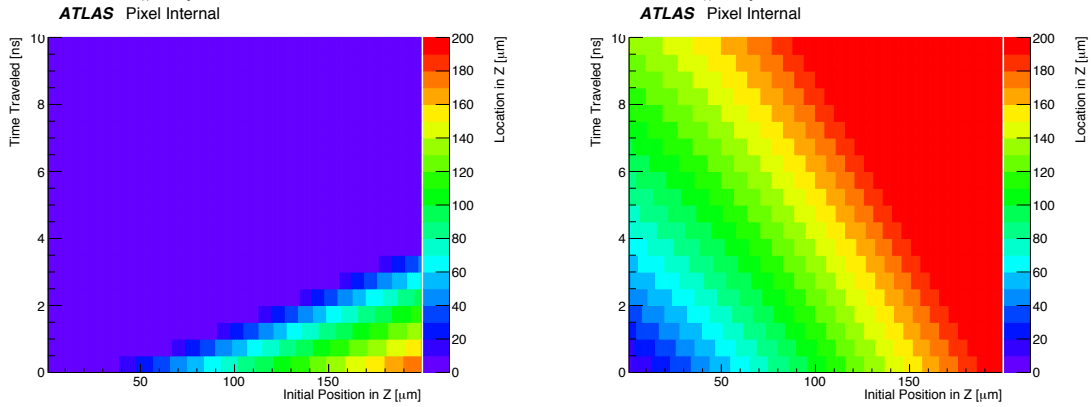
Figure 6.14: The z position of the trapped electrons (left) or holes (right) as a function of their starting position and the time traveled for $\Phi = 10^{14}$ n_{eq}/cm^2. The collecting electrode is at origin while the backplane is at 200 μm. (After [127])

6.2.5 Lorentz angle

In addition to drifting with the electric field, electrons and holes also move in reaction to the 2 T magnetic field that surrounds the ATLAS inner detector. Due to the orientation of the electrodes, this has nearly no impact on the 3D sensors, but is significant for planar sensors. The tilt angle of charge carrier drift with respect to the pixel axis is called the *Lorentz angle* and is given by $\tan\theta_L = r\mu(E)B$, where r is the Hall scattering factor and $\mu(E)$ is the mobility as a function of the electric field, defined in Section 6.2.4. Due to the dependence of the electric field on the sensor depth, the Lorentz angle can change significantly along the trajectory of an electron or hole. The left plot of figure 6.15 demonstrates the change in the Lorentz angle along the trajectory of electrons and holes. As the mobility increases with decreasing electric field strength, the Lorentz angle is largest near the center of the sensors when irradiated.

The Lorentz angle can have important implications for charge sharing and it is therefore important to correct for the path dependence of the angle. This is modeled in a similar manner to the maps from Section 6.2.3.5 by integrating the Lorentz angle along the path:

$$\tan\theta_L^{\text{integrated}}(z_{\text{initial}}, z_{\text{final}}) = \frac{rB}{|z_{\text{final}} - z_{\text{initial}}|} \int_{z_{\text{initial}}}^{z_{\text{final}}} \mu(E(z))\,dz. \tag{6.19}$$

The drift along the ϕ direction (the azimuthal angle transverse to the beam) is then modified as $|z_{\text{final}} - z_{\text{initial}}| \tan\theta_L^{\text{integrated}}(z_{\text{initial}}, z_{\text{final}})$, where the direction is the same for both electrons and holes because both the charge and velocity sign are reversed for holes with respect to electrons. The size of the integrated Lorentz angle variations are shown in Figure 6.15; for this fluence and bias voltage, the integrated Lorentz angle can change by as much as a factor of two, depending on the starting and ending position.

6.2.6 Trapping

As a result of irradiation, defects form in the silicon and are sites for charge trapping. In the simulation, charge chunks are declared trapped if the projected time to reach the
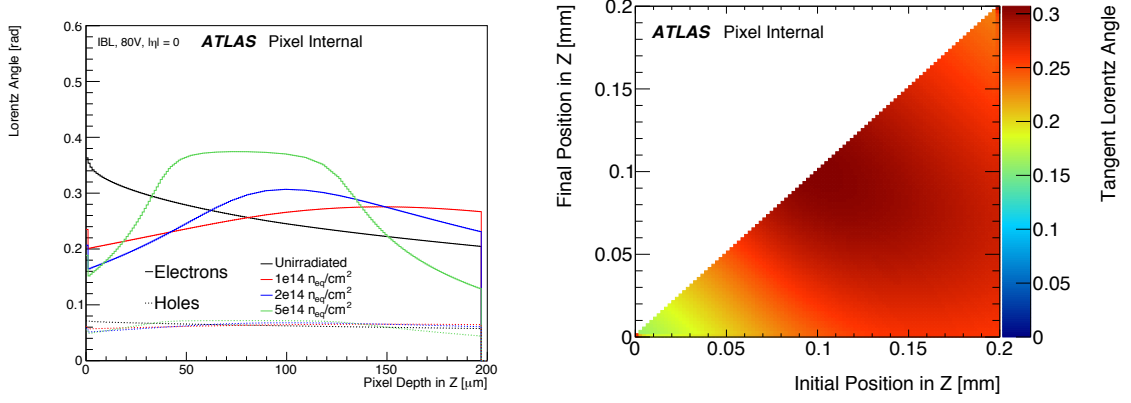
Figure 6.15: Left: The depth dependence of the Lorentz angle for electrons and holes for four fluences in an ATLAS IBL planar sensor biased at 80 V. Right: The integrated Lorentz angle for electrons (see Equation 6.19) as a function of the starting and ending position for a fluence of $\Phi = 2 \times 10^{14}\ n_{eq}/cm^2$. The collecting electrode is at a z position of 0. (After [127])

electrode from Section 6.2.4 exceeds a random trapping time t that is exponentially distributed with mean value $1/(\kappa\Theta)$, where Θ is the fluence. The constant κ (sometimes called β in the literature) has been measured in ATLAS pixel modules in 2001 during a CERN beam test and is approximately $\kappa = 3 \times 10^{-16}\ cm^2/ns$ [147]. Charge trapping reduces the collected signal and thus degrades track reconstruction efficiency.

6.2.7   Ramo Potential and the Induced Charge

Even though radiation damage causes charges to be trapped, the measured signal need not be zero. This is because charge is registered as soon as the electrons or holes start to move. One can compute the total induced charge without modeling the detailed time-dependent current via the the *Ramo potential* from the Shockley-Ramo theorem (see Section 2.4.1). As a reminder, the theorem states that the amount of induced charge is the particle charge multiplied by the difference in the Ramo potential V_w from its starting and ending (trapped) location:

$$Q_{induced} = -Q[V_w(\vec{x}_{end}) - V_w(\vec{x}_{start})], \tag{6.20}$$

where Q is the charge of the drifting carrier. The Ramo potential for a particular electrode is computed by calculating the electrostatic potential with the boundary condition of the electrode held at unit voltage and setting all other electrodes to have zero potential. For example, for a an infinite parallel plate capacitor, the field is constant in between the plates, so the Ramo potential is linear (starting at 1 and decreasing to zero - see also Appendix A). This potential depends only on geometry and therefore can be computed once prior to any event simulation.

The Ramo potential is calculated using TCAD to solve the Poisson's equation. For planar sensors, most of the variation in the Ramo potential is in the z direction, but one must include the x and y dependence in order to account for charge induced on the neighboring pixels. The left plot of Figure 6.16 shows a slice of the three-dimensional Ramo potential at $x = 0$. Vertical lines indicate the position of the pixels: the potential can be as much as 20-30% in the nearest neighboring pixel. The right plot of Figure 6.16 shows a one-dimensional projection of the Ramo potential along the z axis. Due to the simple

109

geometry of a planar sensor, the full TCAD simulation is well-approximated by a series expansion that solves Poisson's equation with periodic boundary conditions. The expansion matches the full three-dimensional potential well and is shown in the right plot of Figure 6.16 for illustration.
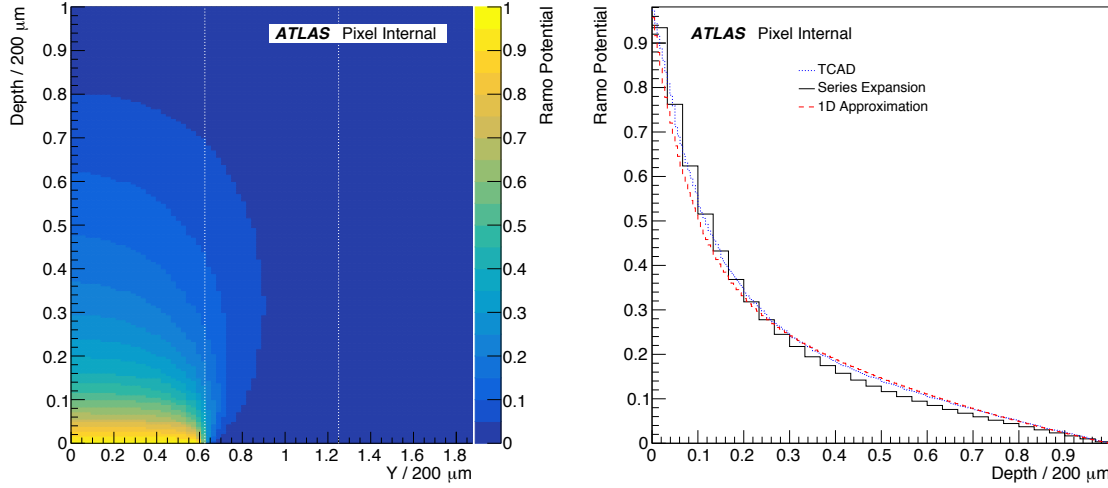
Figure 6.16: Left: A two-dimensional slice of the full three-dimensional ATLAS planar sensor Ramo potential as computed with TCAD at $x = 0$. Dashed vertical lines indicate pixel boundaries. Right: A one-dimensional slice of the Ramo potential at $x = y = 0$. Overlaid on top of the TCAD simulation are a series expansion solution of the Poisson's equation as well as double-exponential defined by Equation 6.21. (After [127])

In the digitizer code, if the user does not supply a Ramo potential calculated with TCAD, this series expansion is substituted instead so that geometries for which a TCAD model has not yet been created can be studied. The z-dependence of the planar Ramo potential alone is also very well approximated by a double exponential of the form

$$V_{w,z}(z) = [e^{-z/\alpha L} + e^{-z/L} - e^{-\alpha} - e^{-1}]/(2 - e^{-\alpha} - e^{-1}), \tag{6.21}$$

where $L = 200\ \mu m$ and the denominator is chosen to make $V_{w,z}(0) = 1$. Good agreement is found for $\alpha \sim 3L/p$, where p is the sensor pitch in the short direction (see Figure 6.16).

The implementation of the Ramo potential and charge trapping are illustrated in Figure 6.17 for planar sensors. On the electrode from the same pixel as the electrons and holes originate, the induced charge equals the electron charge as the time to be trapped exceeds the time to drift toward the electrode. The average collected charge is an asymmetric function of the depth inside the sensor because the drift and trapping times are different for electrons and holes and the Ramo potential is very asymmetric: the average fraction is lower far away from the collecting electrode. In addition to inducing a charge on the electrode from the same pixel as the electron-hole pair generation, charge is induced in the neighboring pixels. This is demonstrated in the middle and right plots of Figure 6.17. In the limit where the induced charge is the electron charge in the same pixel as the electron-hole pair, the induced charge in the neighbors approaches zero. For some combinations of starting location and time to trap, the induced charge can even be negative. This happens when holes are trapped very close to the pixel implants. Even

though the Ramo potential map extends beyond one neighbor pixel, in practice the nearest neighbor pixels are considered in the simulation. The right plot of Figure 6.17 indicates that this is good approximation.
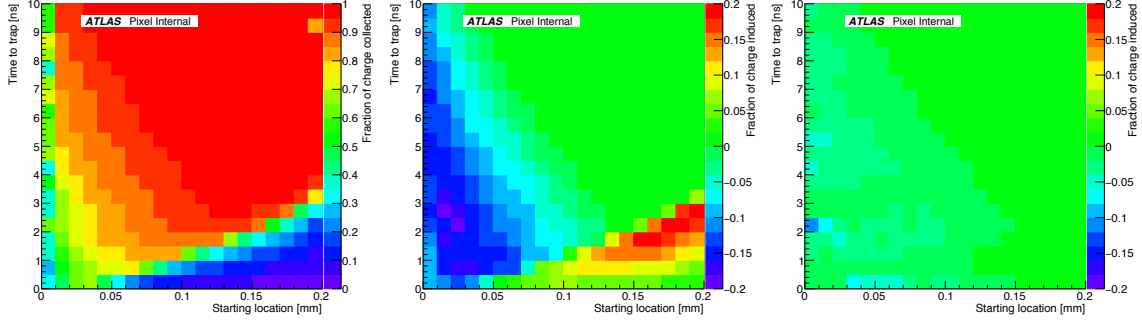
Figure 6.17: The average charge collected as a function of the starting location and the time to be trapped for the same pixel as the electron-hole pair generation (left), the neighbor pixel in the short (50 µm) pitch direction (middle) and the pixel in the long pitch direction (250 µm) (right). For simplicity, the electric field field is simulated without radiation damage and the vertical axis is a hypothetical trapping time. (After [127])

6.3   Predictions and Validation

6.3.1   Data and Simulation

Given the models presented in the previous sections, it is critical to validate the physics as well as the implementation by comparing the simulations with data. This Section present results for the key observable for studying radiation damage: the charge collection efficiency[3]. The charge collection efficiency is measured as a function of time in Run 2 for the innermost pixel layer, which was installed during the shutdown between Run 1 and Run 2 and thus was unirradiated at the start of Run 2. The data were collected in the fall of 2015 and throughout 2016 with single muon triggers. Charged particle tracks are reconstructed from hits in the Pixel detector, silicon strip detector, and transition radiation tracker. Clusters on the innermost pixel layer associated to tracks are considered for further analysis. The IBL is operated at 80 or 150 V at a temperature of 270 K in 2015 and 288 K in 2016. The analog threshold is 2550 e with 4 bits of ToT for the digital charge readout. The ToT is calibrated so that a ToT of 8 corresponds to 20 ke and a digital threshold of ToT > 1 is applied. The ADC is modeled in simulation using the same charge to ToT conversion.

Simulated datasets are based on Geant4 [139] with digitization implemented in the full ATLAS simulation framework (ATHENA) [129] or a standalone package called Allpix [148]. The latter is a lightweight wrapper of Geant4 that is optimized for beam test analysis and is a powerful test-bench for digitizer development.

6.3.2   Charge Collection Efficiency

The collected charge is represented by the mode of the charge distribution, which is approximately Landau [37]. The charge collection efficiency is defined to be the collected

---

[3]Results for the Lorentz angle are being prepared

charge at one fluence divided by the charge for unirradiated sensors in overdepletion. Figure 6.18 shows the measured and predicted charge collection efficiency as a function of integrated luminosity in Run 2 [149].
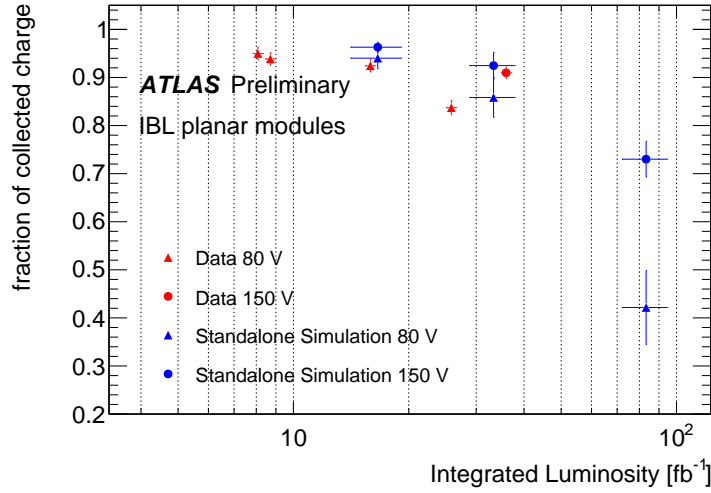
Figure 6.18: The charge collection efficiency as a function of integrated luminosity. (After [149])

Data points are corrected in order to account for the drift in the ToT calibration [150, 151], as it can be seen in Figure 6.19, where the mean and RMS evolution of the ToT for all the IBL modules is shown, as measured in calibration scans. The tuning point was 10 for 16k electrons for 2015 and 8 for 2016.
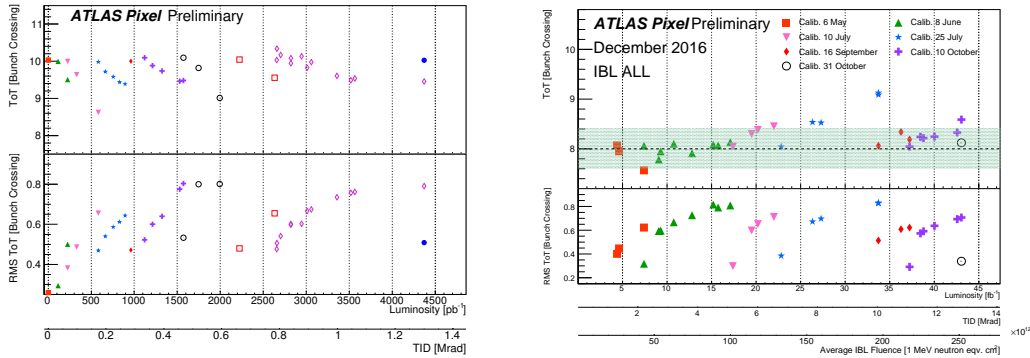
Figure 6.19: The evolution of the mean and RMS of the measured Time-over-Threshold (ToT) over all pixels in the IBL detector as a function of the integrated luminosity and the corresponding total ionizing dose (TID) in 2015 (left) and 2016 (right), as measured in calibration scans. Each color/symbol series corresponds to a single tuning of the detector.(After [150, 151])

Radiation effects are assumed to cause the measured ToT to drift with integrated luminosity, but short periods of annealing and regular re-tunings brought the mean ToT back to the tuning point. The drift is assumed linear between calibration and the correction is evaluated in the middle of the run considered. To this correction is assigned an error of 30 % (which is then propagated to the charge collection efficiency value. MPV value of the fitted Landau distribution are then scaled up or down (accordingly to the direction of the drift). This effect depends run by run, but is in general below 5% with a final error on the measure of ∼ 2/3 %. The error on the predicted value of the charge collection efficiency is evaluated by taking the squared sum of the differences between the nominal value and

the one obtained with the variation of the radiation damage parameters, as explained in detail in Section 6.2.3.5. In addition is also considered a variation of the trapping probability constant of 10% up and down. An error of 3% is also assigned to the luminosity value of the data points (the horizontal error bars in Figure 6.18). Instead, for the Allpix simulation points, the integrated luminosity is converted to a fluence and an error of 15% is assigned to the conversion.

A breakdown of the impact of the systematics variations is reported in Table 6.8.

Table 6.8: List of systematics considered in the errors in the simulation and their relative impact on the nominal value

bias Voltage [V]	80	80	80	150	150	150
fluence	1	2	5	1	2	5
Variation	impact [%]	impact [%]	impact [%]	impact [%]	impact [%]	impact [%]
Energy acceptor +10%	0.42	2.23	0.76	0.21	1.57	1.51
Energy donor +10%	0.55	-	4.46	0.16	0.35	5.67
Energy acceptor −10%	-	1.68	3.77	0.09	0.31	1.60
Energy donor −10%	0.47	0.14	2.91	0.10	0.90	-
η acceptor +10%	0.43	0.33	3.77	0.12	0.87	1.28
η donor +10%	0.25	0.96	4.22	0.14	0.40	5.72
η acceptor −10%	0.27	1.71	13.83	0.06	0.29	1.54
η donor −10%	0.03	0.41	6.82	0.14	0.67	6.87
σ_e acceptor +10%	0.30	1.39	0.88	0.06	0.37	2.36
σ_e donor +10%	0.25	1.01	1.81	0.01	0.38	0.65
σ_e acceptor −10%	0.44	0.33	1.91	0.12	0.84	4.70
σ_e donor −10%	0.13	0.65	0.12	0.11	0.61	5.53
σ_h acceptor +10%	0.34	1.55	1.33	0.12	0.83	2.64
σ_h donor +10%	0.28	0.09	1.41	0.11	0.57	5.04
σ_h acceptor −10%	0.30	1.96	0.95	0.08	0.33	2.17
σ_h donor −10%	0.29	0.55	0.76	0.015	0.32	0.83
trapping constant +10%	0.68	2.25	3.56	1.24	1.10	1.34
trapping constant −10%	0.60	0.10	8.83	0.14	0.37	7.20
total error	2.36	5.20	20.41	1.37	2.98	16.47

Figure 6.18 shows that the level of agreement between data and simulations produced using the new digitizer model is satisfactory for what concerns the charge collection efficiency. As expected, the charge collectionefficiency drops with fluence due to charge trapping.

6.4 Summary and Perspectives

This Chapter presented a digitization model for ATLAS planar sensors that includes radiation damage effects. In addition to describing the physics processes incorporated in the digitizer, the charge collection efficiency is studied using Run 2 data; it shows good agreement between the simulation and the observations. The focus here was on Run 2 and 3 conditions, but the models can be used to make important design decisions for the upgraded ATLAS detector that must survive the harsh HL-LHC radiation environment.

Chapter 7

Pixels Detectors for the new ATLAS Inner Tracker

In this Chapter the Pixel Detector of the new ATLAS Inner Tracker (ITk) of the ATLAS detector will be discussed. It is intended to be ready for the data taking in 2026, in time for the beginning of the High Luminosity phase of the LHC (HL-LHC). The plans for the upgrades of the LHC are presented in Section 7.1, along with the physics case and the list of ATLAS sub detector upgrades for the Phase-II; Section 7.2 will cover the performance and specifications for the new ATLAS ITk. After describing the R&D efforts for ITk pixels detectors in general (Section 7.3), in Section 7.4 results for radiation hard pixel sensors will be presented. The concept of slim edge, already applied to IBL pixel sensors (Section 5.3.2) will be pushed to its limits for the ITk pixels sensors; this topic will be discussed in details in Section 7.5, together with results from beam tests. Finally conclusions and perspectives will be drawn in Section 7.6.

7.1 High Luminosity LHC and the Phase-II of the LHC experiments

The timeline of the CERN LHC is presented in Figure 7.1, together with the future plans. The High Luminosity LHC (HL-LHC) [152] is a project, recently approved [153], to upgrade the existing LHC to a high luminosity machine, capable to deliver an instantaneous luminosity of $L = 7.5 \times 10^{34}/cm^2/s$; as a reminder the design luminosity of LHC is of $L = 1.0 \times 10^{34}/cm^2/s$. After the HL-LHC upgrade completion the data taking is expected to restart in 2026; the goal is to integrate a dataset of 3000 fb^{-1} by 2037; there is an option to extend this program to arrive at 4000 fb^{-1}.

As it can be seen in Figure 7.1 the upgrade plans do not include any increase of the center-of-mass energy $\sqrt{s}$: the main motivation for the HL-LHC project is reducing the error halving time. Indeed, taking data beyond 2023 at the same instantaneous luminosity of Run 3 would imply to take data for more than 15 years to reduce the statistical error by a factor of 2.

The large dataset at the end of the so-called Phase 2 (or Phase-II) for the experiments should enable a large program of precision measurements of the Higgs boson and New Physics (NP) discoveries. As an example of the potential of the HL-LHC dataset, the projected precision on coupling of the Higgs boson to muons is of about 7% with 3000 fb^{-1}; the Higgs trilinear self coupling parameter λ_{HHH} can be probed at about 1 σ significance in the range $-0.8 < \lambda_{HHH}/\lambda_{SM} < 7.7$ (λ_{SM} is the SM predicted value) in the final state
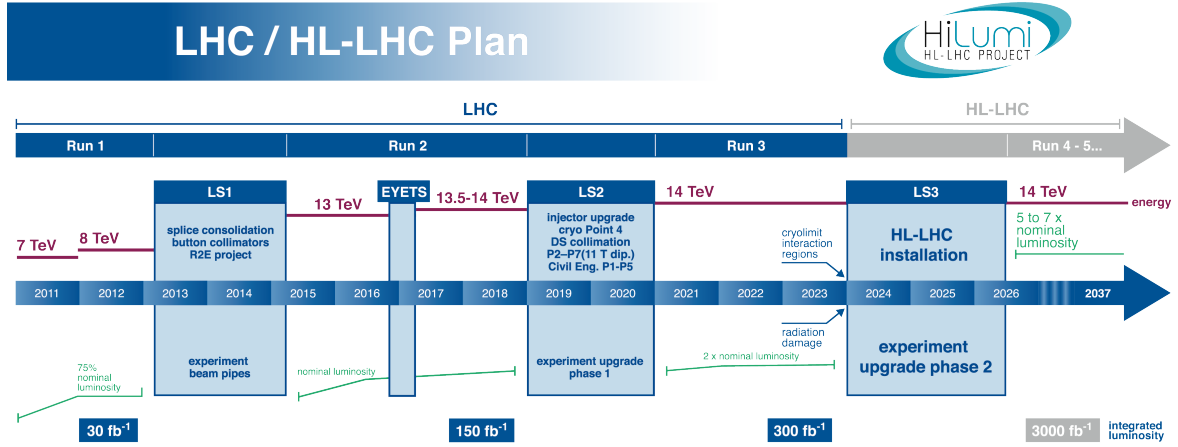
Figure 7.1: LHC/ HL-LHC Plan (last update 22.02.2016, after [152])

HH $\to b\bar{b}\gamma\gamma$ [154]. For what concerns NP potential discoveries, as an example, with the expected HL-LHC dataset the supersymmetric top quark partner $\tilde{t}$ discovery mass range extends up to 480 GeV, and the exclusion one to 700 GeV [155]; for the electroweak SUSY particles a factor of ten increase in luminosity translates into a 30-40% increase in mass reach. Other than SUSY the physics program during the Phase-II of the LHC experiments include searches of vector bosons resonances like W′, Z′, extra dimensions and more [156].

The high luminosity foreseen for the Phase-II implies a much harsher environment than in Run 2 for the ATLAS sub-detectors; indeed high luminosity means higher event rate, more pile-up events and higher radiation doses and fluences. To cope with the severe data taking conditions expected at the HL-LHC it is planned to upgrade the ATLAS detector [156, 157]. Upgrades include:

- a longer latency trigger system, to cope with higher event rates,

- new inner muon barrel trigger chambers, to assure redundancy and improve efficiency,

- upgrading the tile calorimeter electronics, since the actual system will not survive the doses expected by the time of HL-LHC and

- a complete new silicon only tracker, with coverage down to pseudorapidity |η| = 4, the *Inner Tracker* (ITk)

The constraints, requirements, layout and expected performance of the proposed ATLAS ITk will be discussed in the next Section.

7.2 The Quest for a New ATLAS Inner Tracker

The new ATLAS Inner Tracker will have to face unprecedented levels of radiation doses and fluences, pile-up events and events rate. Table 7.1 summarises some of the most important figures.

Within this hostile environment the ITk will have to guarantee the same level of performance or better of the ATLAS Inner Detector (ID). The project is presented in a series

Table 7.1: Environment conditions for the inner detector at the LHC and HL-LHC

Parameter	LHC	HL-LHC
instantaneous luminosity L [cm^{-2}s^{-1}]	1.0×10^{34}	7.5×10^{34}
average number of pile-up events μ	25	200
track rate density for the innermost pixel layer $\mathcal{N}$ [MHz cm^{-2}]	0.25	2
fluence to the innermost pixel layer Φ [1 MeV n_{eq}/cm^2]	5×10^{15}	2×10^{16}
total ionising dose to the innermost pixel layer TID [MRad]	160	1700

of documents, from the "Letter of Intent for the Phase-II Upgrade of the ATLAS Experiment" [156] to the "ATLAS Phase-II Upgrade Scoping Document" [157]. Technical Design Report (TDR) for strip detector of the ITk was recently published [158]; the ITk pixel detector TDR is due by the end of 2017. This Section is built on those documents.

7.2.1 Performance Requirements of the ITk

In what follows a short list of performance requirements of the ITk.

Track Reconstruction Efficiency   The required track reconstruction efficiency in the central part ($|\eta| < 2.7$) has to be above 99% for muons with p_T above 3 GeV/c, above 85% for pions (electrons) with p_T above 1(5) GeV/c. Fake tracks rate has to be kept below 1% to avoid degrading resolution of objects built using tracks, like tracks jets.

Track Resolution and Vertex Reconstrucion   The resolution on transverse momentum will be better than 0.5% up $|\eta| = 1$ for muons of 100 GeV/c p_T and will degrade moderately till $|\eta| = 2$. For $|\eta| \geq 2.7$ the solenoid field diminishes, particularly at low radius, leading to poorer p_T resolution. Resolution on longitudinal (transverse) parameter $d_0(z_0)$ are required to be better than 100 μm in the very central region $|\eta| < 0.5$ for tracks with $p_T = 1$GeV/c and better than 8 (50) μm in the limit of very large transverse momentum.

With 200 pile-up events, the mean separation of primary vertices is typically less than 1 mm. It is therefore not possible for all vertices in a triggered event to be reconstructed individually. However, it is important that high transverse momentum objects (muons, electrons and tracks in high transverse energy jets) coming from a common vertex can all be correctly associated to the same vertex with good efficiency. This requirement corresponds, in the case of $t\bar{t}$ events, to the probability of the $t\bar{t}$ vertex being among the reconstructed vertices having to be greater than 0.95. In addition, the probability that the $t\bar{t}$ decay is associated to the correct reconstructed vertex should be greater than 0.90.

Tracking-reconstruction efficiency and minimisation of multiple scattering effects requirements impose a low material budget. For the ITk, generally it is required to be in total <1 X$_0$ up to $|\eta| \leq 2.7$. In Figure 7.2. The ITk material budget is around 30% lower in the region $|\eta| \leq 4.0$, compared to the Run 2 detector.

7.2.2 ITk detector layout

The ITk will be an all silicon tracker; the main reason for abandoning the TRT is the projected occupancy in its straw tubes, which is about 100% at L = 5.0×10^{34}cm^{-2}s^{-1}. The ITk will consist of an inner detector made of pixel modules and an outer one made of strips. In the central region of the ITk Detector, sensors are arranged in cylinders around
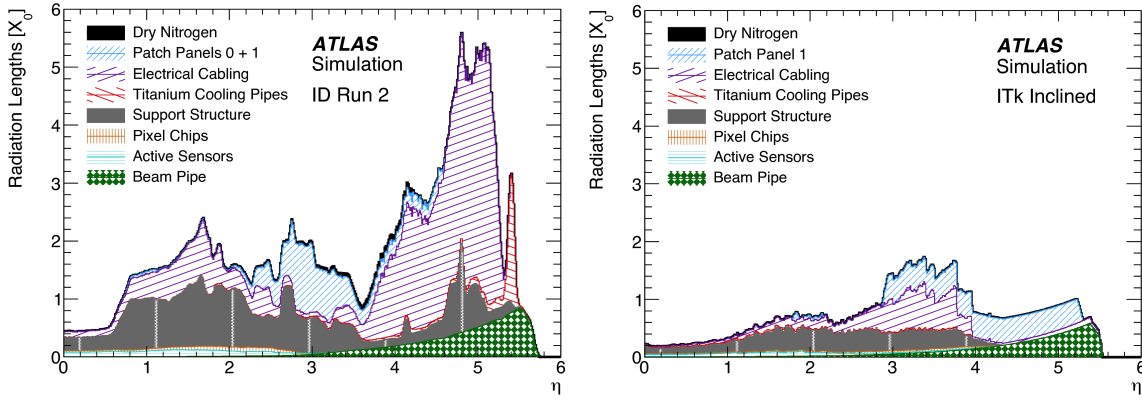
Figure 7.2: Material budget expressed as fraction of radiation lengths as a function of the pseudorapidity. (left) ATLAS ID (right) ATLAS ITk. (After [158])

the beam axis, with (starting from inside) five pixel layers followed by two short-strip layers of paired stereo modules then two long-strip layers of paired stereo modules. The forward regions will be covered by six strip disks and a number of pixel rings leading to one or more hits depending on the ring layer and η position. The proposed ITk layout is presented in Figure 7.3. The new tracker will cover a pseudorapidity range down to $|\eta| = 4$.
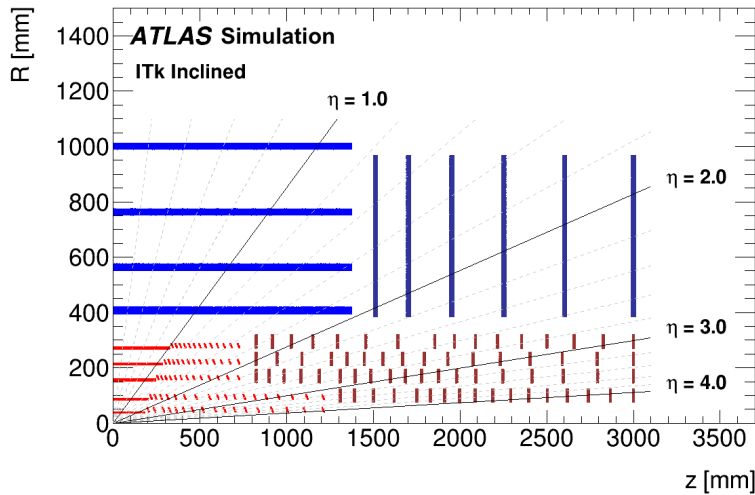
Figure 7.3: Schematic layout of the ITk for the HL-LHC phase of ATLAS. Here only one quadrant and only active detector elements are shown. The horizontal axis is the axis along the beam line with zero being the interaction point. The vertical axis is the radius measured from the interaction point. The outer radius is set by the bore of the solenoid. (After [158])

The peculiarity of the chosen ITk baseline layout, the so called "Inclined" layout, is the presence of inclined sensors in the forward part of the barrel layers; the inclined sensor hangs from long barrel staves. This allows the material traversed by particles at large η to be minimised and at the same time requires less silicon surface to cover the full η range. In addition, these inclined sensors provide two or more hits in the first layer, providing redundancy for the local track finding close to the interaction point even at large pseudorapidity. One possible support design of the Inclined layout is called ALPINE; a detail of the ALPINE stave prototype is shown in Figure 7.4. The sensor modules are located on the stave face closer to the interaction point so that incoming particles are detected by a pixel sensor before crossing the inactive material (local support structure, cooling tubes and electrical services).
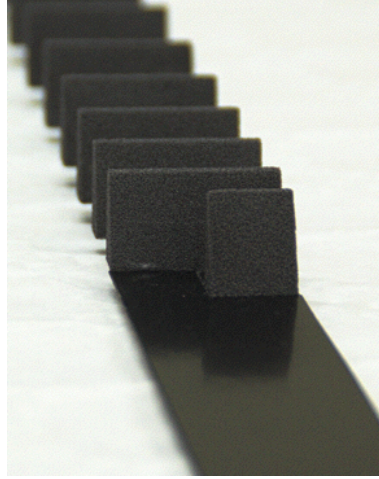
Figure 7.4: ALPINE design for the inclined layout (After [158])

7.3   Pixels Detectors for ITK

The innermost pixel barrel layer, Layer 0, of the ITk will be at a radius of 40 mm from the interaction point; the Layer 1 at 85 mm. Layer 2, 3 and 4 will be placed respectively at 155, 213 and 271 mm from the beam axis. The expected fluences for the ITk are reported in Figure 7.5.
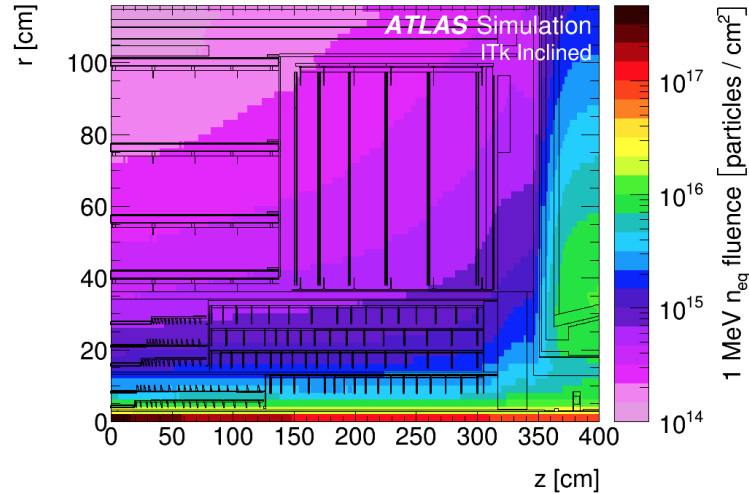
Figure 7.5: The 1 MeV neutron equivalent fluence for the ITk layout (After [158])

The maximum fluence predicted for the Layer 0 at the end of the Phase-II program is about 1.5-2×10^{16} n_{eq}/cm^2; for the pixel end-cap the largest fluence will be of about 5×10^{15} n_{eq}/cm^2, similar to what it is expected for the Layer 1 of the barrel section.

Pixels will have a smaller pitch than today ATLAS pixel and IBL detectors; this is mandatory to keep the occupancy below 1%, in order to assure a good two particle separation and limit dead time. The proposed ITk layouts are designed to meet this requirement, thus the pixel pitches are dictated by this constraint. Moreover physics and performance simulations indicated that 50 μm × 50 μm pitch pixels, or 25 μm × 100 μm are suited (the smaller pitch is to achieve better momentum resolution). Small pixel cells imply also less leakage current fed into and small capacitance coupled to the front end electronics, hence less noise.

The basic unit of the ITk pixel detector is a module. The baseline module concept for the ITk pixel detector is the well proven hybrid pixel detector in which modules are composed of a sensor and the read-out chip (ROIC) bump bonded to each other on a pixel level. In addition other concepts are also investigated such as monolithic CMOS pixel detectors, especially for the outer layers.

The choice of sensors depends mainly on the requirement that the detector has to withstand the integration of an expected dataset of $3000 \, \text{fb}^{-1}$. This is particularly challenging for the innermost layer, which after the high-luminosity running will have integrated, as it was said above, an estimated fluence Φ of $1.5\text{-}2 \times 10^{16} \, \text{n}_{\text{eq}}/\text{cm}^2$ for the innermost pixel layer.

There will be two main types of modules: dual-modules (two chips bump bonded to a sensor, around $4 \times 2 \, \text{cm}^2$) for the the innermost layer to accommodate the limited space, quad-modules (four chips bump bonded to a sensor, around $4 \times 4 \, \text{cm}^2$ for the outer layers and in the rings. The pixel read-out chip is presently under development within the RD53 collaboration [159], which will produce an RD53 prototype chip. Following this chip an ATLAS ITk pixel chip will be developed using the basic blocks designed by RD53 while integrating additional functionality to meet ATLAS specifications.

At this stage three possible sensor types are considered for the pixels modules:

- planar sensors, for an hybrid detector

- 3D sensors, again for an hybrid detector,

- monolithic CMOS sensors

3D sensors   3D silicon detectors are candidates to be used for the inner most layer(s) of the barrel pixel system and some of the inner end-cap rings due to their excellent radiation hardness at low operational voltages and moderate temperature with low power dissipation compared to planar sensors. The 3D sensors will be produced on either 4" or 6" high resistivity $p-$type wafers. The total thickness of the sensors will be 200 μm, and and the active thickness[1] will be between 150 and 200 μm, with 150 μm being the baseline. The 3D sensors shall be produced by etching the $p-$ and $n-$columns from the same side (single side process). At the moment the pixel geometry will have a single readout column in the centre of the pixel (1E), surrounded by four ohmic columns. Figure 7.6 shows the proposed design of the pixel cell for the ITk 3D pixel modules.

The column diameter will be ≤ 8 μm, while the depth of the junction (ohmic) columns will be slightly shorter (longer) than the nominal 150 μm active thickness. Thus ohmic columns will be in contact with the sensor backside, while junction columns termination will be away from it, to avoid too early junction break down.

IBL-generation 3D pixel detectors coupled to FE-I4 pixel electronics have been found to have hit efficiencies in test beam measurements larger than 97% at 170 V after irradiation to Φ of $1.0 \times 10^{16} \, \text{n}_{\text{eq}}/\text{cm}^2$ for normally incident minimum ionizing particles with a power dissipation of 15 mW/cm^2 at a temperature of -25° C [160].

Planar sensors   In this Paragraph only a short description of the planar sensors specification and performance for the ITk will be given as they will be discussed more in depth in the next two Sections. A new generation of planar pixel sensors are under development

---

[1]sensors can be realised in thin high resistivity wafers bonded to thick low resistivity ones; at the end of the fabrication process the latter can be lapped, completely or not. This approach is used to realise thin planar sensors too
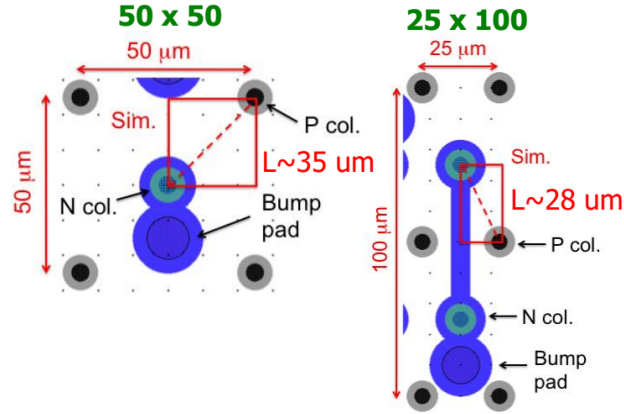
Figure 7.6: Design of 3D pixel cells with 50 μm × 50 μm and 25 μm × 100 μm pitch pixels. (After [158])

for the ATLAS ITk pixel system. The main differences with respect to the planar sensors implemented in the present detector are the different electrode arrangement ($n - on - p$ versus the traditional $n - on - n$) and the reduced thickness in the range of 100-150 μm with respect to the 200 μm for the sensors used in IBL and 250 μm in the three outer ATLAS pixel layers.

The $n - on - p$ technology allows for cost reduction given the single side processing and the reduced complexity in handling and testing. The guard ring structure is implemented on the front side, leaving the edges of the sensor at a potential close to the one of the backside. This arrangement potentially induces the risk of electrical sparks between the sensor periphery and the chip. Isolation techniques, like the deposition of a layer of Benzocyclobutene (BCB) on the sensor surface at wafer level or of parylene after module assembly have been successfully employed to prevent this problem [161, 162].

Monolithic CMOS sensors   Recent developments of CMOS pixel detectors, originally designed for charge collection in an epitaxial layer of 10-20 μm thickness, use new approaches to cope with the rate and radiation environment expected at the HL-LHC [163–165] based on the following enabling technology features: HV add-ons that allow to use high depletion voltages; high resistivity wafers for large depletion depths; radiation hard processed with multiple nested wells to allow CMOS electronics embedded with sufficient shielding into the sensor substrate; and backside processing and thinning for material minimisation and backside voltage application.

A typical CMOS sensor pixel cell with sensing substrate and a CMOS electronics layer embedded in multiple cells is shown in Figure 7.7.

Since 2014 a demonstrator programme is carried on, to prove DMAPS that are suited for high rate and high radiation operation at LHC. For this a number of technologies have been explored and characterised (AMS 350 nm and 180 nm, Global Foundry 130 nm, ES-PROS 150 nm, LFoundry 130nm, TowerJazz 180nm, etc.); the designs have been characterised as stand-alone sensors as well as bonded to the FE-I4 pixel chip (as a hybrid) either via bump bonds or via glue bonding (capacitively coupled pixel detector, CCPD).

The results within the demonstrator programme can be summarised as follows:

- Technologies complying with the above list of enabling technology are principally suited to fabricate depleted monolithic sensors that can cope with the HL-LHC run-
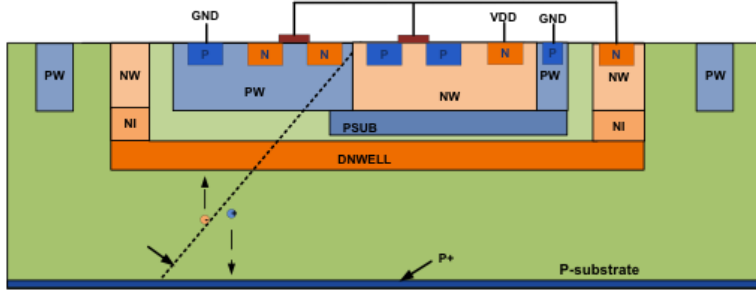
Figure 7.7: DMAPS schematic showing fully or partially depleted bulk, multiple nested wells for CMOS electronics and charge collection node. (After [158])

ning condition, at least at distances larger than 20-25 cm away from the interaction point (outer layers).

- DMAPS pixel sensors detect mips with integrated efficiencies above 98% and with spatial resolutions similar to those as hybrid pixels

- DMAPS pixel sensors can stand radiation fluences of more than 1.0×10^{15} n_{eq}/cm^2 when properly designed. This is demonstrated in Figure 7.8 showing the collection width obtained after irradiation to a neutron fluence of 8.0×10^{15} n_{eq}/cm^2 determined using edge TCT measurements [166, 167].

- Beam test measurements have shown high rate capability as detectors bonded to the FE-I4 chip.

- Fully monolithic DMAPS pixel sensors have been designed incorporating read-out architectures suitable to cope with the expected rates at the HL-LHC (such as column-drain architectures and direct hit transfer architectures). Such designs have been submitted for fabrication in 2016 and are currently being evaluated.
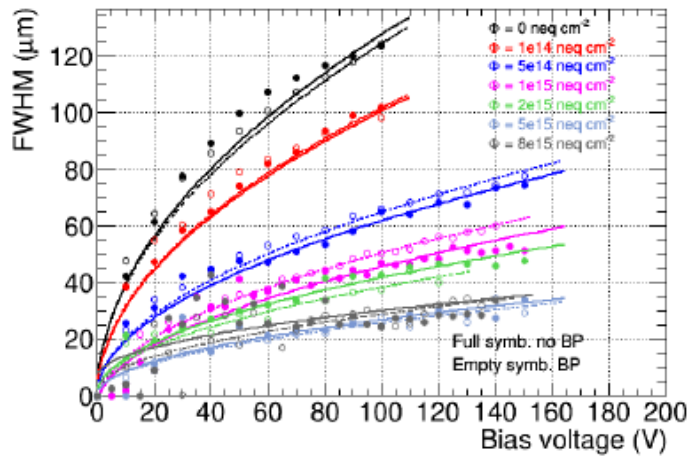
Figure 7.8: FWHM of the charge collection profile measures using the edge TCT technique as a function of bias voltage after different irradiation fluences up to 8.0×10^{15} n_{eq}/cm^2 for un-thinned detector (700 μm thick) without back plane (full symbols) and 300 μm sample with back plane (empty symbols). (After [166])

7.4   Radiation Hard Planar Pixel Sensors

The ATLAS Upgrade Planar Pixel Sensor (PPS) R&D Project [168] carried out the optimisation of the well-known technology of planar silicon pixel sensors for the Phase-II of the ATLAS experiment. The PPS R&D project existed from 2009 to 2014 and investigated the radiation hardness of pixels sensors realised in planar technology. The main research directions were: optimisation of the $n-$bulk material; exploration of $p-$bulk sensors; reduction of thickness; novel biasing structures. Reduction of the dead are at the detector periphery was investigated too, and it will be discussed in the next Section. These efforts continued then within the ITk pixel forming collaboration.

In what follows some results from the PPS activities.

7.4.1   Radiation hardness of $n-on-n$ FE-I3 samples.

In [6, 169] examples of the searches within the PPS group are reported. Using pixel modules based on the ATLAS Pixel FE-I3 readout chip the charge collection efficiency (CCE) of $n-on-n$ modules was tested up to fluences Φ=2.0×10^{16} n_{eq}/cm^2. Table 7.2 summarizes the fluences to which the sensors were irradiated.

Table 7.2: Summary of irradiated $n-on-n$ samples in the beam tests. KIT stands for 25 MeV energy proton irradiation; reactor neutrons for the TRIGA reactor [170].

name	thickness (µm)	fluence (10^{15} n_{eq}/cm^2)	irradiation type
DO6	285	0	–
DO7	250	1	protons (KIT)
DO8	250	1	reactor neutrons
DO9	250	5	reactor neutrons
DO10	250	20	reactor neutrons

These modules have been evaluated in several beam tests in 2009 and 2010. Data presented in [6] were taken in two different periods in 2010 at the CERN SPS beamline H6; in both periods pion beams of 120 GeV/c were used. Measurements on samples have been carried out at temperatures well below 0° C to reduce the large leakage current from irradiated sensors. As an example, we measured a leakage current of 24 µA (10 µA) for DO10 (DO9), at a bias voltage of 1200 V and at -47° C.

Hit Efficiency   Hit efficiency was studied as a function of the bias voltage, for the module irradiated with $5 \times 10^{15} n_{eq}/cm^2$. Results are in Table 7.3.

Table 7.3: Hit efficiency of an irradiated (fluence = $5 \times 10^{15} n_{eq}/cm^2$) FEI3 $n-on-n$ 200 µm thick module at different bias voltages.

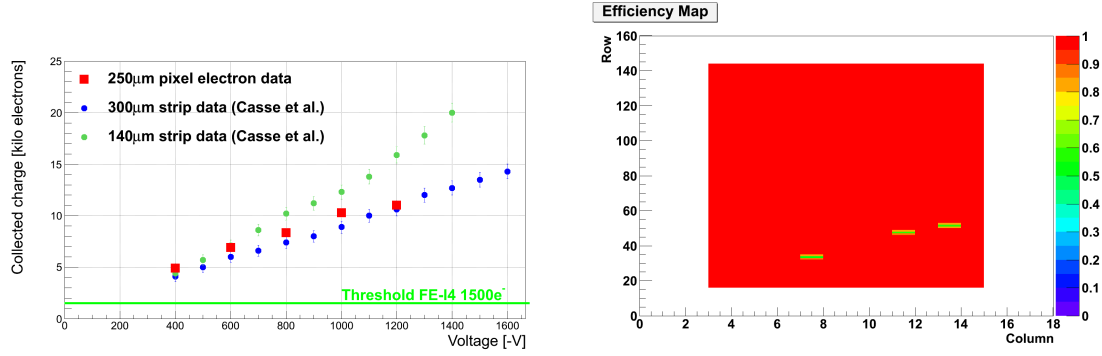| Bias voltage (V)	Hit efficiency (%)
350	93.2
500	97.3
1000	99.6

Figure 7.9: left: Collected charge as a function of the bias for sensors irradiated with fluence of $5 \times 10^{15} n_{eq}/cm^2$; right: Hit efficiency map for the same assembly

In Figure 7.9, on the left, a study of the collected charge vs bias voltage for a module irradiated with a fluence of $5 \times 10^{15} n_{eq}/cm^2$ is shown[2] (only data collected with the ^{90}Sr source are shown). In the figure the expected threshold for the FE-I4 chip is shown too. A signal of about 10 ke$^-$ is observed at 1000 V. This was very promising for the ATLAS IBL [45], and the outer pixel layers at HL-LHC.

In Figure 7.9, on the right, the hit-efficiency map for the module irradiated with a fluence of $5 \times 10^{15} n_{eq}/cm^2$, as measured at the beam test for particles at normal incidence. The pixel module was biased at 1000 V and the hit-efficiency was 99.6%.

Charge Collection Efficiency   One of the main effects of irradiation is the increased trapping, which leads to a reduced signal amplitude. As the trapping probability depends on the charge carrier velocity, the collected charge was measured as a function of the bias voltage. Figure 7.10 shows the results for all irradiated $n-on-n$ samples in the two beam test periods; see also Table 7.2. A systematic error on the collected charge of 400 e is assumed, due to the finite charge resolution of the ToT mechanism; a 5% systematic uncertainty is also taken into account, due to non-uniformity in the injection capacitances.
After 5×10^{15} n$_{eq}$/cm^2, the collected charge still exceeds 10 ke at a bias voltage of 1000 V. Even if the collected charge is shared equally between two neighboring pixels, this charge is sufficient to detect the hit with FE-I3.

Figure 7.11 top, shows that charge is predominantly lost in the region of the punch-through bias grid system.

At very high fluences (2×10^{16} n$_{eq}$/cm^2, DO10 sample) it is no longer possible to say which region is less efficient than the others, using the charge collection method (Figure 7.11, bottom).

Charge Sharing Probability   To calculate the charge sharing probability for each hit within a cluster, it is determined whether a hit is found in a pixel cell adjacent to the one matched to a track. This probability increases towards the edge of the pixel since charge carriers are more likely to drift to the neighbouring pixel. The corresponding plot, referred to as a charge sharing map, is centred on one pixel, also showing half of the adjacent pixel in each direction. The overall charge sharing is defined as the number of tracks with at least one hit in a neighbouring pixel divided by the number of all tracks.

Figure 7.12 shows the charge sharing probability for DO9 at a bias voltage of 1200 V. Reduced charge sharing probability is visible in the region of the bias dot and the bias

---

[2]as a comparison data from strip detectors [171] are reported too.
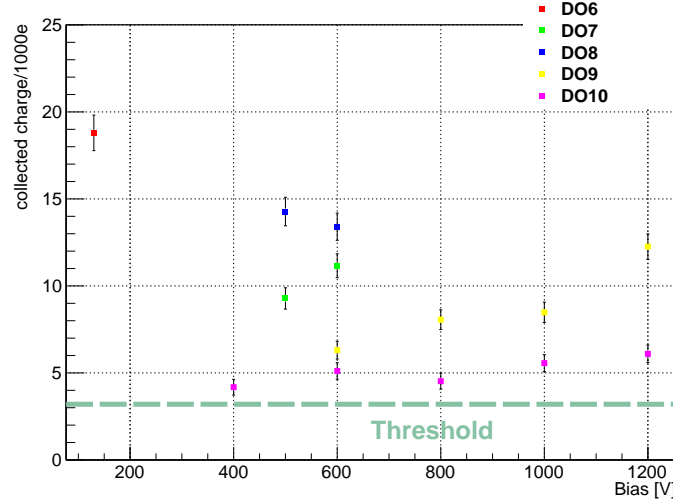
Figure 7.10: Collected charge as a function of bias voltage for $n-on-n$ samples irradiated to different fluences (see details in the text). A threshold of 3200 e is indicated.
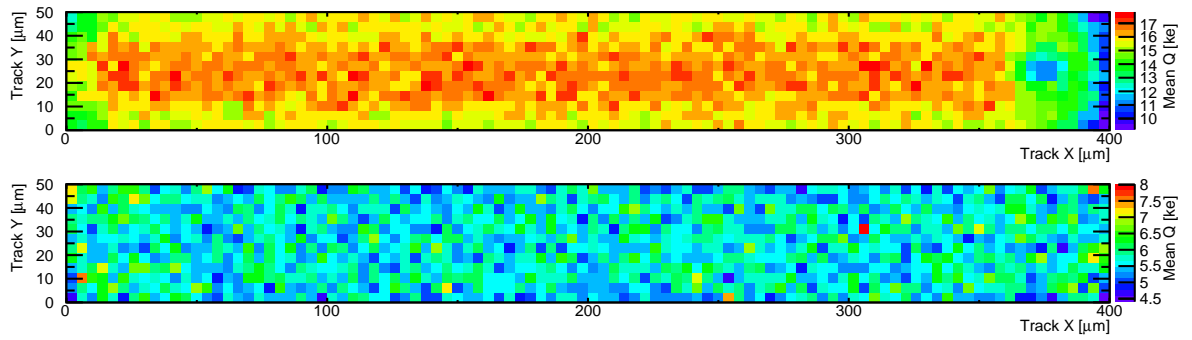
Figure 7.11: Charge collection within a pixel. Top: DO9 at V_{bias}=1200 V. Bottom: DO10 at V_{bias}=1000 V.

grid network.[3] Less charge is deposited here, so there is a higher probability for the second pixel in a two-pixel cluster to be below threshold. As only the bias trace makes the difference between both pixel sides, it might cause the lower charge sharing probability. Furthermore, one can see that the region of the bias dot is not affected.

While for DO9 a clear increase in charge sharing probability towards the edges of the pixel is visible, at higher fluence the collected charge becomes too small for any significant charge sharing to be observable.

Residuals   To estimate the intrinsic spatial resolution of the devices under test (DUTs), the distribution of hit residuals was studied. The intrinsic spatial resolution was estimated by the RMS of the residual distribution for clusters of all sizes, while the residual distribution of 2-pixel clusters is used to estimate the width of the area between pixels, where charge sharing occurs. The distribution is fitted with the sum of two Gaussian functions, where one accounts for misreconstructed hits, resulting in large residual values (equal to 2 times the pixel pitch or more), and the other for correctly reconstructed hits. The width

---

[3]The bias grid network is an aluminum trace arranged on top of the intermediate pixel region connecting all bias dots.
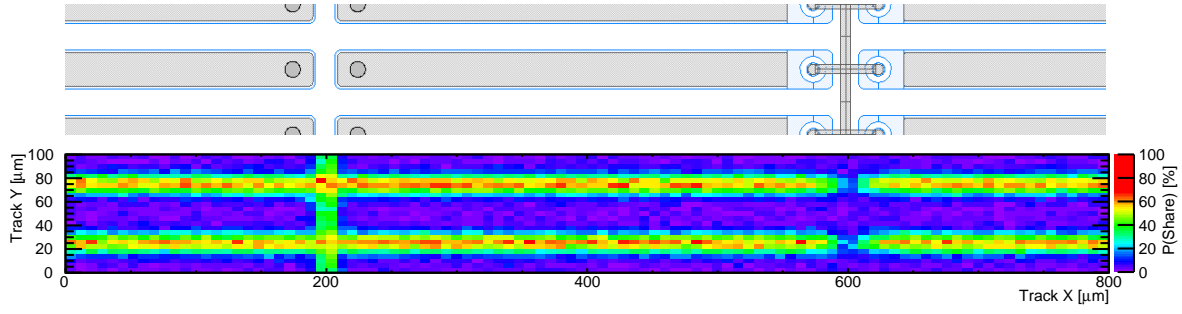
Figure 7.12: Top: Design of the sample of the region shown in the plot below. Bottom: Charge sharing probability for DO9 at V$_{bias}$=1200V. Note the reduced charge sharing in the bias grid region on the right-hand side of the central pixel.

of this "core" Gaussian gives the width of the charge sharing region.

Figure 7.13 shows the residual distributions in the 50 μm pixel direction for the unirradiated sample (DO6) and the sample irradiated to 2×10^{16} n$_{eq}$/cm^2, respectively. The widths of the distributions are 16 μm and 15.4 μm, comparable with the expected digital resolution of 14.4 μm. Thus, no influence of radiation damage on the spatial resolution can be observed.
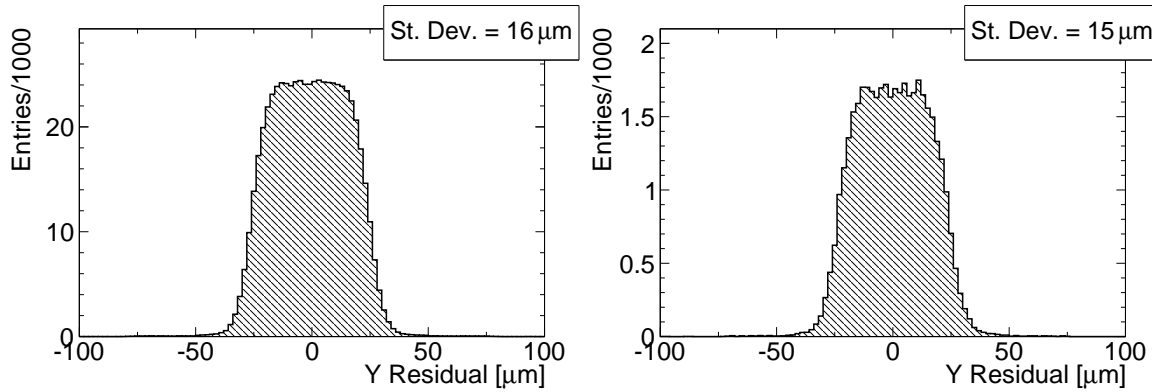
Figure 7.13: Residual distributions in the short pixel direction for an unirradiated sample (DO6, left) and a sample irradiated to 2×10^{16} n$_{eq}$/cm^2 operated at a bias voltage of 1000 V (DO10, right). No deterioration of the spatial distribution with irradiation is visible.

Plotting the residual distribution for two-pixel clusters only allows the width of the charge sharing region between pixels to be determined. Figure 7.14 shows the distributions for DO9 (5×10^{15} n$_{eq}$/cm^2) and DO10 (2×10^{16} n$_{eq}$/cm^2). After correcting for the telescope resolution, the widths of the charge sharing regions are 7.1 μm and 7.7 μm. These values correspond very well with the width found for an unirradiated sample of 6.4 μm. This indicates that the lateral diffusion of the charge cloud does not change significantly with irradiation.

Comments The radiation hardness of $n-$bulk sensors was tested up to unprecedented fluences, with a maximum of 20×10^{15} n$_{eq}$/cm^2. At a bias voltage of 1.2 kV a collected charge of about 6 ke was observed, corresponding to about one third of the collected charge before irradiation. A much thinner detector should be able to collect a much larger fraction of charge at a bias voltage lower than 1000 V. Despite the rather small collected
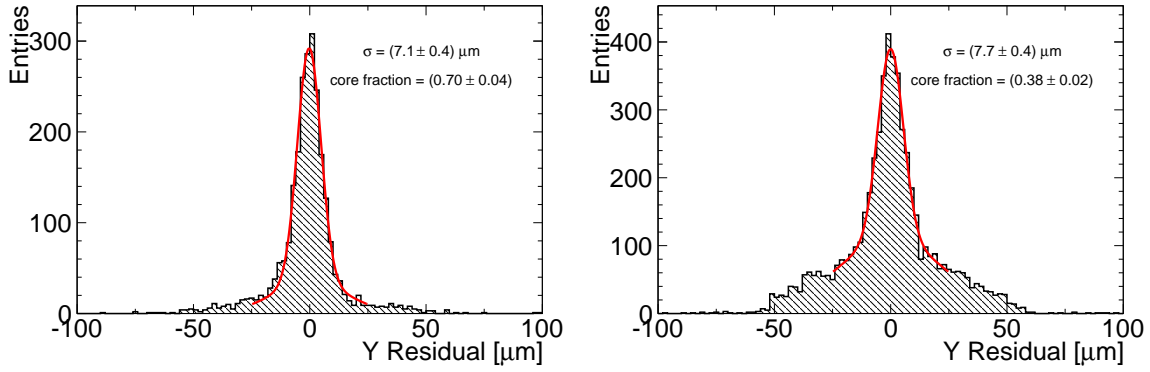
Figure 7.14: Residual distributions for 2-pixel clusters only. Shown are distributions samples irradiated to $5 \times 10^{15}\,\mathrm{n_{eq}/cm^2}$ (left: DO9, bias voltage 1000 V) and $2 \times 10^{16}\,\mathrm{n_{eq}/cm^2}$ (right, DO10, bias voltage 1200 V), respectively.

charge and the reduced charge sharing between pixels, no significant deterioration of the spatial resolution was observed. Important charge losses were observed in proximity of the punch-through dot used for biasing the sensor.

7.4.2 Thin $n-on-p$ FE-I4 samples.

While $n-$type bulk sensors require patterned guard rings on the back side of the sensor, for $p-$type material these can be moved to the pixelated side of the sensor (front side); then metallisation is the only process for the back side. This makes it a very cost-effective material for future pixel detectors.

Thin $n-on-p$ planar pixel sensors have been realised at FBK[4] on high resistivity type 6" wafers within the framework of the INFN Phase-2 program [172]. Si-Si Direct Wafer Bonded (DWB) wafers were chosen to fabricate pixel detectors; Si-Si DWB are obtained bonding together two different wafers: a high-resistivity (HR) Float Zone sensor wafer and a low-resistivity (LR) Czochralski handle wafer. The FZ wafer is thinned to the desired thickness value, so as to obtain a wafer with a thin active layer plus a relatively thick mechanical support layer. P-type wafers of two different active depths (100 and 130 μm) with 500 μm thick handle wafer were used. In Figure 7.15 a picture of one wafer from this production.

7.4.2.1 Beam test studies

Radiation hardness of that production was tested using irradiated pixel sensors compatible with the FE-I4 [126] readout chip. Two sensors, *W80* and *W30*, were taken from two different sensor wafers, with thickness of 130 (100) μm for W80 (W30); and had different number of GRs, 2 and 5, respectively. In both detector assemblies the 500 μm thick handle wafer was not thinned.

Irradiations were carried at CERN PS using the 24 GeV/c proton beam. The irradiation was staged; in Table 7.4 the detail of the irradiation program for the two modules tested from that production, W80 and W30, along with their characteristics.

---

[4]FBK-CMM (Trento, Italy): http://cmm.fbk.eu/
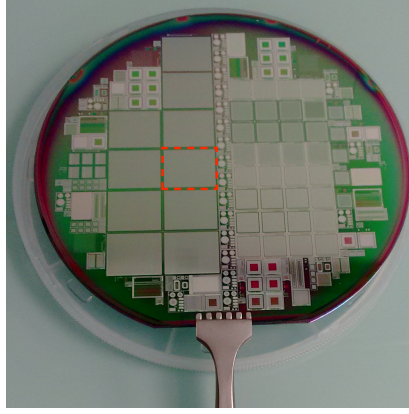
Figure 7.15: Wafer from the $n-on-p$ planar technology production [172] whose layout was mainly based on ATLAS FEI4 and CMS PSI46 designs. The red rectangle encircles one pixel sensors compatible with the FE-I4 [126] readout chip.

Table 7.4: Irradiation program for the two FE-I4 pixel modules W80 and W30.

Module name (thickness [µm], # of GRs)	Beam spot size (FWHM - [mm^2])	Fluence φ [10^{15} n$_{eq}$/cm^2]	Cumulative fluence at peak Φ [10^{15} n$_{eq}$/cm^2]
W80 (130, 2)	20×20	3	same
W30 (100, 5)	12×12	4	same
W80 (130, 2)	20×20	7	10
W30 (100, 5)	20×20	7	11

The sensors were indeed bump bonded to an FE-I4 chip at IZM, Berlin[5] and measured on beam before and after irradiation. In Figure 7.16 some pictures of the pixel modules on PCB are shown.
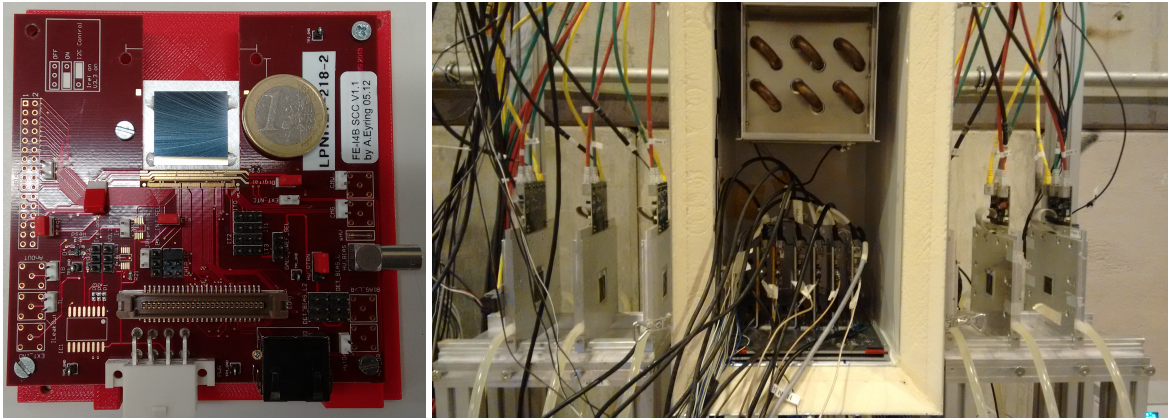
Figure 7.16: Thin $n-on-p$ planar pixel sensor modules. (left) Module mounted on a PCB card. (right) Module inside the DUT cooling box at the CERN H6 beamline; W80 is the second module from the left; outside of the box the six planes of the ACONITE telescope [173].

The modules were tested on beam after each irradiation step at CERN H6 beam line (120 GeV/c pions) and at DESY T21 beam line (4 GeV/c electrons). In both cases tracks were reconstructed thanks to a EUDET-type beam telescope [173], composed of six pixel

---

detector planes equipped with fine-pitch MIMOSA 26 sensors [75]. The DUTs where mounted inside a box that shed them from light and kept them cold (~-35°C).
In what follows some results are presented for hit and charge collection efficiency [174, 175].

Hit Efficiency   Hit efficiency were tested as a function of the bias voltage for both W80 and W30 after each irradiation step. In Figure 7.17 the hit efficiency of W80 is reported after each irradiation step.
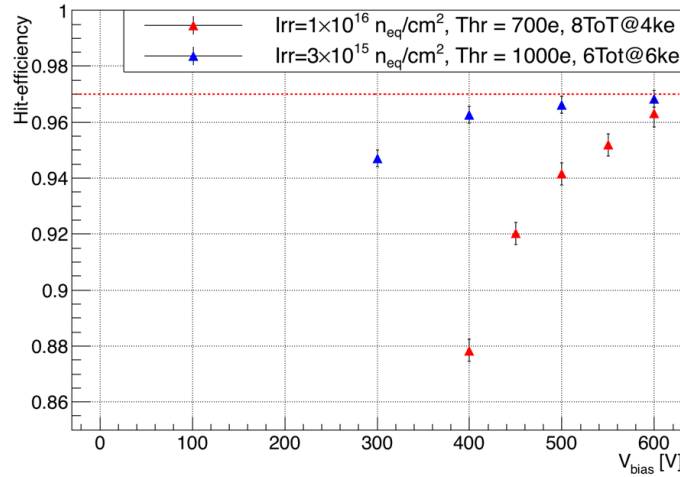
Figure 7.17: Hit efficiency as a function of the bias voltage for the W80 module after each irradiation step.The fluence, the threshold and the tuning are indicated. The red dashed line indicate the 97% hit efficiency.

For the lower fluence the module hit efficiency is 97% or more for bias voltages larger than 500 V. This result is good but somewhat below the expectations as the detector is only 130 μm thick and the fluences not so large (3×10^{15} n_{eq}/cm^2). One possible explanation for this not so large hit efficiency is the threshold: 1000 e was probably too high for such detector.

After a fluence of $\Phi = 1 \times 10^{16}$ n_{eq}/cm^2 the W80 module efficiency is close to 97% at a bias voltage of 600 V for a threshold of 700 e (the signal amplitude for a MIP in an unirradiated module of the same thickness is about 8000 e). This result is very promising and it meets the specifications for the Layer 1 of the ITk pixel detector.

The hit efficiency within the pixel cell was investigated too. In Figure 7.18 the result for W80 after the first irradiation step. It can be seen that there are inefficient regions at the short sides of the pixel cell. This is consistent with the presence of permanent biasing structures like the n^+ bias dot implant and the bias rail shorting the bias dots together.

Charge Collection Efficiency   The charge collection efficiency was studied for the W30 module after the irradiation. The cluster charge distribution, measured in Time-over-Threshold bins of 25 ns [126] was fitted with a Landau function convoluted with a Gaussian. In Figure 7.19 the comparison of the cluster charge distribution for the W30 module before and after the first irradiation step, at 100 V and 600 V bias voltage respectively.

Both before and after irradiation the module was tuned always with a threshold of 1000 e and 6 ToT corresponded to 6000e. It can be seen that after the irradiation the most probable value (MPV) of the distribution is reduced by about 33%, going from 9 to 6.
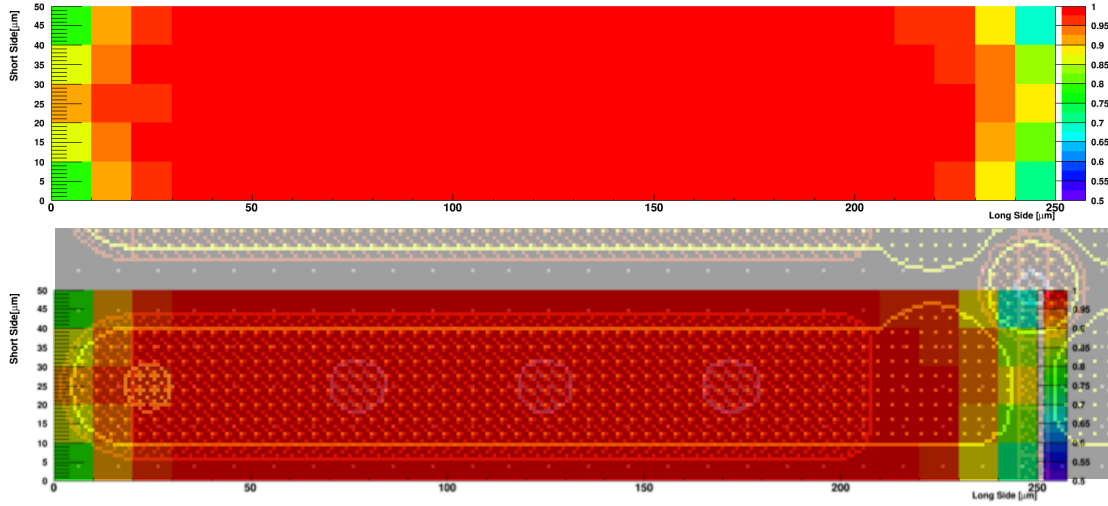
Figure 7.18: (top) Hit efficiency within a pixel of the W80 module after the first irradiation step. (bottom) The pixel cell layout is superimposed.
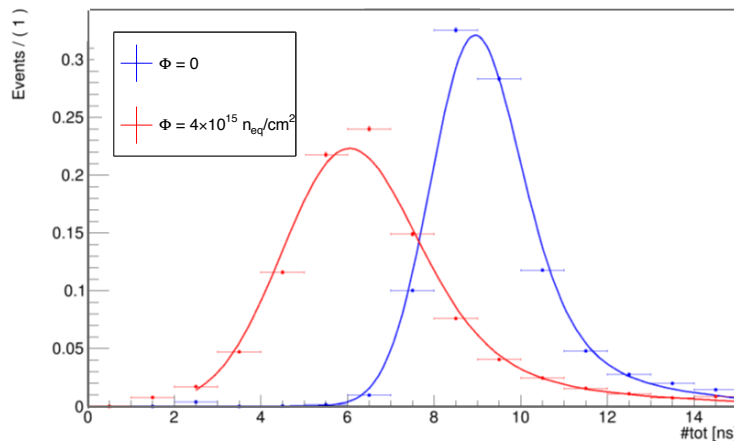
Figure 7.19: Cluster charge distribution, measured in ToT, for the W30 module before and after the first irradiation step; the bias voltages were 100 V and 600 V, respectively.

In Figure 7.20 the cluster charge distribution for the for the W80 module after the second irradiation step, *i.e.* after a total fluence of 1×16 n_{eq}/cm^2, at different bias voltages.
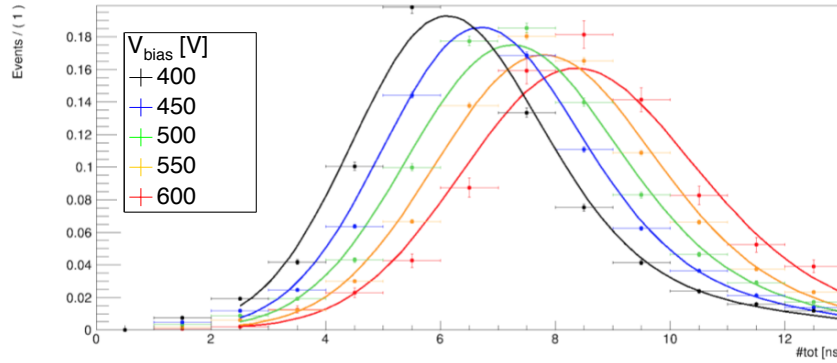
Figure 7.20: Cluster charge distribution, measured in ToT, for the W80 module after the second irradiation step.

The module was tuned always with a threshold of 700 e and 8 ToT corresponded to 4000e. The MPV of the cluster charge in ToT increases from ~6 to ~9 as the bias voltage changes from 400 to 600 V.

A crude estimation of the loss in the amount of collected charge can be made comparing Figures 7.19 and 7.20. At 600 V, after a fluence of 1×16 n_{eq}/cm^2, the 130 µm thick W80 detector collects about half of the charge it was collecting before irradiation.

Comments   Thin planar detectors are envisaged for the ITk pixel detector. The results reported here for 130 µm thick $n - on - p$ pixel modules are very promising since they exhibit an hit efficiency close to 97% at a bias voltage of 600 V after a fluence of 1.0×10^{16} n_{eq}/cm^2; the charge collected is half of the original one before irradiation. The tested modules were just prototypes that used the existing FE-I4 readout chip. New thin pixels sensors prototypes, compatible with the RD53A chip are in preparation; thanks to new readout chip, which should have the possibility to get lower in threshold, it should be possible to recover full hit efficiency even at bias voltages lower than 600 V.

7.5   Edgeless $n - on - p$ Planar Pixel Sensors

ITk pixel sensors, other than meeting radiation hardness specifications, have to assure highest possible geometrical acceptance, being "active" almost till the physical detector edge. In what follows edgeless sensors using the active technology will be discussed. In particular the results from the joint LPNHE-FBK active edge planar pixel sensors production will be presented. They are documented in a series of documents which will be referred to.

7.5.1   Edgeless Pixel Sensors and the Active Edge Technology

As for the IBL (see Section 5.3.2) for the ITk pixel barrel layers too there will be no space for module tiling in the z (beam) direction. So the fractions of inactive regions have to be kept low by having larger pixels at the edge and in the regions between chips, and by minimising the edge region while still preventing voltage breakdown. The ITk specifications

indicate that the distance from the active region to the cut edge of pixel modules has to be smaller than 100 μm [158] in all pixel layers and rings.

The 3D sensor technology inherently allows for slim edges of 15-150 μm [176] Planar sensors can adopt slim edge designs, as it was done for the IBL pixels sensors, or an edge-less design, through the "active edge" technology.

The active edge is one of the possible choices to realize "edgeless" detectors, *i.e.* detectors with no (or very limited) insensitive area. Along the sensor border a trench is dug by deep reactive ion etch (DRIE), reaching through the whole thickness of the substrate (hence a support wafer is required). The trench is then doped with boron (for $p-$type bulks) and filled with polysilicon. The cut realized through DRIE produces an edge region much less damaged than the one resulting from a standard diamond-saw cut. This leads to less generation centers hence lower leakage current generated at the border. Moreover, the edge doping prevents the depletion region from reaching the physical trench walls, hence carriers created at the edge do not experience an electric field, are not effectively separated and just recombine, without contributing significantly to the device leakage current. Active edge technology can routinely obtain very uniform, well defined and narrow trenches, as shown for example in Figure 7.21. For a 200 μm thick bulk the typical trench width is of 5 μm.
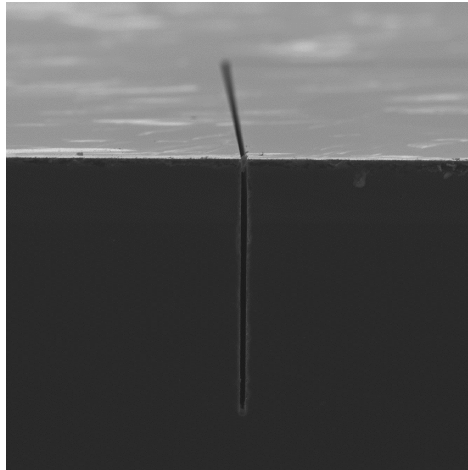
Figure 7.21: SEM picture of a test trench, after cleaving the wafer perpendicularly to the surface and to the trench itself.(After [7])

7.5.2   Joint LPNHE-FBK Active Edge Planar Pixel Sensors Production

The active edge technology was chosen by LPNHE [6] for a planar pixel production with reduced inactive zone [7]. The production, composed of 200 μm thick $n-on-p$ sensors, was realised at FBK[7].

7.5.2.1   The Active Edge Sensor Fabrication at FBK

Since the trench extends all the way through the sensor wafer thickness, the support wafer has to be bonded to the sensor one before starting the etching step. Given the presence of

---

[6]Laboratoire de Physique Nucleaire et de Hautes Énergies (LPNHE), Paris, France; `http://lpnhe.in2p3.fr/`

[7]FBK-CMM (Trento, Italy): `http://cmm.fbk.eu/`

the support wafer accessing the backside after wafer-bonding is impossible. Thus, as first process steps, a uniform high-dose boron implant has been performed on the back side, followed by a thermal oxide growth on both sides.

Up to the trench definition, the process follows standard steps. Since the read-out electrodes are n-type, they will be shorted together by the electron inversion layer, induced by the positive fixed charge present in the oxide, unless a p-type implant, compensating such charge, surrounds the pixels. Both homogeneous ("p-spray") and patterned ("p-stop") implants have been used; the process splittings adopted in the fabrication batch only concern the presence and the doses of these implants, as detailed in Table 7.5.

Table 7.5: List of the different isolation solutions adopted in the process.

p-spray	p-stop
low dose	absent
high dose	absent
low dose	present
high dose	present
absent	present

Two patterned high dose implants, a phosphorus implant forming the pixel and GR junctions and a boron implant for the ohmic contact to the substrate ("bias tab"), are then performed.

The etching of the trench is accomplished by a Deep Reactive Ion Etching (DRIE) machine, the same used for the fabrication of 3D detectors [177]. The trenches in an active edge sensor must be fully passing, *i.e.* their bottom has to reach the silicon oxide, which separates the active wafer from the support wafer.

After the trench is etched, its walls are boron-doped in a diffusion furnace. Thus, a continuous ohmic contact to the substrate is created on the trench wall and to the backside.

The trenches are then oxidized and filled with polysilicon. The remaining processing, arriving at the final device, whose cross-section is sketched in Figure 7.22, is quite standard, and includes the following steps:

- contact opening

- metal deposition and patterning

- deposition of a passivation layer (PECVD oxide) and patterning of the same in the pad and bump-bonding regions.

Since some sensors were intended to be bump-bonded to FE-I4 [126] read-out chips, it was necessary to select good sensors at the wafer level, by measuring their I-V characteristics. For this purpose, an additional layer of metal was deposited over the passivation and patterned into stripes, each of them shorting together a row of pixels, contacted through the small passivation openings foreseen for the bump bonding. This so-called *temporary metal* solution has already been adopted for the selection of good 3D FE-I4 sensors for the ATLAS IBL [178]. After the automatic current-voltage measurement on each FE-I4 sensor, the metal was removed by wet etching, which does not affect the electrical characteristics
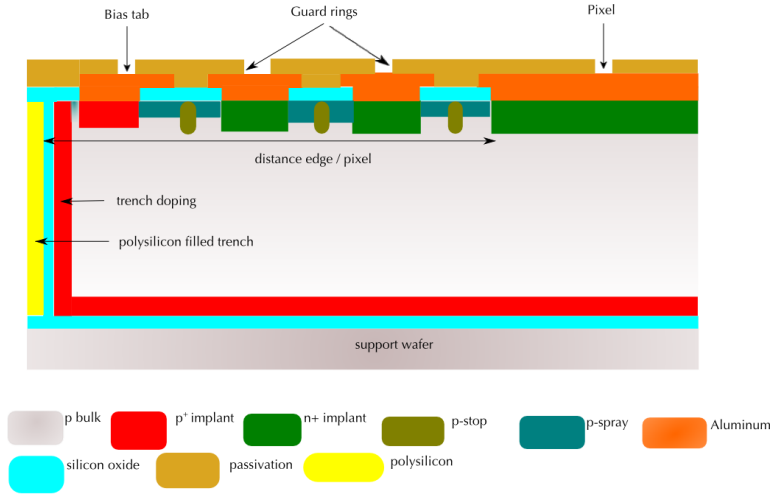
Figure 7.22: Schematic section of the pixel sensor. The region close to the sensor's edge is portrayed, including the pixel closest to the edge, the edge region, including GRs (when present), the bias tab (present only on one edge of the device), the vertical doped trench, and the support wafer.

of the devices. Pictures of FE-I4 sensor pixels before and after the metal layer removal can be seen in Figure 7.23.
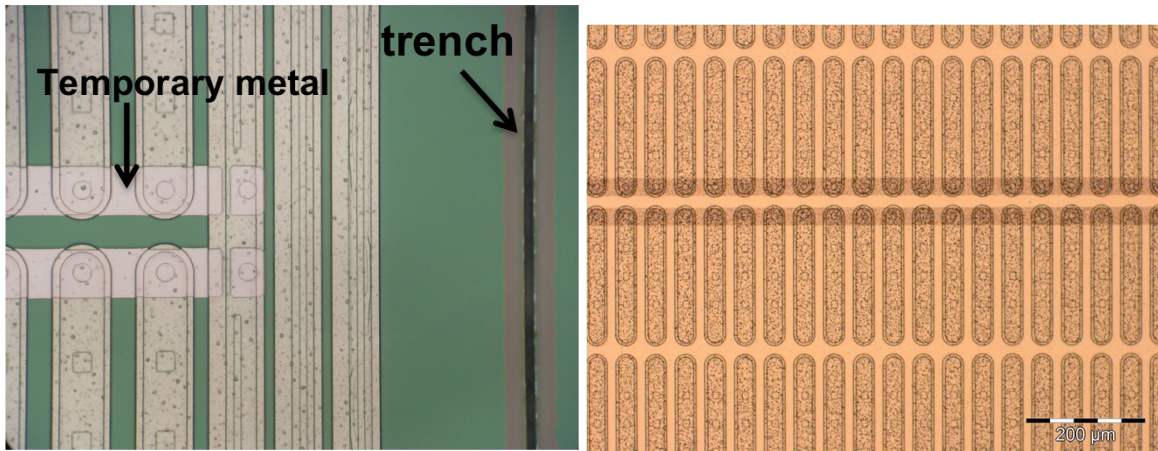
Figure 7.23: Pictures of the pixels-side of a FE-I4 sensor. (left) Sensors before temporary metal removal; region covered with temporary metal and the trench are highlighted. (right) Same sensor as above (different scale, though) after temporary metal removal.

To further proceed in module construction the support wafer has to be removed. The approach followed is illustrated in Figure 7.24 [179]. Each FE-I4 sensor is surrounded by the trench on all sides, so the sensor is effectively isolated on all sides from the silicon wafer. After having deposited a dicing tape on the pixel side, the support wafer can be back-lapped completely. Since the trench penetrates the whole sensor wafer thickness, once the support wafer has been completely lapped, each sensor can separated from the others by removing the tape.

After the temporary metal and the support wafer removed, the diced sensors were ready to be bump-bonded to the FE-I4 readout chip.
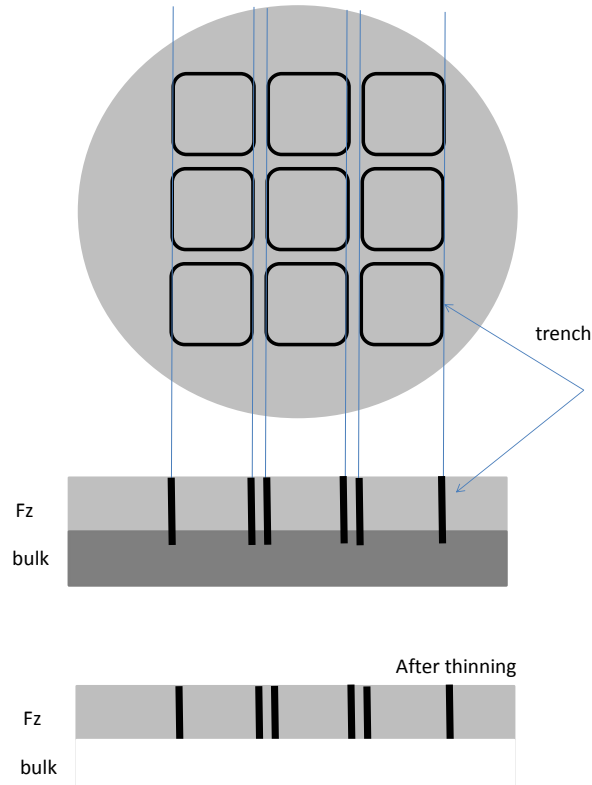
Figure 7.24: Sensors separation from wafer.

7.5.2.2 The Wafer Layout

The production included nine FE-I4 compatible pixel sensors, differing in the pixel-to-trench distance (100, 200, 300, and 400 µm) and in the number of the guard rings (0, 1, 2, 3, 5, and 10) surrounding the pixel area (see Figure 7.22). As a reminder the ATLAS pixels feature 100 µm pixel-to-edge distance; IBL ones 250 µm.

   The sensor with 3 GRs and a 200 µm pixel-to-trench distance featured two different GR designs, and each of them is repeated twice. A list of the different FE-I4 sensor versions is reported in Table 7.6.

Table 7.6: List of FEI4 sensors. The number of the sensors (first column) is reported for each combination of number of GRs and pixel-to-trench distance. Two different designs are envisaged for the sensor with 3 GRs and 200 µm pixel-to-trench distance. See text for more details.

Multiplicity	Number of GRs	pixel-to-trench distance (µm)
1	0	100
1	1	100
1	2	100
4	3	200
1	5	300
1	10	400

   A bias tab for substrate biasing (either by probing or by wire bonding), located internally to the surface delimited by the trench, was placed at about 1.5 mm from the pixe-

lated area on one of the sides (see also Figure 7.22).

The production included FE-I3 [121] compatible pixels, baby strips detectors and a large number of test structures, *i.e.* square diodes and small arrays of FE-I4-like pixels, which differ in the number of GRs surrounding the active area and in the trench-to-pixel distance. Several possible combinations have been implemented, including all those used for the FE-I4 sensors. The aim of these structures was to test the isolation and to measure the high-voltage behavior before and (possibly) after irradiation, in order to find the best sensor configuration to be bump-bonded to the read-out chip and to select the best combination of GR number and trench distance for possible future productions.

7.5.3 Electrical Characterization

Only one out of 20 processed wafers was not usable due to bad wafer-bonding. The electrical characterization of the production for non-irradiated sensors was been performed [36]. It started with measurements on specially designed test structures, to assess mainly bulk and surface properties, then tests on large sensors followed. The first part of the measurement program was carried mainly on structures reported in Figure 7.25.
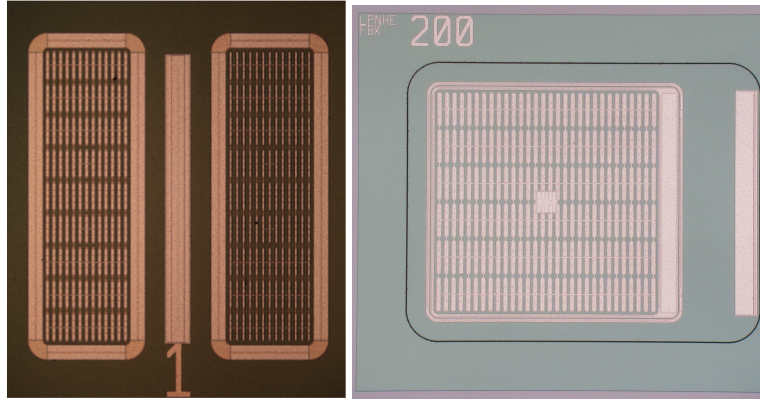
Figure 7.25: Left: test structures consisting of 2 arrays of 9 × 13 FE-I4-like pixel cells each ("inter-pixel structure"); the pixels in the left (right) structure have (no) field-plate. Right: test structures consisting of an array of 6 × 30 FE-I4-like pixel cells ("FE-I4 test structure"), where all the pixels were shorted together.

A test structure consisting of an array of 9 × 13 FE-I4-like pixel cells was used to measure the interpixel and the pixel-to-backside capacitance; the central pixel was isolated with respect to all the other pixels; the first 8 neighbours were shorted together, but isolated from all the other remaining (which, again, were shorted together). These structures are shown on the left in Figure 7.25, where two versions are present: one with metal field-plate and one without. "Interpixel structure" will be used for the sake of brevity in the remaining of the text to refer to this structure.

In Figure 7.25, on the right, an array of 6 × 30 FE-I4-like pixel cells is shown; all the pixels were shorted together allowing the measurement of the current voltage characteristics of the whole array and of the inner GR (if present), and the break-down (BD) voltage dependence on the number of GRs and on the pixel-to-trench distance. Several combinations of values for the latter parameters are present on the wafer; in Figure 7.25, on the right, a structure with a 200 µm pixel-to-trench distance and 2 GRs is shown. "FE-I4 test structure" will be used for the sake of brevity in the remaining of the text to refer to this structure.
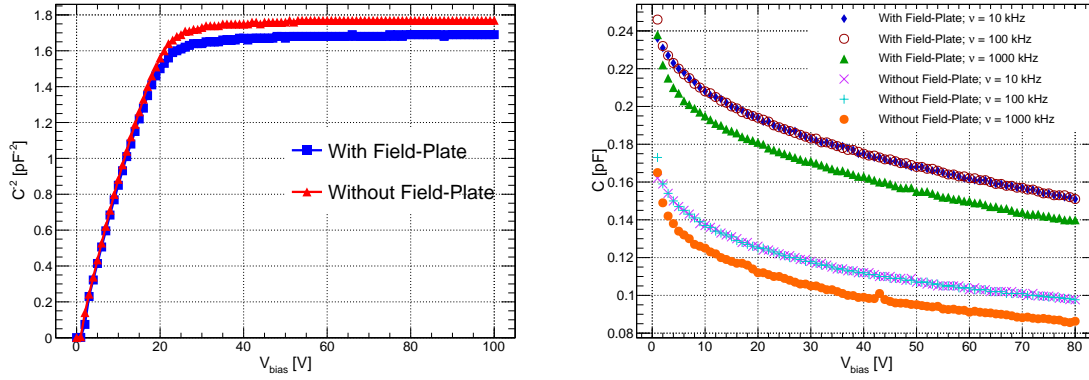
Figure 7.26: Measurements results for the intepixel structure; (left) inverse squared capacitance between all the pixels and the sensor backside as a function of the bias voltage; both pixels with and without field-plate were tested; (right) interpixel capacitance for test structure with FEI4-like cells; the capacitance between the central pixel and all the other pixels surrounding it in the test structure is reported as a function of the bias voltage for pixel cells with a field-plate, and without it; the results are reported for three different frequencies: 10, 100 kHz and 1 MHz.

For the interpixel structure, in Figure 7.26, the inverse of the square capacitance between all the pixels and the sensor backside is presented as a function of the bias voltage; the measurement was performed at a frequency of 10 kHz. From this measurement the sensors' depletion voltage was derived (~20 V). For the same structure, in Figure 7.26, the capacitance between the central pixel and all the other ones is presented as a function of the bias voltage; the measurement has been carried out at three different frequencies ν: 10, 100 kHz and 1 MHz. It can be seen that the presence of a field-plate increases the interpixel capacitance. The coupling is particularly important due to the presence of the uniform p-spray implant. However, the level of capacitive coupling, even with a field-plate, is acceptable in term of electronic noise for the read-out.

Using the interpixel structure the interpixel resistance R_{int} was evaluated; the results are reported in Figure 7.27 for the 2 different p-spray doses. It can be seen that for the high p-spray dose value, at depletion voltage, the interpixel resistance is four times larger than the low p-spray dose corresponding value; nonetheless, excellent pixel isolation is already assured by low p-spray dose. After irradiation, this test will be crucial to prove the pixels isolation.

FE-I4 test structures were used to evaluate the current voltage characteristics of the production. The effect of GRs on the breakdown voltage can be seen in Figure 7.27, where the current-voltage curves of test structures featuring FEI4-like pixels and different number of GRs are reported; the distance between the last pixels and the doped trench is 100 µm [8]. The breakdown voltage increases by more than 70% (from 70 to 120 V) by adding a second, floating GR.

7.5.4 Beam test results

Three sensors were bump-bonded to FE-I4 readout chips at IZM Berlin[8] and were evaluated on beam [8].

---

[8]Fraunhofer-Institut für Zuverlässigkeit und Microintegration: https://www.izm.fraunhofer.de/en.html
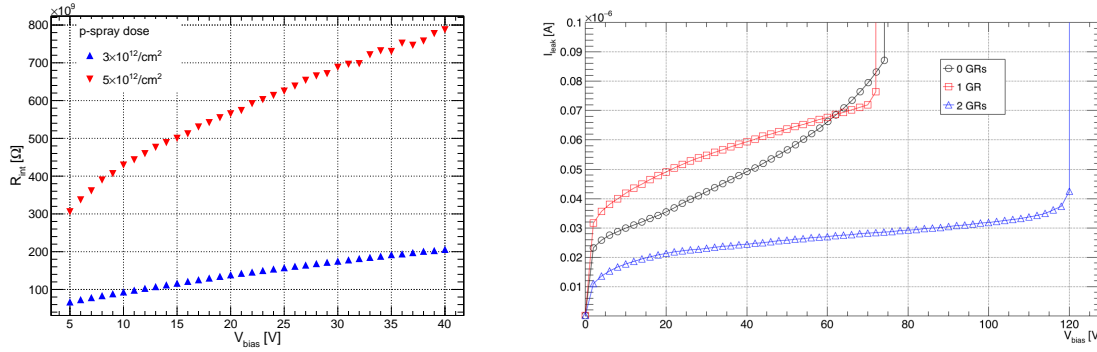
Figure 7.27: (left) Interpixel resistance R_{int} as a function of the bias voltage for two different p-spray doses. (right) Current-Voltage curves for test structures featuring different number of GRs. The innermost GR, if present, was kept at ground voltage. The shortest distance from the pixels to the trench is 100 μ*m*. The measurement for the test structure with 2 GRs was taken at a lower temperature with respect to the other two samples.

7.5.4.1   Description of Tested Devices

The main difference among the three sensors is the number of guard rings (GRs) surrounding the active area, ranging from zero to two. In Figure 7.28 a detail of the sensor edge can be seen for all the three samples.
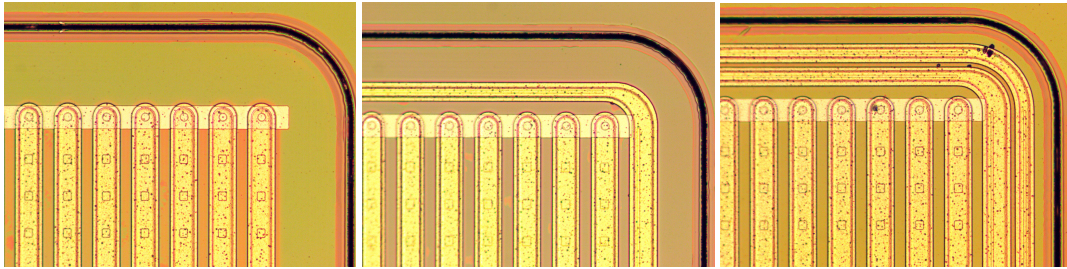
Figure 7.28: Microscope picture of corners of the (left) LPNHE5, (middle) LPNHE4 and (right) LPNHE7 sensor. The black line at the top and on the right is the trench. The shortest distance from the pixels to the trench is 100 μ*m* for all the three sensors. For LPNHE4 there is one GR surrounding the pixel matrix; for LPNHE7 there are two GRs. The pictures show also a temporary metal strip [178] shorting the pixels: it was used at wafer level for checking the sensor current but it was removed from the detectors tested in this work.

LPNHE5 has no GRs, LPNHE4 has one GR and LPNHE7 has two GRs. All sensors are 200 μm thick $n - on - p$ and include a uniform p-spray implant on the pixels side to provide enough insulation among them. LPNHE4 and LPNHE5 sensors have, in addition, p-stops implants that surround the implants of pixels and GRs. The main characteristics of the devices are summarized in Table 7.7.

Table 7.7: Tested devices characteristics.

Name	Number of GRs	p-stop implant
LPNHE5	0	yes
LPNHE4	1	yes
LPNHE7	2	no

The LPNHE4 module was used in an irradiation experiment before the beam tests. Laboratory measurements after irradiation showed that, due to the lack of electrical insulation layer between the sensor and the FEI4-B readout chip (for a discussion of this issue see for example [33]), it could not be biased up to full depletion. Hence there are no beam test results for irradiated detectors from this pixel sensors production but only laboratory measurements with radioactive sources which will be presented at the end of the Section.

During all measurements the innermost GR, if present, was kept at ground voltage by the FE-I4 readout chip; the second GR, when present, was left floating. The depletion voltage for all three devices was about 20 V.

7.5.4.2   Detector Configuration and Experimental Setup

Before laboratory and beam tests the threshold and gain settings of the readout electronics are carefully tuned. When choosing the threshold, a compromise has to be found between a high threshold, which decreases the number of noise hits but decreases the signal efficiency as well, and a low threshold, with opposite effects. For our detectors, a typical threshold is 1400 e, which corresponds to a tenth of the expected most probable value signal amplitude due to a minimum ionizing particle (MIP) crossing the sensor at normal incident angle. A typical result from threshold tuning [126, 180] can be see in Figure 7.29; the threshold dispersion is of the order 200 e. The signal amplitude in the sensor is measured in units of Time over Threshold (ToT): a clock counts when the shaped signal goes above threshold and stops when the signal falls below threshold; the difference between those two crossings is the ToT [126]. During the tuning of the electronics, the correspondence between ToT value and input charge is calibrated.
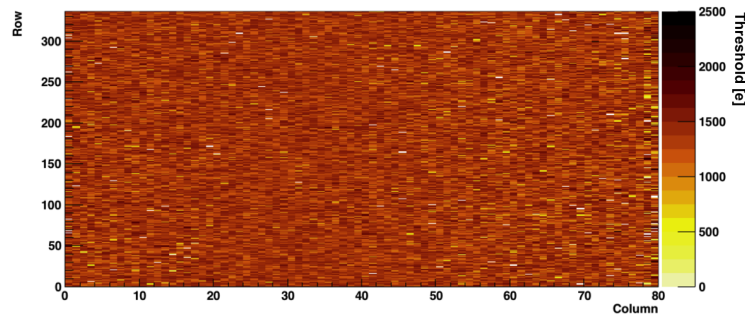
Figure 7.29: Pixel threshold values for LPNHE7. On the abscissa is the pixel column index, on the ordinate axis is the pixel row index. The tuning target value was 1400 e; the sensor bias voltage was 40 V.

The results presented here are based on data taken at the DESY beam test facility[9] and at the CERN North Area experimental area[10]. At DESY 4 GeV/c momentum electrons were used; at CERN 120 GeV/c momentum positive pions were used.

At both laboratories the data were recorded using a copy of the Eudet/AIDA telescope [173] already presented elsewhere. The data from the DUTs were recorded using two different Data Acquisition (DAQ) systems: the Reconfigurable Cluster Element (RCE) [181] system and the UsbPix [180] system. The typical averaged[11] trigger rate was

---

[9]http://testbeam.desy.de/

[10]http://sba.web.cern.ch/sba/

[11]Averaged over a supercycle at CERN

in the range of 250-1000 Hz, depending on the beam conditions and on the DAQ system used for the devices under test (DUTs).

The DUTs were located between the two arms of the telescope (each arm having three detection planes). To screen the DUTs from the light, they were operated inside a cooling box, capable of maintaining the DUT temperature constant.

7.5.4.3 Data Reconstruction and Analysis

Raw data were processed into tracks using the algorithms implemented in the EUTelescope framework [182]. At the end of the process a ROOT [183] file is created containing basic observables ready to be analyzed in the data analysis framework, TBmon2 software [184]. TBmon2 allows studying the quantities discussed below.

Global, In-Pixel and Edge Hit Efficiency   The global hit efficiency is defined as the fraction of reconstructed tracks crossing a sensor that have an associated hit in that sensor. A bad bump bonding can degrade severely the efficiency of the sensor. The quoted efficiency is measured in a fiducial region, defined by the surface of the pixel module where each pixel cell is hit by at least 1 track. From Figure 7.30 it can be seen that the fiducial region, defined by the trigger scintillators area, is smaller than the surface of the detector. Nonetheless the uniformity in threshold show in Figure 7.29 is a good indication that the performance measured in the fiducial area can be taken as valid also outside it, hence the hit efficiency be interpreted as global.
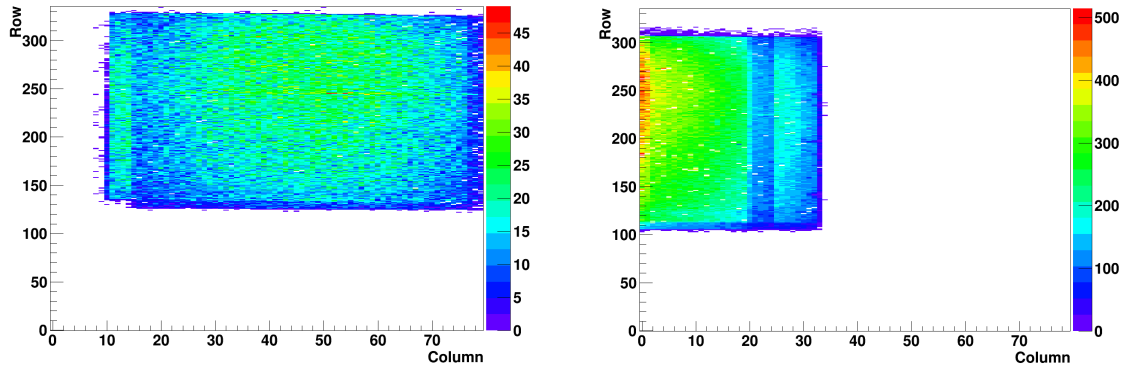
Figure 7.30: Hit map of a tested sensor in beam. On the abscissa is the pixel column index, on the ordinate axis is the pixel row index. (Left) the beam is focused on the center of the sensor; (right) the beam is focused on the edge, which allows to perform edge efficiency scan. The area where hits are seen is a 1 cm^2 rectangle and correspond to the area of the trigger scintillator.

The in-pixel hit efficiency is obtained by superimposing the 2D maps of efficiency as a function of the local position in each pixel cell of the sensor, the granularity of this analysis being of the order of the total pointing resolution (sum of the telescope resolution and the multiple scattering average shift). The in-pixel efficiency gives valuable information on the homogeneity of the charge collection, stressing the presence of low efficiency areas due, for instance, to permanent biasing structures. Our sensors do not include permanent biasing structures, since for testing purposes they are polarized thanks to a temporary metal line [178], which is then removed before bump bonding.

To assess whether the active edge ensures a high hit efficiency in the area between the last pixels and the doped trench, an efficiency measurement as a function of the track position in the edge area is performed, using data collected with the beam focused on

the edge area; see also Figure 7.30. The impact of the GRs on the efficiency is studied by comparing numerical device simulations with the edge hit efficiency profiles. The lateral depletion can be investigated looking at the edge efficiency performance for several values of the bias voltage.

7.5.4.4 Efficiency Results for the Edgeless Sensors

In what follows the global hit, in-pixel and edge hit efficiency results from the beam tests will be presented.
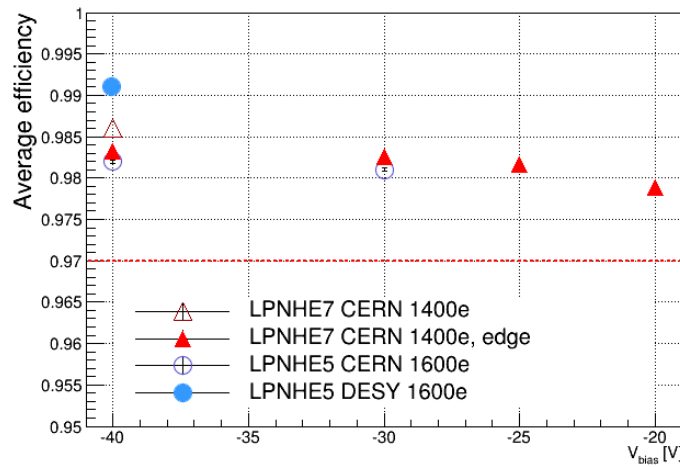
Figure 7.31: Global hit efficiency for the 2 sensors (LPNHE7 and LPNHE5), for various bias points, threshold configurations (1600 e or 1400e) and beam tests (CERN or DESY). "Edge" identifies data taken when the beam was focused at the detector periphery.

Global Hit Efficiency   The hit efficiency has been investigated at CERN SPS and DESY with a set of two thresholds corresponding to an input charge of 1400 electrons or 1600 electrons and for various bias points. The global hit efficiency is higher than 97.5 % for both the LPNHE5 and LPNHE7 sensors, as shown in Figure 7.31. For LPNHE7 at the CERN SPS with a threshold of 1400 electrons, two beam configurations were investigated, one with the beam focused on the center of the sensor (open triangles), the other with the beam focused on the edge of the sensor (full triangles). Biasing the sensor above 25 V allows the sensors to reach a 98 % efficiency whatever the threshold.

In-Pixel Hit Efficiency   As observed in Figure 7.32, the in-pixel efficiency is very homogeneous. This high homogeneity shows the interest of using a temporary metal to bias the sensors for electrical tests before bump-bonding instead of adding a permanent structure such as punch-through bias dots. A tiny drop of efficiency can be observed at the pixel corner, where it decreases to 95%. This is due to the charge sharing occurring between 3 or 4 neighboring pixels. In those clusters, the charge induced in one of the pixels could be under threshold and then not taken into account, which biases the hit reconstruction and the hit efficiency.

This result is to be compared to the one in Figure 7.11 where charge is lost in the bias grid area and Figure 7.18 where the bias rail is responsible for lower hit efficiency.
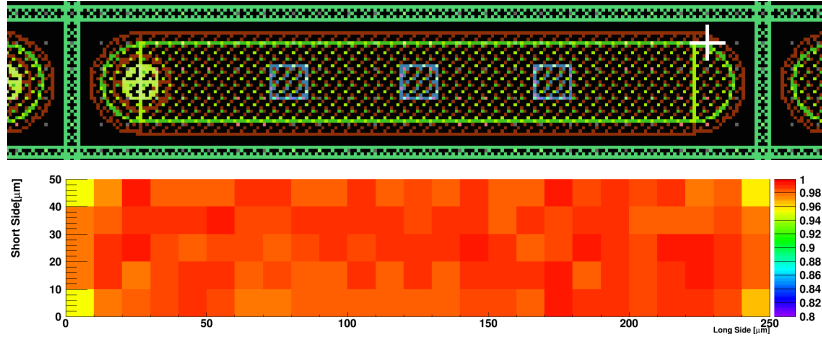
Figure 7.32: Pixel scheme (top) with inner structures: n$^+$-implant, metal contacts, bump bond pad, p-stop... and in pixel efficiency (bottom) for LPNHE7 at 40 V.

Edge Efficiency   The hit efficiency at the detector edge for both LPNHE5 and LPNHE7 is presented in Figure 7.33. LPNHE5 and LPNHE7 were measured at DESY and at CERN respectively; the threshold was set to 1600 (1400) e for LPNHE5 (LPNHE7), while the bias voltage was 40 V for both detectors.
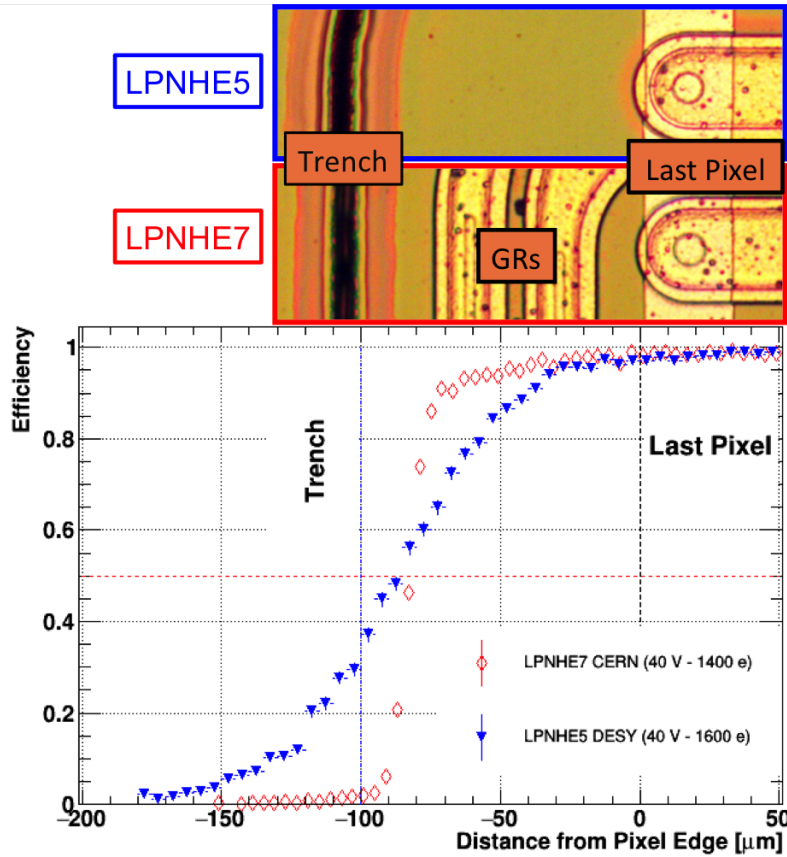
Figure 7.33: Edge efficiency profiles for LPNHE5 (no GRs - full markers) and LPNHE7 (2 GRs - open markers). Laboratory were the data were taken, device bias voltage and threshold are indicated too. The horizontal dashed line marks the 50%-point efficiency. The devices photograph on top helps in visualizing which physical area of the pixel is related to the efficiency profile.

Thanks to the active edge technology both detectors are efficient even in the un-instrumented area: for both LPNHE5 and LPNHE7 the efficiency is higher than 50% up to about 90 μm away from the last pixel, that is only 10 μm from the cut edge. This performance meets the specifications of ATLAS ITk pixel modules [158] in terms of distance from the active

region to the cut edge.

As a reminder, LPNHE7 has 2 GRs, one connected to ground laying between 13 µm and 50 µm from the last pixel, one floating between 55 µm and 80 µm; LPNHE5 has no GRs. The behavior of the 2 samples is rather similar in the first 30 µm, where the efficiency is basically flat. Then the efficiency drops faster for LPNHE5, while for LPNHE7 the efficiency is a plateau between 0 and -50 µm then it smoothly decreases to reach 90 % at -80 µm, before sharply dropping to 0.

Even if data taking conditions were different and clearly sub-optimal for LPNHE5 (higher threshold, multiple scattering, ...), the detector is still quite efficient in the edge area. In particular, it is to be noted that the slope of the hit efficiency curve is consistent with the smearing in the telescope tracking resolution due to the multiple scattering. Nevertheless, further tests on active edge sensors without GRs are necessary, with better experimental conditions.

For LPNHE7, the good performance in terms of efficiency in the edge area indicates that the presence of GRs does not degrade too much the hit efficiency, even in the area of the innermost connected GR.

To better understand the efficiency in the GRs region,, two dimensional numerical simulations (for details see [7]) were run; the edge area of sensors with 0 and 2 GRs and a 100 µm distance between the last pixel and the doped trench were studied. The results are shown in Figure 7.34 for a simulated bias voltage value of 40 V.
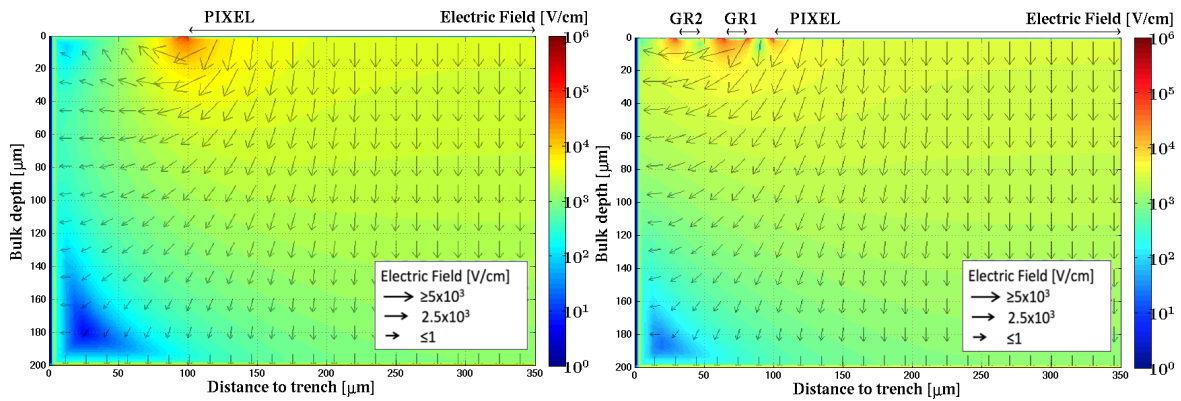
Figure 7.34: Numerical simulation of the electric field. Left: 0 GRs; right: 2 GRs. The simulated bias voltage value was 40 V.

From Figure 7.34 it can be seen that the GRs do not deeply influence the electric field lines. The charge carriers, following the electric field lines, are collected by the last pixels if they are electrons or by the trench or backside if they are holes. This seems to be the case from the simulation results, except for electrons generated within a small depth below the GRs. This picture is consistent with the efficiency results shown in Figure 7.33.

From Figure 7.34 it can also be seen that the depleted area is slightly larger for the sensors with 2 GRs and extends till the sensor edge: the GRs are contributing to the depletion of the sensor bulk. The simulated electric field magnitude in Figure 7.34 shows a weak electric field region in the bottom left corner; this is due to the presence of two close equipotential planes, the doped trench and the sensor backside. Carriers generated here drift so slowly that they do not produce a signal during the useful integration time of the read-out electronics, and the efficiency drops.

In summary, based on the above results, supported by numerical simulations, it can be stated that GRs do not preclude the possibility to have edgeless detectors; their presences make possible at the same time high hit efficiency at the detector edge, by extending

laterally the depletion region, and high breakdown voltage (as shown in Figure 7.27).

In order to further investigate the lateral depletion of the LPNHE7 sensor in the un-instrumented area between the last pixel and the trench, the hit efficiency was measured as a function of the track distance from the edge for several values of the bias voltage, as shown in Figure 7.35.
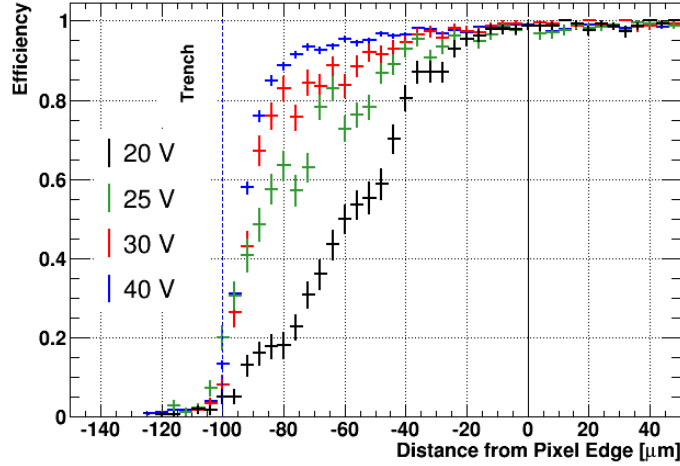
Figure 7.35: Comparison of edge efficiency profile of LPNHE7 for several bias voltages

The edge efficiency is highest at 40 V, where the lateral depletion is such that the efficiency exceeds 50% up to a distance of 90 μm from the pixel edge. At 20 V, the lateral depletion is clearly not completed as the 50% efficiency point is reached at 60 μm. The 30 V efficiency profile is quite close to the 40 V curve, although the high efficiency (>95%) in the region between 50 μm and 70 μm is possible only at the 40 V. A few events yield non zero efficiency up to 20 μm beyond the edge. This is consistent with the spatial resolution of the hits formed by one pixel cell.

7.5.4.5   Comments on the Irradiated Pixel Module LPNHE4

The LPNHE4 module was irradiated at KIT[12] with 25 MeV protons at a fluence $\Phi = 1 \times 10^{15}$ $n_{\mathrm{eq}}/\mathrm{cm}^2$. After irradiation the LPNHE4 detector was then tested at low temperature to limit reverse annealing which could degrade its performance, but also to avoid possible thermal runaways due to the expected high level of leakage current after irradiation. As it can be seen in Figure 7.36 unfortunately the irradiated LPNHE4 detector goes into breakdown at very low bias voltage values, when the detector bulk is not completely depleted.

Two concurring causes have been identified about the origin of this too early breakdown. The first one deals with electrical discharges at the detector periphery. In Figure 7.37 a sketch to illustrate the problem can be found.

As already discussed before in the Section the doped trench is equipotential with the detector backside (at High Voltage, HV, as it can be seen in Figure 7.37). The trench is electrically connected with the front-side detector periphery through the bulk and the isolation implants (either p-spray or p-stop). The pixels are kept at ground via the connection to the readout chip. The readout chip area extends beyond the sensor pixel area, overlapping with the sensor front-side part that is at a voltage very close to HV. So there is an area where a voltage difference of 100 V drops on less than 20 μm. For a more detailed

---

[12]http://www.etp.kit.edu/english/irradiation_center.php
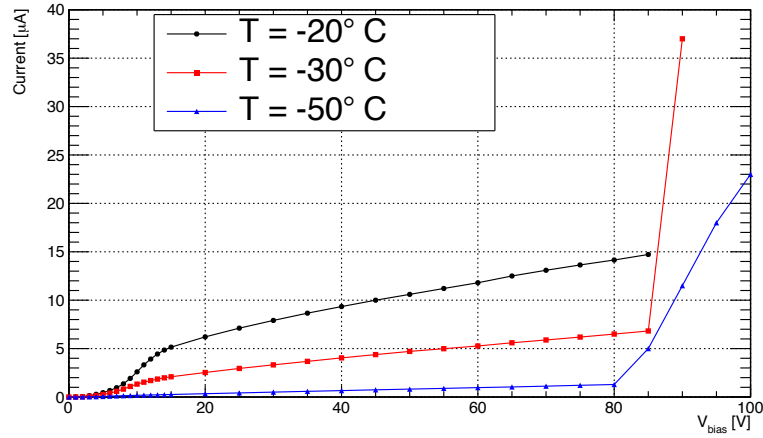
Figure 7.36: IV curves at different temperatures for LPNHE4

discussion please refer to [33]. In addition no electrical insulation layer was deposited on the sensor surface, nor on the readout chip one. The second cause for the too early break-
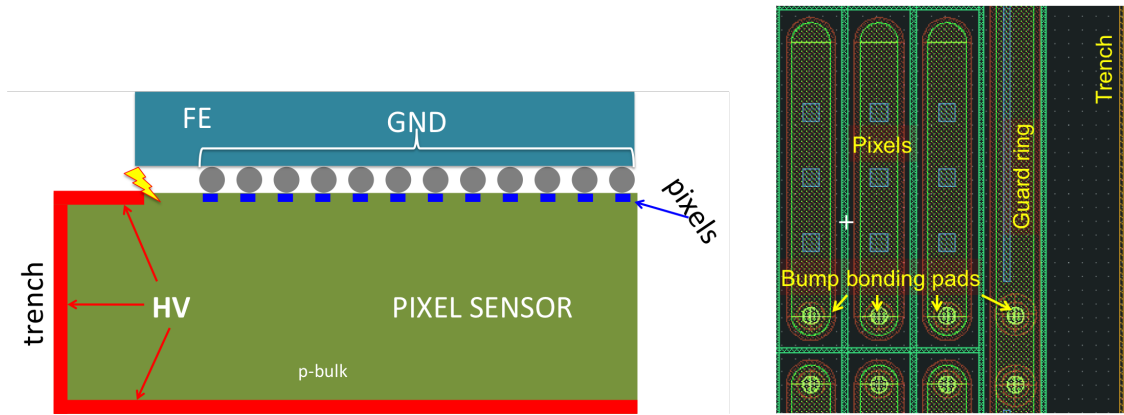
Figure 7.37: (left) Sketch to illustrate the problem of electrical discharges at the edge of the detector. (right) Sketch to illustrate the problem of electrical discharges at the edge of the detector.

down is related to the fact that the GR was kept at 0 V thanks to a bump-bond connection to the readout chip; see also Figure 7.37. This reduces the area where the voltage can drop from HV to 0 V.

Despite the too early breakdown voltage it was possible to use LPNHE4 to record events from a ^{90}Sr source. The detector was biased at V_{bias} = 80 V, 2 million events were recorded and the resulting hit map is reported in Figure 7.38; the source halo is clearly visible. This result makes us confident that the sensor itself is still alive.

7.5.5   Conclusions on the Edgeless Sensors

It was shown that the active edge technology allows a drastic reduction of the dead area at the detector periphery. The doped trench at the detector edge allows the depleted area to extend almost to the border of the silicon sensor, without drawing any current from the edge, and making it possible to have a hit efficiency higher than 90% up to 80 μm from the last pixel cell, hence assuring very high hit efficiency almost everywhere in the detector volume. It was also shown that the presence of guard rings does not degrade the hit efficiency; on the contrary, guard rings help the lateral extension of the depleted region

145
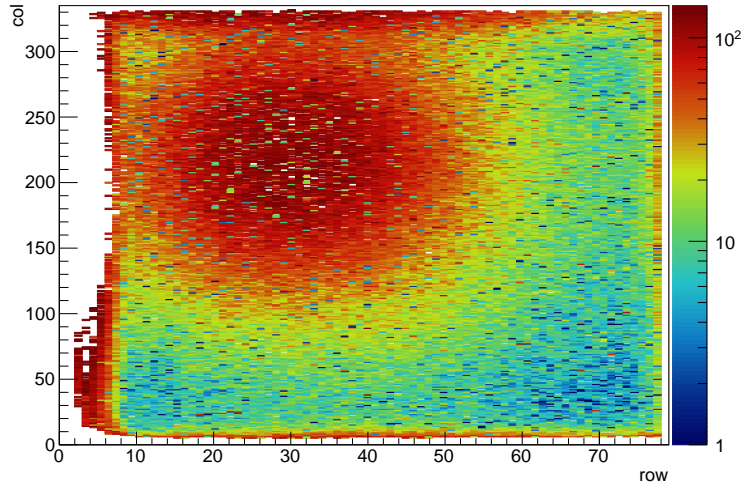
Figure 7.38: LPNHE4: ^{90}Sr source scan after two million events. The bias voltage was V_{bias} = 80 V.

and do not interfere severely with charge collection, making it possible at the same time to achieve a high hit efficiency in the sensor edge area and fairly large operation voltages.

New planar pixel productions exploiting the active edge technology are under development at FBK-Trento, in collaboration with LPNHE-Paris and INFN-Italy. The goal is to reduce the sensor thickness, to better cope with the radiation damage, to further reduce the size of the insensitive edge area and to have smaller pixels for better performance at higher particle rates.

7.6   Summary and Outlook

The High Luminosity LHC will allow to achieve instantaneous luminosities a factor of five larger than the LHC nominal value, thereby enabling the experiments to increase their data sample by one order of magnitude compared with the LHC baseline programme.

With the integrated luminosity of 3000 fb^{-1} expected by the end of the HL-LHC phase, ATLAS and CMS collaborations will be able to make Higgs couplings measurements at the % level; these and other measurements are crucial because deviations of the Higgs boson properties from the SM expectations would indicate the existence of New Physics. Furthermore, the HL-LHC will provide experimental access, for the first time, to Higgs boson couplings to particles of the second family through studies of the rare Higgs decays. Direct searches for New Physics will continue at the HL-LHC with enhanced sensitivity. The discovery potential will increase in terms of masses of new particles compared with the baseline LHC programme, reaching several TeVs for singly- produced particles.

Due to the higher beam luminosity in the HL-LHC era, in particular the larger number of protons per bunch, the ATLAS and CMS experiments will have to cope with an average of 140 simultaneous proton-proton interactions occurring at each crossing of the two beams every 25 ns, with maximum values extending up to 200 interaction events per crossing. This is only one example of the challenges the experiments will have to face to operate at the HL-LHC. ATLAS will undergo substantial upgrades to be able to cope with the increased luminosity of the HL-LHC and with the harsher environment arising from the larger event pile-up. Furthermore, some of the detector components will near the end of their lifetime at the beginning of the next decade due to radiation damage, and will

need to be replaced. The higher luminosity requires highly-granular, very radiation-hard silicon tracking devices in the regions closer to the beam line.

The development of the components for the new ATLAS Inner Tracker (ITk) detector are ongoing. R&D activities in the sensor, read-out chip and infrastructure area show already feasible solutions for future modules concepts.

ITk pixels sensors will have to face radiation fluences and doses 10 times higher and more than today. Results on thin planar detectors are very promising in terms of hit efficiency. Active edge detectors will assure the needed hermeticity close to the interaction point; this is crucial to avoid degradation in vertexing efficiency and resolution, which would affect severely the discovery potential in many important physics channels.

The large radiation fluences will impact the charge collection efficiency of the ITk pixel modules. It will be essential to optimise clustering, tracking, vertexing and flavour tagging algorithms to make sure the highest precision physics results can be achieved even with a detector severely hit by radiation damage.

Chapter 8

Perspectives

In this Chapter future research topics in the domain of tracking at high luminosity colliders will be presented. The search for thin and edgeless pixel sensors will continue with new productions which will be tested throughly after irradiation to fluences expected at the HL-LHC (Section 8.1). The data extracted from beam test measurements of irradiated pixel modules can be used to improve the modelling of radiation damage (Section 8.2). Some comments will be made on the importance of optimising the algorithm of clustering, vertexing, tracking and flavour tagging when the pixel sensors will be severely hit by radiation damage (Section 8.3). A novel solutions for thermal management and mechanical structures for future silicon detector system will be presented in Section 8.4.

8.1   Radiation Hard Pixels Sensors

The results for thin pixel detectors presented in 7.4.2 and for edgeless ones in 7.5 are very promising in terms of hit-efficiency after irradiation of the former and of performance at the detector edge for the latter. The next step is to prove that thin edgeless pixel detectors are suited for the HL-LHC phase of ATLAS. For this a new planar pixel production was realised [185] on high resistivity 6" $p-$bulk material wafers; sensor wafers active thickness is as thin as 100 µm. Edgeless pixels detectors compatible with the FE-I4 chip have been designed, featuring a pixel-to-edge distance as low as 50 µm. As we write some of these new pixel sensors prototypes are being bump-bonded to FE-I4 chip and should be tested before the end of the year. Sensors compatible with the new RD53A chip prototype were included in the production, with both 50 µm × 50 µm and 25 µm × 100 µm pitch pixels. The plan is to have some of them connected to the RD53A chip and test them on beam next year.

For both FE-I4 and RD53A modules the plan is to irradiate them at fluences of the order of 1.0×10^{16} n_{eq}/cm^2 and retest them on beam after irradiation. This time, thanks to the deposition of a layer of Benzocyclobutene (BCB) on the readout chip surface at wafer level it will be possible to verify the efficiency at the detector edge after those very large fluences.

Diodes, test-structures and baby detectors will be irradiated too, to be then studied in laboratory to extract valuable information to be used to better understand and model the effects of the radiation damage in silicon.

8.2   Improved TCAD and Monte Carlo Pixels Simulations

Concerning radiation damage modelling for TCAD based simulations, as already mentioned in Chapter 4 all of the radiation damage models work fine for certain type of sensors and conditions, even more if they were tuned for specific measurements. A nice review of the situation can be found in [186]. Despite the fact that the detector properties after irradiation depend on the initial detector material, particle and energy of the irradiation step (one recent example is here [187]), an effort to define a minimal set of radiation damage models should be pursued. This is very important in view of the HL-LHC phase of ATLAS, where a mix of several hadrons with different energies spectra will be responsible for the radiation damage to the tracking detector. Data from beam test campaigns will be fundamental, but also collision data from LHC Run 2 and 3 will be valuable for this purpose; indeed, given the excellent luminosity performance of LHC as we write, effects due to radiation damage are already visible in the actual ATLAS tracker, as shown in Chapter 6.

During the Phase-II data taking of ATLAS it will be important to update often the Monte Carlo simulations, following the changing conditions of the pixel detector due to the accumulated fluence. Using more accurate radiation damage models in combination with a good knowledge of the composition in energy and particles of the radiation received by the detector, through an approach as the one outlined in Chapter 6, reliable simulation of the the detector behaviour will be prepared.

Accurate and detailed simulations of the pixel detectors after large irradiation fluences will be also important during the preparation of the data taking at the HL-LHC but also during the actual and next LHC Run. Clustering, tracking, vertexing and flavour tagging algorithms will need to be updated to assure they will still deliver high performance on physics objects, even with a damaged tracking detector.

8.3   ITk Performance Optimisation

The possibilities offered by the dataset foreseen at the HL-LHC are many. For the search of Higgs boson decaying to second generation fermions, for other Higgs sector studies, and for many New Physics (NP) scenarios not only outstanding tracking and vertexing of charged particles are needed but excellent reconstruction of jets is mandatory too. To achieve the highest possible performance tracker information should be exploited at maximum together with calorimeter. The chief advantages of integrating tracking and calorimetric information into one hadronic reconstruction step are [188]:

- the momentum resolution of the tracker is significantly better than the energy resolution of the calorimeter for low-energy charged particles;

- the angular resolution of a single charged particle, reconstructed using the tracker is much better than that of the calorimeter;

- a better association of low p_T charged particles to the right jet, and

- a better association to the correct production vertex so important reduction of degradation due to pile-up

It is clear that the ATLAS Inner Tracker is of the uttermost importance for all the searches and studies of ATLAS. As it was already mentioned in the previous Section, clustering, tracking, vertexing and flavour tagging algorithms will need to be updated to reflect the changes in the inner tracker detector.

A good test case to study the radiation damage impact on physics performance and analysis is offered by the H $\rightarrow b\bar{b}$ decay channel; this is a study case that is in perspective very important given the excellent luminosity performance of LHC as we write.

8.3.1 Impact of Radiation Damage on Higgs Analysis

The decay of the SM Higgs boson to pairs of b−quarks is expected to have a branching ratio of 58% for a mass of the Higgs boson m_H of 125 GeV [107]. At the LHC the very large backgrounds arising from multi-jet production make the inclusive search extremely challenging. Careful reconstruction of secondary vertices is needed, to ensure the correct association of b−vertices to the same primary vertex, rejecting the huge QCD $b\bar{b}$ background, but also to identify the flavour of the jets with good efficiency and high purity. All these ingredients of course strongly depend on the tracker performance. As shown in Chapter 6 radiation damage effects can already be measured in the actual detector. Hence it would be very interesting to produce Monte Carlo simulations with a pixel detector at a reduced charge collection efficiency and then process them using un-optimised tracks reconstruction algorithms to see which is the impact of silicon pixel sensors hit by radiation damage on jets flavour tagging and then on the H $\rightarrow b\bar{b}$ analysis itself. Two scenarios are possible:

1. if algorithms performance are still acceptable then scenarios with different levels of charge collection losses can be simulated and analysed, to understand when the algorithms will need to be optimised;

2. if there is the need to retune algorithms a study of their performance should be performed as a function of the integrated fluence by the pixel detector; this could help in assessing better the systematic uncertainties to jet reconstruction and flavour tagging.

8.4 Microchannel Cooling for the ITK Pixels

The need of highly performing cooling systems using small amounts of fluids is nowadays mandatory for silicon detectors in fundamental physics and in general for all the applications requiring a high level of miniaturisation. There are indeed two conflicting trends concerning many modern devices: the need to dissipate increasing amounts of heat and and the quest for more compact and lightweight designs.

One very promising solution consists in exploiting CO_2 latent and sensible heat, rather than sensible heat only. Indeed the cooling system for the ITk Strip and Pixel Detectors will be based on evaporating CO_2 in a liquid pumped cycle cooled by an external primary chilling source. CO_2 cooling is chosen as this gives significant mass savings inside the detector due to the possibility of having smaller diameter tubing than conventional refrigerants or liquid cooling applications.

The two innermost barrel layers and the innermost endcap ring layer are placed inside an Inner Support Tube, allowing for their potential replacement. In contrast, the three outer barrel layers and three outer end- cap ring layers are between the Inner Support Tube (IST) and the Pixel Support Tube (PST), and are, like the Strip Detector, designed to operate for the entire lifetime of the HL-LHC.

The replacement of the innermost layers of the ITk pixel detector could offer the possibility to move from a cooling system based on metal pipes to one based on microchannels etched in the silicon.

Channels with a hydraulic diameter below 1 mm are defined as microchannels. Microchannels have been etched on many materials, like Polyimide, Silica Glass, Quartz, Steel, Silicon, Copper, and more [189]. In Figure 8.1 a sketch of pixel detector module with micro channel cooling system integrated.
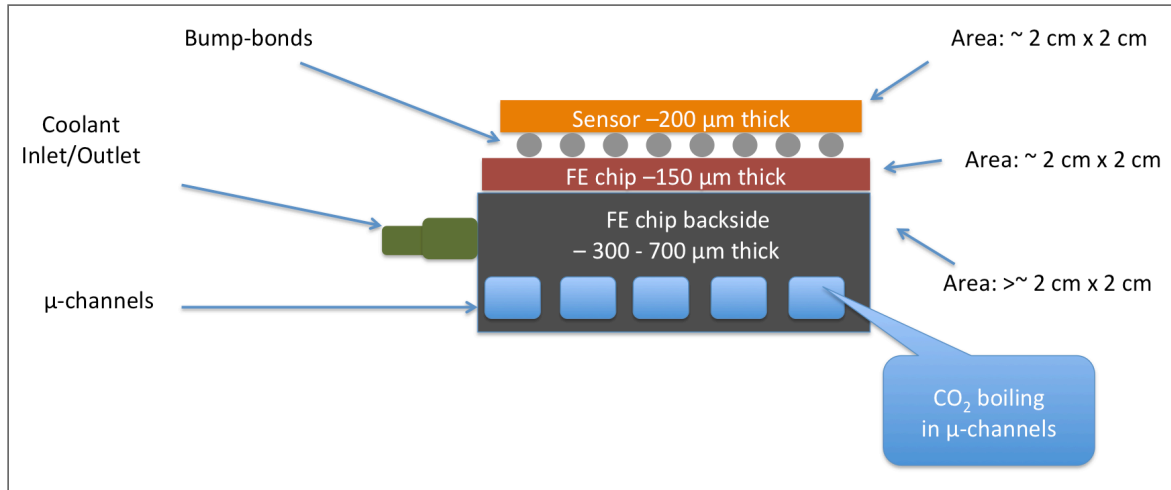
Figure 8.1: Schematic sketch of a pixel detector module with micro channel cooling system integrated.

The microchannels are etched on the backside of the unprocessed wafer that will be used for realising later the front-end chips. After the microchannels are etched a silicon oxide layer to seal them is grown. The opposite side of the wafer can be thinned down to the desired thickness before realising the readout circuitry.

A cooling system based on CO_2 evaporating in microchannels etched in silicon offers:

- very uniform and efficient heat removal; the channels position can be optimised to maximise the cooling efficiency;

- reduction of all possible thermic transmission inefficiencies and reflections to interfaces between materials with different thermal properties thanks to the fact that the cooling unit is made of silicon as the detector module;

- for the same reason above mechanical stress due to thermal expansion will be minimised too, being the system more homogenous;

- the system will be more lightweight in terms of material budget since made of silicon only, and the material distribution will be more uniform with respect to a stave with a metal pipe.

For the future LHCb vertex detector a microchannel based cooling system was proposed [190]. This is very promising since the LHCb experiment has a fixed target geometry and mass can be placed immediately outside active elements. For more classical collider experiments geometries like ATLAS the problem of having long barrel staves (500-1000 mm) dictates the need of connecting many cooling units together. Low mass and high pressure resistant connector are at the moment object of intense research.

Within the *REFLECS* and *REFLECS2* projects [191] microchannels-based cooling units, created by etching silicon wafers, were created, with two scientific goals: realize cooling prototype units for the future ATLAS Inner Tracker (ITk); study the basics of the two-phase microfluidics. If the first research axe should be by now clear, for the second it must be

said that at the moment a valid numerical model for the two-phase fluid flowing in microchannels is missing [192], especially in high pressure applications (50-200 bars and more). Once etched the silicon wafers were sealed by a pyrex wafer through anodic bonding. Figure 8.2 shows details of the wafers produced at FBK within the project. Another
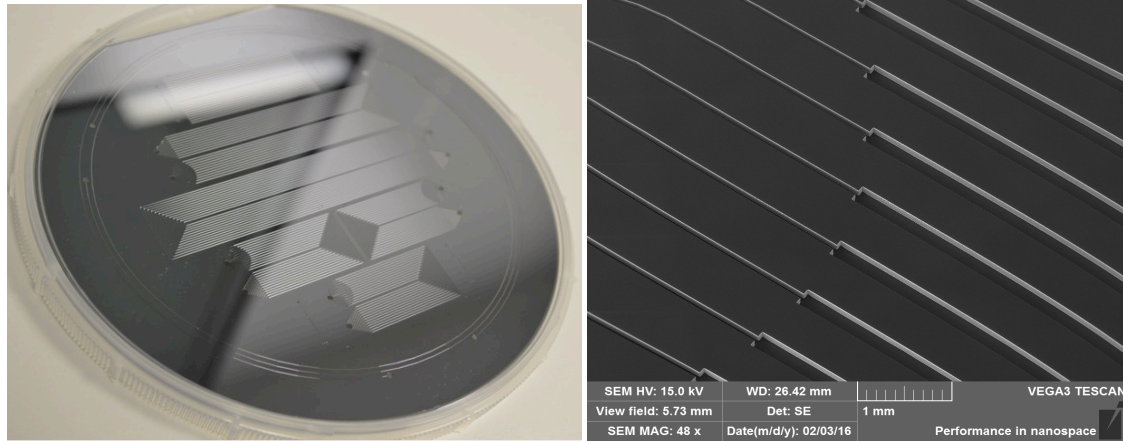
Figure 8.2: Silicon etched microchannels. (left) Wafer of microchannels prototypes, sealed by a pyrex wafer. (right) Channel restrictions to favour the start of the fluid boiling; channels are 120 µm deep and 60 (200) µm in the narrow (wide) section.

research axis within these projects is the idea of using 3D printed ceramics connectors, exploiting the good thermal specifications of ceramics.

The first samples from the REFLECS2 project wafers were cut and they will be soon connected to a CO_2 plant for tests, using a high resolution camera to study the bubbles formation and the biphasic flow. These data will be valuable to better understand the flow and boiling of two-phase fluid in microchannels at high pressure.

These studies could lead to a microchannel based cooling stave for the replacement of the innermost ITk layers.

Summary

In this report, prepared to obtain the "Habilitation à Diriger des Recherches", I have presented the highlights of my work after getting my PhD degree. All my research activities had in common the development of silicon tracking systems for high luminosity colliders, first for e^+e^- machines then for hadron colliders.

I have started focusing on strip detectors (Chapter 3) for Linear Collider and Super Flavour Factories experiments, working on the sensor characterisation and the beam test data simulation, reconstruction and analysis.

Later, after moving to the "Laboratoire de Physique Nucléaire et de Hautes Energies" (LPNHE), to work with the local ATLAS group, my focus shifted to pixel detectors for the High Luminosity LHC experiments. Here I have coordinated and contributed to the research and development of thin and edgeless pixel sensors, participating in all the R&D steps, from sensor design conception and simulations to the tests on beam of prototypes (Chapters 4 and 7). This reasearch activity saw the decisive contribution of students I have advised.

The knowledge I gained about radiation damage and TCAD simulations allowed me to make important contributions to the understanding and the simulation of the actual ATLAS pixel detector system (Chapter 6). This activity is being done in the framework an ATLAS Pixels sub-working group, which I chair together with a colleague; the group is composed, among others, by several master and PhD students.

I am very eager to continue my research on high luminosity silicon trackers development, a field that I wanted and had the opportunity to join 10 years ago. With the ITk pixel detector construction about to start in two years it is time to focus on pixel module construction, to which I will contribute thanks to my experience, by organising the work on crucial aspects like Q&A assurance of the new pixel modules and measurement campaigns on beam. But other than pixel sensor modules I want also to pursue innovative solutions for pixel detector services, like the micro-channels based cooling solution.

Beyond pixel detector construction itself, I see myself preparing the data taking at the HL-LHC, working on the understanding of the expected performance of the new ATLAS tracker in terms of tracking, vertexing and flavour tagging. The combination of my expertise in pixel detector characterisation, simulation and data analysis will be very important for these tools which are crucial for precision measurements and discoveries.

Within the LPNHE ATLAS group I will fulfil my research program, including possibly a contribution to future studies on Higgs boson decays, in preparation for the analysis at the High Luminosity LHC.

Appendix A

Charge Collection Efficiency in Irradiated Silicon Pads

In this Section estimates of the expected charge collection efficiencies for irradiated pads will be derived under some simplistic assumptions.

A.1 Introduction

In this part the assumptions made will be outlined after having reminded how signal is formed when carrier moves towards the collecting electrodes.

A.1.1 Ramo Theorem

We remind here that the instantaneous current $i(t)$ appearing on the electrodes of a silicon pad can be expressed in terms of the charge of the carriers $q_{e,h}$, the drift velocity $\vec{v}_{e,h}$ and the weighting field $\vec{E}_w$. For the sake of simplicity the time/position/temperature/voltage dependence of the drift velocity are here omitted, as well the dependence on position of the weighting field. The following formula holds separately for electrons and holes:

$$i(t) = q\,\vec{v}\cdot\vec{E}_w \qquad (A.1)$$

A.1.2 Assumptions to Simplify the Calculation

A simple 1D diode will be considered; its bulk depth is equal to w. The direction of the carriers drift will be identified with z; electrons will move toward the $z = 0$ position, the holes toward $z = w$. With the above assumptions, when focusing on the electrode collecting electrons the weighting field is simply equal to:

$$\vec{E}_w = \frac{1}{w}\hat{z} \qquad (A.2)$$

Diffusion is neglected as well as temperature dependence for whatsoever variable. The drift velocity is assumed to be saturated: $v_{e,h} = v_{e,h}^{(sat)}$; still the values can be different for electrons and holes. With the above assumptions the vectorial drift velocity is simply equal to:

$$\vec{v}_{e,h} = (\mp)\,v_{e,h}^{(sat)}\hat{z} \qquad (A.3)$$

The trapping effect will be modeled through an exponential attenuation with time of drifting carriers:

$$q_{e,h}(t) = q_{e,h}(0)e^{-\frac{t}{\tau_{e,h}}} \tag{A.4}$$

The trapping time $\tau_{e,h}$ is related to the fluence ϕ through:

$$(\tau_{e,h})^{-1} = \beta_{e,h}\phi \tag{A.5}$$

$\beta_{e,h}$ are the trapping constants.

The event of trapping and de-trapping within the current integration time will be neglected.

The passage of a MIP through the entire sensor thickness will be considered. The rate of charge created per unit length is $\mathcal{Q}(\sim \frac{80e}{\mu m})$. The total charge released in the silicon bulk by the MIP is $Q_0 = \mathcal{Q}w$

A.2   From Instantaneous Current to Charge on Electrodes

Under the assumptions made in Section A.1.2 the instantaneous current $i(t)$ from electrons and holes is simply equal to:

$$i_{e,h}(t) = e\frac{v_{e,h}^{(sat)}}{w}e^{-\frac{t}{\tau_{e,h}}} \tag{A.6}$$

To get the charge on electrodes the Equation A.6 has to be integrated over the collection time t_{coll} and over all the possible initial z position of the carriers. Given that the drift velocities are constant the collection times are equal to:

$$t_{coll_{e,h}} = \frac{(z, w - z)}{v_{e,h}^{(sat)}} \tag{A.7}$$

The charge appearing on the electrode due to electrons is Q_e:

$$Q_e = \int_0^w dz \int_0^{\frac{z}{v_e^{(sat)}}} dt \, \mathcal{Q}\frac{v_e^{(sat)}}{w}e^{-\frac{t}{\tau_e}} \tag{A.8}$$

Integrating Equation A.8, and introducing the collecting distance $d_e = v_e^{(sat)}\tau_e = \frac{v_e^{(sat)}}{\beta_{e,h}\phi}$, the charge Q_e due to electrons is found to be:

$$Q_e = Q_0\frac{d_e}{w}\left[1 - \frac{d_e}{w}\left(1 - e^{-\frac{w}{d_e}}\right)\right] \tag{A.9}$$

Similarly, the charge appearing on the electrode due to holes is Q_h:

$$Q_h = Q_0\frac{d_h}{w}\left[1 - \frac{d_h}{w}\left(1 - e^{-\frac{w}{d_h}}\right)\right] \tag{A.10}$$

The charge collection efficiency, hence, is $CCE = \dfrac{Q}{Q_0}$:

$$CCE = \frac{Q}{Q_0} = \left[\frac{d_e + d_h}{w}\right] - \left(\frac{d_e}{w}\right)^2 \left(1 - e^{-\frac{w}{d_e}}\right) - \left(\frac{d_h}{w}\right)^2 \left(1 - e^{-\frac{w}{d_h}}\right) \tag{A.11}$$

From Equation A.9 and A.10 it is also possible to get the contribution to CCE for electrons and holes separately.

A.3 Predictions for Interesting Cases: Unirradiated vs Large Fluences

A.3.1 Unirradiated Sensor

In the case of unirradiated sensors the fluence ϕ is zero, so the trapping time τ and the collecting distance d are infinite. Working out the limits the CCE is found to be:

$$\lim_{\phi \to 0} CCE \sim$$
$$\lim_{d_e, d_h \to \infty} \left\{ \left[\frac{d_e + d_h}{w}\right] - \left(\frac{d_e}{w}\right)^2 \left(\frac{w}{d_e} - \frac{1}{2}\left(\frac{w}{d_e}\right)^2 + \frac{1}{6}\left(\frac{w}{d_e}\right)^3\right) - \left(\frac{d_h}{w}\right)^2 \left(\frac{w}{d_h} - \frac{1}{2}\left(\frac{w}{d_h}\right)^2 + \frac{1}{6}\left(\frac{w}{d_h}\right)^3\right) \right\} =$$
$$\frac{1}{2} + \frac{1}{2} - \frac{w}{6}\left(\frac{1}{d_e} + \frac{1}{d_h}\right) = 1 - \frac{w}{6}\left(\frac{1}{d_e} + \frac{1}{d_h}\right) \tag{A.12}$$

To summarise: $CCE(\phi \to 0) \sim 1 - \dfrac{w}{6}\left(\dfrac{1}{d_e} + \dfrac{1}{d_h}\right)$; for infinite collecting distances the CCE is exactly one. It is interesting to notice that there's a contribution $1/2$ from electrons and $1/2$ from holes to the CCE. Neglecting holes in case of no trapping for electrons the CCE would be merely $1/2$: all the holes would be trapped and screen on average half of the total charge Q_0.

A.3.2 Large Fluences

In the case of sensors irradiated to large fluences the collecting distance d is negligible with respect to the sensor thickness w.
Working out the limits the CCE is found to be:

$$\lim_{\phi \to \infty} CCE \sim$$
$$\lim_{d_e, d_h \to 0} \left\{ \left[\frac{d_e + d_h}{w}\right] - \left(\frac{d_e}{w}\right)^2 - \left(\frac{d_h}{w}\right)^2 \right\} \tag{A.13}$$
$$\sim \left[\frac{d_e + d_h}{w}\right]$$

To summarise: $CCE(\phi \to \infty) \sim \left[\dfrac{d_e + d_h}{w}\right]$; for zero collecting distances the CCE is exactly zero. The result in Equation A.13 means that in case of heavily irradiation the charge can be effectively collected only within a distance from the electrode that is equal to the collection distance d; all the remaining $w - d$ have a negligible contribution. As for the unirradiated case, if holes are neglected the CCE would be only about $1/2$ of what it should be (in general the collection distances are different for electrons and holes).

A.4 Estimates for Some Scenarios

In Table A.1 some estimates for the CCE at certain fluences Φ for certain diode thicknesses w are reported. For the trapping constant $\beta_{e,h}$ a value of 5.6 (7.7)$\times 10^{-16}$ cm^2/ns was used [193]; for the thermal velocities $v_{th_{n,p}}$ a value of 1.06×10^7 cm/s was used for both electrons and holes.

Table A.1: CCE estimates at fluences Φ for certain diode thicknesses w.

w [µm]	Φ [1×10^{15} n$_{eq}$/cm^2]	CCE [%]
50	3	75
50	5	63
50	7	54
50	10	45
50	15	34
50	20	27
100	1	82
100	3	59
100	5	45
100	7	36
100	10	27
100	20	15
200	0.1	96
200	0.2	92
200	0.5	82
200	1	69
200	3	40
200	5	27
200	7	21
200	10	15

It can be seen that already for moderate fluences, 1-2$\times 10^{14}$ n$_{eq}$/cm^2, the signal amplitude loss is sizeable if the detector is 200 µm thick. For fluences in the range of 5-10$\times 10^{15}$ n$_{eq}$/cm^2 only very thin diodes can still deliver more than 1/4 of the original signal amplitude.

It is interesting to observe that for 1-2$\times 10^{16}$ n$_{eq}$/cm^2 there's little or no difference in expected CCE between 100 and 50 µm thick diodes, since charge is collected within a very thin layer close to the collected electron, the thickness of this layer being smaller than the diode one w.

Appendix B

Trap occupation probability

The purpose of this section is to motivate the variations in the electric field profiles in Section 6.2.3.5 with changes in the defining parameters of the two-trap radiation damage model presented in the same Section. Many of the concepts described here are discussed in more detail in [144].

Variations in the electric field profile are driven by modifications to the space charge distribution. The contribution to the space charge density from radiation damage is due to charged traps. The Chiochia model [82] has two non-degenerate traps with two possible charge states, one of them neutral. A trap is occupied if it can emit an electron; a donor-like trap is charged if it is not occupied and an acceptor-like trap is charged if it is occupied. For one of the two traps t in the Chiochia model, the occupation probability P_t can be estimated from its energy level E_t and its electron and hole capture cross sections $\sigma_{n,p}$. Once the trap occupation probability is known, its average charge state Q_t can be calculated. In particular, $Q_t = (1 - P_t)$ for donors and $Q_t = -P_t$ for acceptors.

It is useful to start with the limiting cases. When $E_t \sim E_c$ a donor trap is a shallow donor, which is most of the time ionized ($Q_t \approx +1$); on the contrary, when $E_t \sim E_v$ an acceptor trap is a shallow acceptor, which is most of the time ionized ($Q_t \sim -1$). In contrast, the occupation probability is exactly 50% at the Fermi energy level. The intrinsic energy level $E_i = \dfrac{E_v + E_c}{2} + \dfrac{1}{2} k_B T \ln\left(\dfrac{N_v}{N_c}\right) \sim 0.534$ eV is almost exactly half way between the valence and conduction bands: $E_g = E_c - E_v = 1.09$ eV. In the Chiochia model, the acceptor (a) and donor (d) states are very close to the intrinsic energy: $E_a = 0.525$ e and $E_d = 0.48$ eV ($kT \sim 0.023$ eV). As the acceptor trap is only 0.031 eV above the intrinsic level (about 1.4 kT) and the donor trap is only 0.054 eV below the intrinsic level (about 2.4 kT), small changes to the model parameters can result in significant changes in the space charge.

The full expression for the occupation probability for a trap t is given by [144]

$$P_t = \frac{1}{1 + \dfrac{c_p p + c_n n_i x_t}{c_n n + c_p n_i / x_t}},$$

(B.1)

where $x_t(E_t) = e^{\frac{E_t - E_i}{kT}}$, $c_{n,p} = v_{th_{n,p}} \sigma_{n,p}$ for electron/hole thermal velocities $v_{th_{n,p}}$, and n_i denotes the intrinsic carrier concentration. If the bulk is depleted, hence the electron and hole concentrations are negligible with respect to the intrinsic one ($n, p \ll n_i$), then the Eq. B.1 simplifies to:

$$P_t = \frac{c_p/x_t}{c_n x_t + c_p/x_t} = \frac{1}{1 + \dfrac{c_n x_t}{c_p/x_t}} \tag{B.2}$$

The space charge density (in units of elementary charge per volume) is then given by $\mathcal{Q}_t = N_t(1 - P_t)$ for donors and $\mathcal{Q}_t = N_t P_t$ for acceptors. By substituting Eq. B.2 into these formulae, it is possible to assess the impact of changes in $E_a, E_d, \sigma_{d,n}, \sigma_{d,p}, \sigma_{a,n}, \sigma_{a,p}, \eta_a$, and η_d on the space charge density. The relationships are concisely summarized in Table B.1 for the energy levels and Eq. B.2 for the capture cross-sections and introduction rates. An upward or downward pointing arrow indicates how the parameter in the second columns of the table is changed. Then, the penultimate and final columns indicate the trend in the occupation probability and average charge. For η, a higher rate (lower) rate results in a higher (lower) space charge density: positive for donors, negative for acceptors. The more negative the space charge, the stronger the electric field is near the front (bias electrode) side of the sensor and vice versa.

Table B.1: Change in occupation probability P_t and charge state Q_t for changes of trap energy values.

Parameter	Increasing?	Decreasing?	closer to?	P_t	Q_t
E_d	↗		E_c	$1 \to 0$	$0 \to +$
E_d		↘	E_v	$0 \to 1$	$+ \to 0$
E_a	↗		E_v	$0 \to 1$	$0 \to -$
E_a		↘	E_c	$1 \to 0$	$- \to 0$

Table B.2: Change in occupation probability P_t and charge state Q_t for changes of trap cross sections values.

Trap type	Parameter	Increasing?	Decreasing?	P_t	Q_t
Donor	σ_n	↗		$1 \to 0$	$0 \to +$
Donor	σ_n		↘	$0 \to 1$	$+ \to 0$
Donor	σ_p	↗		$0 \to 1$	$+ \to 0$
Donor	σ_p		↘	$1 \to 0$	$0 \to +$
Acceptor	σ_n	↗		$1 \to 0$	$- \to 0$
Acceptor	σ_n		↘	$0 \to 1$	$0 \to -$
Acceptor	σ_p	↗		$0 \to 1$	$0 \to -$
Acceptor	σ_p		↘	$1 \to 0$	$- \to 0$

Bibliography

[1] BABAR Collaboration Collaboration, B. Aubert et al., *Measurement of the* $\overline{\text{B}}^0 \to \text{D}^{*+}\ell^-\overline{\nu}_\ell$ *decay rate and* $|\text{V}_{cb}|$, Phys. Rev. D **71** (Mar, 2005) 051502. 1

[2] BABAR Collaboration Collaboration, B. Aubert et al., *Determination of the form factors for the decay* $\text{B}^0 \to \text{D}^{*-}l^+\nu_l$ *and of the CKM matrix element* $|\text{V}_{cb}|$, Phys. Rev. D **77** (Feb, 2008) 032002. 1

[3] V. Re et al., *New effects observed in the babar silicon vertex tracker: interpretation and estimate of their impact on the future performance of the detector*, pp. 1044–1048. WORLD SCIENTIFIC, 2011. 1

[4] The BABAR Collaboration Collaboration, B. Aubert et al., *Measurement of the Time-Dependent* CP *Asymmetry in* $\text{B}^0 \to \text{D}_{\text{CP}}^{(*)}h^0$ *Decays*, Phys. Rev. Lett. **99** (Aug, 2007) 081801. 2

[5] S. Bettarini et al., *The SLIM5 low mass silicon tracker demonstrator*, Nucl. Instr. and Meth. A **623** (2010) no. 3, 942 – 953. 2, 35, 39, 41

[6] J. Weingarten, S. Altenheiner, M. Beimforde, M. Benoit, M. Bomben, et al., *Planar Pixel Sensors for the ATLAS Upgrade: Beam Tests results*, JINST **7** (2012) P10028. 2, 123

[7] M. Bomben *et al.*, *Development of Edgeless n-on-p Planar Pixel Sensors for future ATLAS Upgrades*, Nucl. Instr. and Meth. A **712** (2013) 41–47. 2, 22, 55, 132, 143

[8] M. Bomben, A. Ducourthial, et al., *Performance of active edge pixel sensors*, JINST **12** (2017) no. 05, P05006. 3, 137

[9] S. L. Glashow, *Partial-symmetries of weak interactions*, Nuclear Physics **22** (1961) no. 4, 579 – 588. 5

[10] S. Weinberg, *A Model of Leptons*, Phys. Rev. Lett. **19** (Nov, 1967) 1264–1266. 5

[11] A. Salam, *Weak and Electromagnetic Interactions*, Conf. Proc. **C680519** (1968) 367–377. 5

[12] D. J. Gross and F. Wilczek, *Ultraviolet Behavior of Non-Abelian Gauge Theories*, Phys. Rev. Lett. **30** (Jun, 1973) 1343–1346. 5

[13] H. D. Politzer, *Reliable Perturbative Results for Strong Interactions?*, Phys. Rev. Lett. **30** (Jun, 1973) 1346–1349. 5

[14] W. Commons, *File:Standard Model of Elementary Particles.svg — Wikimedia Commons, the free media repository*, 2017.
https://commons.wikimedia.org/w/index.php?title=File:
Standard_Model_of_Elementary_Particles.svg&oldid=247917323. [Online; accessed 18-June-2017]. 5

[15] P. Higgs, *Broken symmetries, massless particles and gauge fields*, Physics Letters **12** (1964) no. 2, 132 – 133. 5

[16] F. Englert and R. Brout, *Broken Symmetry and the Mass of Gauge Vector Mesons*, Phys. Rev. Lett. **13** (Aug, 1964) 321–323. 5

[17] ATLAS Collaboration, G. Aad et al., *Observation of a new particle in the search for the Standard Model Higgs boson with the ATLAS detector at the LHC*, Phys. Lett. **B716** (2012) 1–29. 5

[18] CMS Collaboration, S. Chatrchyan et al., *Observation of a new boson at a mass of 125 GeV with the CMS experiment at the LHC*, Phys. Lett. **B716** (2012) 30–61. 5

[19] N. Cabibbo, *Unitary Symmetry and Leptonic Decays*, Phys. Rev. Lett. **10** (Jun, 1963) 531–533. 7

[20] M. Kobayashi and T. Maskawa, *CP Violation in the Renormalizable Theory of Weak Interaction*, Prog. Theor. Phys. **49** (1973) 652–657. 7

[21] J. H. Christenson, J. W. Cronin, V. L. Fitch, and R. Turlay, *Evidence for the 2π Decay of the K_2^0 Meson*, Phys. Rev. Lett. **13** (Jul, 1964) 138–140. 7

[22] W. Commons, *File:B-tagging diagram.png — Wikimedia Commons, the free media repository*, 2016.
https://commons.wikimedia.org/w/index.php?title=File:
B-tagging_diagram.png&oldid=216090609. [Online; accessed 2-September-2017]. 8

[23] *PEP-II: An Asymmetric B Factory. Conceptual Design Report. June 1993*, 1994.
https://doi.org/10.2172/10112145. 7

[24] B. Aubert et al., *The BABAR detector*, Nucl. Instr. and Meth. A **479** (2002) no. 1, 1 – 116. 8, 36

[25] R. Gluckstern, *Uncertainties in track momentum and direction, due to multiple scattering and measurement errors*, Nuclear Instruments and Methods **24** (1963) 381 – 389. 9

[26] Particle Data Group Collaboration, C. Patrignani et al., *Review of Particle Physics*, Chin. Phys. **C40** (2016) no. 10, 100001. 9

[27] M. Garcia-Sciveres and N. Wermes, *Advances in pixel detectors for experiments with high rate and radiation*, 2017. arXiv:1705.10150 [physics.ins-det], https://arxiv.org/abs/1705.10150. 9, 10, 11, 27, 28

[28] G. Lutz, *Semiconductor radiation detectors: device physics.* Springer, Berlin, 1999.
https://cds.cern.ch/record/411172. 11, 12, 13, 14, 22, 23, 27, 28, 31, 55, 60

[29] S. M. Sze, *Physics of semiconductor devices.* John Wiley & Sons, 1981. 11, 60

[30] S. Wang, *Fundamentals of Semiconductor Theory and Device Physics.* Prentice-Hall International, Inc., 1989. 11, 60

[31] M. Krammer, *Silicon Detectors*, 2010-11. http://www.hephy.at/fileadmin/user_upload/Lehre/Unterlagen/Praktikum/Halbleiterdetektoren.pdf. [Online; accessed 02-July-2017]. 11, 12, 15, 19, 25, 26

[32] W. Shockley, *Electrons And Holes In Semiconductors.* D. Van Nostrand Company, Inc., 1950. 11, 18, 60

[33] L. Rossi, P. Fischer, T. Rohe, and N. Wermes, *Pixel detectors: From fundamentals to applications.* Springer Science & Business Media, 2006. 11, 27, 28, 29, 139, 145

[34] F. Hartmann, *Silicon tracking detectors in high-energy physics*, Nucl. Instrum. Meth. **A666** (2012) 25–46. 11, 23

[35] A. Chilingarov, *Temperature dependence of the current generated in Si bulk*, Journal of Instrumentation **8** (2013) no. 10, P10003. 22, 31, 62

[36] M. Bomben, A. Bagolini, M. Boscardin, L. Bosisio, G. Calderini, J. Chauveau, G. Giacomini, A. La Rosa, G. Marchori, and N. Zorzi, *Electrical characterization of thin edgeless N-on-p planar pixel sensors for ATLAS upgrades*, JINST **9** (2014) C05020. 22, 136

[37] L. Landau, *On the energy loss of fast particles by ionization*, J. Phys.(USSR) **8** (1944) 201–205. 23, 111

[38] W. Shockley, *Currents to Conductors Induced by a Moving Point Charge*, Journal of Applied Physics **9** (1938) 635. 23

[39] S. Ramo, *Currents Induced by Electron Motion*, Proceedings of the IRE **27** (1939) 584–585. 23

[40] Z. He, *Review of the Shockley-Ramo theorem and its application in semiconductor gamma-ray detectors*, Nucl. Instr. and Meth. A **463** (2001) no. 1, 250 – 267. 23

[41] S. R. Amendolia et al., *A Multielectrode Silicon Detector for High-energy Physics Experiments*, Nucl. Instrum. Meth. **176** (1980) 457. 25

[42] R. Turchetta, *Spatial resolution of silicon microstrip detectors*, Nucl. Instr. and Meth. A **335** (1993) no. 1, 44 – 58. 25, 45, 48

[43] S. L. Shapiro, *Si PIN Diode Array Hybrids for Charged Particle Detection*, Nucl. Instr. and Meth. A **275** (1989) 580. 26

[44] L. Rossi, *Pixel Detectors Hybridisation*, Nucl. Instr. and Meth. A **501** (2003) 239. 26

[45] ATLAS Collaboration, M. Capeans, G. Darbo, K. Einsweiller, M. Elsing, T. Flick, M. Garcia-Sciveres, C. Gemme, H. Pernegger, O. Rohne, and R. Vuillermet, *ATLAS Insertable B-Layer Technical Design Report*, Tech. Rep. CERN-LHCC-2010-013. ATLAS-TDR-19, CERN, Sep, 2010. https://cds.cern.ch/record/1291633. 26, 78, 79, 86, 89, 124

[46] S. Parker, C. Kenney, and J. Segal, *3D - A proposed new architecture for solid-state radiation detectors*, Nucl. Instr. and Meth. A **395** (1997) no. 3, 328 – 343. 26, 86

[47] G. Claus, C. Colledani, W. Dulinski, D. Husson, R. Turchetta, J. Riester, G. Deptuch, G. Orazi, and M. Winter, *Particle tracking using CMOS monolithic active pixel sensor*, Nucl. Instr. and Meth. A **465** (2001) no. 1, 120 – 124. SPD2000. 27

[48] V. Re, *Status and perspectives of deep N-well 130 nm CMOS MAPS*, Journal of Instrumentation **4** (2009) no. 03, P03005. 27

[49] T. Hirayama et al., *The evolution of CMOS image sensors,* in *2013 IEEE Asian Solid-State Circuits Conference (A-SSCC)*, pp. 5–8. 2013. 28

[50] T. R. Oldham and F. B. McLean, *Total ionizing dose effects in MOS oxides and devices*, IEEE Transactions on Nuclear Science **50** (June, 2003) 483–499. 28, 92

[51] M. Moll, *Radiation damage in silicon particle detectors: Microscopic defects and macroscopic properties.* PhD thesis, Hamburg U., 1999. http://www-library.desy.de/cgi-bin/showprep.pl?desy-thesis99-040. 29, 30, 31, 32, 71, 72, 92, 95, 97, 105

[52] V. Van Lint, *Mechanisms of Radiation Effects in Electronic Materials.* No. v. 1 in Mechanisms of Radiation Effects in Electronic Materials. Wiley, 1980. https://books.google.fr/books?id=b_K8AAAAIAAJ. 29

[53] ASTM Subcommittee E10-07 on Radiation Dosimetry for Radiation Effects on Materials and Devices, *Standard Practice for Characterizing Neutron Energy Fluence Spectra in Terms of an Equivalent Monoenergetic Neutron Fluence for Radiation-Hardness Testing for Electronics*, E **772-94** (1994) 1–16. 29

[54] M. Moll, E. Fretwurst, M. Kuhnke, and G. Lindström, *Relation between microscopic defects and macroscopic changes in silicon detector properties after hadron irradiation*, Nucl. Instr. and Meth. A **186** (2002) no. 1, 100 – 110. 29

[55] I. Pintilie, *Experimental techniques for defect characterization of highly irradiated materials and structures*, in *25th International Workshop on Vertex Detectors (VERTEX2016).* 25-30 September, 2016. https://pos.sissa.it/cgi-bin/reader/contribution.cgi?id=287/033. 29, 30

[56] R. Wunstorf, *Systematische Untersuchungen zur Strahlenresistenz von Silizium-Detektoren fuer die Verwendung in Hochenergiephysik-Experimenten.* PhD thesis, Hamburg, 1992. https://cds.cern.ch/record/243081. 32

[57] Z. Li and H. W. Kraner, *Fast neutron radiation damage effects on high resistivity silicon junction detectors*, Journal of Electronic Materials **21** (Jul, 1992) 701–705. 32, 67

[58] V. Eremin et al., *The origin of double peak electric field distribution in heavily irradiated silicon detectors*, Nucl. Instr. and Meth. A **476** (2002) 556–564. 33, 67, 68, 96, 100, 104

[59] V. Chiochia et al., *Simulation of Heavily Irradiated Silicon Pixel Sensors and Comparison With Test Beam Measurements*, IEEE Transactions on Nuclear Science **52** (Aug, 2005) 1067–1075. 33, 67, 68

[60] G. Kramberger, V. Cindro, I. Mandić, M. Mikuž, and M. Zavrtanik, *Effective trapping time of electrons and holes in different silicon materials irradiated with neutrons, protons and pions*, Nucl. Instr. and Meth. A **481** (2002) no. 1, 297 – 305. 34

[61] G. Kramberger, V. Cindro, I. Mandić, and M. Mikuž, *Impact of annealing of trapping times on charge collection in irradiated silicon detectors*, Nucl. Instr. and Meth. A **579** (2007) no. 2, 762 – 765. 34

[62] M. Bomben, *Highly segmented thin microstrip detector with data-driven fast readout*, Nucl. Instr. and Meth. A **623** (2010) no. 1, 159 – 161. 1st International Conference on Technology and Instrumentation in Particle Physics. 35, 47

[63] N. Neri et al., *Deep n-well MAPS in a 130nm CMOS technology: Beam test results*, Nucl. Instrum. Meth. **623** (2010) no. 1, 195 – 197. 1st International Conference on Technology and Instrumentation in Particle Physics. 35, 39

[64] *Silicon detectors with low interaction with material*, http://www.pi.infn.it/slim5/. 35

[65] *INFN National Scientific Committee 5*, https://web.infn.it/csn5/index.php/en/. 35

[66] SuperB Collaboration, M. Baszczyk et al., *SuperB Technical Design Report*, 2013. arXiv:1306.5655 [physics.ins-det]. 35, 36

[67] *Technical Review of BaBar Improvement Plans*, https://www.slac.stanford.edu/BFROOT/www/Organization/Gilchriese/. 36

[68] G. Rizzo et al., *The superB silicon vertex tracker*, Nuclear Instruments and Methods **617** (2010) no. 1, 585 – 587. 11th Pisa Meeting on Advanced Detectors. 37

[69] *ILC Technical Design Report*, 2013. https://www.linearcollider.org/ILC/Publications/Technical-Design-Report. 37

[70] The ILD concept group Collaboration, *International Large Detector Letter Of Intent*, 2010. http://arxiv.org/abs/1006.3396. 37

[71] The SiD concept group Collaboration, *SiD Letter of Intent*, 2010. http://arxiv.org/abs/0911.0006. 37

[72] S. P. Martin, *A Supersymmetry primer*, arXiv:hep-ph/9709356 [hep-ph]. [Adv. Ser. Direct. High Energy Phys.18,1(1998)]. 37

[73] A. Besson, *The ILC Vertex Detector requirements*, in *25th International Workshop on Vertex Detectors (VERTEX2016)*. 25-30 September, 2016. https://pos.sissa.it/287/047/pdf. 38

[74] R. Lipton, *ILC Vertex detector issues and thoughts*, in *16th International Workshop on Vertex Detectors (VERTEX2007)*. 23-28 September, 2007. http://pos.sissa.it//archive/conferences/057/036/Vertex%202007_036.pdf. PoS(Vertex 2007)036. 38

[75] C. Hu-Guo et al., *First reticule size {MAPS} with digital output and integrated zero suppression for the EUDET-JRA1 beam telescope*, Nucl. Instr. and Meth. A **623** (2010) no. 1, 480 – 482. 1st International Conference on Technology and Instrumentation in Particle Physics. 38, 129

[76] L. Ratti, *Continuous Time-Charge Amplification and Shaping in CMOS Monolithic Sensors for Particle Tracking*, IEEE Trans. Nucl. Sci. **53** (2006) 3918–3928. 39

[77] V. Re, M. Manghisoni, L. Ratti, J. Hoff, A. Mekkaoui, and R. Yarema, *FSSR2, a self-triggered low noise readout chip for silicon strip detectors*, IEEE Trans. Nucl. Sci. **53** (2006) 2470–2476. 40, 41

[78] G. Rizzo et al., *Recent developments on CMOS MAPS for the SuperB Silicon Vertex Tracker*, Nucl. Instrum. Meth. **A718** (2013) 283–287. 51

[79] N. Dinu, *Instrumentation on silicon detectors: from properties characterization to applications.* Habilitation à diriger des recherches, Université Paris Sud - Paris XI, Oct., 2013. https://tel.archives-ouvertes.fr/tel-00872318. 54

[80] M. Barozzi, *Depth profiles of P and B concentrations in silicon*, 2010. European Integrated Activity of Excellence and Networking for Nano and Micro-Electronics Analysis. 54

[81] L. Long, *The application of Silvaco process and device simulation program to the development of silicon detector for the high energy particle detection*, 2014. https://indico.in2p3.fr/event/9786/session/2/contribution/7/material/slides/1.pdf. In SIM-détecteurs 2014. 55

[82] V. Chiochia et al., *A double junction model of irradiated silicon pixel sensors for LHC*, Nucl. Instr. and Meth. A **568** (2006) no. 1, 51 – 55. New Developments in Radiation Detectors. 56, 67, 68, 69, 96, 100, 104, 105, 161

[83] B. Henrich, W. Bertl, K. Gabathuler, and R. Horisberger, *Depth Profile of Signal Charge Collected in Heavily Irradiated Silicon Pixels*, Tech. Rep. CMS-NOTE-1997-021, CERN, Geneva, Apr, 1997. http://cds.cern.ch/record/687041. 56, 68

[84] T. Lari, *Lorentz angle variation with electric field for ATLAS silicon detectors*, . https://cds.cern.ch/record/684187. 56, 68

[85] T. Lari, *Measurement of trapping time constants in irradiated DOFZ silicon with test beam data*, Nucl. Instr. and Meth. A **518** (2004) no. 1, 349 – 351. Frontier Detectors for Frontier Physics: Proceedin. 56, 68

[86] M. Bomben, *Radiation damage models: comparison between Silvaco and Synopsys*, 2016. https://agenda.infn.it/contributionDisplay.py?contribId=3&confId=11109. In 28th RD50 Workshop. 59, 71

[87] J. W. Slotboom, *The pn-product in silicon*, Solid-State Electronics **20** (1977) no. 4, 279 – 283. 61

[88] P. Calzolari and S. Graffi, *A theoretical investigation on the generation current in silicon p-n junctions under reverse bias*, Solid-State Electronics **15** (1972) no. 9, 1003 – 1011. 61

[89] *Atlas User's Manual - DEVICE SIMULATION SOFTWARE*, `https://www.silvaco.com/products/tcad/device_simulation/atlas/atlas.html`. 67

[90] D. Passeri, M. Baroncini, P. Ciampolini, G. M. Bilei, A. Santocchia, B. Checcucci, and E. Fiandrini, *TCAD-based analysis of radiation-hardness in silicon detectors*, IEEE Transactions on Nuclear Science **45** (Jun, 1998) 602–608. 67

[91] D. Passeri, P. Ciampolini, G. M. Bilei, and F. Moscatelli, *Comprehensive modeling of bulk-damage effects in silicon radiation detectors*, IEEE Transactions on Nuclear Science **48** (Oct, 2001) 1688–1693. 67

[92] Moscatelli, F. and others, *An enhanced approach to numerical modeling of heavily irradiated silicon devices*, Nucl. Instrum. Meth. B **186** (2002) 171. 67

[93] Moscatelli, F. and others, *Comprehensive device simulation modeling of heavily irradiated silicon detectors at cryogenic temperatures*, IEEE Trans. Nucl. Sci. **51** (2004) no. 4, 1759–1765. 67

[94] Petasecca, M. and others, *Numerical simulation of radiation damage effects in p-type silicon detectors*, Nucl. Instrum. Meth. A **563** (2006) no. 1, 192–195. 67, 68, 70

[95] D. Pennicard, C. Fleta, R. Bates, V. O'Shea, C. Parkes, G. Pellegrini, and N. Tartoni, *Simulations of radiation-damaged 3D detectors for the Super-LHC*, Nucl. Instrum. Meth. **A592** (2008) 16–25. 67, 68

[96] R. Dalal, A. Bhardwaj, K. Ranjan, K. Lalwani, and G. Jain, *Simulation of irradiated Si detectors*, PoS (Vertex2014) **30** (2014) . `http://pos.sissa.it/archive/conferences/227/030/Vertex2014_030.pdf`. 67, 96

[97] D. Passeri, F. Moscatelli, A. Morozzi, and G. M. Bilei, *Modeling of Radiation Damage Effects in Silicon Detectors at High Fluences HL-LHC with Sentaurus TCAD*, Nucl. Instrum. Meth. **A824** (2016) 443–445. 67

[98] A. Macchiolo, R. Nisius, N. Savic, and S. Terzo, *Development of n-in-p pixel modules for the ATLAS Upgrade at HL-LHC*, Nucl. Instrum. Meth. **A831** (2016) 111–115. 68, 70

[99] N. Savic, M. Bomben, A. Macchiolo, R. Nisius, and S. Terzo, *Investigation of hit efficiency of n-in-p pixels with different designs*, 2015. `https://indico.cern.ch/event/381195/contributions/905636/`. In 26th RD50 Workshop. 68, 70

[100] D. Passeri, F. Moscatelli, A. Morozzi, and G. Bilei, *Modeling of radiation damage effects in silicon detectors at high fluences HL-LHC with Sentaurus TCAD*, Nucl. Instrum. Meth. A **824** (2016) 443 – 445. Frontier Detectors for Frontier Physics: Proceedings of the 13th Pisa Meeting on Advanced Detectors. 71

[101] A. Affolder, P. Allport, and G. Casse, *Collected charge of planar silicon detectors after pion and proton irradiations up to 2.2 x 10**16 n(eq) cm**-2*, Nucl. Instrum. Meth. **A623** (2010) 177–179. 73

[102] RD50 Collaboration, *RD50 - Radiation hard semiconductor devices for very high luminosity colliders*, http://rd50.web.cern.ch/rd50/. 74

[103] ATLAS Collaboration, ATLAS Collaboration, *The ATLAS Experiment at the CERN Large Hadron Collider*, JINST **3** (2008) S08003. 75, 77

[104] CMS Collaboration, *The CMS Experiment at the CERN LHC*, JINST **3** (2008) S08004. 75

[105] L. Evans and P. Bryant, *LHC Machine*, Journal of Instrumentation **3** (2008) no. 08, S08001. 75

[106] LHC/LC Study Group Collaboration, G. Weiglein et al., *Physics interplay of the LHC and the ILC*, Phys. Rept. **426** (2006) 47–358. 76

[107] ATLAS Collaboration, M. Aaboud et al., *Evidence for the* $H \rightarrow b\bar{b}$ *decay with the ATLAS detector*, 2017. arXiv:1708.03299 [hep-ex]. 76, 151

[108] CMS Collaboration, C. Collaboration, *Observation of the Higgs boson decay to a pair of tau leptons*, 2017. arXiv:1708.00373 [hep-ex]. 76

[109] ATLAS Collaboration Collaboration, *Search for the dimuon decay of the Higgs boson in pp collisions at* $\sqrt{s}$ *= 13 TeV with the ATLAS detector*, Mar, 2017. https://cds.cern.ch/record/2257726. 76

[110] ATLAS Collaboration, *Delivered Luminosity versus time for 2011-2017*, https://twiki.cern.ch/twiki/bin/view/AtlasPublic/ LuminosityPublicResultsRun2#Multiple_Year_Collision_Plots. [Online; accessed 11-August-2017]. 76, 77

[111] ATLAS Collaboration Collaboration, S. Haywood, L. Rossi, R. Nickerson, and A. Romaniouk, *ATLAS inner detector: Technical Design Report, 2*, 1997. https://cds.cern.ch/record/331064. 77

[112] ATLAS Collaboration, *Expected performance of the ATLAS b-tagging algorithms in Run-2*, Jul, 2015. https://cds.cern.ch/record/2037697. 78

[113] K. Potamianos, *The upgraded Pixel detector and the commissioning of the Inner Detector tracking of the ATLAS experiment for Run-2 at the Large Hadron Collider*, PoS **EPS-HEP2015** (2015) 261, arXiv:1608.07850 [physics.ins-det]. https: //cds.cern.ch/record/2209070/files/ATL-PHYS-PROC-2016-104.pdf. 78

[114] ATLAS Collaboration, M. Aaboud et al., *Performance of the ATLAS Trigger System in 2015*, Eur. Phys. J. **C77** (2017) no. 5, 317. 79

[115] M. Shochet, L. Tompkins, V. Cavaliere, P. Giannetti, A. Annovi, and G. Volpi, *Fast TracKer (FTK) Technical Design Report*, 2013. https://cds.cern.ch/record/1552953. 79

[116] G. Aad, M. Ackers, F. Alberti, M. Aleppo, G. Alimonti, et al., *ATLAS pixel detector electronics and sensors*, JINST **3** (2008) P07007. 79, 82, 83, 84

[117] M. Backhaus, *The upgraded Pixel Detector of the ATLAS Experiment for Run 2 at the Large Hadron Collider*, Nucl. Instr. and Meth. A **831** (2016) 65 – 70. Proceedings of the 10th International Hiroshima Symposium on the Development and Application of Semiconductor Tracking Detectors. 79

[118] ROSE Collaboration Collaboration, G. Lindström, S. Watts, and F. Lemeilleur, *3rd RD48 status report: the ROSE collaboration (R&D on silicon for future experiments)*, Dec, 1999. https://cds.cern.ch/record/421210. 81, 98

[119] G. Lindström et al., *Developments for radiation hard silicon detectors by defect engineering - results by the CERN RD48 (ROSE) Collaboration*, Nucl. Instrum. Meth. A **465** (2001) no. 1, 60 – 69. SPD2000. 81

[120] S. Altenheiner, C. Gossling, J. Jentzsch, R. Klingenberg, T. Lapsien, D. Muenstermann, A. Rummler, G. Troska, and T. Wittig, *Planar slim-edge pixel sensors for the ATLAS upgrades*, JINST **7** (2012) C02051. 83

[121] I. Peric et al., *The FEI3 readout chip for the ATLAS pixel detector*, Nucl. Instrum. Meth. **A565** (2006) 178–187. 83, 136

[122] M. Keil, *ATLAS Pixel Detector: Running Experience*, 13-18 September, 2009. https://pos.sissa.it/archive/conferences/095/001/VERTEX%202009_001.pdf. PoS(Vertex 2009)001. 84

[123] ATLAS Collaboration, G. Darbo, *Experience on 3D Silicon Sensors for ATLAS IBL*, JINST **10** (2015) no. 05, C05001. 87

[124] T. Wittig, *Slim Edge Studies, Design and Quality Control of Planar ATLAS IBL Pixel Sensors.* PhD thesis, University of Dortmund, 2013. https://inis.iaea.org/search/search.aspx?orig_q=RN:47053488. 87

[125] M. Kocian, *ATLAS Pixel, Phase 0 (IBL)*, 16-21 September, 2012. https://pos.sissa.it/archive/conferences/167/035/Vertex%202012_035.pdf. PoS(Vertex 2012)035. 87

[126] M. Garcia-Sciveres et al., *The FE-I4 pixel readout integrated circuit*, Nucl. Instrum. Meth. **A636** (2011) S155–S159. 88, 127, 128, 129, 133, 139

[127] M. Benoit, M. Bomben, R. Carney, G. Giugliarelli, T. Lari, L. Meng, B. P. Nachman, A. Ducourthial, et al., *Modeling Radiation Damage Effects for Pixel Sensors in the ATLAS Detector*, In preparation (Mar, 2017) . https://cds.cern.ch/record/2255825. 91, 94, 98, 101, 107, 108, 109, 110, 111

[128] L. Rossini, *Operation and Radiation Damage studies of the ATLAS Pixel Detector*, April, 2017. https://agenda.infn.it/getFile.py/access?contribId=45&sessionId=22&resId=0&materialId=poster&confId=12289. In Incontri di Fisica delle Alte Energie 2017. 91

[129] ATLAS Collaboration, *The ATLAS Simulation Infrastructure*, Eur. Phys. J. **C70** (2010) 823–874. 92, 111

[130] ATLAS Collaboration, *Expected Performance of the ATLAS Inner Tracker at the High-Luminosity LHC*, 2016. ATL-PHYS-PUB-2016-025 (2016) , https://cds.cern.ch/record/2222304. 92

[131] T. Sjöstrand, S. Mrenna, and P. Z. Skands, *PYTHIA 6.4 Physics and Manual*, JHEP **05** (2006) 026. 92

[132] T. Sjöstrand, S. Ask, J. R. Christianss en, R. Corke, N. Desai, P. Ilten, S. Mrenna, S. Prestel, C. O. Rasmussen, and P. Z. Skands, *An Introduction to PYTHIA 8.2*, Comput. Phys. Commun. **191** (2015) 159. 92

[133] G. Battistoni, S. Muraro, P. R. Sala, F. Cerutti, A. Ferrari, S. Roesler, A. Fasso, and J. Ranft, *The FLUKA code: Description and benchmarking*, AIP Conf. Proc. **896** (2007) 31–49. [,31(2007)]. 92

[134] A. Ferrari, P. R. Sala, A. Fassò, and J. Ranft, *FLUKA: A multi-particle transport code (program version 2005).* CERN, Geneva, 2005. https://cds.cern.ch/record/898301. 92

[135] S. Baranov et al., *Estimation of Radiation Background, Impact on Detectors, Activation and Shielding Optimization in ATLAS*, 2005. https://cds.cern.ch/record/814823. 92

[136] ATLAS Collaboration, G. Aad et al., *Operation and performance of the ATLAS semiconductor tracker*, JINST **9** (2014) P08009. 92, 93

[137] ATLAS Collaboration, M. Aaboud et al., *Luminosity determination in pp collisions at $\sqrt{s}$ = 8 TeV using the ATLAS detector at the LHC*, Eur. Phys. J. **C76** (2016) no. 12, 653. 93

[138] S. van der Meer, *Calibration of the effective beam height in the ISR*, 1968. https://cds.cern.ch/record/296752. 93

[139] GEANT4 Collaboration, GEANT4 Collaboration, *GEANT4: A Simulation toolkit*, Nucl. Instrum. Meth. **A506** (2003) 250–303. 93, 111

[140] H. Bichsel, *Straggling in Thin Silicon Detectors*, Rev. Mod. Phys. **60** (1988) 663–699. 93

[141] M. Petasecca, F. Moscatelli, D. Passeri, and G. U. Pignatel, *Numerical Simulation of Radiation Damage Effects in p-Type and n-Type FZ Silicon Detectors*, IEEE Transactions on Nuclear Science **53** (2006) no. 5, 2971–2976. 96, 101

[142] ATLAS Collaboration Collaboration, J.-C. Beyer, *Simulation of the depletion voltage evolution of the ATLAS Pixel Detector*, . https://cds.cern.ch/record/2252757. 99

[143] V. Chiochia et al., *Simulation of heavily irradiated silicon pixel sensors and comparison with test beam measurements*, IEEE Trans. Nucl. Sci. **52** (2005) 1067–1075. 101

[144] G. Lutz, *Effects of deep level defects in semiconductor detectors*, Nucl. Instrum. Meth. **A377** (1996) no. 2, 234 – 243. 101, 161

[145] C. Jacoboni et al., *A review of some charge transport properties of silicon*, Solid-State Electronics **20** (1977) 77 – 89. 106, 107

[146] I. G. Kirnas et al., *Concentration dependence of the hall factor in n-type silicon*, Phys. Stat. Sol. **A23** (1974) K123–K127. 107

[147] G. Alimonti et al., *A study of charge trapping in irradiated silicon with test beam data*, ATL-INDET-2003-014 (2003) [cds.cern.ch:685542]. 109

[148] J. Idarraga and M. Benoit, *Generic Geant4 implementation for pixel detectors*, The AllPix Simulation Framework (2006) [twiki.cern.ch:AllPix]. 111

[149] ATLAS Collaboration, L. Rossini, T. Lari, M. Battaglia, B. P. Nachman, M. Bomben, A. Ducourthial, L. Meng, and R. Carney, *Charge Collection Efficiency as a function of integrated luminosity*, Tech. Rep. ATL-INDET-INT-2017-013, CERN, Geneva, Jul, 2017.
https://atlas.web.cern.ch/Atlas/GROUPS/PHYSICS/PLOTS/PIX-2017-004.
112

[150] A. Miucci and L. Jeanty, *IBL Calibration Plots and Drift of Calibration with Luminosity*, Tech. Rep. ATL-INDET-INT-2016-003, CERN, Geneva, Feb, 2016.
https://cds.cern.ch/record/2129027. 112

[151] ATLAS Collaboration Collaboration, S. Higashino and T. Imasaka, *IBL Calibration Plots and Drift of Calibration with Luminosity in 2016*, Tech. Rep. ATL-INDET-INT-2017-004, CERN, Geneva, Feb, 2017.
https://cds.cern.ch/record/2252674. 112

[152] *The HL-LHC project*,
http://hilumilhc.web.cern.ch/about/hl-lhc-project. 115, 116

[153] *The High-Luminosity LHC Project. 298th Meeting of Scientific Policy Committee*, Jun, 2016. https://cds.cern.ch/record/2199189. 115

[154] *Projections for measurements of Higgs boson signal strengths and coupling parameters with the ATLAS detector at a HL-LHC*, Tech. Rep. ATL-PHYS-PUB-2014-016, CERN, Geneva, Oct, 2014.
https://cds.cern.ch/record/1956710. 116

[155] ATLAS Collaboration Collaboration, *Prospects for a search for direct pair production of top squarks in scenarios with compressed mass spectra at the high luminosity LHC with the ATLAS Detector*, Tech. Rep. ATL-PHYS-PUB-2016-022, CERN, Geneva, Oct, 2016. https://cds.cern.ch/record/2220904. 116

[156] ATLAS Collaboration, *Letter of Intent for the Phase-II Upgrade of the ATLAS Experiment*, Dec, 2012. https://cds.cern.ch/record/1502664. 116, 117

[157] ATLAS Collaboration Collaboration, *ATLAS Phase-II Upgrade Scoping Document*, Sep, 2015. https://cds.cern.ch/record/2055248. 116, 117

[158] ATLAS Collaboration, *Technical Design Report for the ATLAS Inner Tracker Strip Detector*, Apr, 2017. https://cds.cern.ch/record/2257755. 117, 118, 119, 121, 122, 132, 142

[159] *RD53 Collaboration*, https://rd53.web.cern.ch/RD53/. 120

[160] J. Lange, M. C. Areste, E. Cavallaro, F. Förster, S. Grinstein, I. L. Paz, M. Manna, G. Pellegrini, D. Quirion, S. Terzo, and D. V. Furelos, *3D silicon pixel detectors for the High-Luminosity LHC*, Journal of Instrumentation **11** (2016) no. 11, C11024. 120

[161] S. Terzo, *Development of radiation hard pixel modules employing planar n-in-p silicon sensors with active edges for the ATLAS detector at HL-LHC.* PhD thesis, Technische Universitat Munchen, Max-Planck-Institut fur Physik,, 2015. https://mediatum.ub.tum.de/doc/1276352/1276352.pdf. 121

[162] Y. Unno et al., *Development of novel n+-in-p Silicon Planar Pixel Sensors for HL-LHC*, Nucl. Instrum. Meth. **A699** (2013) 72 – 77. 121

[163] I. Perić, *A novel monolithic pixelated particle detector implemented in high-voltage CMOS technology*, Nucl. Instrum. Meth. **A582** (2007) no. 3, 876 – 885. VERTEX 2006. 121

[164] P. Rymaszewski, M. Barbero, P. Breugnon, S. Godiot, L. Gonella, T. Hemperek, T. Hirono, F. Hügging, H. Krüger, J. Liu, P. Pangaud, I. Peric, A. Rozanov, A. Wang, and N. Wermes, *Prototype Active Silicon Sensor in 150 nm HR-CMOS technology for ATLAS Inner Detector Upgrade*, Journal of Instrumentation **11** (2016) no. 02, C02045. 121

[165] T. Hemperek, T. Kishishita, H. Krüger, and N. Wermes, *A Monolithic Active Pixel Sensor for ionizing radiation using a 180nm HV-SOI process*, Nucl. Instrum. Meth. **A796** (2015) 8 – 12. Proceedings of the 10th International Conference on Radiation Effects on Semiconductor Materials Detectors and Devices. 121

[166] I. Mandič, V. Cindro, A. Gorišek, B. Hiti, G. Kramberger, M. Mikuž, M. Zavrtanik, T. Hemperek, M. Daas, F. Hgging, H. Krüger, D.-L. Pohl, N. Wermes, and L. Gonella, *Neutron irradiation test of depleted CMOS pixel detector prototypes*, Journal of Instrumentation **12** (2017) no. 02, P02021. 122

[167] G. Kramberger, V. Cindro, I. Mandic, M. Mikuz, M. Milovanovic, and M. Zavrtanik, *Investigation of electric field and charge multiplication in silicon detectors by Edge-TCT,* in *2009 IEEE Nuclear Science Symposium Conference Record (NSS/MIC)*, pp. 1740–1748. Oct, 2009. 122

[168] *ATLAS Upgrade Planar Pixel Sensor R&D Project*, https://twiki.cern.ch/twiki/bin/view/Atlas/PlanarPixelUpgrade. 123

[169] M. Bomben, *Recent progress of the ATLAS Planar Pixel Sensor R&D Project*, Physics Procedia **37** (2012) 940 – 949. Proceedings of the 2nd International Conference on Technology and Instrumentation in Particle Physics (TIPP 2011). 123

[170] L. Snoj, A. Trkov, R. Jacimovic, P. Rogan, G. Zerovnik, and M. Ravnik, *Analysis of neutron flux distribution for the validation of computational methods for the optimization of research reactor utilization*, Applied Radiation and Isotopes **69** (2011) no. 1, 136 – 141. 123

[171] G. Casse, A. Affolder, P. Allport, H. Brown, and M. Wormald, *Enhanced efficiency of segmented silicon detectors of different thicknesses after proton irradiations up to 1x10**16 neq cm2*, Nucl. Instr. and Meth. A **624** (2010) no. 2, 401 – 404. New Developments in Radiation Detectors. 124

[172] G.-F. D. Betta, M. Boscardin, M. Bomben, M. Brianzi, G. Calderini, G. Darbo, R. Dell'Orso, A. Gaudiello, G. Giacomini, R. Mendicino, M. Meschini, A. Messineo, S. Ronchin, D. Sultan, and N. Zorzi, *The INFN-FBK "Phase-2" R&D program*, Nucl.

Instr. and Meth. A **824** (2016) 388 – 391. Frontier Detectors for Frontier Physics: Proceedings of the 13th Pisa Meeting on Advanced Detectors. 127, 128

[173] S. Jansen, H. Spannagel et al, *Performance of the EUDET-type beam telescopes*, EPJ Techniques and Instrumentation **3** (2016) no. 1, 7. 128, 139

[174] A. Ducourthial, M. Bomben, et al., *FBK-INFN-LPNHE thin n-on-p pixel detectors: beamtest results*, 2017. https://indico.cern.ch/event/587631/contributions/2467357/. 12th Trento Workshop on Advanced Silicon Radiation Detectors. 129

[175] A. Ducourthial et al., *FBK-INFN-LPNHE thin n-on-p pixel detectors: beamtest results*, https://indico.cern.ch/event/615961/contributions/2659621/. In Position Sensitive Detectors 11. 129

[176] J. Lange, E. Cavallaro, S. Grinstein, and I. L. Paz, *3D silicon pixel detectors for the ATLAS Forward Physics experiment*, Journal of Instrumentation **10** (2015) no. 03, C03031. 132

[177] C. D. Via et al., *3D silicon sensors: Design, large area production and quality assurance for the ATLAS IBL pixel detector upgrade*, Nucl. Instr. and Meth. A **694** (2012) 321 – 330. 133

[178] E. Vianello, A. Bagolini, P. Bellutti, M. Boscardin, G.-F. Betta, G. Giacomini, C. Piemonte, M. Povoli, and N. Zorzi, *Optimization of double-side 3D detector technology for first productions at FBK,* in *Nuclear Science Symposium and Medical Imaging Conference (NSS/MIC), 2011 IEEE*, pp. 523–528. Oct, 2011. 133, 138, 140

[179] M. Bomben, A. Bagolini, M. Boscardini, L. Bosisio, G. Calderini, J. Chauveau, G. Giacomini, A. La Rosa, G. Marchori, and N. Zorzi, *Performance of Irradiated Thin Edgeless N-on-P Planar Pixel Sensors for ATLAS Upgrades,* in *Proceedings, 2013 IEEE Nuclear Science Symposium and Medical Imaging Conference (NSS/MIC 2013): Seoul, Korea, October 26-November 2, 2013*, p. 6829425. 2013. 134

[180] M. Backhaus et al., *Development of a versatile and modular test system for ATLAS hybrid pixel detectors*, Nucl. Instr. Meth. A **650** (2011) no. 1, 37 – 40. International Workshop on Semiconductor Pixel Detectors for Particles and Imaging 2010. 139

[181] *Reconfigurable Cluster Element, https://rceproject.web.cern.ch/.* https://rceproject.web.cern.ch/. 139

[182] *http://eutelescope.web.cern.ch/.* http://eutelescope.web.cern.ch/. 140

[183] *ROOT Data Analysis Framework.* https://root.cern.ch/. 140

[184] *https://bitbucket.org/TBmon2/tbmon2/overview.* https://bitbucket.org/TBmon2/tbmon2/overview. 140

[185] S. Ronchin et al., *Edgeless planar pixel sensors with ATLAS and CMS designs produced by FBK-CMM*, 2017. https://indico.cern.ch/event/587631/contributions/2471721/. 12th Trento Workshop on Advanced Silicon Radiation Detectors. 149

[186] Gregor Kramberger, *Radiation damage models, comparison and perfomance of TCAD simulation*, 25-30 September, 2016. https://indico.cern.ch/event/452781/contributions/2297596/. 150

[187] H. Hara, P. P. Allport, et al., *Charge collection and field profile studies of heavily irradiated strip sensors for the {ATLAS} inner tracker upgrade*, Nucl. Instrum. Meth. A **831** (2016) 181 – 188. 150

[188] ATLAS Collaboration, M. Aaboud et al., *Jet reconstruction and performance using particle flow with the ATLAS Detector*, Eur. Phys. J. **C77** (2017) no. 7, 466. 150

[189] Ali Koşar, *Effect of substrate thickness and material on heat transfer in microchannel heat sinks*, International Journal of Thermal Sciences **49** (2010) no. 4, 635 – 642. 152

[190] A. Nomerotski, J. Buytart, P. Collins, R. Dumps, E. Greening, M. John, A. Mapelli, A. Leflat, Y. Li, G. Romagnoli, and B. Verlaat, *Evaporative CO 2 cooling using microchannels etched in silicon for the future LHCb vertex detector*, Journal of Instrumentation **8** (2013) no. 04, P04004. 152

[191] M. Bomben, *Development and production of silicon micro-channels prototypes: Paris contribution*, 4-7 April, 2017. https://indico.cern.ch/event/590645/contributions/2542241/. 152

[192] S.-M. Kim and I. Mudawar, *Review of databases and predictive methods for pressure drop in adiabatic, condensing and boiling mini/micro-channel flows*, International Journal of Heat and Mass Transfer **77** (2014) 74 – 97. 153

[193] G. Kramberger et al., *Effective trapping time of electrons and holes in different silicon materials irradiated with neutrons, protons and pions*, Nucl. Instr. and Meth. A **481** (2002) no. 1-3, 297 – 305. 160